warwick.ac.uk/lib-publications

Developments in Scanning Electrochemical Cell Microscopy for Applications to Multiphase Systems
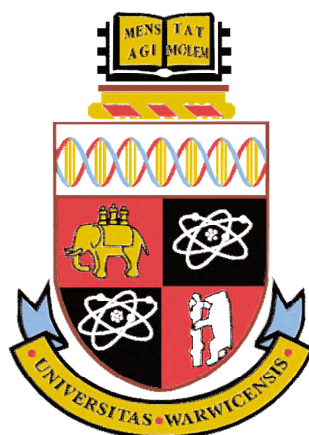
Enrico Daviddi

Degree of Doctor of Philosophy in Chemistry

Department of Chemistry

University of Warwick

December 2020

"O frati," dissi, *"che per cento milia
perigli siete giunti a l'occidente,
a questa tanto picciola vigilia*

*d'i nostri sensi ch'è del rimanente
non vogliate negar l'esperïenza,
di retro al sol, del mondo sanza gente.*

*Considerate la vostra semenza:
fatti non foste a viver come bruti,
ma per seguir virtute e canoscenza."*

Inferno, Canto XXVI

Contents

List of Figures

CHAPTER 2

CHAPTER 3

CHAPTER 4

Figure 5.5. (a) E_{surf} map for the Cu^{2+}/Cu process (Cu electrodeposition) on a polycrystalline Cu foil electrode immersed in dodecane, obtained with SECCM with I_{app} = − 0.88 mA cm^{-2}. The nanopipette probe contained aerated 10 mM H_2SO_4 and contacted an area of 6.4×10^{-9} cm^2. The map was extracted at time 0.25 s of Movie S2. **(b)** Map of $\tau_{Cu^{2+}/Cu}$, extracted from Movie A5. The grain areas determined from Figure 5.4b are overlaid on the maps in (a) and (b). **(c – d)** Full grain orientation correlation analysis of (c) E_{surf} at 0.25 s and (d) $\tau_{Cu^{2+}/Cu}$, extracted from (a) and Figure A.14c, and (b) and Figure A.14d, respectively, with the average grain orientation extracted from Figure 5.4b and Figure A.14b. The insets in (c) and (d) show the distributions of E_{surf} and $\tau_{Cu^{2+}/Cu}$, extracted from grains γ, δ and ε, marked in Figure 5.4b. Details of the data extracted for each grain can be found in Appendix, section A.5.1 (Figure A.15 and Table A.2). 173

Figure 5.6: **(a)** SECCM E_{surf} map at OCP on a polycrystalline Cu foil electrode immersed in dodecane. The nanopipette probe contained aerated 10 mM H_2SO_4 and contacted an area of 6.4×10^{-9} cm^2 at each location in the map. The map was extracted at time − 0.01 s of Movie A5 (negative times are used for indicating the pre-cathodic OCP step). The grain boundaries from Figure 5.4b are overlapped on the map. **(b)** Full grain orientation correlation analysis of E_{surf} at − 0.01 s from (a) and Figure A.14e *versus* the average grain orientation, extracted from Figure 5.4b and Figure A.14b. Details of the data extracted for each single grain can be found in Appendix, section A.5.1 (Figure A.15 and Table A.2). Relevant orientation areas are marked on the graph. **(c)** Plot of the general correlation between $\tau_{Cu^{2+}/Cu}$ from Figure 5.5b and Figure A.14d, *versus* the E_{surf} in the OCP step for each point measurement (from Figure 5.6a and Figure A.14e). τ is represented as the median values of τ for each recorded value of OCP (with a step size of 0.31 mV, corresponding to the sensitivity of the measurement), with an error bar representing the standard deviation for the same set of data. Only the OCP points with at least 10 τ values are represented. 176

Figure 5.7: **(a)** SEM image of the scanned area of Figure 5.4 and Figure 5.5 (Movie A5), with main surface scratches labelled with the letters *a-e*. **(b)** Raw EBSD map (*i.e.* without grain boundaries drawn) of the area scanned in the ESI, Movie A5. Five main surface defects (scratches), labelled *f – i*, are identified. Note that scratches can be generally identified as a black zone in EBSD images, due to the fact that the "shadow effect" of the scratches walls generally do not allow the underlying crystallographic orientation to be

CHAPTER 6

Figure 6.8: **(a)** Extract of E_{5mA} maps from Movie A10 (aerated conditions) and **(b)** the corresponding EBSD map (extract of Figure A.17d). **(c-d)** Extracts of (c) E_{5mA} and (d) GOS vs. structure (average grain orientation) correlation plots, respectively from Figure 6.6f and Figure 6.9

Figure 6.9: Correlation plot for the GOS and the crystallographic orientation for the aerated case, obtained by data extracted form Figure 6.6d and Figure A.17d. Significant grains mentioned in the text are highlighted on the plot

CHAPTER 7

Figure 7.1: Chemical structures of **(a)** 1,2,3-Benzotriazole and **(b)** 1-N,N-bis-(2-ethylhexyl)-ARmethyl-benzotriazole-1-methanamine (BTA–R), the oil soluble derivative considered in this contribution. The red structure in (b) highlights the part of the molecule in common between (a) and (b).

Figure 7.2: **(a-b)** SECCM current maps extracted from Movie A11, respectively at **(a)** the beginning (E = − 0.45 V) and **(b)** the end (E = + 0.64 V) of the LSV sweep. **(c)** Crystallographic orientation map (IPFz) measured with EBSD on the same area. The grain boundaries extracted from (c) were overlaid on (a) and (b). **(d)** Exemplar average LSV curves extracted from selected grains marked in (c) and magnification of respectively the cathodic wave **(e)** and the anodic wave **(f)**. The overall average curve was also added in (d-f). **(g-h)** Statistical distribution of the current measured (a) and (b), respectively in **(g)** for the cathodic current and **(h)** for the anodic current, for the specific grains highlighted in (c).

Figure 7.3: **(a-b)** comparison of the average LSV curves before and after the addition of BTA–R to the oil layer, respectively in **(a)** the de-aerated case (comparing the averages obtained from Movies A7-A8, with those obtained from Movies A11-A13, averaging respectively 5200 and 7440 single measurements) and **(b)** the aerated case (comparing the averages obtained from Movies A9-A10 with those obtained from Movies A14-A15, averaging respectively 5100 and 5200 single measurements). **(c)** Contact angle measurement obtained with a 10 mM H2SO4 solution droplet (300 μL) deposited on a mirror polished polycrystalline Cu surface covered in pure dodecane (black spots) or a 100 ppm solution of BTA–R in dodecane. In each case the uninhibited case is represented by black colour and inhibited case by red colour.

Figure 7.4: 2D correlation plots between the crystallographic orientation and E_{2mA} of the cathodic process in de-aerated condition, respectively **(a)** in absence and **(b)** in

APPENDIX

List of Tables

Table A.6: List of all grains analysed by SECCM in aerated condition (Movie A14 and A15), with the average Euler angles, Miller indices and Projection Coordinates and anodic and cathodic E_{2mA} listed for each one. The grain IDs correspond to those defined

Acknowledgments

Saying thanks is always very long and complicated, especially for a work, such as this thesis, that comprehends hundreds of pages and the contribution of many, many people, which I wish to thank even if they are not mentioned here.

Firstly I would like to thank my supervisor, Pat, for welcoming me in his research group, giving me continuous help in these four years and, above all, always trusting and believing in me in everything I did under his watch. On top of that, I have always been amazed by the continuous discussion and reasoning of, often, a very limited amount of experimental data, that ended up in a completely different place from where it started, opening infinite possibilities of new research and developments.

A big thank also to my sponsor, Lubrizol, for funding my PhD and giving constant support, as well as keeping funding several projects of research that mean so much for young researcher like me. In particular, I wish to thank the two people, Paul and Mat, that were not only my industrial supervisors but also a precious guide through the complicated world of industry, and a constant point of reference during this PhD.

An enormous thank to Cameron, who has taken on his shoulders the ungrateful task of listening to my doubts and queries every three seconds, and reading and correcting literally every word I

wrote. I will never thank you enough for that.

Another special thank to Slava, who essentially made me realise that I did not know anything about corrosion and really helped me scaling up my research with a different point of view.

Thanks to Minkyung because she is just amazing, and she knows it.

Thanks to all the WEIG group, which, I know, I should thank one by one but I don't think I could stay in the limit of words. Thanks particularly to Julie for her continuous support and for being a wonderful teacher, and to all the others for creating a nice and interesting environment for work and after work.

Thanks also to Erin and her fantastic group at the University of Arizona, for always reminding us how actually the best opportunities sometimes come from chance and interpersonal relationships, i.e. how to take a random meeting at a conference and transform it into a proficient collaboration.

A very special thanks to Prof. Giovanni Costantini and Prof. Frédéric Kanoufi, respectively the internal and external member of my final examination panel. I found our discussion during the Viva extremely enriching, and I really appreciated the great amount of time you decided to spend revising my work.

Well, for a person that is usually very stingy with thanks (sorry for that, this is just who I am), I think I have given quite a lot of them in these few lines. However, there are final special thanks that I would like to deliver. To my friends (I am not going to name anyone in order not to make anyone else upset, but you know who you are), for making me laugh in the face of quite a committing PhD life; and to my family, which despite I decided to continue my studies 1500 km far from home, have always been on my side in every choice I made. Thank you.

General Declaration

The work presented in this thesis is entirely original and carried out completely by myself, except where acknowledged in the list below. This thesis has not been submitted for a degree at another University. Some of the material present in the main text has been published, as noted below.

Chapter 3

The work presented in Chapter 3 was carried out in collaboration with the Laboratory for Interface Science of Printable Electronic Materials at the University of Arizona, which provided the sample and carried out some of the electrochemical analysis presented here (as highlighted in the text). It was published as:

Enrico Daviddi, Zhiting Chen, Brooke Massani, Jaemin Lee, Cameron Bentley, Patrick Unwin, Erin Ratcliff, **Nanoscale Visualization and Multiscale Electrochemical Analysis of Conductive Polymer Electrodes**, *ACS Nano*, 2019, **13** *(11)*, 13271-13284.

Chapter 4

The work presented in Chapter 4 was published as:

Enrico Daviddi, Katerina L Gonos, Alex W Colburn, Cameron L Bentley, Patrick R Unwin, **Scanning Electrochemical Cell Microscopy (SECCM) Chronopotentiometry: Development and Applications in Electroanalysis**

and Electrocatalysis, *Analytical Chemistry*, 2019, **91** *(14)*, 9229-9237.

Chapter 5

The work presented in Chapter 5 was published as:

<u>Enrico Daviddi</u>, Viacheslav Shkirskiy, Paul M. Kirkman, Mathew P. Robin, Cameron L. Bentley1, and Patrick R. Unwin, **Nanoscale Electrochemistry in a Copper/Aqueous/Oil Three-phase System: Surface Structure-Activity-Corrosion Potential Relationships**, *Chemical Science,* 2021, *Accepted Manuscript*, DOI: 10.1039/D0SC06516A.

Other publications

Additionally, during my PhD I have contributed to the following research articles whose results are not presented in this thesis:

Binglin Tao, Lewis C Yule, <u>Enrico Daviddi</u>, Cameron L Bentley, Patrick R Unwin, **Correlative Electrochemical Microscopy of Li-Ion (De)intercalation at a Series of Individual LiMn2O4 Particles**, *Angewandte Chemie,* 2019, **131** (*14*), 4654-4659.

Viacheslav Shkirskiy, Lewis C. Yule, <u>Enrico Daviddi</u>, Cameron L. Bentley, Jolyon Aarons, Geoff West and Patrick R. Unwin, **Nanoscale Scanning Electrochemical Cell Microscopy and Correlative Surface Structural Analysis to Map Anodic and Cathodic Reactions on Polycrystalline Zn in Acid Media**, *Journal of The Electrochemical Society*, 2020, **167**, 041507

Lewis C Yule, <u>Enrico Daviddi</u>, Geoff West, Cameron L Bentley, Patrick R Unwin, **Surface microstructural controls on electrochemical hydrogen absorption at polycrystalline palladium**, *Journal of Electroanalytical Chemistry*, 2020, 114047.

Viacheslav Shkirskiy, Minkyung Kang, Ian J McPherson, Cameron L Bentley, Oluwasegun J Wahab, <u>Enrico Daviddi</u>, Alex W Colburn, Patrick R Unwin, **Electrochemical Impedance Measurements in Scanning Ion Conductance Microscopy**, *Analytical Chemistry*, 2020, **92** (*18*), 12509-12517

Abstract

Scanning Electrochemical Cell Microscopy (SECCM) has proven powerful for gaining electrochemical knowledge of microscopically structured surfaces, and this work is aimed at expanding the horizon of its application to complex multiphase systems, through new examined materials, electrochemical methods, experimental configurations and methods of data analysis. Firstly, SECCM is applied in the conventional voltammetric mode to a microscopically mixed polymer electrode blend consisting of conductive P3HT and insulating PMMA, revealing that P3HT is still able to exhibit relatively facile electron transfer kinetics when in the blend, contrary to macroscale electrochemistry results, which are mostly controlled by parasitic resistance. Then, a new, current controlled (chronopotentiometric) SECCM setup is developed and tested on model systems of increasing complexity, demonstrating stable and reproducible local electrochemistry with widespread applicability, *e.g.*, to measure the "onset potential" in an electrocatalytic system at minimal driving force. Chronopotentiometric SECCM is then applied to the study of structure-dependent Cu corrosion in a novel triple-phase aqueous nanodroplet/oil/metal configuration, where a newly developed electrochemistry/crystallography correlation analysis is applied to visualise the trend in surface activity across the whole spectrum of orientations within a polycrystal. The high-index facets present a complex pattern of surface reactivity that cannot be simply interpreted as combination of the behaviour of the low-index grains. Using the same system, but applying the conventional voltammetric SECCM mode, two possible oil related effects and their intercorrelations are then explored: the effect of dissolved O_2 and the effect of an oil-soluble corrosion inhibitor. A strongly grain dependent and unique action is observed on both the anodic and cathodic reactions that drive Cu corrosion, with the high flux of O_2 across the three phase interface dramatically enhancing (anodic) electro-dissolution, as well as changing the apparent mechanism of corrosion inhibition. Overall this work opens up a wide range of new possibilities for SECCM in the study of complex multiphase systems, with relevant application in the fields of opto-electronics, energy transformation and corrosion.

Abbreviations

AFM	Atomic Force Microscopy
BTAH	1,2,3 - Benzotriazole
BTA−R	1-N,N-bis-(2-ethylhexyl)-ARmethyl-benzotriazole-1-methanamine
c-AFM	Conductive Atomic Force Microscopy
CE	Counter Electrode
CV	Cyclic Voltammetry, Cyclic Voltammogram
DFT	Density Functional Theory
DOS	Density of States
EBSD	Electron Backscattered Diffraction
ECR	Electrochemical CO_2 Reduction
EIS	Electrochemical Impedance Spectroscopy
Fcc	Face centered cubic
FcDM	1,1′-Ferrocenedimethanol
FEM	Finite Element Method
FPGA	Field-Programmable Gate Arrays
GC	Glassy Carbon
GDP	Gross Domestic Product
GID	Grazing Incidence Diffraction
GOS	Grain Orientation Spread

HER	Hydrogen Evolution Reaction
HOPG	High Oriented Pyrolytic Graphite
IPFz	Inverse Pole Figure in the z Direction
ITO	Indium Tin Oxide
KPFM	Scanning Kelvin Probe Force Microscopy
LSV	Linear Sweep Voltammetry
OCP	Open Circuit Potential
OHP	Outer Helmholtz Plane
ORR	Oxygen Reduction Reaction
P3HT	Poly(3-hexylthiophene)
PANI	Polyaniline
PMMA	Poly(methyl methacrylate)
PTFE	Poly(tetrafluoroethylene)
QRCE	Quasi-Reference Counter Electrode
RE	Reference Electrode
RHE	Reversible Hydrogen Electrode
RDS	Rate Determining Step
RMS	Root Mean Square
SECCM	Scanning Electrochemical Cell Microscopy
SECM	Scanning Electrochemical Microscopy
SEM	Scanning Electron Microscopy
SEPM	Scanning Electrochemical Probe Microscopy
SERS	Surface Enhanced Raman Spectroscopy
SEXAFS	Surface Extended X-ray Absorption Fine Structure
SHE	Standard Hydrogen Electrode
SICM	Scanning Ion Conductance Microscopy
SPIP	Scanning Probe Image Processing
SPM	Scanning Probe Microscopy
STEM	Scanning Electron Transmission Microscopy

STM	Scanning Tunnelling Microscopy
TEM	Transmission Electron Microscopy
UME	Ultramicroelectrode
WE	Working Electrode
WEC-SPM	Warwick Electrochemical Scanning Probe Microscopy
XPS	X-Ray Photoelectron Spectroscopy

Glossary of Symbols

A	Electrode area
a	Activity
$a(0,t)$	Activity at the surface, at time t
A_{ac}	Alternate current amplitude
C	Concentration
$C(0,t)$	Concentration at the surface, at time t
C^*	Bulk concentration
C_1	Grain orientation coordinate 1
C_2	Grain orientation coordinate 2
C_{OHP}	Double layer capacitance
D	Diffusion coefficient
d	Distance from the electrode
E	Cell potential
E^0	Standard potential
$E^{0'}$	Formal potential
E_1	Bias potential in double channel SECCM
$E_{1/2}$	Half wave potential
$E_{1/4}$	One quarter-wave potential
E_2	Potential between QRCE and the surface
E_{2mA}	Onset potential, current density of 2 mA cm^{-2}

$E_{3/4}$	Three quarters-wave potential
E_{5mA}	Onset potential, current density of 5 mA cm^{-2}
E_{corr}	Corrosion potential
E_{eff}	Effective potential
E_{eq}	Equilibrium potential
E_f	Final potential
E_i	Initial potential
E_{OCP}	Esurf at OCP
E_{output}	Galvanostat output potential
E_p	Voltammetric peak potential
E_{surf}	Surface potential
E_λ	Switch potential
$E_{\tau/4}$	Potential at $\tau/4$
F	Faraday constant
h	Plank constant
h	Pipette height
h,k,l	Miller indexes
h_{dod}	Dodecane layer height
h_{dr}	Droplet height
i	Current
I	Current density
i_0	Exchange current
I_∞	Bulk current density
I_{app}	Applied current density
i_{app}	Applied current
i_C	Capacitive current
i_{corr}	Corrosion current
i_{dc}	Double channel current
i_F	Faradaic current

i_p	Voltammetric peak current
I_{ss}	Stationary state current density
i_{ss}	Stationary state current
i_{surf}	Surface current
i_T	SECM tip current
J	vectorial flux
J_x	x component of the flux
J_y	y component of the flux
J_z	z component of the flux
k	Kinetic constant
k^0	Heterogeneous electron transfer constant
k_B	Boltzmann constant
k_{et}	Electron transfer rate
k^{et}	Heterogeneous standard rate constant
k_{in}	Inward flux rate constant
k_m	Mass transport rate
k_o	Overall rate
k_{O2}	Kinetic constant of O_2 reaction with $Cu(I)$
k_{out}	Outward flux rate constant
K_{part}	Partition coefficient
n	Number of exchanged electrons
n_a	Point to average
Q	Charge
R	Universal gas constant
r	Radial coordinate
r_0	Electrode radius
r_a	FEM electrode radius
r_b	FEM insulating area range

R_{CT}	Heterogeneous charge-transfer resistance
r_{da}	Data acquisition rate
r_{dod}	Dodecane phase size, bottom
r_{e}	Electrode radius
R_{f}, R_{film}	Polymer film resistance
r_{g}	Pipette glass thickness
r_{i}	Interface between nanodroplet and dodecane
R_{LT}	Lateral charge-transfer resistance
r_{p}	Pipette aperture radius
R_{s}	Solution resistance
r_{t}	Capillary radius
r_{td}	Dodecane phase size, top
r_{tr}	Transition distance
R_{u}	Uncompensated resistance
T	Absolute temperature
t	Time
t_{L}	Stationary state limit time
t_{m}	Time per data points
t_{λ}	Switch time
v	Voltammetric sweep rate
z	Normal coordinate
z	Nominal charge
α	Forward electron transfer coefficient
β	Backward electron transfer coefficient
γ	Activity coefficient
γ_{1}	Angle with (001)
γ_{2}	Angle with (011)
γ_{3}	Angle with (111)
ΔE_{drop}	Potential drop in solution

ΔE_u	Potential drop by uncompensated resistance
$\Delta G^{\ddagger}$	Free energy of the transition state
$\Delta \phi$	Electromotive force
ε	Relative dielectric constant
ε_0	Absolute dielectric constant
η	Overpotential
κ	Transmission coefficient
μ_e	Chemical potential of the electron
σ	Standard deviation
τ	Transition time
υ	Charge flux
Φ	Euler angle 2
φ_1	Euler angle 1
φ_2	Euler angle 3
∇C	Concentration gradient
$\nabla \phi$	Potential gradient

Chapter 1

Introduction

This thesis is about the exploration of the complexity of electro-active surfaces. The centrality of surface processes, especially in electrochemical applications, has been widely appreciated for a long time, with even Walter Brattain, the father of modern transistors, highlighting it at the very beginning of his Nobel Prize lecture, not later than 1956:[1]

> *"It is at a surface where many of our most interesting and useful phenomena occur. We live for example on the surface of a planet. It is at a surface where the catalysis of chemical reactions occur. It is essentially at a surface of a plant that sunlight is converted to a sugar. In electronics, most if not all active circuit elements involve non-equilibrium phenomena occurring at surfaces. Much of biology is concerned with reactions at a surface."*

After this statement, however, Brattain observed how little progress had been made by physicists to that moment in understanding surface properties, if compared to bulk gases and solids. At a distance of 64 years, his words are still rather pertinent; indeed, even though enormous progress has been made in understanding surface processes and properties,[2-5] it is

still considerably easier to study the physics and chemistry of a bulk material rather that its interfacial behaviour.

Particularly in electrochemistry, whose definition lays in the notion of electron transfer between two different phases, the concept of surface and surface reactivity relative to interfacial processes is still a hot topic for any new research. The study of the electrochemical reactivity of surfaces is therefore fundamental in fields such as energy storage,[6-8] electrocatalysis,[9-12] fuel cells[13,14] and photo electrochemical devices,[15-18] only for citing a few, but also in fields that, despite not involving an electrochemical cell, are based on electron transfer processes across an interface, such as metal corrosion[19-26] and some fundamental metabolic processes.[27-30]

In general, the surface presents a peculiar reactivity, if compared to the bulk material, because of the non-ideal status of the atoms, ions or molecules on the top-most layer, whose interaction with the surroundings is somehow disrupted due to the lack of their counterparts in one or more coordination site(s).[31-33] Furthermore, the composition of the surface could be relatively different from the composition of the bulk, due to chemical reactions with the surrounding environment and/or contamination, and complex topographical features can be present, adding unique active sites for chemical and physical processes.

Over the years, specific techniques have been developed to examine the properties of very thin layers, in order to distinguish the surface properties from those of the bulk.[3,5,34,35] Important examples include spectroscopic methods such as surface enhanced Raman spectroscopy (SERS)[36] or surface extended X-ray absorption fine structure (SEXAFS)[37] and X-Ray photoelectron spectroscopy (XPS),[38] or diffraction techniques such as grazing incidence X-Ray or neutron diffractions (GID),[39,40] and many others.[41,42] If the overall difference between the surface and the bulk is already *per se* a wide field of study, another factor of complexity of a surface behaviour resides in its heterogeneity on a microscopic level.

The study of surface features in the micrometric to nanometric range (even to the atomic scale), is often determinant for a comprehensive understanding of the macroscopic surface behaviour.[43,44] Such features span from the crystallographic orientation and defects in crystallographic structure (if the material is crystalline), to the patterns of mixing of different materials (if the material is a mixture), to the presence of certain topographical features and so on. Therefore, a fundamental tool in the study of surface properties is represented by the microscopy techniques,[45] which can be generally divided into two broad categories. First, the techniques that use the properties of the interaction of the surface with radiation, such as optical and electron microscopy. Second, the techniques that take advantage of the interaction between the surface and a motile microscopic probe, collectively classified as scanning probe microscopy (SPM).

The first group includes important widespread techniques such as transmission electron microscopy (TEM),[46] scanning electron microscopy (SEM),[47] which use an electron beam to visualise the sample, techniques that use visible light (from the classical optical microscopy to the extremely advanced fluorescence near-field microscopy),[48,49] and many other sorts of radiation.[50,51] The second group includes techniques that have been developed mostly in the last 40 years, and are based on the interaction between the sample surface and a microscopic probe.[52] Starting from scanning tunnelling microscopy (abbr. STM, which involves measuring the tunnelling current between the substrate and the probe),[53,54] several techniques have been developed. This includes atomic force microscopy (abbr. AFM, where the mechanical force between the probe and the substrate is measured)[55] scanning kelvin probe (KPFM)[56,57] and, finally, various scanning electrochemical probe microscopies (SEPMs), where the measured signal between the probe and the substrate is electrochemical in nature (such as the current or the electromotive force).[24,58-62]

As explored in the following paragraphs, SEPM has proved to be extremely useful in characterising the microscopical properties of electroactive materials in the environment where they are supposed to operate, rather than ideal experimental conditions (such as high-ultra-vacuum or controlled atmospheres). It comprises methods such as scanning electrochemical microscopy (SECM)[58] and scanning ion conductance microscopy (SICM)[59] the first of these techniques, both developed in 1989, [63,64] and the electrochemical microcell techniques[24,60] such as scanning electrochemical cell microscopy (SECCM)[61,62,65] which is the main topic of this dissertation.

Improving these techniques and expanding their fields of application is a hot topic in microscopy and a great challenge in electrochemical research,[66] and this thesis was developed along this line. But in order to give a context to the data that will be presented, this introductory chapter will first describe the fundamentals of electrochemical processes and electrochemical techniques, before moving on to describe the principles and main accomplishments of the SEPM techniques most relevant to this work. Finally, a few topics will be introduced where SEPM has the potential to be revolutionary, both in terms of the study of the subject/phenomenon, as well as in the application of the technique itself.

1.1. BASICS OF ELECTROANALYSIS

This section will give an overview of the main principles of electrochemistry and how they are applied in classical electroanalytical techniques, with particular focus on the ones that are most relevant for this work.

1.1.1. Fundamental parameters

Electrochemistry involves the study of the electron transfer that happens at the interface between two distinct chemical phases, and how the composition and the reactivity of these phases influence it.[67] Usually, the

electron transfer happens between an electronic conductor, generally a solid electrode (M_1), and an ionic conductor or electrolyte, *i.e.* a liquid solution containing dissociated ions (S). The electrochemical system is usually completed by putting S in contact with another metallic conductor (M_2), and connecting M_1 and M_2 to a power source (V) through metal cabling (M_3).[68] Therefore, a typical electrochemical system can be described as a series of subsequent connections forming an electrochemical cell, in sequence V/M_3, M_3/M_1, M_1/S, S/M_2, M_2/M_3', M_3'/V. Within this kind of system, two parameters are considered fundamental for characterising the electrochemical reaction at the interface M_1/S, the electromotive force ($\Delta\phi_{M1/S}$), intended as the electrical work necessary to transport a charge from M_1 to S, and the charge flux through the surface (v), as indicator of the rate of the reaction. Such parameters are not directly measured, but can be related to the two main instrumental parameters, the cell potential (E) and the current (i).

The electromotive force $\Delta\phi_{M1/S}$ is the effective driving force for the electron transfer that happens at the interface of interest, and it is related to the cell potential E (applied at the power source V) through this relation:[69]

$$E = \left(\Delta\phi_{M_1/S} - \frac{\mu_e^{M_1}}{F} \right) - \left(\Delta\phi_{M_2/S} - \frac{\mu_e^{M_2}}{F} \right) \tag{1.1}$$

where

$$E_i = \Delta\phi_{M_i/S} - \frac{\mu_e^{M_i}}{F} \tag{1.2}$$

is the half-cell potential corresponding with the interface between the solution and the metallic conductor (M_i). In the equations, $\Delta\phi_{Mi/S}$ is the electrical driving force of the reaction, while μ_e^{Mi} is the chemical potential of the electron, *i.e.* the chemical driving force of the reaction, and F the Faraday constant. Therefore, the potential, *E*, applied at the electrode is

an indirect measure of the reaction driving force, being expressed as a difference between the two electrodic processes. In electrochemical studies, in order to focus on the interface of interest (M_1/S), E_2 is ideally kept constant and set as a reference in order to make E_1 the only variable in the system, such that it can be expressed solely as E; however, such E represents the difference relative to a constant reference value.[69]

The flux v, which is an indicator of the rate of the reaction carried out at the electrode surface,[67,68] is proportional to i through the following equation:

$$v = \frac{i}{nFA} \tag{1.3}$$

where n is the number of electrons exchanged in the reaction and A is the total area of the electrode.

v is influenced by several factors, first and foremost the rate of the electrochemical reaction at the surface, determined by the electromotive force and the intrinsic properties of the reactants and the two interacting phases. Secondly, the mass transport of the reactant and the products to and from the electrode surface, dependent mainly on diffusion, convection and electrical migration. Thirdly, the presence of additional non electrochemical processes, such as homogeneous reactions in solution, and surface interaction processes such as adsorption, desorption and modification of the surface itself (*e.g.* because of material deposition and degradation).

In equilibrium conditions, the neat flux of electrons through the surface (*i.e.* net i) is zero so, for a typical redox process, with O being the oxidised species and R the reduced one,

$$O + n\,e^- \rightleftharpoons R \tag{1.4}$$

The electrochemical potential (*i.e.* the chemical potential corrected with

an electrostatic term $-nF\phi$) of the reactants equals that of the products, so that the equilibrium potential, E_{eq} can be expressed by the Nernst equation:[67,70]

$$E_{eq} = E^0_{O/R} + \frac{RT}{nF}\ln\left(\frac{a_O}{a_R}\right) \tag{1.5}$$

where $E^0_{O/R}$ is the standard reduction potential of the redox couple O/R, a_O and a_R are the activities of the two species, R is the universal gas constant and T the absolute temperature. E measured in this case can be described as equilibrium potential (E_{eq}) and depends solely on the aforementioned thermodynamic parameters. To simplify the treatment and express E as a function of the concentration rather than the activity, it is useful to introduce the formal potential, $E^{0'}$.[67] If the activity of the species j is defined as

$$a_j = \gamma_j C_j \tag{1.6}$$

where C_j is the concentration and γ_j is the activity coefficient, then $E^{0'}_{O/R}$ is expressed as

$$E^{0'}_{O/R} = E^0_{O/R} + \frac{RT}{nF}\ln\left(\frac{\gamma_O}{\gamma_R}\right) \tag{1.7}$$

Therefore, equation (1.5) can be re-arranged as

$$E_{eq} = E^{0'}_{O/R} + \frac{RT}{nF}\ln\left(\frac{C_O}{C_R}\right) \tag{1.8}$$

1.1.2. Basic principles of electron transfer kinetics

The fundamental reaction happening at the electrode interface involves, in the simplest case, a generic redox process between and oxidised species O and a reduced species R, as mentioned above and reported in more details here:

$$O + n\,e^- \underset{k_b}{\overset{k_f}{\rightleftharpoons}} R \tag{1.9}$$

where k_f is the kinetic constant of the forward reaction (arbitrarily defined as the reduction reaction in this case), k_b is the kinetic constant of the backward process and n is the number of electrons exchanged in the redox reaction. In this simple case the fluxes (*i.e.* the reaction rates) of each of the species involved can be simply written as[71,72]

$$\upsilon_f = k_f C_O(0,t) \tag{1.10}$$

$$\upsilon_b = k_b C_R(0,t) \tag{1.11}$$

with $C_j(z,t)$ being the concentration of the species j at a distance z from the electrode and at time t. z is equal to 0 at the surface, as in the case considered here, and ideally equal to infinite in the bulk solution. The total flux υ_t, therefore, will be the difference $\upsilon_f - \upsilon_b$:

$$\upsilon_t = \upsilon_b - \upsilon_f = k_f C_O(0,t) - k_b C_R(0,t) \tag{1.12}$$

By the combination of equation (1.12) with (1.3), an expression for the net current resulting from the electron transfer at the surface is expressed as

$$i = i_f - i_b = nFA\left[k_f C_O(0,t) - k_b C_R(0,t)\right] \tag{1.13}$$

with i_f and i_b being respectively the oxidation and the reduction current:

$$i_f = nFA\,k_f C_O(0,t) \tag{1.14}$$

$$i_b = nFA\,k_b C_R(0,t) \tag{1.15}$$

The current i is usually referred as faradaic current, being originated from a redox process at an electrode. The theories of electron transfer kinetics aim to relate i with the applied electrodic potential E, in order to extract fundamental parameters that can help describe the mechanism of the reaction. This means linking the kinetic constant to the energetic factor, and evaluating the relation between such factors and E.

Taking the case of the simplest electron transfer, involving only one electron $(n = 1)$, the relation of between the two kinetic constants and the energy of the transition state can be expressed by an exponential relation, of which the most useful form is represented by the Eyring equation:[73,74]

$$k_j = \frac{\kappa k_B T}{h} \exp\left(-\frac{\Delta G_j^\ddagger}{RT} \right) \qquad (1.16)$$

where j can either stand for the forward or the backward process. In the equation, $\Delta G_j^\ddagger$ represents the free energy of the transition state of the considered reaction, T is the absolute temperature, k_B, and h are respectively the Boltzmann constant and the Plank constant, and κ is the transmission coefficient, a probability factor related to the vibration states of the system, assumed equal to 1 in this treatment.[67,75]

$\Delta G_j^\ddagger$, the difference in free energy between the reactant and the transition state, is assumed to be dependent on the electrode potential, given the characteristics of the electrochemical cell described above.[76] The simplest model for such relation involves a linear relation, as described by the Butler-Volmer theory.[71,72,77,78] Therefore, the two transition state energies can be described by the following equations:

$$\Delta G_f^\ddagger = \Delta G_0^\ddagger + \alpha F\left(E - E_{eq} \right) \qquad (1.17)$$

$$\Delta G_b^\ddagger = \Delta G_0^\ddagger - \beta F\left(E - E_{eq} \right) \qquad (1.18)$$

where $\Delta G_0^\ddagger$ is the barrier in absence of electrical perturbation, E_{eq} the equilibrium potential [*i.e.* the potential given by the Nernst equation, therefore related to the formal potential $E^{0'}$, as shown in Eq.(1.8)], and α and β are the electron transfer coefficients. For an elementary process such as a one electron reduction, α and β are considered complementary, with $\beta = 1 - \alpha$. Therefore, by combining equations (1.13), (1.16), (1.17)

and (1.18), a fundamental kinetic relation is obtained, known as the Butler-Volmer equation:

$$i = nFAk^0 \left\{ C_O(0,t)e^{-\alpha\frac{RT}{F}\left(E-E^{0'}\right)} - C_R(0,t)e^{(1-\alpha)\frac{RT}{F}\left(E-E^{0'}\right)} \right\} \qquad (1.19)$$

where k^0 is defined as

$$k^0 = \frac{\kappa k_B T}{h}\exp\left(-\frac{\Delta G_0^{\ddagger}}{RT}\right) \qquad (1.20)$$

thus representing the intrinsic rate constant of the system, *i.e.* the rate constant in the absence of an electric perturbation. k^0 is called heterogeneous electron transfer constant, and together with the electron transfer coefficient *α* represent the fundamental parameters for characterising the kinetics of electron transfer in a heterogeneous phase.[67] The Butler-Volmer equation can be re-written as a function of E_{eq}, and will assume the following shape:

$$i = i_0 \left\{ \frac{C_O(0,t)}{C_O^*}e^{-\alpha\frac{RT}{F}\left(E-E_{eq}\right)} - \frac{C_R(0,t)}{C_R^*}e^{(1-\alpha)\frac{RT}{F}\left(E-E_{eq}\right)} \right\} \qquad (1.21)$$

where $E - E_{eq}$ is the overpotential (η), C_O^* and C_R^* are the bulk concentrations of O and R, and i_0 is the *exchange current*, defined as:

$$i_0 = nFAk^0 \left(C_O^*\right)^{(1-\alpha)} \left(C_R^*\right)^{\alpha} \qquad (1.22)$$

i_0 is the kinetic parameter (similarly to k^0), associated with the condition of dynamic equilibrium (at $\eta = 0$), being either i_f or i_b when $i_f - i_b = 0$.

This treatment, which is valid for a simple one electron reaction [Eq. (1.9) with $n = 1$], is at the basis for the study of different electrochemical systems. However, it needs to be considered that many electrochemical systems involve several electrochemical and chemical reactions, with more than one electron involved in each of the redox steps. The overall reaction kinetics are determined mainly by the kinetics of the slowest step

of the mechanism, often referred as the rate determining step (RDS). The identification of the RDS and if such process can be ascribed to the theory discussed above is an important part of molecular electrochemistry studies.[67]

Even considering the single electrochemical reaction introduced in Eq. (1.9), several different cases can be identified. The simplest one in electrochemistry is that both forward and backward reactions (characterised by the kinetic constants k_f and k_b) are fast and no other chemical or physical process intervenes to seize O or R. In this case the reaction can be considered electrochemically reversible, and the conversion of the reactant at the electron surface is instantaneous on the time scale of mass transport. Such processes are referred to as "Nernstian", because the concentration of the two species at the electrode can be defined simply by the Nernst equation; so, by re-arranging equation (1.5):

$$\frac{a_O(0,t)}{a_R(0,t)} = \exp\left[\frac{nF}{RT}\left(E(t) - E^0_{O/R}\right)\right] \tag{1.23}$$

or, if concentrations are used

$$\frac{C_O(0,t)}{C_R(0,t)} = \exp\left[\frac{nF}{RT}\left(E(t) - E^{0'}_{O/R}\right)\right] \tag{1.24}$$

where the label $(0,t)$ indicates the specific parameter measured at the surface (with $z = 0$ for a planar and a disc electrode, as mentioned earlier) and at any time t of the electrochemical analysis. The electrochemically reversible case is common for systems that are characterised by an outer-sphere electron transfer on a perfectly conductive electrode, such as gold, platinum or glassy carbon. It is the case, for example, of the oxidation of ferrocene dimethanol $(Fc(MeOH)_2 \rightarrow Fc(MeOH)_2^+)$ or the reduction of ruthenium hexamine $(Ru[NH_3]_6^{3+} \rightarrow Ru[NH_3]_6^{2+})$ in electrolyte-rich aqueous solution, and usual mass transport rates (see next section).[79,80]

Another typical encountered case is the completely irreversible reaction. This can be achieved in different ways: the most obvious is when reaction (1.9) is chemically irreversible, if $k_b = 0$; otherwise, the same effect can be caused by a side reaction able to consume the product R considerably faster than the rate k_b. In between the two extreme cases (fully reversible and fully irreversible) it is possible to define a quasi-reversible situation, *i.e.* where k_f and k_b are both non-zero but also not critically fast on the mass transport timescale (*vide infra*). In both of the irreversible and quasi-reversible cases, the concentration of O and R at the electrode surface will be determined both by thermodynamic and kinetic parameters (*i.e.* $E^{0'}$, k^0 and a of the electron transfer).[67,81]

Regardless of the reversibility of the main electrochemical reaction, it needs to be remarked that a system described only by reaction (1.9) represents a limited numbers of model cases, as the ones of the ferrocene or ruthenium derivatives mentioned above. In the overwhelming majority of the electrochemical systems, the process will have contribution of several electrochemical and non-electrochemical reactions, the latter of which can happen both at the electrode surface and in the homogeneous phase. As an example, reactions that involve the loss or acquisition of a proton in solution (*i.e.* acid-base reactions) are often a key step in many electrochemical processes.[82]

Naming other typical reactions following the electrochemical step: further reduction or oxidation of the product, rearrangement of the molecule, disproportionation, dimerization, reactions with electrophiles and nucleophiles in solution and many others.[67,83] In several cases, the ideality of the electrode itself cannot be assumed, *e.g.* in the case of non-perfectly conductive surfaces,[84] or irreversible modifications of it, such as corrosion and other forms of degradation,[19,85,86] or phenomena of chemical and physical adsorption of species in solution, and so on.[67,87,88]

The formation and consumption of every species involved in these

processes provokes a dramatic change in the local or bulk solution properties (depending on the timescale), such as concentration and conductivity. These properties, in turn, influence the movement of the species within the solution, and their possibility of reaching the site where the reaction is carried out. For this reason, the second fundamental parameter in an electrochemical system, and often the main parameter for determining the outcome of an electroanalysis, is the mass transport in solution, to which the next section will be dedicated.

1.1.3. Mass transport in solution

The movement of species in a solution can follow, within an electrochemical system, three different mechanisms: diffusion, migration and convection.[67,89,90] Diffusion is the flux of a species in solution caused by a gradient in concentration; migration is the flux of a charged species caused by a gradient in the electric field and; convection is caused by the mechanical movement of the solution relative to the electrode. Convection can become fundamental in systems where the electrode undergoes rotation or the solution is flowed across the electrode surface, however, with few exceptions (concerning mostly natural convection),[91] it is considered to have very little impact on measurements conducted under stagnant conditions. Therefore, under such conditions, mass transport can be described by a simplified form of the Nernst-Planck equation,[92] that associate $\mathbf{J}_j$, the vectorial flux of the species j (made of the three cartesian components $J_{j,x}$, $J_{j,y}$ and $J_{j,z}$) with the two fundamental parameters involved in diffusion and in migration, *i.e.* the concentration gradient ∇C_j and the potential gradient $\nabla \phi$:

$$\mathbf{J}_j = -D_j \nabla C_j - \frac{z_j F}{RT} D_j C_j \nabla \phi \qquad (1.25)$$

In the equation, the first term relates to diffusion, with D_j being the diffusion coefficient, while the second accounts for migration, being z_j the

nominal charge of the species *j*. In normal conditions, the contribution of the migration factor on the species involved in the electrochemical reaction can be minimised by adding a relatively high concentration of an inert supporting electrolyte.[93] With such approximation, equation (1.25) is reduced to the following:

$$\mathbf{J}_j = -D_j \nabla C_j \tag{1.26}$$

which is known as Fick's first law of diffusion.[90,94] Such equation can be re-arranged, assuming conservation of the mass of each species *j* in absence of any chemical reaction, to obtain the time dependent version, also known as Fick's second law of diffusion:[94]

$$\frac{\partial C_j}{\partial t} = D_j \nabla^2 C_j \tag{1.27}$$

where ∇^2 is the second derivative respect to the spatial coordinates, *i.e.* the Laplace operator. It is clear that electrode kinetics and diffusion have a high degree of intercorrelation, with the concentration gradient of any species *j* depending on the rate *v* at which such species is transformed at the electrode, but with that same rate depending on $C_j(0,t)$, as described by eq. (1.19).

It is also clear that ∇C_j and $\nabla^2 C_j$, and therefore the diffusion flux, are highly dependent on the geometry of the system, generating dramatic differences in the mode of the mass transport under different conditions. Two relevant examples of geometry are:

◆ Planar electrode: an electrode where edge effects are negligible, and therefore the only component of $\nabla^2 C_j$ is the variation on the normal direction to the electrode surface (z). This case is defined as planar semi-infinite diffusion, as the diffusion wave front is always parallel to the surface:[90]

$$\nabla^2 C_j = \frac{\partial^2 C_j}{\partial z^2} \tag{1.28}$$

◆ Microdisc electrode: a disc electrode small enough that the edge effects cannot be neglected, as in the previous case. In this case $\nabla^2 C_j$ is expressed in cylindrical coordinates, and depends on the radial distance from the disc centre (r) and the normal distance from the surface (z). This case is referred to as radial diffusion:[95]

$$\nabla^2 C_j = \frac{\partial^2 C_j}{\partial r^2} + \frac{1}{r}\frac{\partial C_j}{\partial r} + \frac{\partial^2 C_j}{\partial z^2} \tag{1.29}$$

In addition to these two cases, many other electrode geometries and arrangement can be used, sometimes operating in a mixed regime, for example with mass transport contributions that can have partial characteristic of a planar electrode. Typically employed geometries are hemispherical electrodes, nanopipette micro-cells, array or microdisc electrodes and series of band electrodes.[67,90,96-98] In most of the cases the diffusion equation [*i.e.* eq. (1.26)] is too complex to be solved analytically, and therefore numerical solutions and simulations are often employed for these kind of systems.

The rate of mass transport, as mentioned above, can have a dramatic influence over the observed relation between i and E. When the electron transfer across the surface is fast relative to mass transport, the latter becomes the limiting factor of the reaction, functioning as a bottleneck for $C_j(0,t)$ and therefore the current. As a general kinetic rule, the overall rate of the electrochemical reaction (k_o) is dependent on both the electron transfer rate (k_{et}) and the mass transport rate (k_m) through this simple relation:

$$\frac{1}{k_o} = \frac{1}{k_{et}} + \frac{1}{k_m} \tag{1.30}$$

Hence the slowest process acts as a bottle-neck for the kinetics of the

whole system. The balance between electrode kinetics and mass transport is of fundamental importance in determining the total current of the system; however, it is not the only factor, and in some cases, other contributions could be predominant. Firstly, the current includes also a non-faradaic component, the double layer charging, which cause a capacitive current that in specific cases can be predominant. Besides, the different components of the electrochemical cell (particularly the solution, but in many cases also the electrode), tend to oppose a resistance to the passage the current, which influences the effective value of *E* applied to the system. Therefore, it is useful to discuss such contributions in more details.

1.1.4. Non-Faradaic current: double layer charging

The capacitive contribution arises from the fact that each ion in solution is solvated, *i.e.* surrounded by molecules of the solvent. When the charge is transferred, the molecules of the solvent between the charged species in solution and the charged electronic conductor (specifically M_1, but the same process happens with M_2) will act as a di-electric barrier, *de facto* creating a double layer capacitor on the electrode surface. In the ideal case (*i.e.* with the ion perfectly solvated and no adsorption of them on the electrode), all ions will be distributed at a constant distance from the electrode, on the so called outer Helmholtz plane (OHP)[99-101] and, for a macroscopic planar electrode, the capacitive contribution can be approximated to the one of a planar capacitor of capacitance C_{OHP}:

$$C_{OHP} = \frac{\varepsilon \varepsilon_0 A}{d} \qquad (1.31)$$

with ε and ε_0 being respectively the relative and absolute dielectric constants, *A* being the area of the electrode and *d* the distance between the electroactive ions and the surface usually a few angstroms. More gener-

ally, the capacitance is the differential of the stored charge Q and the potential $\Delta\phi$ (and therefore E):

$$C_{OHP} = \frac{\partial Q}{\partial E} \tag{1.32}$$

Since Q is linked to a current flow, the total current i will be a sum of the contribution of the faradaic process (i_F) and the double layer "capacitor" charging (i_C):[67]

$$i = i_F + i_C \tag{1.33}$$

with

$$i_C = \frac{dQ}{dt} = C_{OHP}\frac{dE}{dt} \tag{1.34}$$

The contribution of the capacitive current on the overall process can differ massively depending on the system and the technique employed; in some cases it can account for almost the 100% of the measured current,[102-104] and therefore needs to be carefully calibrated for.

1.1.5. Resistance effect

The charge passing through an electrochemical system has to traverse several phases, characterised by extremely different conductivity properties. Whereas within the metallic conductors (such as M_1, M_2 and M_3, as defined in section 1.1.1) the contribution of the resistance, or ohmic term, can be considered negligible, the same cannot be said for the ionic conductor S. Besides that, most electrochemical system will have a high degree of complexity, involving several semi-conducting phases between M and S (such as in the case of electrochemical solar cells or transistor, as described in Chapter 3).

The resistance to the flux of charge though the solution can be described as an ohmic drop of the potential between the double layer OHP of the two electrode conductors M_1 (working electrode, WE) and M_2, (counter electrode, CE), as shown in Figure 1.1. Such potential drop is
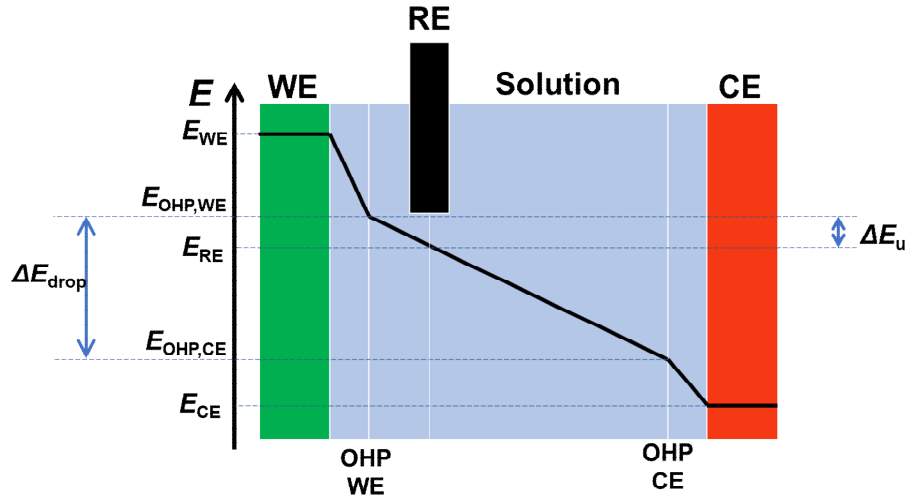
Figure 1.1: scheme of the potential drops in a typical three electrodes electrochemical cell, WE, CE and RE being respectively the working electrode, the counter electrode and the reference electrode, ΔE_{drop} the total potential drop in solution and ΔE_u the component of the potential drop caused by the uncompensated resistance (R_u).

quantifiable through Ohm's law as

$$\Delta E_{drop} = iR_S \tag{1.35}$$

where R_s is the solution resistance. Thus, the variation in the applied potential is proportional on the intrinsic resistivity of the solution (dependent on the nature of the solvent/solutes and the geometry of the system) and the overall current. In order to address the problem of *iR* drop in solution, a further electrode, called reference electrode, is added in proximity of the working electrode (indicated as RE in Figure 1.1); such electrode is, in principle, insensitive to the reaction carried out in the cell, so that its potential is effectively constant and the cell potential can be calibrated for taking into account the *iR* drop. However, since the reference electrode has to be put at a finite distance from the working electrode, part of the solution resistance will still influence the measurement. Such resistance is referred as uncompensated resistance (R_u),[105-109] and its effect needs to be added to the electrode potential in order to obtain the effective electromotive force (E_{eff}):

$$E_{eff} = E - \Delta E_{drop,u} = E - iR_u \tag{1.36}$$
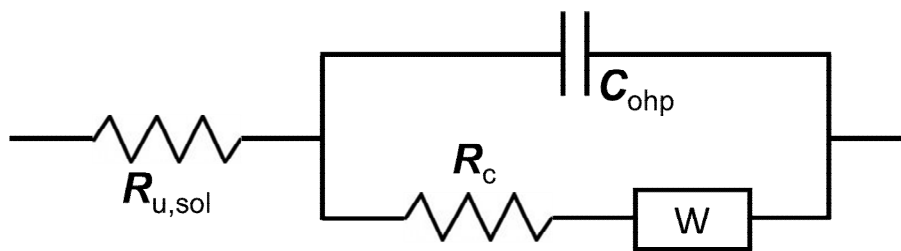
Figure 1.2: Schematic representation of a Randles circuit for a single electrochemical reaction at the working electrode. In a typical 3-electrode setup, an equivalent circuit for the counter electrode will be connected to this, with a reference in the middle to compensate most of the resistance responsible for the ohmic drop in solution. Reproduced from Ref. [110].

Since the resistance contribution over the potential widely depends on the amount of current passed and the conductivity of the solution, its action can be mitigated, when possible, by changing the solution composition or employing techniques that involve a small amount of current passed, such as electrochemical microscopy techniques (*vide infra*). Furtherly, since resistance of the solution can be measured by most commercial instruments, its contribution can be often isolated and corrected for.[111] However, despite such possibilities, the problem of solution and contact resistances remain a fundamental issue in potential applications in energy devices, such as solar cells, light emitting diodes, batteries and transistors, where often the resistance accounts for most of the efficiency losses of the device.[112-114]

1.1.6. Randles circuit and electrodes setup

In order to visualise all of the processes (faradaic and non-faradaic) that contribute the to the *i–E* characteristics of a system, an electrochemical cell can be usefully represented by an equivalent circuit. The simplest instance, accounting only for the electron transfer at the interface, mass transport in solution, double layer charging and uncompensated resistance, is called Randles equivalent circuit and is shown in Figure 1.2.[67,110,115] Charge transfer and the solution resistance are represented by resistors (respectively R_c and $R_{u,sol}$ in Figure 1.2), the double layer charg-

ing by a capacitor (C_{ohp} in Figure 1.2), and mass transport by a custom element called Warburg impedance (identified as W in Figure 1.2). Further elements can be added in order to account for the complexity of the electrode material and the eventual additional reactions that may take place in solution and/or at the interface.[116]

In most cases each electrode (working and counter) is represented by a separate Randles circuit, therefore a typical electrochemical cell is represented by two of them, connected through the solution resistance and with the reference electrode set in the middle. In specific conditions the perturbation to the counter electrode can be relatively small, for example when the current density is negligible, due to the area of CE being several times larger than the WE. Assuming that the products of the reactions at the CE do not affect the solution significantly, it is possible to omit the reference electrode and use a simpler two electrode configuration, wherein a quasi-reference counter electrode (QRCE) is employed. Usually (but not always) the three electrode setup is employed in electrochemistry on macroscopic electrodes, while the two electrode setup is more common with (sub)microscale measurements.

1.2.   ELECTROCHEMICAL TECHNIQUES

The main electrochemical techniques can be divided into two different categories on the bases of what kind of perturbation is applied to the system: in the first case, the potential-controlled techniques, E is set by the instrument (a potentiostat) to specific values relative to the reference electrode, and the resulting current i is measured as a consequence. In the second case, the current-controlled methods, the current is the variable that is set by the instrument (a galvanostat), while the measured parameter is the potential necessary for sustaining the applied current.[67]

1.2.1. Potential Controlled: Potential Sweep Voltammetry

Controlled potential electrochemical methods are the most widely

used nowadays in electroanalysis. The potential can be applied to the system in several different time dependent ways, such as constant potential pulses, potential sweep and more complex perturbations (*e.g.,* sinusoidal or square-wave waveforms). For the sake of this work it is useful to introduce the techniques that employ a linear variation of the potential with time, collectively known as potential sweep voltammetries.[81] When the potential is swept in only one direction, known as linear sweep voltammetry (LSV), the applied potential can be described by this relation:

$$E = E_i + vt \tag{1.37}$$

where E_i is the initial potential ad v is the scan rate, expressed in V s^{-1}. Depending on the analysed system and the employed instrumentation, v can widely vary from a few millivolts per second to several thousand volts per second.[81,117] The rate at which the potential is varied can have important implication on the possibility of measuring dynamic and out of equilibrium processes, as well as discriminating processes with different reaction kinetics.

In cyclic voltammetry (CV), which is perhaps the most widely used technique in modern electrochemistry, E is instead swept back towards the initial value after reaching a specific point, characterised by t_λ (switch time) and $E_\lambda = E_i + vt_\lambda$ (switch potential):

$$\begin{cases} E = E_i + vt \text{ if } E \leq E_\lambda \\ E = E_\lambda - v(t - t_\lambda) \text{ if } E > E_\lambda \end{cases} \tag{1.38}$$

Cyclic voltammetry offers considerable versatility in terms of sweep rate, cycle number, switch potential etc. A visualisation of the applied potential described in Eqs. (1.37) and (1.38) is shown in Figure 1.3a and b, respectively. In all potential-controlled techniques, the resulting current will be determined by the simultaneous contribution of electrode kinetics, mass transport and non-faradaic contribution, as discussed earlier. In order to clarify the influence of such factors on the *i–E* response, it is useful to
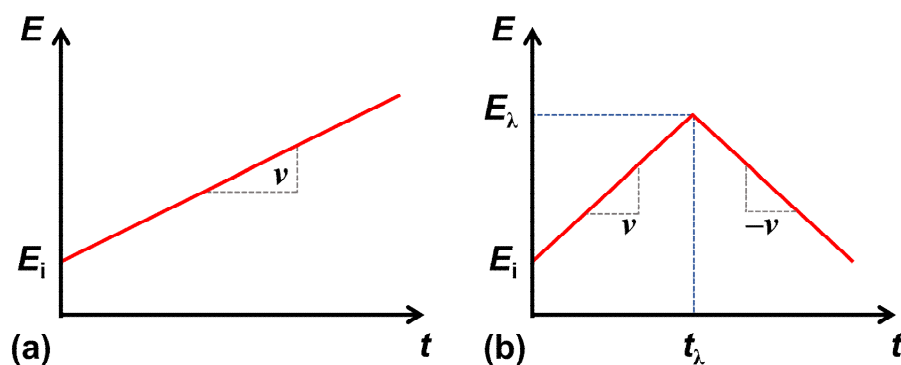
Figure 1.3: Examples of modes of application of the potentials in some common potential-controlled techniques: (**a**) Linear Sweep Voltammetry and (**b**) Cyclic Voltammetry.

consider the characteristics of the voltammograms from some specific model systems in greater detail.

The first case is a voltammogram obtained from a Nernstian process in absence of any non-faradaic contribution, on a planar electrode. This case is useful for understanding the contribution of mass transport itself, specifically (semi-infinite) diffusion, which can be simply described by eq. (1.28). As discussed before, the reaction in eq. (1.9) can be considered a Nernstian process when k_f and k_b are very high, such that the concentrations of O and R at the electrode surface can be described at any time t by eq. (1.24). In this case, the shape of the voltammogram is controlled purely by thermodynamics and mass transport, and can thus provide information on $E^{0'}$, C^*, D_j etc. Therefore, the interpretation of the data in this case is relatively simple, and some characteristics of the curves may also be valid in non-reversible cases.[67,81,117]

While the electrochemical reaction can be described by the Nernst equation, the diffusion of O and R is described by Fick's second law [eq. (1.27)], which, for this reaction and in case of planar semi-infinite diffusion, becomes

$$\frac{\partial C_O}{\partial t} = D_O \frac{\partial^2 C_O}{\partial z^2} \tag{1.39}$$

and

$$\frac{\partial C_R}{\partial t} = D_R \frac{\partial^2 C_R}{\partial z^2} \tag{1.40}$$

where z is the spatial coordinate. These equation clearly identifies a system of partial differential equations, where the contour conditions are defined, at the electrode, with eq. (1.24) at any given time t, where $E(t)$ is given by eq. (1.37) for the linear sweep voltammetry and eq. (1.38) for the cyclic voltammetry. Besides, further conditions are added to account for the initials $(t = 0)$ and bulk $(z \rightarrow \infty)$ concentrations:

$$C_O(z,0) = C_O(\infty,t) = C_O^* \tag{1.41}$$

and

$$C_R(z,0) = C_R(\infty,t) = C_R^* \tag{1.42}$$

where C_i^* is the bulk concentration of the species i. The presented problem can generally be solved numerically. One of the few cases in which the problem has a closed solution is at high values of overpotential $(E \gg E^{0'})$, where it is assumed that the species O is constantly totally consumed at the electrode, such that

$$C_O(0,t) \rightarrow 0 \tag{1.43}$$

In that case, the current is proportional to $t^{-1/2}$, in an expression known as the Cottrell equation:[118]

$$i = nFAC_O^* \left(\frac{D_O}{\pi t} \right)^{\frac{1}{2}} \tag{1.44}$$

The full solution of the problem, however, results in a graph that is qualitatively similar to the ones shown in Figure 1.4. Assuming that $C_R^* = 0$

and $D_O = D_R$, the curve starts with a null current, then undergoes an exponential growth while the species O is consumed (area 1 in Figure 1.4a), up to the point $C_O(0,t) = 0$, when the current, being limited by the finite rate of mass transport, will decrease with a trend such as the one described by eq. (1.44), and shown in area 2 of Figure 1.4a. The point at which such condition is reached is marked by a peak in the current, characterised by values of current and potential (respectively i_p and E_p, Figure 1.4b), which depend only on thermodynamics and diffusional parameters and v:

$$i_p = 0.4463 \, nFAC_O^* \left(\frac{nFvD_O}{RT} \right)^{\frac{1}{2}} \tag{1.45}$$

$$E_p = E_{O/R}^{0'} + \frac{RT}{nF} \left[\ln\left(\frac{D_O}{D_R} \right)^{\frac{1}{2}} + 1.109 \right] \tag{1.46}$$

Eq. (1.45) is known as the Randles-Ševčík equation and is of fundamental importance in the analysis and determination of diffusional parameters for Nernstian and near-Nernstian processes.[119,120] In condition of equality of diffusion coefficients and room temperature (298.15 K), eq. (1.46) simply becomes

$$E_p = E_{O/R}^{0'} + \frac{28.5\text{mV}}{n} \tag{1.47}$$

which is an important parameter for verifying the reversibility of the process. After the peak, a quadratic decrease in the current as *per* the Cottrell equation continues until after the potential is reversed (at $t = t_\lambda$). At that point, when E becomes again sufficiently close to $E^{0'}$, the reverse reaction (*i.e.* consumption of R) will become the most significant contribution, generating a new exponential growth of the current (albeit in the opposite direction, as shown in Figure 1.4a, area 3), until a new peak is reached, and the trend comes back to a purely diffusive behaviour (area 4, Figure 1.4a), with a decrease in the absolute value of the current, which however,
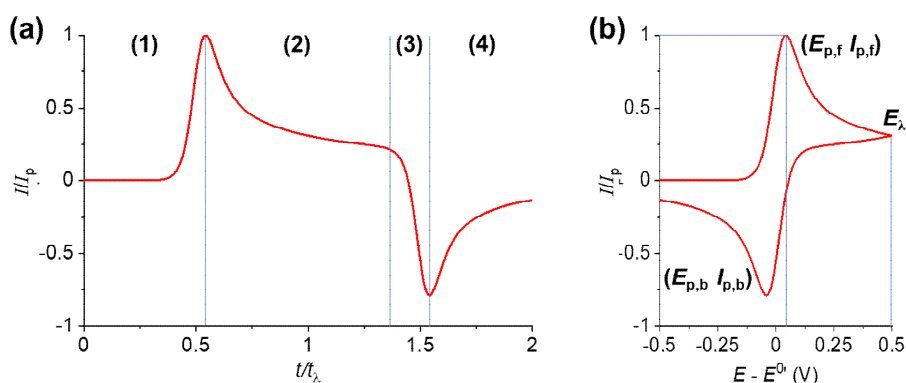
Figure 1.4: Typical cyclic voltammogram obtained for a Nernstian system conditioned only by planar semi-infinite diffusion, representing the current density as a function of (**a**) t/t_λ and (**b**) the electrode potential (expressed as E-$E^{0'}$). Reproduced from Ref. [67].

does not reach a value of 0 at $E = E_i$ due to the permanent modification (within the timescale of the measurement) in the concentration profiles of O and R.[*] Interestingly, the separation between E_p of the forward and the backward peak is also an important indicator relative to the reversibility of the process and the eventual presence of further heterogeneous and homogeneous processes that can alter the concentration of either O and/or R.

For non-Nernstian systems (*i.e.* a non-reversible redox reaction at the interface), the peak potential depends on the kinetics of the electron transfer reaction and the scan rate. As an example, Figure 1.5a shows how the curve changes by decreasing k^0, and thereby slowing down the electron transfer kinetics. In this case the forward and the backward peaks are shifted to more positive and negative potentials, respectively, while the waveshape becomes more asymmetric. The asymmetry between the forward and backward peak can also depend on the presence of homogeneous coupled reaction; as an example, if a homogenous reaction(s) consumes R as it is formed, i_p of the backward peak will decrease and eventually disappear at high reaction rates. Furthermore, there are several cases

---

[*]A practical visualisation of the variation of the concentration profiles of O and R during the CV of a Nernstian system can be found in Ref. [121], Figure 3a-g.

where, independent on the rate of the reaction at the electrode, in common experimental conditions a diffusional profile such as the one described by eq. (1.44) is not observed. As an example, the hydrogen evolution reaction (HER) is usually carried out in conditions of high concentration of protons, so that it is not possible to observe the diffusion limited profile before the solvent itself is reduced, thus showing only the exponential growth part of the curve, for the reaction in strong acidic conditions.[122] However, such reaction can be brought to diffusional control adopting specific experimental conditions.[123]

Among the physical processes that can affect the curve, adsorption of the species on the electrode plays a major role. Figure 1.5b shows the limiting case of a Nernstian process where only the adsorbed species O and R are electroactive, resulting in a perfectly symmetrical voltammetric curve where i_p is proportional to v [contrarily to eq. (1.45)].[67] Very important is also the capacitive contribution of the current, with the effect of increased capacitance shown in Figure 1.5c. The first part of the curve shows an increase of the current that is unrelated with the faradaic process, due to the charging of the double layer, which is summed to the faradaic response. However, since this contribution is generally proportional to the scan rate v, so in planar semi-infinite conditions, at high values of v the capacitive current could even overtake the faradaic contribution (which for a non-surface related process has a peak current that is proportional to the square route of v).[67,117]

Finally it is useful to mention the role of uncompensated resistance, which can affect the potential felt at the electrode surface dependently on the measured current. This results in a linearized *i–E* characteristic (as per Ohm's first law) that tends to shift the voltammetric peaks to more extreme potentials (as in slow electron-transfer kinetics, *vide supra*).[105,106,124] As shown in Figure 1.5d, a resistive voltammogram is often indistinguishable from one obtained from a slow kinetic system; there-
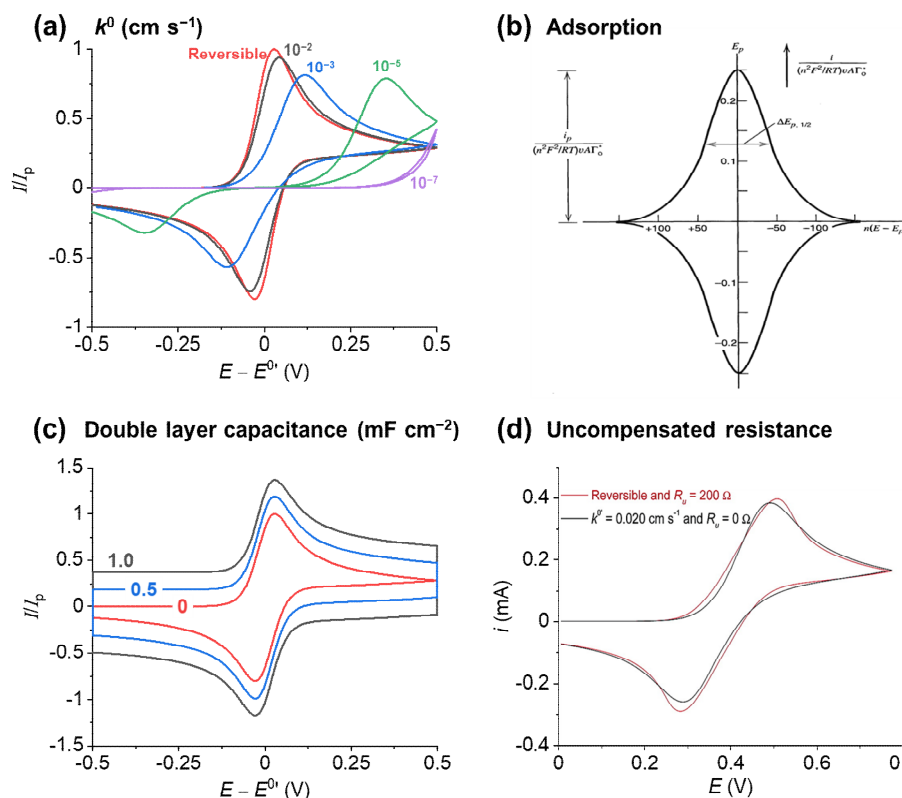
Figure 1.5: Examples of the influence of some important chemical and physical factors on a voltammetric curve. (**a**) Cyclic voltammograms obtained with different values of k^0 (shown on the graph), at $v = 1$ V s^{-1} (**b**) Simulated voltammograms for a nernstian system in presence of high uncompensated resistance, compared to a slow kinetics system in absence of resistance, at a scan rate $v = 30$ V s^{-1}, reproduced from Ref. [124]. (**c**) Cyclic voltammograms obtained from of a Nernstian system where both species are electroactive only when adsorbed on the surface, reproduced from Ref. [67]. (**d**) Cyclic voltammograms of a Nernstian system in presence of different values of double layer capacitance (indicated on the graph).

fore, the decoupling of the effective applied potential from its resistive contribution is not always straightforward.[124]

Planar semi-infinite diffusion is a good approximation for a macrodisc electrode, *i.e.* where the size of the electrode is so large compared to the diffusion layer thickness, such that the flux at edges of the electrode can be considered negligible. On the contrary, when the electrode is on the same scale as the diffusion layer, the mass transport at the edges acquires a fundamental importance.[125,126] In the specific case examined here, a flat

microdisc facing an infinitely large solution, the diffusion equation is generally written in cylindrical coordinates, as per eq. (1.29), such that the second Fick's law of diffusion for the single redox process [eq. (1.9)] becomes:

$$\frac{\partial C_O}{\partial t} = D_O \left(\frac{\partial^2 C_O}{\partial r^2} + \frac{1}{r}\frac{\partial C_O}{\partial r} + \frac{\partial^2 C_O}{\partial z^2} \right) \tag{1.48}$$

and

$$\frac{\partial C_R}{\partial t} = D_R \left(\frac{\partial^2 C_R}{\partial r^2} + \frac{1}{r}\frac{\partial C_R}{\partial r} + \frac{\partial^2 C_R}{\partial z^2} \right) \tag{1.49}$$

where r and z are respectively the radial distance from the centre of the disc and the normal distance from its surface. The solution of this problem, assuming the same contour conditions as in the planar case, will result in a peculiar i–E profile, as shown in Figure 1.6a. Due to the enhanced flux of reactant at the edges of the electrode, the system assumes a steady state in a very small limit time (t_L), depending on the area of the electrode and the diffusion coefficient:[127]

$$t_L \approx 6\frac{A}{D_O} \tag{1.50}$$

which, for a 10 μm diameter electrode and a typical D_O in aqueous solution of $1 \cdot 10^{-5}$ cm^2 s^{-1}, assumes a value of *ca.* 0.5 s. At large driving potentials the current assumes a stationary value, i_{ss}, which depends only on diffusional parameters and the radius of the electrode:

$$i_{ss} = 4nFD_O C_O^* r_0 \tag{1.51}$$

where r_0 is the radius of the electrode. Interestingly, i_{ss} unlike i_p on a planar electrode, is independent of timescale (*i.e. v*), as long as a steady-state has been achieved. In case of slower reaction kinetics and faster scan rate, the curve tends to assume a peaked shape similar to the one observed at the macroscale.[128]
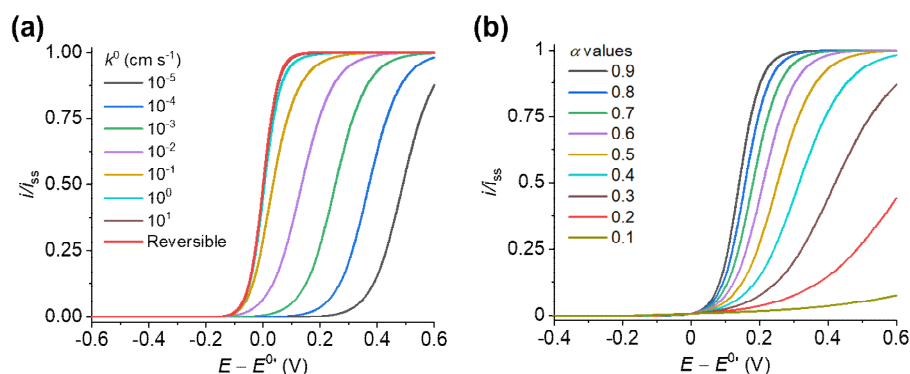
Figure 1.6: Cyclic voltammograms in conditions of radial diffusion at a micro-disk electrode in different kinetic condition. (**a**) Curves depicting the effect of different values of k^0 (with a fixed value of $a = 0.5$). (**b**) Curves depicting the effect of different values of a (for a reduction process, with a fixed value of $k^0 = 10^{-3}$ cm s^{-1}).

In the ideal case (*i.e.* simple, electrochemically reversible process), the position of the electrochemical wave is linked to the standard potential of the reaction, in this case through the half wave potential $(E_{1/2})$, *i.e.* the potential at which $i = i_{ss}/2$:

$$E_{1/2} = E_{O/R}^{0'} + \frac{RT}{nF}\ln\left(\frac{D_O}{D_R}\right) \tag{1.52}$$

so that $E_{1/2}$ coincides with $E^{0'}$ if $D_O = D_R$. Also in this case the curve is highly dependent on chemical and physical factors that also affects the macroscale curve, even though on a different scale. In the case of quasi-reversible and irreversible systems, k^0 and a additionally influence the shape and position of the curve, as shown in Figure 1.6a and b. Slowing down the kinetics, in this case, pushes $E_{1/2}$ to more extreme values, even though without influencing i_{ss}, and the value of a influences the symmetry of the curve relative to $E^{0'}$. This factors, and the relative insensitivity of the shape of the curve on several kind of additional homogeneous reactions taking place in solution, make cyclic voltammetry at microdisc electrode a powerful technique for characterising the kinetics of electrochemical reactions.[129]

A few other fundamental factors affect microdisc electrodes in a radically different way when compared to conventional macroscale electrodes. As an example, in most measurements carried out at micro- and nano-scale electrodes, the effect of the uncompensated resistance in solution can be neglected, mostly due to the extremely lower magnitude of the measured current [see Eq. (1.36)]. Indeed, microelectrodes can be used to make measurements in resistive solutions that would otherwise be impossible with conventional macroscale electrodes.[130] Furthermore, while the double layer charging current is proportional to v also in case of a microdisc electrode, i_{ss} is effectively independent of it (within the limits of the conditions for which the reaction can reach a steady state, *i.e.* small r_0 and low v), allowing the measured current to be unambiguously assigned to faradaic processes.[126,131,132]

1.2.2. Current Controlled: Chronopotentiometry

This class of methods is characterised by the control of the current, through an instrument called galvanostat, and the measure of the potential, which is adopted at the working electrode in order to maintain the applied current (i_{app}).[67,133,134] i_{app} can be imposed in several different ways, utilising various time dependent functions. However, the most common techniques involve the application of a constant current for a determined amount of time, or multiple pulses with different current values. Such techniques are known with the collective term chronopotentiometry.[133,135] Even though current-controlled techniques are less widespread in electroanalysis, they still have important applications. One of the most common uses is in the characterisation of the charge and discharge characteristics of batteries and supercapacitors.[136-139†]

In the planar semi-infinite diffusion regime, the diffusion equation [Eq. (1.28)] can be solved analytically, in conditions of constant i_{app}, for

---

† Further discussion about the applications of current controlled electrochemical techniques can be found in Chapter 4, section 4.1.

the one step electron transfer process described in eq. (1.9). Regardless of the value of i_{app}, the concentration of electroactive species O at the electrode surface (assuming that the current is flowing in the direction of the process $O \rightarrow R$) decreases until reaching a value of zero. The time at which this occurs, termed the "transition time" (τ), is given by the Sand equation,[67,140] and is independent of the electrochemical reversibility (*i.e.* electron-transfer kinetics) of the redox process:

$$\frac{i_{app}\tau^{1/2}}{C_O^*} = \frac{nFAD_O^{1/2}\pi^{1/2}}{2} \tag{1.53}$$

At time $t = \tau$, the concentration of O at the surface $[C_O(0,t)]$ reaches zero in any condition of reversibility. In fact, $C_O(0,t)$ can be described by the following equation:[67]

$$\frac{C_O(0,t)}{C_O^*} = 1 - \left(\frac{t}{\tau}\right)^{1/2} \tag{1.54}$$

When i_{app} is imposed to the system by the galvanostat, the instrument itself tunes to the potential E necessary to sustain the reaction $O \rightarrow R$ [Eq. (1.9)], dependent on kinetic and thermodynamic factors. As $t = \tau$ is reached the concentration gradient of O at the electrode would start to decrease and therefore the sole conversion of O would not be sufficient to sustain i_{app} [in a predominantly diffusive system, in fact, the electron flux v is proportional to the diffusive flux $\mathbf{J}_O$, given by eq. (1.26)]. Thus, the instrument tunes E to a more extreme value where a new electron transfer process can occur. As a consequence, E shifts dramatically at $t = \tau$ (and therefore the term "transition time" is used).

For the reaction described in Eq. (1.9), an analytical form of the function $E(t)$ can be found in two different cases: the fully reversible (Nernstian) and the fully irreversible. For the quasi reversible a numerical solution has to be calculated. In the Nernstian case, where the concentrations of O and R at the electrode are described by eq. (1.24), $E(t)$ assumes the

following form:[67]

$$E(t) = E_{\tau/4} + \frac{RT}{nF} \ln \frac{\tau^{1/2} - t^{1/2}}{t^{1/2}} \tag{1.55}$$

where $E_{\tau/4}$ is the potential measured at $t = \tau/4$, and it is dependent on the standard potential $E^{0'}{}_{O/R}$:

$$E_{\tau/4} = E^{0'}_{O/R} + \frac{RT}{2nF} \ln \frac{D_O}{D_R} \tag{1.56}$$

The typical shape of a chronopotentiogram described by eq. (1.55) is shown in Figure 1.7a. The curve observes a quasi-plateau situation (in the range $E_{\tau/4} \pm 25$ mV) followed by a sharp potential shift at the transition time, with the potential of the plateau depending only on the thermodynamic and mass transport parameters. In the other two cases (irreversible and quasi-reversible), even though the curve assumes a qualitatively similar shape, the measured potential is actively linked to both the applied current and the kinetic parameters of the reaction, specifically the heterogeneous electron transfer constant k^0 [Eqs. (1.19) and (1.20)].

Equation (1.55) describes an asymptotic growth of the potential at the transition time. However, in a real electrochemical cell, further reactions will intervene to sustain the applied current, *e.g.* the oxidation or the reduction of the solvent of the electrolyte solution, or the redox transformation of another electroactive solute. Therefore, after the transition E will stabilize on a new quasi-plateau, with a value depending on the process involved. According to the number of electrochemically active species present in the solution, as well as to the presence of complex multistep mechanisms, the curve could present several plateaus and transitions.[141] Therefore, several processes in a single electrochemical system can be discriminated all at once if their potential is different enough to allow every single one to independently contribute to i_{app}.
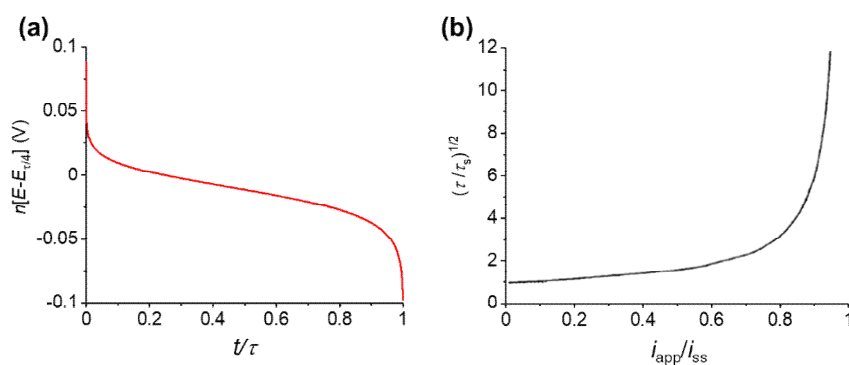
Figure 1.7: **(a)** Shape of a Chronopotentiometry described for a Nernstian system by eq. (1.55). **(b)** Trend of the deviation of τ from the value theorised by Eq. (1.53)(τ_s), in a system governed by radial diffusion (microdisc electrode), when the applied current (i_{app}) approaches the steady state current (i_{ss}), reproduced from Ref. [142].

As described for the potential-controlled techniques, many different processes can influence the shape of the curve, such as double layer charging, presence of further homogeneous reactions, adsorption and uncompensated resistance.[67] Chronopotentiometry can be useful for analysing system, such as batteries, where a constant current flow represents the normal way of operating.[143,144] As it will be discussed in Chapter 4 and 5, such measurement can be useful also in electrocatalysts characterisation and corrosion research.

As in the potential controlled techniques, a few peculiarities are observed when chronopotentiometry is applied on a microdisc electrode, where radial diffusion needs to be accounted for, and therefore the mass transport is governed by Eqs. (1.48) and (1.49) for the single step reaction $O \rightarrow R$. In this case the diffusion equations do not have an analytical solution even for a reversible system and the potential-time behaviour is highly dependent on i_{app}, particularly in relation to i_{ss} [as defined in eq. (1.51)].[142,145,146] If $i_{app}/i_{ss} \gg 1$, the approximate solution for τ can be obtained from eq. (1.53), resulting in a macroelectrode-like response, whereas if i_{app} approaches i_{ss} τ will tend to infinity as shown in Figure 1.7b for a Nernstian process, with the concentration of electroactive species

(O in this case) adopting a constant, non-zero value at the electrode surface, and a steady state diffusion regime established. Furthermore, the measured potential itself is influenced by the edge effects present in a microdisc electrode, slightly shifting towards more extreme values as the radius of the electrode is decreased, but maintaining the general shape of the curve.[142]

1.3. SCANNING ELECTROCHEMICAL PROBE MICROSCOPY

As briefly overviewed in the previous paragraphs, the classical electrochemistry can be applied to characterise the complex physicochemical properties of an electrochemical system. However, as stated in the opening, perhaps one of the most interesting properties of electroactive materials is the heterogeneity of the surface structure/composition. For this reason, in recent years, classical electrochemical techniques have been adapted to operating at the (sub)microscale, and coupled with precision positioning systems to attain spatial resolution over the measured signal, thus developing the SEPM techniques. In this paragraph, a brief overview of the historically more important techniques is given, leading to closer look on the technique that is the object of this work specifically, Scanning Electrochemical Cell Microscopy (SECCM).

1.3.1. SECM and SICM

The very base principle of any scanning probe microscopy technique is the presence of a small probe, moved by an extremely precise motor, which is used to measure a specific signal that is dependent on the distance between the probe and the examined surface, and a feedback system that allows the probe to approach the sample according to such signal.[147] SEPM techniques use electrochemical variables, such as potential, current, conductivity and related properties, both as a feedback signal and as a measure of the surface properties.
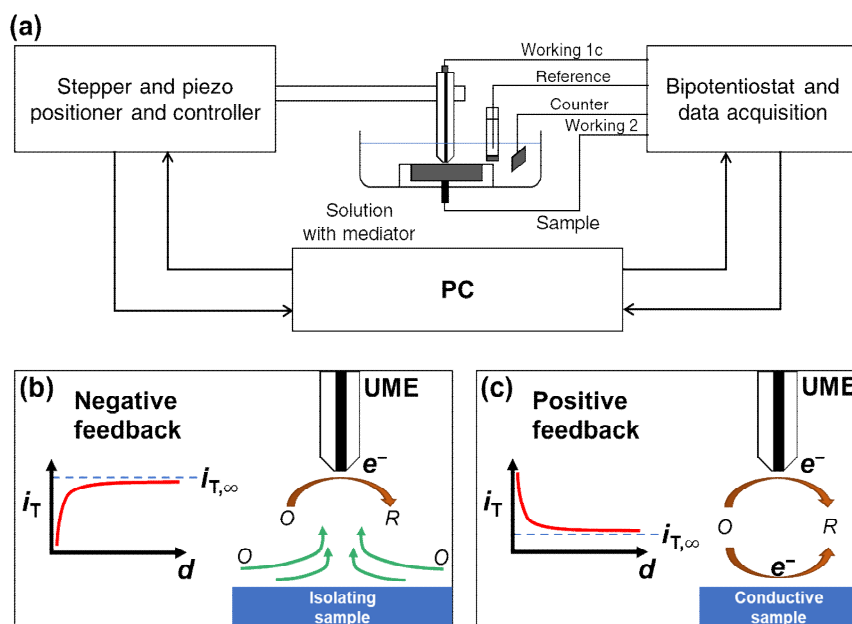
Figure 1.8: (**a**) Scheme of the setup of a typical SECM experiment, reproduced from Ref. [148]. (**b**) Scheme of the negative feedback mode of operation, (**c**) scheme of the positive feedback mode. i_T in both cases is the "tip current", *i.e.* the current at the probe, with $i_{T,\infty}$ being the current with the tip far from the sample surface.

The first and most widely studied SEPM technique is SECM, introduced and developed by Engstrom and Bard and co-workers at the end of the 1980s. [63,149-151] The technique is based on the use of an ultramicroelectrode (*i.e.* a microdisc electrode of micrometric or nanometric size, UME) as the probe, functioning as working electrode of the electrochemical system, measuring the local electrochemical properties of the surface of a macroscopic substrate (*i.e.* another electrode). During operation, both the UME and the substrate are immersed in solution, which usually contains an electrochemical mediator that undergoes a simple, Nernstian redox reaction and does not strongly interact with the surface of interest. The main setup of a typical SECM experiment is shown in Figure 1.8a. The UME probe and the sample (if conductive) are two different working electrodes immersed in the electrolyte, together with a common counter and the reference electrodes.[58,148]

SECM is usually conducted in potential controlled conditions (at the UME tip). During operation, the UME is approached to the surface with

an applied constant potential, to drive an electrochemical process at the mass transport limit. The proximity of the probe with the surface will severely influence the extent of the diffusion layer (because of the confined space), therefore influencing the current measured at the UME. If the substrate is non-conductive (Figure 1.8b), the diffusion layer is dramatically compressed when in the vicinity of the surface, inducing a reduction in the measured current (negative feedback). Instead, if the substrate is conductive (Figure 1.8c), and biased at the appropriate potential, the mediator is regenerated at the surface, thus increasing the current (positive feedback). A threshold current is generally set as a feedback signal to stop the approach, allowing the measure of topography or local electrochemical properties by translating the probe in two dimensional space.[148,150,152]

Due to the possibility of working in physiologically relevant solutions and not requiring physical contact with the sample, SECM has often being applied to study the metabolic processes of single living cells or tissues.[153-157] Other exemplar fields of applications include the study of transport phenomena at liquid/liquid interfaces[158-160] and biological membranes,[161,162] micro and nanopatterning,[163,164] electrocatalysis[165] and photooxidation,[160] as well as surface corrosion and degradation.[26,166]

Another important SEPM technique operating in solution is SICM, which was also first developed in 1989.[64] SICM is based on the principle of sensing the surface through a change in conductivity of the solution in the narrow space between the sample and sharp pulled nanopipette probe.[59,167-169] The main setup of the technique is shown in Figure 1.9a. SICM does not require a redox mediator, as only the conductance current (*i.e.* the current arising from applying a potential in a solution of finite conductivity, as discussed in section 1.1.4) is measured. The sample and the probe are immersed in an electrolyte, having two QRCEs inserted respectively in the pipette and the bulk solution, with a bias potential applied between them, inducing a conductance current. As the pipette tip
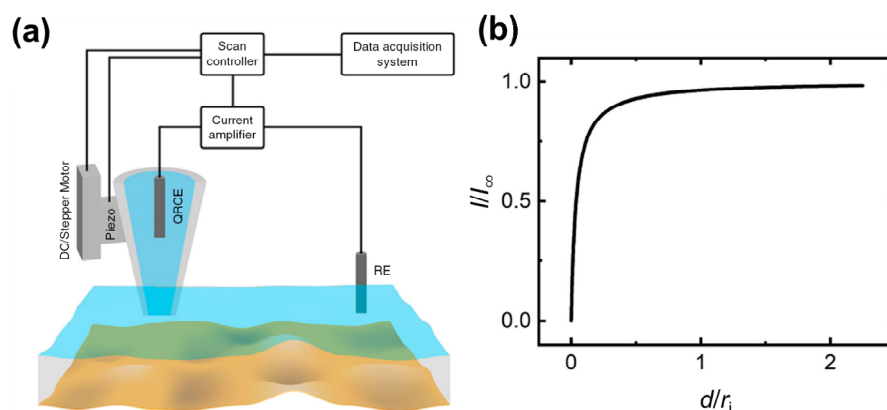
Figure 1.9: (**a**) Scheme of a typical SICM instrument setup. (**b**) A typical SICM approach curve plotted as the normalized ion current (I/I_∞) *versus* tip–sample distance normalized to the tip radius (d/r_i). Both figures are reproduced from Ref. [169].

approaches the substrate, the access resistance increases and the conductance current between the two QRCEs decreases, as shown in Figure 1.9b, serving as a feedback parameter for detecting the surface.

Since the substrate surface is probed indirectly, SICM is very suitable for measuring the topography of soft and delicate samples, and as such has been widely used for high resolution mapping of living tissues.[59,170-172] The resolution of the technique is mostly limited by the size of the tip aperture of the probe, which can be fabricated extremely precisely, down to tens of nanometres in size.[168,173,174] Besides topography, SICM allowed to calculate surface charge[175] and ion transport arising from surface reactions in electroactive materials,[176,177] which can be connected as working electrode to the system and play an active role into the measured current.[167]

While both SECM and SICM, as well as most other SEPM techniques, have proven very powerful in the investigation of the phenomena discussed above, they rely on the principle that the whole examined sample is immersed and connected in the solution of interest. Therefore, while the probe measures activity at a precise micro/nanoscale site, the electrochemical reaction takes place globally, across the entire substrate surface. This can be seen as a limitation, especially for reactions that have a huge

impact on the surface and the solution properties, such as corrosion or in general degradation reactions, electrochemical synthesis, or specific cases of electrocatalytic reactions.[178] Besides, especially in SECM, it is very difficult to separate the feedback signal (*i.e.* the signal used for detecting the approach to the surface by the probe) and the electrochemical signal from the surface itself, meaning that surface topography and activity are convoluted. In addition to this, except in a few cases, in SECM the surface activity is often measured indirectly, using a redox mediator rather than reactive flux (*i.e.* products) from the process of interest.[179]

The necessity of probing the electrochemical activity of a substrate *locally* and *directly* has stimulated the development of innovative techniques that are able to probe a limited area of a surface without affecting the whole sample. These methods are collectively known as microcell techniques, and SECCM is the most modern and significant advance of them.

1.3.2. Microcell techniques and SECCM

The idea of confining an electrochemical cell in a very small area at the end of a micro-capillary probe was firstly developed, mainly for corrosion research (especially affected by the issues highlighted above) in early works such as the ones of Howard *et al.*,[180] Suter, Böhni *et al.*[24,181] and Lohrengel *et al.*[60,182,183] in the 1990s. The technique consists mainly in the use of a thin capillary filled with the solution of interest; the electrolyte forms a microdroplet meniscus at the open sharp end of the capillary, which is used to make a "droplet contact" on the sample, in a delimited area often sealed by a non-conductive layer around the edge. Such confining of the droplet meniscus was designed to effectively create a micrometric size electrochemical cell, with the substrate being the working electrode, and with the other electrodes placed in contact with the solution in the glass capillary. This setup has allowed localised electrochemistry to be performed with high control of the cell confinement.[184-188]

The particular appeal of such techniques arises from the possibility of examining only small areas of the sample, with the advantage of needing a very small amount of electrolyte and avoiding laborious solution-containment preparation procedures of the sample. However, these techniques are often limited in their capabilities of performing systematic scan of the sample by the relatively slowness of the approach and contact of the microdroplet probe with the surface, as well as the size of the probe itself, which is often within the scale of tens of micrometres or larger.[65]

SECCM was developed in order to try to address most of these concerns and nonetheless preserve the key advantages of the microcell techniques, *i.e.* the ability to perform electrochemistry in clear confined area. SECCM was introduced in 2010 in seminal contributions by Unwin and co-workers,[189] and its developments are based on some key characteristics:[61,189-191]

◆ The use of very sharp laser-pulled pipettes as probes, which can reach aperture size (and therefore microcell droplet size) down to the tens of nanometres scale, allowing extremely fine nanometric mapping. Such development is mostly due to the improvement of nano-pipette technology throughout the year, particularly employed in techniques such as SICM.[173]

◆ The better control of the positioning system and a low noise in the electrochemical measurements, allowing currents in the sub-pA order of magnitude to be detected.

◆ An improved way of isolating the micro-nanodroplet probe within the selected area, allowing faster and less laborious ways of approaching and contacting the surface.

The common trait of any SECCM setup them is the presence of an electrolyte filled micro/nano-pipette probe [equipped with QRCE(s)], mounted on a piezoelectric positioning system and connected to electrochemical instrumentation. The pipette can be single or double channel

depending on the type of measurement and substrate. The technique's configuration in the two cases is shown, respectively, in Figure 1.10a and b. In the single channelled configuration the probe is obtained by a cylindrical tube capillary, and a single quasi-reference counter electrode (QRCE) is inserted in the nano pipette. The QRCE and the analysed substrate (which is the working electrode) are then connected to the electronic instrumentation, and the only current flowing in the system is the one between them (indicated as i_{surf} in Figure 1.10).

In the double channel configuration, instead, the probe is made by pulling a theta shaped capillary, effectively creating two separate semi-pipettes (channels), whose filling electrolyte solutions merge only through the droplet meniscus at the end. In this configuration, two individual QRCEs are inserted in the channels, allowing two different currents to be measured synchronously, the one between the two channels (i_{dc} in Figure 1.10) and the one between the QRCE and the sample (i_{surf}, similarly to the single channel configuration).

The advantage of the single channel setup is the easier electrochemical instrumentation and the rapidity of the feedback response, which allows to do faster imaging of the surface. Furthermore, since the single channel pipettes can generally achieve smaller sizes (down to 30 nm in diameter, reported), it is possible to achieve higher imaging resolution.[192] The advantage of the dual channel system, instead, arises from the complete separation between the feedback signal for detecting the meniscus-surface contact (indicated by i_{dc}) and the electrochemical activity of the surface itself (indicated by i_{surf}), which allows the analysis of surfaces with areas of different electrical conductivity (as well as completely non-conductive substrates). SECCM with quad channel nanopipettes has also been reported, with two channels performing the standard meniscus cell contact, and the others functionalised to acquire complementary electrochemical information of the system.[193]
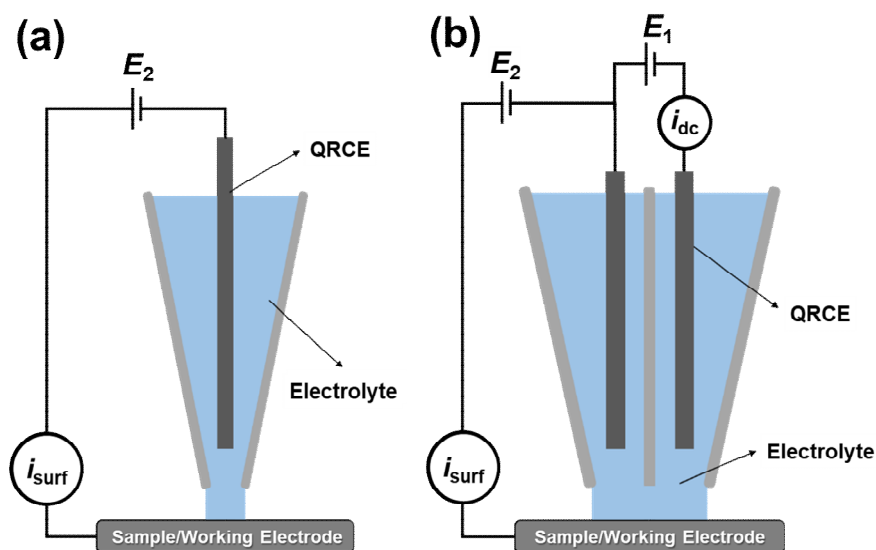
Figure 1.10: Scheme of SECCM setup for (**a**) single channel and (**b**) double channel experiments. Both the setups are shown for a typical potential-controlled experiment.

In SECCM , topography and electrochemical activity mapping are measured synchronously, with no convolution, which is an important advantage over SECM, as discussed above. This is clearly verified for the multiple channel configuration, but also true for the single channel configuration, since the detection of the surface does not depend on a gradual modification of the detected property, but rather in an on/off configuration where there is complete absence of electrochemical signal until the nanodroplet makes contact with the surface.

Relevant applications of the technique over the years include, among others, the study of nanoscale electrochemical characteristic of graphene, graphite and carbon nanotubes,[194-198] the electrosynthesis and electroanalysis of polymers,[199,200] the study of electrocatalytic material for hydrogen evolution reaction,[201-205] CO_2 reduction,[206] oxygen reduction[207-209] and oxygen evolution[210] reactions, the study of Li de-intercalation in energy storage materials,[139,211,212] the electrochemical activity of polycrystalline Pt,[208,213,214] Pd[215] and boron doped diamond,[216] the kinetics of crystal dissolution,[217] the collision and growth of single nanoparticles,[218,219] the study of photoelectrochemical processes[220,221] and the study of the microscopic corrosion properties of polycrystalline Zn,[222] Steel[223-225] and Al.[226]

From a theoretical point of view, the SECCM nanopipette probe shares some characteristics with a conventional microdisc electrode, being the contact area approximately a circle of micrometric or nanometric size, but with the solution geometrically limited at the edges of the electrode, as shown in Figure 1.10. Due to the conical shape of the nanopipette probe, radial diffusion is also the dominant mode of mass transport in SECCM, albeit with an overall flux that is *ca.* 10% of a microdisc of the same radius. The exact value of the steady state current depends on both the size and the geometry (*e.g.,* cone angle) of the probe, and can be precisely modelled by finite element method (FEM) simulations.[97] In a double channel pipette, the presence of two nominally identical QRCEs biased at different potentials (one is normally grounded, while the other is biased with respect to ground) generates a split in the electric field that is equally distributed through the two the different channels. As a consequence, the potential applied between the two QRCEs (E_1 in Figure 1.10b) influences the effective potential applied at the working electrode surface (E_2), such that the effective driving force (E_{surf}) 'felt' at the surface is calculated as

$$E_{surf} = -\left(E_2 + \frac{E_1}{2} \right) \tag{1.57}$$

However, i_{surf} is completely independent of i_{dc}, and therefore these two current signals are readily employed for collecting different information. While i_{surf} describes the electrochemical activity of the sample, i_{dc} gives crucial information on the shape of the droplet and how that is affected by surface contact.

1.4. SYSTEMS OF INTEREST

As mentioned at the beginning of this chapter, there are several fields where the heterogeneity of the surface at the nanoscale can play a crucial role in determining the macroscopic electrochemical properties of a material. The work presented in this thesis focuses mainly on two relevant

electroactive surfaces, conductive polymers and corroding metals. Therefore, it is useful to give an overview on the electrochemical characteristics of these systems, as well as a brief description of the wealth of information that can be revealed with SEPM.

1.4.1. Conductive polymers for electrochemical applications

Polymers that manifest conductive or semiconductive properties have become prominent in the last 40 years as important materials in optoelectronics, showing exceptional promise as active elements in next-generation energy harvesting and storage.[227] These materials are particularly interesting because they pair electrical conductivity with some other properties that are not typical of traditional electrode materials (*e.g.* metals), such as a high mechanical flexibility, printability, biocompatibility, light weight, and the possibility of being synthesized from relatively cheap and sustainable sources. In addition, their conductivity, optical and electronic properties can be tuned relatively easily through chemical synthesis and functionalisation of the consistent molecule(s) (monomers), a process that in traditional electrode materials is far less versatile.[228,229]

Important examples of such macromolecules include chains of aromatic amines (*e.g.* polyanilines) or heterocyclic compounds (*e.g.* polypyrroles, polycarbazoles and polythiophenes) or compounds that, despite not having a conductive backbone chain, possess side groups that can easily undergo redox reactions originating charged conductive species.[227] The structures of two heavily studied polymers, polyaniline (PANI) and poly[3-hexylthiophene] (P3HT) are shown respectively in Figure 1.11a and b.

Conduction in polymers

The conduction of charge through a polymer can happen essentially with two different mechanism, either a movement of delocalised electrons (or electron holes) within a conjugated system (namely electronic
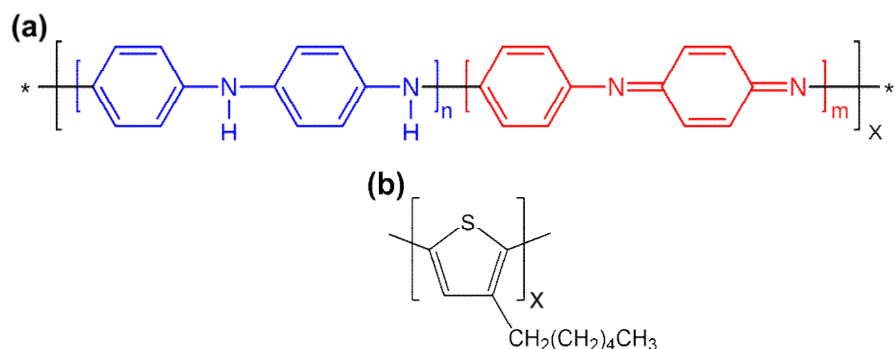
Figure 1.11: Chemical structure of (**a**) polyaniline (PANI), with m + n = 1, and (**b**) poly[3-hexylthiophene] (P3HT).

conduction, or intrinsic conduction) or an electron exchange reaction between neighbouring redox sites (electron hopping and tunnelling mechanisms). In general, the polymers made of a highly conjugated system largely utilise the first mechanism for intra-chain charge transport and the second for interchain conduction (or charge transport at defects within the macromolecule).[227,230,231]

The intrinsic conductivity of the polymers can be usually described in terms of band theory, similar to inorganic conductors and semiconductors, even though the organic structure will present a peculiar set of states that can also assume a discrete energy configuration.[232,233] The injection of charge will cause a change within the band structure, with the formation of localised and delocalised charged structures such as solitons polarons and bipolarons.[229,234,235] This kind of transport is believed to be extremely fast at least in macromolecules with little defects, while the transfer between different chains, governed by the hopping mechanism, is generally the rate determining step and strictly depend on the distance, and therefore on the supramolecular structure and the presence of crystallinity.[233,236,237]

Polymers can be electrochemically doped by oxidation or reduction, which can dramatically increase the conduction properties. Given the permeability and the ionisation of the material during the charge transfer, the conduction in polymers is usually associated with transport of ions

through the polymeric phase, thus resulting in an electron-ion hybrid conduction mechanism.[238,239]

Applications and microstructural implications

A considerable number of polymer-based electrochemical devices and architectures have been developed to date, including supercapacitors,[240,241] redox-flow batteries[242] and organic bioelectronics,[243-245] thermogalvanics,[246] electrochromics[247-249] and photo-electrochemical devices.[15,250] Recent advances in emergent wearable health-monitoring devices have inspired the inclusion of conductive polymers as sensing elements on fabrics and textiles, on the skin as electronic tattoos, and *in vivo*.[249,251]

All these applications often involve the complex microscale blending of one or more conducive polymer with other conductive and non-conductive materials, in order to create a p-n junctions, to improve the charge transport properties, increase the contact area of the active surface and improve resistance of the device to aging and environmental degradation.[252-255] As an example, in a typical organic photovoltaic cell, a conducting polymer is usually employed as electron donor, and because of its non-uniform and short-distanced conduction properties, it needs to be carefully blended, at a nanometric level with the electron acceptor (*e.g.* a fullerene derivative) in order to facilitate the electron transfer between them. The nature of such blending is one of the main parameters affecting the efficiency of the cell.[256-258]

Another relevant example is represented by organic field effect transistors.[259] In these devices, a polymer such as P3HT acts as the semiconductor layer connecting the two main electrodes (Source and Drain) and being "activated" when an appropriate potential is applied to a third electrode (Gate), separated by the rest of the structure by a dielectric layer.[260] In such devices, it was observed that mixing the P3HT with insulating

polymers in various proportions can improve the carrier mobility (electrons or electron holes, depending on the type of transistor) and the stability toward degradation. With adequate synthesis procedures, the insulating polymer can create an encapsulation layer that prevent contact with air, improve mechanical properties and form a scaffold for the conductive polymer, allowing the creation of stratified structures that actually improve charge transport properties.[261,262]

The design of more efficient devices generally leads to more complex blend and structures, and therefore an increase complexity of the material surface on the micro and nanoscale. However, as it will be discussed in Chapter 3, most of the characterization of such materials still relies heavily on macroscopic electrochemical techniques, which for their own nature can only give a partial picture of the properties of microstructured surfaces.[62] For this reason, techniques in the SEPM family, such as SECCM, have the potential to revolutionise the study of complex conductive polymers blends, revealing previously unseen phenomena at the scale of surface heterogeneities.

1.4.2. Metal corrosion and corrosion protection

Corrosion is regarded as one of the most compelling and expensive issues in the modern world, being a major cause of degradation of machinery, cultural artefacts, buildings etc., therefore impacting several aspects of industrial production and everyday life. The cost of the direct and indirect effects of *metallic* corrosion (*e.g.* machine parts replacements, building refurbishments, malfunctioning because of faults and breakdowns, etc.) is estimated to amount to *ca.* 3% of the GDP of an industrialised country.[263,264]

Corrosion itself is intrinsically an electrochemical process, where the metallic surface (which can be referred as the working electrode in a hy-

pothetical corroding electrochemical cell) provides the main anodic re-action (*i.e.* the metal oxidation), while the cathodic process is provided by the phase the metal is in contact with, which could be an electrolyte solution or other kind of liquid, a gas (*e.g.* air), or another metal, or any combination of them.[265] To cite an example, in the atmospheric corrosion of copper, where the metal is generally in contact with open air and covered by a thin layer of aqueous solution, the cathodic process is mostly the oxygen reduction reaction by atmospheric O_2.[266] In many cases the corroding system is characterised by a complex multiphase interface, with multiple layers of the metallic element in different states of oxidation, (*e.g.* oxides, hydroxides, salts, coordination compounds, etc., depending on the metal and the electrolyte), metal-metal junctions and liquid layers in contact with gas phases.[19,265,267]

Mixed potential theory and corrosion characterisation

Different kinetic and thermodynamic parameters can be used to characterise metal corrosion. As a base "textbook" example, the corrosion of Zn immersed in an HCl solution is considered, with the anodic reaction being the oxidation of the metal to the completely solvated ion,

$$Zn_{(s)} \rightarrow Zn^{2+}_{(aq)} + 2e^-, \qquad (1.58)$$

and the cathodic reaction being the hydrogen evolution reaction (HER),

$$2H^+ + Cl^- + 2e^- \rightarrow H_2 + 2Cl^-. \qquad (1.59)$$

Both processes are characterised by their own kinetic and thermodynamic parameters, with the overall corrosion rate depending on the combination of them. In the simplest case, the two reactions can be related with the mixed potential theory, which assumes each electrochemical half-reaction acts as an independent process governed by Butler-Volmer kinetics [described by eq. (1.19)].[265,268] At high values of overpotential for both cathodic and anodic reactions, one of the two terms of the Butler-

Volmer equation can be neglected, and therefore the equation will assume a simple exponential form;[67] for the aforementioned Zn corrosion process, in the ideal case of negligible mass transport (for which $C_x(0,t) \approx C_x^*$) can be arranged as:

$$\ln(I_{Zn^{2+}/Zn}) = \ln(I_{0,Zn}) - \alpha_{Zn}\frac{nF}{RT}\eta_{Zn}. \tag{1.60}$$

$$\ln(I_{HER}) = \ln(I_{0,HER}) + (1-\alpha_{HER})\frac{nF}{RT}\eta_{HER}. \tag{1.61}$$

The ideal processes described by Eqs. (1.60) and (1.61) can be visualised with the η vs $\log(i)$ plot, also known as Evans diagram,[269,270] as shown in Figure 1.12, while the representation of the linear relation between E and $\log(i)$ at high values of η is generally referred as Tafel plot.[271] In particular, the slope of such graph, corresponding to $(RT)/(-anF)$ [or $(RT)/(nF-anF)$, depending on the half-reaction], is called Tafel slope and is an important kinetic and mechanistic parameter, often used for characterising electrocatalytic reactions.[272,273]

The potential at which the anodic and cathodic current are equal, corresponding to the point of dynamic equilibrium of the corrosion reaction, is often referred as the corrosion potential (E_{corr}). The corresponding half-cell current is defined as corrosion current (i_{corr}), and represents the main kinetic parameter of the overall process. These two parameters are often measured with techniques of potentiodynamic polarisation, *i.e.* sweep voltammetry in conditions of minimum influence by mass transport phenomena,[19,274] with E_{corr} and i_{corr} being obtained by the intersection of the extrapolated linear part of the curves, as shown in Figure 1.12 for the aforementioned Zn corrosion. E_{corr} acts as an effective dynamic equilibrium parameter, and can be also estimated by measures of open circuit potential (OCP).
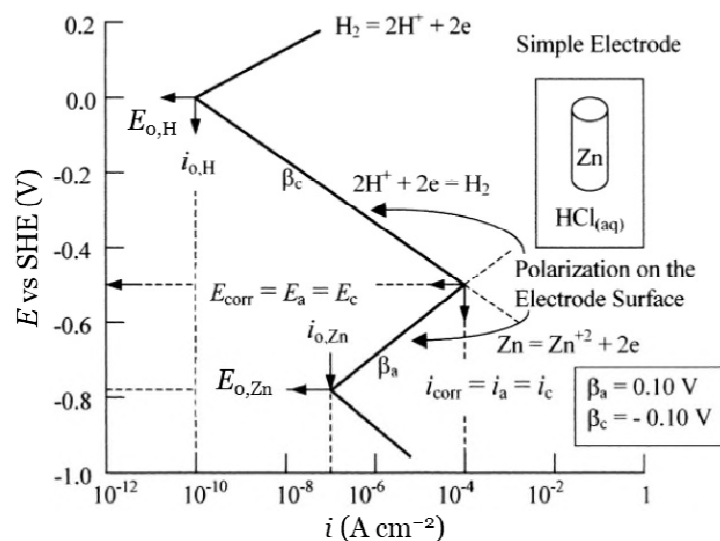
Figure 1.12: Evans diagram for Zn corrosion in HCl solution. Reproduced from Ref. [265].

The mixed potential theory can be useful to give a simple explanation of the corrosion process, however, in many cases corrosion involves several intermediates and multistep mechanisms. Often the oxidation of the metal involves the formation of different layers of oxide, hydroxides, and salt depending on the species dissolved in the electrolyte. Such reactions are heavily influenced by pH, and can bring to the formation of passive layers that hinder the corrosion reaction in a wide potential range.

Regarding copper behaviour, electrochemical and spectroscopy studies have detected many stages of oxidation and, therefore, different layers of partially oxidised Cu on the surface. Some of them are composed by crystalline forms of copper oxides (Cu_2O and CuO, but also Cu_2O_3), hydroxides (in alkaline environment) and many other compounds depending on the electrolyte which is used.[275-278] As an example, in buffered (chloride free) solutions the first resistance to corrosion is given by a thin layer of copper (I) oxide (≈ 10Å). At more anodic potential copper (II) oxide or hydroxide (depending on the pH) start to form, creating defects in the first layer which increase the current until the $CuO/Cu(OH)_2$ layer is thick enough to give a strong resistance, at high anodic potentials.[275,276]

(a)

(b)
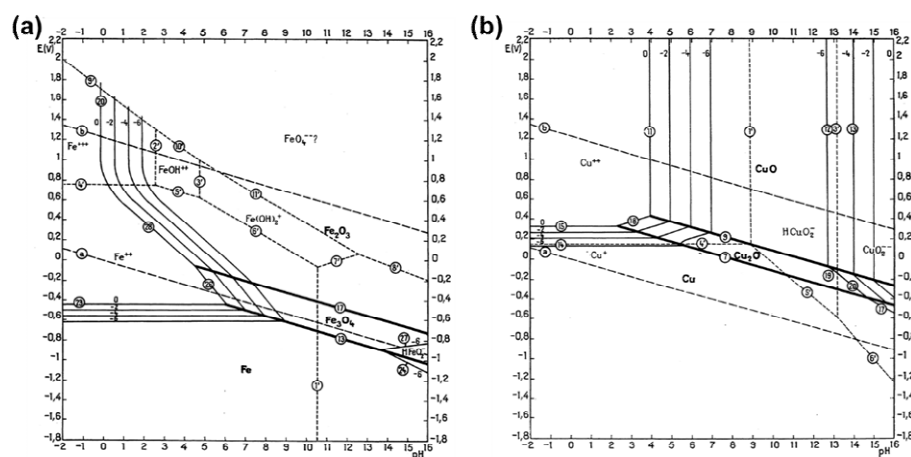
Figure 1.13: Pourbaix diagram for the corrosion of unalloyed **(a)** Fe and **(b)** Cu (both with only oxides and not hydroxides considered). Freely reproduced from Ref. [279]. Each continuous and dotted line describes a change of phase, (where multiple parallel lines represent the same transition at different concentrations of the dissolved species), while the two parallel dashed lines describe, respectively the potential for HER (bottom) and ORR (top).

The thermodynamic and kinetic properties of the different layers of partially oxidised metals, formed at the interface with the electrochemical solution during the corrosion process, largely depend both on the potential applied and on the pH. It is possible to visualise the thermodynamic stability of such layers with phase stability (potential/pH) diagrams, also known as Pourbaix diagrams,[279,280] of which examples for Fe and Cu corrosion are shown respectively in Figure 1.13a and b. Generally, the pH dependent standard potentials for the oxygen reductio reaction, (ORR) and HER are also shown, in order to give an idea of what could be the most relevant cathodic process in aqueous solution. The comparison between Figure 1.13a and b, for example, rapidly shows that Fe can be oxidised by H^+ almost at any pH, while Cu cannot, and that Fe^{2+} can be a stable corrosion product while Cu^+ cannot, except within the oxide layer at high pH. In several metals, the thermodynamic stability of the formed layers on the surface can provide an indication on the range of conditions where they are protected from further oxidation.[19,265] However, these diagrams cannot provide insight on the kinetics of formation of such layers

50

which depend on several factor, notably including the microscopic characteristics of the surface.

Surface complexity

Aside from the intricacy of corrosion mechanisms in a chemical sense (*e.g.* see Figure 1.13), these processes take place at a surface and are therefore heavily influenced by interfacial properties. Surface defects are often points of initiation for corrosion processes, giving rise to specific phenomena such as crevice, pitting and filiform corrosion.[281-283] In polycrystalline metals, grains of different crystallographic orientation typically have a different corrosion activity,[284-287] and additionally, grain boundaries may also play a fundamental role in the process, giving rise to phenomena such as intergranular corrosion.[288-291] Other important factors that can locally affect the corrosion properties at a local level are the presence of points of mechanical, thermal or other stress,[292] the presence of specific microorganisms,[293] the presence of contaminants or particular configurations in alloy metals that causes the surfaces not to be homogeneous. An interesting example of the latter case, could be the presence of particular Zn formations in the Cu matrix of brass,[294,295] or the Mg inclusions in an alloyed steel.[296,297]

The contribution of all these factors generally have dramatic consequences on the overall corrosion reaction, and it is possible, to a limited extent, to study them with macroscopic methods of measure. However, a deep understanding of these phenomena can be obtained only with microscopic techniques of analysis. A common approach in corrosion studies is to apply a corrosion perturbation to the entire system and then examine its effect at the micro/nanoscale with a combination of spectroscopic and microscopy techniques. As a significant example (related to the topics that will be discussed in Chapter 5 to 7), Terryn and co-workers used electron backscattered diffraction (EBSD) in combination with STM, AFM and SECM for studying copper corrosion in chloride media,

and its dependency on the crystallographic orientation.[298-301] With such approach, the activity of different grains was identified (*e.g.* the ones of {111} orientation seem to be more resistant to electrochemical oxidation than the ones of{001 orientation), as well as a difference in the chemical nature of the passivation layer formed different grains. In particular, the {111} was found to have a more passive oxide layer on the top, while the {001} grain has a less stable oxide and, in addition, a top granular film of amorphous hydroxides.[299]

Besides the specific corrosion properties related to the microstructure of the surface, the corroding environment (*i.e.* the other phase in contact with the metal) can have a variability on a microscopic level. As an example, environmental corrosion is often caused by droplet of corroding solution in contact with the metal; it has been shown that in many cases the metal/droplet/air interface is the most active area for corrosion initiation.[23,302,303] Biofilm corrosion usually involve a complex environment formed by cells and associated intercellular matrix.[304] Additionally, as will be discussed in details in Chapter 5 to 7, corrosion by oil products is often caused by aqueous contaminants dispersed as nanodroplet in the non-aqueous phase.[305,306]

Corrosion inhibition

In order to prevent or limit the effect of corrosion, several approaches have been developed and employed. One of the most important is represented by coating the metal with inert organic and inorganic layers, [307-309] or with sacrificial metals that provide corrosion protection by oxidising instead of the coated surface (anodic protection).[310] Other strategies employ functionalisation of the solutions that are in contact with the metal.

Fundamental compounds that can be used in both cases, either as additive in solution or as part of coatings, are the so-called corrosion inhibitors, *i.e.* species with the ability to slow down or hinder the corrosion pro-

cesses. [311-314] They can either act as sacrificial antioxidants in solution (being oxidised instead of the metal surface) or form a layer on the surface that acts as a physical barrier against O_2 and other corroding agents, or actively intervene and increase the activation energy of some critical steps of the corrosion mechanism. The use of corrosion inhibitors is often useful to avoid unpleasant and expensive bulk organic coatings of the metal (such as certain types of paint), and their properties depend strictly on their structure and the specific corroding environment.

One of the most common classes of inhibitors, used especially for preventing Cu corrosion, is that of benzotriazole (BTAH) and its derivatives,[315] whose action will be examined in detail in Chapter 7. The action of BTAH, as well as most other inhibitors that act by strongly interacting with the metallic surface, by definition has a strong dependence on surface microstructure. Several studies, employing both microscopy techniques and quantum mechanical simulations, have shown how the structures that such molecules create on the surface are critical for their inhibition action.[316-320]

Application of SECCM in corrosion science

As alluded to above, electrochemistry at (sub)microscale, and SECCM in particular, is extremely promising for the characterisation of microstructural effects in metal corrosion. SECCM, coupled with other microscopic and spectroscopic techniques, is able to couple the high level of mechanistic information available from classical electrochemical techniques with the local resolution needed for characterising the microstructural properties implicated in corrosion processes. As such, in recent years it has been employed to explore the crystallographic dependent properties of Zn,[222] Steel[223-225] and Al[226] corrosion processes.

In particular, the work carried out by Yule *et al* on the corrosion of low carbon steel in H_2SO_4 (pH $\approx$ 2.2),[225] depicted in Figure 1.14, showed how
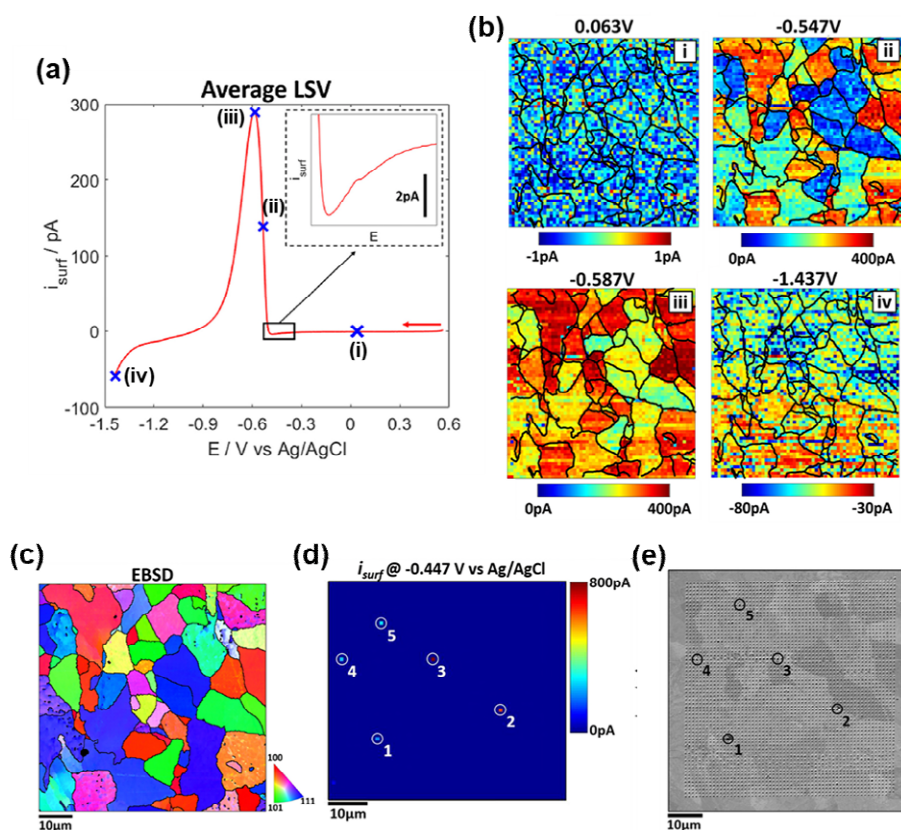
Figure 1.14: (**a**) Average Potentiodynamic polarisation (i–E) curve ($v = 2 \, \text{V s}^{-1}$). (**b**) Spatially resolved i_{surf} maps obtained at the potentials indicated in (**a**), and (**c**) corresponding Crystallographic orientation map (obtained with EBSD). (**d**) Spatially resolved i_{surf} map obtained at a potential of -0.447 V (with enhanced scale to highlight 5 specific outliner pixels) and (**e**) corresponding SEM image. All the figures are reported from Ref. [225].

it is possible to employ SECCM to record the activity of several consecutive processes in the metal dissolution and cross correlate them with crystallographic and compositional information. As shown in Figure 1.14, a voltammetric analysis was carried out (Figure 1.14a) in order to go through the potentials of (i) the Fe_2O_3 passive film formation, (ii) its following reduction, (iii) the active iron dissolution and (iv) the cathodic processes (HER and ORR). Each of these processed was represented by a spatially resolved current map (Figure 1.14b), that was correlated with the co-located crystallographic orientation map Figure 1.14c) obtained through EBSD, to statistically analyse the difference in behaviour on dif-

ferent grains. In addition, the resolution achieved by the technique allowed to explore the activity of single MnS inclusions,[297] which exhibited a more articulated electrochemical behaviour and a larger current, as shown by the comparison between the re-scaled electrochemical image of process (iii) and the co-located SEM image (Figure 1.14d and e respectively).

In addition to the electrochemical/surface structure correlation analysis possibilities, the peculiar nanodroplet meniscus configuration allows the creation of a system of analysis where the examined metal is in contact with both the solution in the nanopipette and the external environment within a confined space. This, in particular conditions, as it will be examined in Chapter 5 to 7 for a Cu surface, can allow the study of corrosion and corrosion inhibition on both a complex surface and a complex corroding multiphase environment.[226]

1.5. OVERVIEW AND AIM OF THE WORK

The previous sections have underlined how combining the power of classical electroanalytical techniques (introduced in paragraphs 1.1 and 1.2) for mechanistic characterisation with the surface analysis possibilities of scanning probe microscopy has led to the development of scanning electrochemical cell microscopy (SECCM, paragraph 1.3). SECCM has proven to be a powerful tool for the characterisation of many different kinds of structurally-heterogeneous electroactive surfaces. Yet SECCM is still constantly being developed, both in terms of measurement capability (*e.g.*, scanning speed, resolution, electrochemical waveforms etc.) and areas of application. On the latter point, two very interesting fields in which SECCM has the potential to reveal considerable new information on surface structure-activity are conductive polymers for energy devices and corroding surfaces. Therefore, this thesis is focused on developing new ways of SECCM analysis and applying them to the study of some exemplar cases belonging to the two fields discussed above.

Firstly, in Chapter 3, SECCM is applied to the study of the electron transfer properties of a complex microscale blend of conductive and non-conductive polymers. This work is aimed not only to demonstrate that SECCM can actually be employed in this important field, revealing a wealth of information that is obscured in conventional macroscopic measurements, but also to overcome some technical limitations associated with the use of double channel pipettes (*i.e.* a generally slow speed of analysis and a relatively low lateral resolution of the imaging, if compared to single channel experiments).[97,179,216]

Secondly, a new approach for the use of SECCM as a electroanalytical technique is introduced. So far, with only very few exceptions (mostly related to battery research),[139,211] SECCM has been mostly employed in a potential controlled setup. Therefore, in Chapter 4 the use of a current controlled technique, chronopotentiometry, is explored on a series of surfaces of increasing complexity, demonstrating that, if needed, chronopotentiometric SECCM can also be a powerful electrochemical imaging tool for characterising heterogeneous interfaces.

Thirdly, a new experimental configuration for studying the corrosion of Cu in a triple-phase microscopic system is introduced. So far, most of SECCM studies have been conducted with the sample and the nanodroplet directly in contact with the atmosphere (either air or other controlled gas phases).[222,225] This work demonstrates that the effect and the activity of an immiscible liquid phase (replacing the gaseous atmosphere) around the aqueous nanodroplet can be as well studied with SECCM.[226] Employed with a mineral oil (dodecane based) immiscible phase, these conditions resemble those encountered in an corrosive industrial environment. This part of the investigation is developed through the three following chapters.

Chapter 5 marries this triple-phase configuration with the new set up introduced in Chapter 4, taking advantage of the unique characteristics

of chronopotentiometric SECCM to study the intercorrelation between the different reactions involved in Cu corrosion. In Chapter 6, instead, a conventional voltammetric approach is adopted to better study the effect of the molecular oxygen, flowing through the different phases, from the atmosphere, through the oil layer and into the aqueous nanodroplet, on the corrosion of metallic copper in a confined environment. Finally, in Chapter 7, the functionalisation of the oil phase with a corrosion inhibitor and its effect on the corrosion happening *in the aqueous phase* is studied, furtherly increasing the level of complexity of this multi-phase application of the SECCM technique.

Moreover, besides the bare study of such reactions at the micro-nanoscale, which is already interesting *per se*, this work is aimed at exploiting the possibility of SECCM to map a polycrystalline surface in all of these three cases, and therefore exploring how such processes are influenced by the crystallographic orientation of the metal, paving the way for a wide spectrum crystallography/electrochemistry correlation analysis.

1.6.   REFERENCES

[1]   Shockley, W.; Bardeen, J.; Brattain, W. H. *Physics 1942–1962*; Elsevier, 2013.

[2]   Plummer, E. W.; Ismail; Matzdorf, R.; Melechko, A. V.; Pierce, J. P.; Zhang, J. Surfaces: a playground for physics with broken symmetry in reduced dimensionality. *Surf. Sci.* **2002,** *500* (1), 1-27.

[3]   Duke, C. B. The birth and evolution of surface science: Child of the union of science and technology. *Proc. Natl. Acad. Sci. U.S.A.* **2003,** *100* (7), 3858.

[4]   Feliu, J. M. Future tasks in interfacial electrochemistry and surface reactivity. *J. Solid State Electrochem.* **2020,** *24* (9), 2073-2075.

[5]   Somorjai, G. A.; Li, Y. Impact of surface chemistry. *Proc. Natl. Acad. Sci. U.S.A.* **2011,** *108* (3), 917.

[6]   Minato, T.; Abe, T. Surface and interface sciences of Li-ion batteries: -Research progress in electrode–electrolyte interface. *Prog. Surf. Sci.* **2017,** *92* (4), 240-280.

[7]   Kempaiah, R.; Vasudevamurthy, G.; Subramanian, A. Scanning probe microscopy based characterization of battery materials, interfaces, and processes. *Nano Energy* **2019,** *65*, 103925.

[8]   Ventosa, E. Why nanoelectrochemistry is necessary in battery research? *Curr. Opin. Electrochem.* **2021,** *25*, 100635.

[9]   Koper, M. T. M. Electrocatalysis on bimetallic and alloy surfaces. *Surf. Sci.* **2004,** *548* (1), 1-3.

[10]   Duca, M.; Koper, M. T. M. In *Surface and Interface Science*, 2020; Vol. 8.

[11]   O'Mullane, A. P. From single crystal surfaces to single atoms: investigating active sites in electrocatalysis. *Nanoscale* **2014,** *6* (8), 4012-4026.

[12]   Zheng, Y.; Jiao, Y.; Vasileff, A.; Qiao, S.-Z. The Hydrogen Evolution Reaction in Alkaline Solution: From Theory, Single Crystal Models, to Practical Electrocatalysts. *Angew. Chem. Int. Ed.* **2018,** *57* (26), 7568-7579.

[13]   Bianchini, C.; Shen, P. K. Palladium-Based Electrocatalysts for Alcohol Oxidation in Half Cells and in Direct Alcohol Fuel Cells. *Chem. Rev.* **2009,** *109* (9), 4183-4206.

[14]   Debe, M. K. Electrocatalyst approaches and challenges for automotive fuel cells. *Nature* **2012,** *486* (7401), 43-51.

[15]   Ratcliff, E. L.; Zacher, B.; Armstrong, N. R. Selective Interlayers and Contacts in Organic Photovoltaic Cells. *J. Phys. Chem. Lett.* **2011,** *2* (11), 1337-1350.

[16]   Badawy, W. A. A review on solar cells from Si-single crystals to porous materials and quantum dots. *J. Adv. Res.* **2015,** *6* (2), 123-132.

[17]   Kavan, L. Electrochemistry and dye-sensitized solar cells. *Curr. Opin. Electrochem.* **2017,** *2* (1), 88-96.

[18]   Wang, H.; Guerrero, A.; Bou, A.; Al-Mayouf, A. M.; Bisquert, J. Kinetic and material properties of interfaces governing slow response and long timescale phenomena in perovskite solar cells. *Energy Environ. Sci.* **2019,** *12* (7), 2054-2079.

[19]   Marcus, P.; Oudar, J. *Corrosion mechanisms in theory and practice*; Marcel Dekker, New York, NY (United States): United States, 1995.

[20]   Tsuru, T. Anodic dissolution mechanisms of metals and alloys. *Materials Science and Engineering: A* **1991,** *146* (1), 1-14.

[21]   Erb, U.; Gleiter, H.; Schwitzgebel, G. The effect of boundary structure (energy) on interfacial corrosion. *Acta Metall.* **1982,** *30* (7), 1377-1380.

[22]   Ralston, K. D.; Birbilis, N. Effect of Grain Size on Corrosion: A Review. *Corrosion* **2010,** *66* (7), 075005-075005-075013.

[23]   Koushik, B. G.; Van den Steen, N.; Mamme, M. H.; Van Ingelgem, Y.; Terryn, H. Review on modelling of corrosion under droplet electrolyte for predicting atmospheric corrosion rate. *J. Mater. Sci. Technol.* **2021,** *62*, 254-267.

[24]   Böhni, H.; Suter, T.; Schreyer, A. Micro- and nanotechniques to study localized corrosion. *Electrochim. Acta* **1995,** *40* (10), 1361 - 1368.

[25]   Oltra, R.; Maurice, V.; Akid, R.; Marcus, P. *Local Probe Techniques for Corrosion Research*; Woodhead Publishing Limited, 2007.

[26]   Payne, N. A.; Stephens, L. I.; Mauzeroll, J. The Application of Scanning Electrochemical Microscopy to Corrosion Research. *Corrosion* **2017,** *73* (7), 759-780.

[27]   Berry, M. N. An electrochemical interpretation of metabolism. *FEBS Lett.* **1981,** *134* (2), 133-138.

[28] Crofts, A. R.; Wraight, C. A. The electrochemical domain of photosynthesis. *Biochim. Biophys. Acta, Rev. Bioenerg.* **1983,** *726* (3), 149-185.

[29] Babauta, J.; Renslow, R.; Lewandowski, Z.; Beyenal, H. Electrochemically active biofilms: facts and fiction. A review. *Biofouling* **2012,** *28* (8), 789-812.

[30] Santos, C. S.; Kowaltowski, A. J.; Bertotti, M. Single Cell Oxygen Mapping (SCOM) by Scanning Electrochemical Microscopy Uncovers Heterogeneous Intracellular Oxygen Consumption. *Sci. Rep.* **2017,** *7* (1), 11428.

[31] Hoffmann, R. A chemical and theoretical way to look at bonding on surfaces. *Rev. Mod. Phys.* **1988,** *60* (3), 601-628.

[32] Groß, A. *Theoretical Surface Science*; Springer Berlin Heidelberg: Berlin, Heidelberg, 2009.

[33] Heinz, K.; Starke, U. In *Surface and Interface Science*; 1 ed.; Wandelt, K., Ed.; Wiley, 2013.

[34] Bozack, M. J.; Muehlhoff, L.; Russell, J. N.; Choyke, W. J.; Yates, J. T. Methods in semiconductor surface chemistry. *J. Vac. Sci. Technol., A* **1987,** *5* (1), 1-8.

[35] Sykes, D. In *Springer Handbook of Electronic and Photonic Materials*; Kasap, S.;Capper, P., Eds.; Springer International Publishing: Cham, 2017.

[36] Stiles, P. L.; Dieringer, J. A.; Shah, N. C.; Van Duyne, R. P. Surface-Enhanced Raman Spectroscopy. *Annu. Rev. Anal. Chem.* **2008,** *1* (1), 601-626.

[37] Citrin, P. H. X-ray absorption spectroscopy applied to surface structure: SEXAFS and NEXAFS. *Surf. Sci.* **1994,** *299-300*, 199-218.

[38] Fadley, C. S. X-ray photoelectron spectroscopy: Progress and perspectives. *J. Electron. Spectrosc. Relat. Phenom.* **2010,** *178-179*, 2-32.

[39] Stoev, K. N.; Sakurai, K. Review on grazing incidence X-ray spectrometry and reflectometry. *Spectrochim. Acta, Part B* **1999,** *54* (1), 41-82.

[40] Müller-Buschbaum, P. Grazing incidence small-angle neutron scattering: challenges and possibilities. *Polym. J.* **2013,** *45* (1), 34-42.

[41] Van Hove, M. A.; Weinberg, W. H.; Chan, C.-M. *Low-Energy Electron Diffraction: Experiment, Theory and Surface Structure Determination*; Springer Berlin Heidelberg: Berlin, Heidelberg, 1986.

[42] Lider, V. V. X-ray diffraction methods for diagnostics of surface and nanolayers of crystalline structures (review). *Inorg. Mater.* **2014,** *50* (15), 1459-1469.

[43] Boudart, M. Heterogeneity of Metal Surfaces. *J. Am. Chem. Soc.* **1952,** *74* (14), 3556-3561.

[44] Duke, C. B.; Plummer, E. W. *Frontiers in surface and interface science*; 1st ed ed.; Elsevier: Amsterdam ; Boston, 2002.

[45] Croft, W. J. *Under the microscope: a brief history of microscopy*; World Scientific: Hackensack, NJ, 2006.

[46] Williams, D. B.; Carter, C. B. *Transmission Electron Microscopy*; Springer US: Boston, MA, 2009.

[47] Reimer, L. *Scanning Electron Microscopy*; Springer Berlin Heidelberg: Berlin, Heidelberg, 1998.

[48]   Herman, B.; Lemasters, J. J. *Optical Microscopy: Emerging Methods and Applications*; Elsevier Science: Saint Louis, 2012.

[49]   Michaelis, J.; Hettich, C.; Mlynek, J.; Sandoghdar, V. Optical microscopy using a single-molecule light source. *Nature* **2000,** *405* (6784), 325-328.

[50]   Holt, M.; Harder, R.; Winarski, R.; Rose, V. Nanoscale Hard X-Ray Microscopy Methods for Materials Studies. *Annu. Rev. Mater. Sci.* **2013,** *43* (1), 183-211.

[51]   Zürch, M. W. *High-Resolution Extreme Ultraviolet Microscopy*; Springer International Publishing: Cham, 2015.

[52]   Heiderhoff, R.; Balk, L. J. In *Handbook of Nanoscopy*, 2012.

[53]   Binnig, G.; Rohrer, H.; Gerber, C.; Weibel, E. Surface Studies by Scanning Tunneling Microscopy. *Phys. Rev. Lett.* **1982,** *49* (1), 57-61.

[54]   Hirjibehedin, C. F.; Wang, Y. Recent advances in scanning tunneling microscopy and spectroscopy. *J. Phys.: Condens. Matter* **2014,** *26* (39), 390301.

[55]   Binnig, G.; Quate, C. F.; Gerber, C. Atomic Force Microscope. *Phys. Rev. Lett.* **1986,** *56* (9), 930-933.

[56]   Melitz, W.; Shen, J.; Kummel, A. C.; Lee, S. Kelvin probe force microscopy and its application. *Surf. Sci. Rep.* **2011,** *66* (1), 1-27.

[57]   Rohwerder, M.; Turcu, F. High-resolution Kelvin probe microscopy in corrosion science: Scanning Kelvin probe force microscopy (SKPFM) versus classical scanning Kelvin probe (SKP). *Electrochim. Acta* **2007,** *53* (2), 290-299.

[58]   Amemiya, S.; Bard, A. J.; Fan, F.-R. F.; Mirkin, M. V.; Unwin, P. R. Scanning Electrochemical Microscopy. *Annu. Rev. Anal. Chem.* **2008,** *1* (1), 95-131.

[59]   Chen, C.-C.; Zhou, Y.; Baker, L. A. Scanning Ion Conductance Microscopy. *Annu. Rev. Anal. Chem.* **2012,** *5* (1), 207-228.

[60]   Lohrengel, M. M.; Moehring, A.; Pilaski, M. Electrochemical surface analysis with the scanning droplet cell. *Fresenius J. Anal. Chem.* **2000,** *367* (4), 334-339.

[61]   Ebejer, N.; Güell, A. G.; Lai, S. C. S.; McKelvey, K.; Snowden, M. E.; Unwin, P. R. Scanning Electrochemical Cell Microscopy: A Versatile Technique for Nanoscale Electrochemistry and Functional Imaging. *Annu. Rev. Anal. Chem.* **2013,** *6* (1), 329-351.

[62]   Bentley, C. L.; Kang, M.; Unwin, P. R. Nanoscale Surface Structure–Activity in Electrochemistry and Electrocatalysis. *J. Am. Chem. Soc.* **2019,** *141* (6), 2179-2193.

[63]   Bard, A. J.; Fan, F. R. F.; Kwak, J.; Lev, O. Scanning electrochemical microscopy. Introduction and principles. *Anal. Chem.* **1989,** *61* (2), 132-138.

[64]   Hansma, P. K.; Drake, B.; Marti, O.; Gould, S. A.; Prater, C. B. The scanning ion-conductance microscope. *Science* **1989,** *243* (4891), 641.

[65]   Aaronson, B. D. B.; Güell, A. G.; McKelvey, K.; Momotenko, D.; Unwin, P. R. In *Nanoelectrochemistry*; Mirkin, M. V.;Amemiya, S., Eds.; CRC Press, 2015.

[66]   Edwards, M. A.; Robinson, D. A.; Ren, H.; Cheyne, C. G.; Tan, C. S.; White, H. S. Nanoscale electrochemical kinetics & dynamics: the challenges and opportunities of single-entity measurements. *Faraday Discuss.* **2018,** *210* (0), 9-

28.

[67] Bard, A. J.; Faulkner, L. R. *Electrochemical Methods: Fundamentals and Applications*; John Wiley and Sons Inc., 2001.

[68] Newman, J. S.; Thomas-Alyea, K. E. *Electrochemical systems*; 3rd ed ed.; J. Wiley: Hoboken, N.J, 2004.

[69] Sato, N. In *Electrochemistry at Metal and Semiconductor Electrodes*; Sato, N., Ed.; Elsevier Science: Amsterdam, 1998.

[70] Shaposhnik, V. A. Walter Nernst and analytical chemistry. *J. Anal. Chem.* **2008,** *63* (2), 199-201.

[71] Erdey-Grúz, T. *Kinetics of electrode processes*; Wiley-Interscience: New York, 1972.

[72] Bockris, J. O. M.; Khan, S. U. M. In *Quantum Electrochemistry*; Springer US: Boston, MA, 1979.

[73] Eyring, H. The Activated Complex in Chemical Reactions. *J. Chem. Phys.* **1935,** *3* (2), 107-115.

[74] Laidler, K. J.; King, M. C. Development of transition-state theory. *J. Phys. Chem.* **1983,** *87* (15), 2657-2664.

[75] Brunschwig, B. S.; Logan, J.; Newton, M. D.; Sutin, N. A semiclassical treatment of electron-exchange reactions. Application to the hexaaquoiron(II)-hexaaquoiron(III) system. *J. Am. Chem. Soc.* **1980,** *102* (18), 5798-5809.

[76] Henstridge, M. C.; Laborda, E.; Rees, N. V.; Compton, R. G. Marcus–Hush–Chidsey theory of electron transfer applied to voltammetry: A review. *Electrochim. Acta* **2012,** *84*, 12-20.

[77] Butler, J. A. V. Studies in heterogeneous equilibria. Part II.—The kinetic interpretation of the nernst theory of electromotive force. *Trans. Faraday Soc.* **1924,** *19* (March), 729-733.

[78] Erdey-Grúz, T.; Volmer, M. Zur Theorie der Wasserstoff Überspannung. *Z. Phys. Chem.* **1930,** *150A* (1).

[79] Sun, P.; Mirkin, M. V. Kinetics of Electron-Transfer Reactions at Nanoelectrodes. *Anal. Chem.* **2006,** *78* (18), 6526-6534.

[80] Lai, S. C. S.; Patel, A. N.; McKelvey, K.; Unwin, P. R. Definitive Evidence for Fast Electron Transfer at Pristine Basal Plane Graphite from High-Resolution Electrochemical Imaging. *Angew. Chem. Int. Ed.* **2012,** *51* (22), 5405-5408.

[81] Compton, R. G.; Banks, C. E. *Understanding Voltammetry*; IMPERIAL COLLEGE PRESS, 2010.

[82] Weinberg, D. R.; Gagliardi, C. J.; Hull, J. F.; Murphy, C. F.; Kent, C. A.; Westlake, B. C.; Paul, A.; Ess, D. H.; McCafferty, D. G.; Meyer, T. J. Proton-Coupled Electron Transfer. *Chem. Rev.* **2012,** *112* (7), 4016-4093.

[83] Savéant, J.-M. In *Elements of Molecular and Biomolecular Electrochemistry*; John Wiley & Sons, Inc.: Hoboken, NJ, USA, 2006.

[84] Gerischer, H. The impact of semiconductors on the concepts of electrochemistry. *Electrochim. Acta* **1990,** *35* (11), 1677-1699.

[85] Jørgensen, M.; Norrman, K.; Krebs, F. C. Stability/degradation of polymer solar cells. *Sol. Energy Mater. Sol. Cells* **2008,** *92* (7), 686-714.

[86] Pender, J. P.; Jha, G.; Youn, D. H.; Ziegler, J. M.; Andoni, I.; Choi, E. J.; Heller, A.; Dunn, B. S.; Weiss, P. S.; Penner, R. M.et al. Electrode Degradation in Lithium-Ion Batteries. *ACS Nano* **2020,** *14* (2), 1243-1295.

[87] Laviron, E. The use of linear potential sweep voltammetry and of a.c. voltammetry for the study of the surface electrochemical reaction of strongly adsorbed systems and of redox modified electrodes. *J. Electroanal. Chem. Interf. Electrochem.* **1979,** *100* (1), 263-270.

[88] Eckermann, A. L.; Feld, D. J.; Shaw, J. A.; Meade, T. J. Electrochemistry of redox-active self-assembled monolayers. *Coord. Chem. Rev.* **2010,** *254* (15), 1769-1802.

[89] Oldham, K. B.; Zoski, C. G. In *Comprehensive Chemical Kinetics*; Bamford, C. H.;Compton, R. G., Eds.; Elsevier, 1986; Vol. 26.

[90] Crank, J. *The mathematics of diffusion*; 2. ed., reprinted ed.; Oxford Univ. Press: Oxford, 2009.

[91] Novev, J. K.; Compton, R. G. Natural convection effects in electrochemical systems. *Curr. Opin. Electrochem.* **2018,** *7*, 118-129.

[92] Planck, M. Ueber die Potentialdifferenz zwischen zwei verdünnten Lösungen binärer Electrolyte. *Ann. Phys. (Berl.)* **1890,** *276* (8), 561-576.

[93] Dickinson, E. J. F.; Limon-Petersen, J. G.; Rees, N. V.; Compton, R. G. How Much Supporting Electrolyte Is Required to Make a Cyclic Voltammetry Experiment Quantitatively "Diffusional"? A Theoretical and Experimental Investigation. *J. Phys. Chem. C* **2009,** *113* (25), 11157-11171.

[94] Fick, A. Ueber Diffusion. *Ann. Phys. (Berl.)* **1855,** *170* (1), 59-86.

[95] Aoki, K. Theory of ultramicroelectrodes. *Electroanalysis* **1993,** *5* (8), 627-639.

[96] Scharifker, B. R. Diffusion to ensembles of microelectrodes. *J. Electroanal. Chem. Interf. Electrochem.* **1988,** *240* (1), 61-76.

[97] Snowden, M. E.; Güell, A. G.; Lai, S. C. S.; McKelvey, K.; Ebejer, N.; O'Connell, M. A.; Colburn, A. W.; Unwin, P. R. Scanning Electrochemical Cell Microscopy: Theory and Experiment for Quantitative High Resolution Spatially-Resolved Voltammetry and Simultaneous Ion-Conductance Measurements. *Anal. Chem.* **2012,** *84* (5), 2483-2491.

[98] Coen, S.; Cope, D. K.; Tallman, D. E. Diffusion current at a band electrode by an integral equation method. *J. Electroanal. Chem. Interf. Electrochem.* **1986,** *215* (1), 29-48.

[99] Gouy, M. Sur la constitution de la charge électrique à la surface d'un électrolyte. *Journal de Physique Théorique et Appliquée* **1910,** *9* (1), 457-468.

[100] Chapman, D. L. LI. A contribution to the theory of electrocapillarity. *Philos. Mag.* **1913,** *25* (148), 475-481.

[101] Stern, O. Zur Theorie der Elektrolytischen Doppelschicht. *Zeitschrift für Elektrochemie und angewandte physikalische Chemie* **1924,** *30* (21-22), 508-516.

[102] Lindström, H.; Södergren, S.; Solbrand, A.; Rensmo, H.; Hjelm, J.; Hagfeldt,

A.; Lindquist, S.-E. Li+ Ion Insertion in TiO2 (Anatase). 2. Voltammetry on Nanoporous Films. *J. Phys. Chem. B* **1997,** *101* (39), 7717-7722.

[103] Wang, Y.; Song, Y.; Xia, Y. Electrochemical capacitors: mechanism, materials, systems, characterization and applications. *Chem. Soc. Rev.* **2016,** *45* (21), 5925-5950.

[104] Wipf, D. O.; Kristensen, E. W.; Deakin, M. R.; Wightman, R. M. Fast-scan cyclic voltammetry as a method to measure rapid heterogeneous electron-transfer kinetics. *Anal. Chem.* **1988,** *60* (4), 306-310.

[105] Milner, D. F.; Weaver, M. J. The influence of uncompensated solution resistance on the determination of standard electrochemical rate constants by cyclic voltammetry, and some comparisons with a.c. voltammetry. *Anal. Chim. Acta* **1987,** *198*, 245-257.

[106] Bond, A. M.; Mahon, P. J.; Oldham, K. B.; Zoski, C. G. Investigation of the influence of residual uncompensated resistance and incomplete charging current correction on the calculation of electrode kinetics when global and convolution analysis methods are used. *J. Electroanal. Chem.* **1994,** *366* (1), 15-27.

[107] Myland, J. C.; Oldham, K. B. Uncompensated Resistance. 1. The Effect of Cell Geometry. *Anal. Chem.* **2000,** *72* (17), 3972-3980.

[108] Oldham, K. B.; Stevens, N. P. C. Uncompensated Resistance. 2. The Effect of Reference Electrode Nonideality. *Anal. Chem.* **2000,** *72* (17), 3981-3988.

[109] van der Vliet, D.; Strmcnik, D. S.; Wang, C.; Stamenkovic, V. R.; Markovic, N. M.; Koper, M. T. M. On the importance of correcting for the uncompensated Ohmic resistance in model experiments of the Oxygen Reduction Reaction. *J. Electroanal. Chem.* **2010,** *647* (1), 29-34.

[110] Alavi, S. M. M.; Mahdi, A.; Payne, S. J.; Howey, D. A. Identifiability of Generalized Randles Circuit Models. *IEEE Trans. Control Syst. Technol.* **2017,** *25* (6), 2112-2120.

[111] He, P.; Faulkner, L. R. Intelligent, automatic compensation of solution resistance. *Anal. Chem.* **2002,** *58* (3), 517-523.

[112] Schroder, D. K.; Meier, D. L. Solar cell contact resistance—A review. *IEEE Trans. Electron Devices* **1984,** *31* (5), 637-647.

[113] Taheri, P.; Hsieh, S.; Bahrami, M. Investigating electrical contact resistance losses in lithium-ion battery assemblies for hybrid and electric vehicles. *J. Power Sources* **2011,** *196* (15), 6525-6533.

[114] Waldrip, M.; Jurchescu, O. D.; Gundlach, D. J.; Bittle, E. G. Contact Resistance in Organic Field-Effect Transistors: Conquering the Barrier. *Adv. Funct. Mater.* **2020,** *30* (20), 1904576.

[115] Randles, J. E. B. Kinetics of rapid electrode reactions. *Discuss. Faraday Soc.* **1947,** *1* (0), 11-19.

[116] Harrington, D. A.; van den Driessche, P. Mechanism and equivalent circuits in electrochemical impedance spectroscopy. *Electrochim. Acta* **2011,** *56* (23), 8005-8013.

[117] Bontempelli, G.; Dossi, N.; Toniolo, R. In *Reference Module in Chemistry,*

Molecular Sciences and Chemical Engineering; Elsevier, 2016.

[118] Cottrell, F. G. Der Reststrom bei galvanischer Polarisation, betrachtet als ein Diffusionsproblem. *Z. Phys. Chem.* **1903**, *42U* (1).

[119] Randles, J. E. B. A cathode ray polarograph. Part II.—The current-voltage curves. *Trans. Faraday Soc.* **1948**, *44* (0), 327-338.

[120] Ševčík, A. Oscillographic polarography with periodical triangular voltage. *Collect. Czech. Chem. Commun.* **1948**, *13*, 349-377.

[121] Elgrishi, N.; Rountree, K. J.; McCarthy, B. D.; Rountree, E. S.; Eisenhart, T. T.; Dempsey, J. L. A Practical Beginner's Guide to Cyclic Voltammetry. *J. Chem. Educ.* **2018**, *95* (2), 197-206.

[122] Khdary, N. H.; Ghanem, M. A. Highly dispersed platinum nanoparticles supported on silica as catalyst for hydrogen production. *RSC Adv.* **2014**, *4* (91), 50114-50122.

[123] Ooka, H.; Figueiredo, M. C.; Koper, M. T. M. Competition between Hydrogen Evolution and Carbon Dioxide Reduction on Copper Electrodes in Mildly Acidic Media. *Langmuir* **2017**, *33* (37), 9307-9313.

[124] Zhang, J.; Guo, S.-X.; Bond, A. M. Discrimination and Evaluation of the Effects of Uncompensated Resistance and Slow Electrode Kinetics from the Higher Harmonic Components of a Fourier Transformed Large-Amplitude Alternating Current Voltammogram. *Anal. Chem.* **2007**, *79* (6), 2276-2288.

[125] Oldham, K. B. Edge effects in semiinfinite diffusion. *J. Electroanal. Chem. Interf. Electrochem.* **1981**, *122*, 1-17.

[126] Amatore, C. In *Physical Electrochemistry: Principles, Methods and Applications*; Rubinstein, I., Ed.; CRC Press: New York, 1995.

[127] Oldham, K. B. In *Microelectrodes: Theory and Applications*; Montenegro, M. I.;Queirós, M. A.;Daschbach, J. L., Eds.; Springer Netherlands: Dordrecht, 1991.

[128] Michael, A. C.; Wightman, R. M.; Amatore, C. A. Microdisk electrodes: Part I. Digital simulation with a conformal map. *J. Electroanal. Chem. Interf. Electrochem.* **1989**, *267* (1), 33-45.

[129] Mirkin, M. V.; Bard, A. J. Simple analysis of quasi-reversible steady-state voltammograms. *Anal. Chem.* **1992**, *64* (19), 2293-2302.

[130] Cooper, J. B.; Bond, A. M.; Oldham, K. B. Microelectrode studies without supporting electrolyte: Model and experimental comparison for singly and multiply charged ions. *J. Electroanal. Chem.* **1992**, *331* (1), 877-895.

[131] Heinze, J. Theory of Cyclic Voltammetry at Microdisk Electrodes. *Ber. Bunsen-Ges. Phys. Chem* **1981**, *85* (12), 1096-1103.

[132] Heinze, J. Ultramicroelectrodes in Electrochemistry. *Angewandte Chemie International Edition in English* **1993**, *32* (9), 1268-1288.

[133] Jain, R. K.; Gaur, H. C.; Welch, B. J. Chronopotentiometry: A review of theoretical principles. *J. Electroanal. Chem. Interf. Electrochem.* **1977**, *79* (2), 211-236.

[134] Sawyer, D. T.; Sobkowiak, A.; Roberts, J. L.; Sawyer, D. T. *Electrochemistry for*

chemists; 2nd ed ed.; Wiley: New York, 1995.

[135] Lingane, P. J.; Peters, D. G. Chronopotentiometry. *CRC Crit. Rev. Anal. Chem.* **1971,** *1* (4), 587-634.

[136] Doyle, M.; Fuller, T. F.; Newman, J. Modeling of Galvanostatic Charge and Discharge of the Lithium/Polymer/Insertion Cell. *J. Electrochem. Soc.* **1993,** *140* (6), 1526-1533.

[137] Bala, H.; Kukuła, I.; Giza, K.; Marciniak, B.; Różycka-Sokołowska, E.; Drulis, H. Evaluation of electrochemical hydrogenation and corrosion behavior of LaNi5-based materials using galvanostatic charge/discharge measurements. *Int. J. Hydrogen Energy* **2012,** *37* (22), 16817-16822.

[138] Mastragostino, M.; Arbizzani, C.; Soavi, F. Conducting polymers as electrode materials in supercapacitors. *Solid State Ionics* **2002,** *148* (3), 493-498.

[139] Tao, B.; Yule, L. C.; Daviddi, E.; Bentley, C. L.; Unwin, P. R. Correlative Electrochemical Microscopy of Li-Ion (De)intercalation at a Series of Individual LiMn2 O4 Particles. *Angew. Chem. Int. Ed.* **2019,** *58* (14), 4606-4611.

[140] Sand, H. J. S. III. On the concentration at the electrodes in a solution, with special reference to the liberation of hydrogen by electrolysis of a mixture of copper sulphate and sulphuric acid. *Philos. Mag.* **1901,** *1* (1), 45-79.

[141] Lingane, P. J. Chronopotentiometry and Chronoamperometry with Unshielded Planar Electrodes. *Anal. Chem.* **1964,** *36* (9), 1723-1726.

[142] Aoki, K.; Akimoto, K.; Tokuda, K.; Matsuda, H.; Osteryoung, J. Chronopotentiometry at very small stationary disk electrodes. *J. Electroanal. Chem. Interf. Electrochem.* **1985,** *182* (2), 281-294.

[143] Ali, G. A. M.; Yusoff, M. M.; Ng, Y. H.; Lim, H. N.; Chong, K. F. Potentiostatic and galvanostatic electrodeposition of manganese oxide for supercapacitor application: A comparison study. *Curr. Appl. Phys.* **2015,** *15* (10), 1143-1147.

[144] Talaie, E.; Bonnick, P.; Sun, X.; Pang, Q.; Liang, X.; Nazar, L. F. Methods and Protocols for Electrochemical Energy Storage Materials Research. *Chem. Mater.* **2017,** *29* (1), 90-105.

[145] Fleischmann, M.; Pons, S. The behavior of microdisk and microring electrodes. Mass transport to the disk in the unsteady state: Chronopotentiometry. *J. Electroanal. Chem. Interf. Electrochem.* **1988,** *250* (2), 257-267.

[146] Abrantes, L. M.; Fleischmann, M.; Li, L. J.; Hawkins, M.; Pons, J. W.; Daschbach, J.; Pons, S. The behavior of microdisk electrodes: Chronopotentiometry and linear sweep voltammetric experiments. *J. Electroanal. Chem. Interf. Electrochem.* **1989,** *262* (1), 55-66.

[147] Voigtländer, B. *Scanning Probe Microscopy: Atomic Force Microscopy and Scanning Tunneling Microscopy*; 1st ed. 2015 ed.; Springer Berlin Heidelberg : Imprint: Springer: Berlin, Heidelberg, 2015.

[148] Bard, A. J.; Mirkin, M. V. *Scanning electrochemical microscopy*; 2nd ed ed.; CRC Press: Boca Raton, Fla, 2012.

[149] Engstrom, R. C.; Pharr, C. M. Scanning electrochemical microscopy. *Anal. Chem.* **1989,** *61* (19), 1099A-1104A.

[150] Kwak, J.; Bard, A. J. Scanning electrochemical microscopy. Theory of the feedback mode. *Anal. Chem.* **1989,** *61* (11), 1221-1227.

[151] Engstrom, R. C.; Meaney, T.; Tople, R.; Wightman, R. M. Spatiotemporal description of the diffusion layer with a microelectrode probe. *Anal. Chem.* **1987,** *59* (15), 2005-2010.

[152] Zoski, C. G. Review—Advances in Scanning Electrochemical Microscopy (SECM). *J. Electrochem. Soc.* **2015,** *163* (4), H3088-H3100.

[153] Schulte, A.; Schuhmann, W. Single-Cell Microelectrochemistry. *Angew. Chem. Int. Ed.* **2007,** *46* (46), 8760-8777.

[154] Schulte, A.; Nebel, M.; Schuhmann, W. Scanning Electrochemical Microscopy in Neuroscience. *Annu. Rev. Anal. Chem.* **2010,** *3* (1), 299-318.

[155] Marcu, R.; Rapino, S.; Trinei, M.; Valenti, G.; Marcaccio, M.; Pelicci, P. G.; Paolucci, F.; Giorgio, M. Electrochemical study of hydrogen peroxide formation in isolated mitochondria. *Bioelectrochemistry* **2012,** *85*, 21-28.

[156] Bergner, S.; Vatsyayan, P.; Matysik, F.-M. Recent advances in high resolution scanning electrochemical microscopy of living cells – A review. *Anal. Chim. Acta* **2013,** *775*, 1-13.

[157] Soldà, A.; Valenti, G.; Marcaccio, M.; Giorgio, M.; Pelicci, P. G.; Paolucci, F.; Rapino, S. Glucose and Lactate Miniaturized Biosensors for SECM-Based High-Spatial Resolution Analysis: A Comparative Study. *ACS Sens.* **2017,** *2* (9), 1310-1318.

[158] Shao, Y.; Mirkin, M. V. Probing Ion Transfer at the Liquid/Liquid Interface by Scanning Electrochemical Microscopy (SECM). *J. Phys. Chem. B* **1998,** *102* (49), 9915-9921.

[159] Cannan, S.; Zhang, J.; Grunfeld, F.; Unwin, P. R. Scanning Electrochemical Microscopy (SECM) Studies of Oxygen Transfer across Phospholipid Monolayers under Surface Pressure Control: Comparison of Monolayers at Air/Water and Oil/Water Interfaces. *Langmuir* **2004,** *20* (3), 701-707.

[160] Li, F.; Unwin, P. R. Scanning Electrochemical Microscopy (SECM) of Photoinduced Electron Transfer Kinetics at Liquid/Liquid Interfaces. *J. Phys. Chem. C* **2015,** *119* (8), 4031-4043.

[161] Matsue, T.; Shiku, H.; Yamada, H.; Uchida, I. Permselectivity of Voltage-Gated Alamethicin Ion Channel Studied by Microamperometry. *J. Phys. Chem.* **1994,** *98* (43), 11001-11003.

[162] Gonsalves, M.; Barker, A. L.; Macpherson, J. V.; Unwin, P. R.; O'Hare, D.; Winlove, C. P. Scanning Electrochemical Microscopy as a Local Probe of Oxygen Permeability in Cartilage. *Biophys. J.* **2000,** *78* (3), 1578-1588.

[163] Cougnon, C.; Mauzeroll, J.; Bélanger, D. Patterning of Surfaces by Oxidation of Amine-Containing Compounds Using Scanning Electrochemical Microscopy. *Angew. Chem. Int. Ed.* **2009,** *48* (40), 7395-7397.

[164] Yatziv, Y.; Turyan, I.; Mandler, D. A New Approach to Micropatterning: Application of Potential-Assisted Ion Transfer at the Liquid–Liquid Interface for the Local Metal Deposition. *J. Am. Chem. Soc.* **2002,** *124* (20), 5618-5619.

[165] Cannan, S.; Cervera, J.; Steliaros, R. J.; Bitziou, E.; Whitworth, A. L.; Unwin, P.

R. Scanning electrochemical microscopy (SECM) studies of catalytic EC′ processes: theory and experiment for feedback, generation/collection and imaging measurements. *Phys. Chem. Chem. Phys.* **2011,** *13* (12), 5403-5412.

[166] Fernández-Pérez, B. M.; Izquierdo, J.; González, S.; Souto, R. M. Scanning electrochemical microscopy studies for the characterization of localized corrosion reactions at cut edges of coil-coated steel. *J. Solid State Electrochem.* **2014,** *18* (11), 2983-2992.

[167] Page, A.; Perry, D.; Unwin, P. R. Multifunctional scanning ion conductance microscopy. *Proc. R. Soc. A* **2017,** *473* (2200).

[168] Tognoni, E.; Baschieri, P.; Ascoli, C.; Pellegrini, M.; Pellegrino, M. Characterization of tip size and geometry of the pipettes used in scanning ion conductance microscopy. *Micron* **2016,** *83*, 11-18.

[169] Zhu, C.; Huang, K.; Siepser, N. P.; Baker, L. A. Scanning Ion Conductance Microscopy. *Chem. Rev.* **2020**.

[170] Happel, P.; Hoffmann, G.; Mann, S. A.; Dietzel, I. D. Monitoring cell movements and volume changes with pulse-mode scanning ion conductance microscopy. *Journal of Microscopy* **2003,** *212* (2), 144-151.

[171] Gorelik, J.; Zhang, Y.; Shevchuk, A. I.; Frolenkov, G. I.; Sánchez, D.; Lab, M. J.; Vodyanoy, I.; Edwards, C. R. W.; Klenerman, D.; Korchev, Y. E. The use of scanning ion conductance microscopy to image A6 cells. *Molecular and Cellular Endocrinology* **2004,** *217* (1), 101-108.

[172] Rheinlaender, J.; Geisse, N. A.; Proksch, R.; Schäffer, T. E. Comparison of Scanning Ion Conductance Microscopy with Atomic Force Microscopy for Cell Imaging. *Langmuir* **2011,** *27* (2), 697-704.

[173] Perry, D.; Momotenko, D.; Lazenby, R. A.; Kang, M.; Unwin, P. R. Characterization of Nanopipettes. *Anal. Chem.* **2016,** *88* (10), 5523-5530.

[174] Zhang, S.; Li, M.; Su, B.; Shao, Y. Fabrication and Use of Nanopipettes in Chemical Analysis. *Annu. Rev. Anal. Chem.* **2018,** *11* (1), 265-286.

[175] McKelvey, K.; Kinnear, S. L.; Perry, D.; Momotenko, D.; Unwin, P. R. Surface charge mapping with a nanopipette. *J. Am. Chem. Soc.* **2014,** *136* (39), 13735-13744.

[176] Chen, C.-C.; Derylo, M. A.; Baker, L. A. Measurement of Ion Currents through Porous Membranes with Scanning Ion Conductance Microscopy. *Anal. Chem.* **2009,** *81* (12), 4742-4751.

[177] Momotenko, D.; McKelvey, K.; Kang, M.; Meloni, G. N.; Unwin, P. R. Simultaneous Interfacial Reactivity and Topography Mapping with Scanning Ion Conductance Microscopy. *Anal. Chem.* **2016,** *88* (5), 2838-2846.

[178] Thomas, S.; Izquierdo, J.; Birbilis, N.; Souto, R. M. Possibilities and Limitations of Scanning Electrochemical Microscopy of Mg and Mg Alloys. *Corrosion* **2015,** *71* (2), 171-183.

[179] Bentley, C. L.; Edmondson, J.; Meloni, G. N.; Perry, D.; Shkirskiy, V.; Unwin, P. R. Nanoscale Electrochemical Mapping. *Anal. Chem.* **2019,** *91* (1), 84-108.

[180] Howard, J. N.; Koval, C. A. Design and performance of a minielectrochemical cell for spatial resolution of two-dimensional structures. *Anal. Chem.* **1991,** *63*

(23), 2777-2786.

[181] Suter, T.; Böhni, H. A new microelectrochemical method to study pit initiation on stainless steels. *Electrochim. Acta* **1997,** *42* (20), 3275-3280.

[182] Hassel, A. W.; Lohrengel, M. M. The scanning droplet cell and its application to structured nanometer oxide films on aluminium. *Electrochim. Acta* **1997,** *42* (20), 3327-3333.

[183] Lohrengel, M. M. Interface and volume effects in biological cells and electrochemical microcells. *Electrochim. Acta* **1997,** *42* (20), 3265-3271.

[184] Andreatta, F.; Fedrizzi, L. The use of the electrochemical micro-cell for the investigation of corrosion phenomena. *Electrochim. Acta* **2016,** *203*, 337-349.

[185] Krawiec, H.; Szklarz, Z. Combining the Electrochemical Microcell Technique and the Electron Backscatter Diffraction method to study the electrochemical behaviour of polycrystalline aluminium in sodium chloride solution. *Electrochim. Acta* **2016,** *203*, 426-438.

[186] Clausmeyer, J.; Henig, J.; Schuhmann, W.; Plumeré, N. Scanning Droplet Cell for Chemoselective Patterning through Local Electroactivation of Protected Quinone Monolayers. *ChemPhysChem* **2014,** *15* (1), 151-156.

[187] Gasiorowski, J.; Kollender, J. P.; Hingerl, K.; Sariciftci, N. S.; Mardare, A. I.; Hassel, A. W. Photoelectrochemical scanning droplet cell microscopy for localized photovoltaic investigations on organic semiconductors. *Phys. Chem. Chem. Phys.* **2014,** *16* (8), 3739-3748.

[188] Kollender, J. P.; Gasiorowski, J.; Sariciftci, N. S.; Mardare, A. I.; Hassel, A. W. Localized photovoltaic investigations on organic semiconductors and bulk heterojunction solar cells. *Science and Technology of Advanced Materials* **2014,** *15* (5), 054201.

[189] Ebejer, N.; Schnippering, M.; Colburn, A. W.; Edwards, M. A.; Unwin, P. R. Localized High Resolution Electrochemistry and Multifunctional Imaging: Scanning Electrochemical Cell Microscopy. *Anal. Chem.* **2010,** *82* (22), 9141-9145.

[190] Bentley, C. L.; Kang, M.; Unwin, P. R. Scanning electrochemical cell microscopy: New perspectives on electrode processes in action. *Curr. Opin. Electrochem.* **2017,** *6* (1), 23-30.

[191] Wahab, O. J.; Kang, M.; Unwin, P. R. Scanning electrochemical cell microscopy: A natural technique for single entity electrochemistry. *Curr. Opin. Electrochem.* **2020,** *22*, 120-128.

[192] Bentley, C. L.; Kang, M.; Unwin, P. R. Nanoscale Structure Dynamics within Electrocatalytic Materials. *J. Am. Chem. Soc.* **2017,** *139* (46), 16813-16821.

[193] Paulose Nadappuram, B.; McKelvey, K.; Byers, J. C.; Güell, A. G.; Colburn, A. W.; Lazenby, R. A.; Unwin, P. R. Quad-Barrel Multifunctional Electrochemical and Ion Conductance Probe for Voltammetric Analysis and Imaging. *Anal. Chem.* **2015,** *87* (7), 3566-3573.

[194] Güell, A. G.; Ebejer, N.; Snowden, M. E.; McKelvey, K.; Macpherson, J. V.; Unwin, P. R. Quantitative nanoscale visualization of heterogeneous electron transfer rates in 2D carbon nanotube networks. *Proc. Natl. Acad. Sci. U.S.A.* **2012,** *109* (29), 11487-11492.

[195] Guell, A. G.; Meadows, K. E.; Dudin, P. V.; Ebejer, N.; Macpherson, J. V.; Unwin, P. R. Mapping nanoscale electrochemistry of individual single-walled carbon nanotubes. *Nano Lett.* **2014,** *14* (1), 220-224.

[196] Güell, A. G.; Cuharuc, A. S.; Kim, Y.-R.; Zhang, G.; Tan, S.-y.; Ebejer, N.; Unwin, P. R. Redox-Dependent Spatially Resolved Electrochemistry at Graphene and Graphite Step Edges. *ACS Nano* **2015,** *9* (4), 3558-3571.

[197] Zhang, G.; Tan, S. Y.; Patel, A. N.; Unwin, P. R. Electrochemistry of Fe3+/2+ at highly oriented pyrolytic graphite (HOPG) electrodes: kinetics, identification of major electroactive sites and time effects on the response. *Phys. Chem. Chem. Phys.* **2016,** *18* (47), 32387-32395.

[198] Unwin, P. R.; Guell, A. G.; Zhang, G. Nanoscale Electrochemistry of sp(2) Carbon Materials: From Graphite and Graphene to Carbon Nanotubes. *Acc. Chem. Res.* **2016,** *49* (9), 2041-2048.

[199] Oseland, E. E.; Ayres, Z. J.; Basile, A.; Haddleton, D. M.; Wilson, P.; Unwin, P. R. Surface patterning of polyacrylamide gel using scanning electrochemical cell microscopy (SECCM). *Chem. Commun.* **2016,** *52* (64), 9929-9932.

[200] Aaronson, B. D. B.; Garoz-Ruiz, J.; Byers, J. C.; Colina, A.; Unwin, P. R. Electrodeposition and Screening of Photoelectrochemical Activity in Conjugated Polymers Using Scanning Electrochemical Cell Microscopy. *Langmuir* **2015,** *31* (46), 12814-12822.

[201] Bentley, C. L.; Kang, M.; Maddar, F. M.; Li, F.; Walker, M.; Zhang, J.; Unwin, P. R. Electrochemical maps and movies of the hydrogen evolution reaction on natural crystals of molybdenite (MoS2): basal vs. edge plane activity. *Chem. Sci.* **2017,** *8* (9), 6583-6593.

[202] Bentley, C. L.; Andronescu, C.; Smialkowski, M.; Kang, M.; Tarnev, T.; Marler, B.; Unwin, P. R.; Apfel, U.-P.; Schuhmann, W. Local Surface Structure and Composition Control the Hydrogen Evolution Reaction on Iron Nickel Sulfides. *Angew. Chem. Int. Ed.* **2018,** *57* (15), 4093-4097.

[203] Takahashi, Y.; Kobayashi, Y.; Wang, Z.; Ito, Y.; Ota, M.; Ida, H.; Kumatani, A.; Miyazawa, K.; Fujita, T.; Shiku, H.et al. High-Resolution Electrochemical Mapping of the Hydrogen Evolution Reaction on Transition-Metal Dichalcogenide Nanosheets. *Angew. Chem. Int. Ed.* **2020,** *59* (9), 3601-3608.

[204] Tao, B.; Unwin, P. R.; Bentley, C. L. Nanoscale Variations in the Electrocatalytic Activity of Layered Transition-Metal Dichalcogenides. *J. Phys. Chem. C* **2020,** *124* (1), 789-798.

[205] Bentley, C. L.; Agoston, R.; Tao, B.; Walker, M.; Xu, X.; O'Mullane, A. P.; Unwin, P. R. Correlating the Local Electrocatalytic Activity of Amorphous Molybdenum Sulfide Thin Films with Microscopic Composition, Structure, and Porosity. *ACS Appl. Mater. Interfaces* **2020,** *12* (39), 44307-44316.

[206] Mariano, R. G.; McKelvey, K.; White, H. S.; Kanan, M. W. Selective increase in CO_2 electroreduction activity at grain-boundary surface terminations. *Science* **2017,** *358* (6367), 1187.

[207] Byers, J. C.; Güell, A. G.; Unwin, P. R. Nanoscale Electrocatalysis: Visualizing Oxygen Reduction at Pristine, Kinked, and Oxidized Sites on Individual Carbon Nanotubes. *J. Am. Chem. Soc.* **2014,** *136* (32), 11252-11255.

[208] Chen, C.-H.; Meadows, K. E.; Cuharuc, A.; Lai, S. C. S.; Unwin, P. R. High resolution mapping of oxygen reduction reaction kinetics at polycrystalline platinum electrodes. *Phys. Chem. Chem. Phys.* **2014,** *16* (34), 18545-18552.

[209] Ustarroz, J.; Ornelas, I. M.; Zhang, G.; Perry, D.; Kang, M.; Bentley, C. L.; Walker, M.; Unwin, P. R. Mobility and Poisoning of Mass-Selected Platinum Nanoclusters during the Oxygen Reduction Reaction. *ACS Catal.* **2018,** *8* (8), 6775-6790.

[210] Tarnev, T.; Aiyappa, H. B.; Botz, A.; Erichsen, T.; Ernst, A.; Andronescu, C.; Schuhmann, W. Scanning Electrochemical Cell Microscopy Investigation of Single ZIF-Derived Nanocomposite Particles as Electrocatalysts for Oxygen Evolution in Alkaline Media. *Angew. Chem. Int. Ed.* **2019,** *58* (40), 14265-14269.

[211] Takahashi, Y.; Kumatani, A.; Munakata, H.; Inomata, H.; Ito, K.; Ino, K.; Shiku, H.; Unwin, P. R.; Korchev, Y. E.; Kanamura, K.et al. Nanoscale visualization of redox activity at lithium-ion battery cathodes. *Nat. Commun.* **2014,** *5*, 5450.

[212] Takahashi, Y.; Yamashita, T.; Takamatsu, D.; Kumatani, A.; Fukuma, T. Nanoscale kinetic imaging of lithium ion secondary battery materials using scanning electrochemical cell microscopy. *Chem. Commun.* **2020,** *56* (65), 9324-9327.

[213] Aaronson, B. D. B.; Chen, C.-H.; Li, H.; Koper, M. T. M.; Lai, S. C. S.; Unwin, P. R. Pseudo-Single-Crystal Electrochemistry on Polycrystalline Electrodes: Visualizing Activity at Grains and Grain Boundaries on Platinum for the Fe2+/Fe3+ Redox Reaction. *J. Am. Chem. Soc.* **2013,** *135* (10), 3873-3880.

[214] Chen, C.-H.; Jacobse, L.; McKelvey, K.; Lai, S. C. S.; Koper, M. T. M.; Unwin, P. R. Voltammetric Scanning Electrochemical Cell Microscopy: Dynamic Imaging of Hydrazine Electro-oxidation on Platinum Electrodes. *Anal. Chem.* **2015,** *87* (11), 5782-5789.

[215] Yule, L. C.; Daviddi, E.; West, G.; Bentley, C. L.; Unwin, P. R. Surface microstructural controls on electrochemical hydrogen absorption at polycrystalline palladium. *J. Electroanal. Chem.* **2020,** *872*, 114047.

[216] Liu, D.-Q.; Chen, C.-H.; Perry, D.; West, G.; Cobb, S. J.; Macpherson, J. V.; Unwin, P. R. Facet-Resolved Electrochemistry of Polycrystalline Boron-Doped Diamond Electrodes: Microscopic Factors Determining the Solvent Window in Aqueous Potassium Chloride Solutions. *ChemElectroChem* **2018,** *5* (20), 3028-3035.

[217] Kinnear, S. L.; McKelvey, K.; Snowden, M. E.; Peruffo, M.; Colburn, A. W.; Unwin, P. R. Dual-Barrel Conductance Micropipette as a New Approach to the Study of Ionic Crystal Dissolution Kinetics. *Langmuir* **2013,** *29* (50), 15565-15572.

[218] Kleijn, S. E. F.; Lai, S. C. S.; Miller, T. S.; Yanson, A. I.; Koper, M. T. M.; Unwin, P. R. Landing and Catalytic Characterization of Individual Nanoparticles on Electrode Surfaces. *J. Am. Chem. Soc.* **2012,** *134* (45), 18558-18561.

[219] Ornelas, I. M.; Unwin, P. R.; Bentley, C. L. High-Throughput Correlative Electrochemistry–Microscopy at a Transmission Electron Microscopy Grid Electrode. *Anal. Chem.* **2019,** *91* (23), 14854-14859.

[220] Aaronson, B. D. B.; Byers, J. C.; Colburn, A. W.; McKelvey, K.; Unwin, P. R. Scanning Electrochemical Cell Microscopy Platform for Ultrasensitive Photoelectrochemical Imaging. *Anal. Chem.* **2015,** *87* (8), 4129-4133.

[221] Strange, L. E.; Yadav, J.; Garg, S.; Shinde, P. S.; Hill, J. W.; Hill, C. M.; Kung, P.; Pan, S. Investigating the Redox Properties of Two-Dimensional MoS2 Using Photoluminescence Spectroelectrochemistry and Scanning Electrochemical Cell Microscopy. *J. Phys. Chem. Lett.* **2020,** *11* (9), 3488-3494.

[222] Shkirskiy, V.; Yule, L. C.; Daviddi, E.; Bentley, C. L.; Aarons, J.; West, G.; Unwin, P. R. Nanoscale Scanning Electrochemical Cell Microscopy and Correlative Surface Structural Analysis to Map Anodic and Cathodic Reactions on Polycrystalline Zn in Acid Media. *J. Electrochem. Soc.* **2020,** *167* (4).

[223] Yule, L. C.; Bentley, C. L.; West, G.; Shollock, B. A.; Unwin, P. R. Scanning electrochemical cell microscopy: A versatile method for highly localised corrosion related measurements on metal surfaces. *Electrochim. Acta* **2019,** *298*, 80-88.

[224] Yule, L. C.; Shkirskiy, V.; Aarons, J.; West, G.; Bentley, C. L.; Shollock, B. A.; Unwin, P. R. Nanoscale Active Sites for the Hydrogen Evolution Reaction on Low Carbon Steel. *J. Phys. Chem. C* **2019,** *123* (39), 24146-24155.

[225] Yule, L. C.; Shkirskiy, V.; Aarons, J.; West, G.; Shollock, B. A.; Bentley, C. L.; Unwin, P. R. Nanoscale electrochemical visualization of grain-dependent anodic iron dissolution from low carbon steel. *Electrochim. Acta* **2020,** *332*, 135267.

[226] Li, Y.; Morel, A.; Gallant, D.; Mauzeroll, J. Oil-Immersed Scanning Micropipette Contact Method Enabling Long-term Corrosion Mapping. *Anal. Chem.* **2020,** *92* (18), 12415-12422.

[227] Inzelt, G. *Conducting polymers: a new era in electrochemistry*; 2. ed ed.; Springer: Berlin, 2012.

[228] Schultze, J. W.; Karabulut, H. Application potential of conducting polymers. *Electrochim. Acta* **2005,** *50* (7), 1739-1745.

[229] Li, Y. In *Organic Optoelectronic Materials*; Li, Y., Ed.; Springer International Publishing: Cham, 2015.

[230] Braun, D. Electronic injection and conduction processes for polymer devices. *J. Polym. Sci., Part B: Polym. Phys.* **2003,** *41* (21), 2622-2629.

[231] Le, T. H.; Kim, Y.; Yoon, H. Electrical and Electrochemical Properties of Conducting Polymers. *Polymers (Basel)* **2017,** *9* (4), 150.

[232] Kivelson, S.; Heeger, A. J. Intrinsic conductivity of conducting polymers. *Synth. Met.* **1988,** *22* (4), 371-384.

[233] Epstein, A. J.; Joo, J.; Kohlman, R. S.; Du, G.; MacDiarmid, A. G.; Oh, E. J.; Min, Y.; Tsukamoto, J.; Kaneko, H.; Pouget, J. P. Inhomogeneous disorder and the modified Drude metallic state of conducting polymers. *Synth. Met.* **1994,** *65* (2), 149-157.

[234] Bredas, J. L.; Street, G. B. Polarons, bipolarons, and solitons in conducting polymers. *Acc. Chem. Res.* **1985,** *18* (10), 309-315.

[235] Mizes, H. A.; Conwell, E. M. Stability of polarons in conducting polymers. *Phys.*

Rev. Lett. **1993,** *70* (10), 1505-1508.

[236] Mauer, R.; Kastler, M.; Laquai, F. The Impact of Polymer Regioregularity on Charge Transport and Efficiency of P3HT:PCBM Photovoltaic Devices. *Adv. Funct. Mater.* **2010,** *20* (13), 2085-2092.

[237] Neelamraju, B.; Rudolph, M.; Ratcliff, E. L. Controlling the Kinetics of Charge Transfer at Conductive Polymer/Liquid Interfaces through Microstructure. *J. Phys. Chem. C* **2018,** *122* (37), 21210-21215.

[238] Inganäs, O. Hybrid electronics and electrochemistry with conjugated polymers. *Chem. Soc. Rev.* **2010,** *39* (7), 2633-2642.

[239] Stavrinidou, E.; Leleux, P.; Rajaona, H.; Khodagholy, D.; Rivnay, J.; Lindau, M.; Sanaur, S.; Malliaras, G. G. Direct Measurement of Ion Mobility in a Conducting Polymer. *Adv. Mater.* **2013,** *25* (32), 4488-4493.

[240] Liu, T.; Finn, L.; Yu, M.; Wang, H.; Zhai, T.; Lu, X.; Tong, Y.; Li, Y. Polyaniline and Polypyrrole Pseudocapacitor Electrodes with Excellent Cycling Stability. *Nano Lett.* **2014,** *14* (5), 2522-2527.

[241] Zhang, Z.; Chen, X.; Chen, P.; Guan, G.; Qiu, L.; Lin, H.; Yang, Z.; Bai, W.; Luo, Y.; Peng, H. Integrated Polymer Solar Cell and Electrochemical Supercapacitor in a Flexible and Stable Fiber Format. *Adv. Mater.* **2014,** *26* (3), 466-470.

[242] Janoschka, T.; Martin, N.; Martin, U.; Friebe, C.; Morgenstern, S.; Hiller, H.; Hager, M. D.; Schubert, U. S. An aqueous, polymer-based redox-flow battery using non-corrosive, safe, and low-cost materials. *Nature* **2015,** *527* (7576), 78-81.

[243] Strakosas, X.; Bongo, M.; Owens, R. M. The organic electrochemical transistor for biological applications. *J. Appl. Polym. Sci.* **2015,** *132* (15).

[244] Rivnay, J.; Owens, R. M.; Malliaras, G. G. The Rise of Organic Bioelectronics. *Chem. Mater.* **2014,** *26* (1), 679-685.

[245] Lin, P.; Yan, F. Organic Thin-Film Transistors for Chemical and Biological Sensing. *Adv. Mater.* **2012,** *24* (1), 34-51.

[246] Wijeratne, K.; Ail, U.; Brooke, R.; Vagin, M.; Liu, X.; Fahlman, M.; Crispin, X. Bulk electronic transport impacts on electron transfer at conducting polymer electrode-electrolyte interfaces. *Proc. Natl. Acad. Sci. U.S.A.* **2018,** *115* (47), 11899-11904.

[247] Mortimer, R. J.; Dyer, A. L.; Reynolds, J. R. Electrochromic organic and polymeric materials for display applications. *Displays* **2006,** *27* (1), 2-18.

[248] Lock, J. P.; Lutkenhaus, J. L.; Zacharia, N. S.; Im, S. G.; Hammond, P. T.; Gleason, K. K. Electrochemical investigation of PEDOT films deposited via CVD for electrochromic applications. *Synth. Met.* **2007,** *157* (22), 894-898.

[249] Arnold, S. P.; Harris, J. K.; Neelamraju, B.; Rudolph, M.; Ratcliff, E. L. Microstructure-dependent electrochemical properties of chemical-vapor deposited poly(3,4-ethylenedioxythiophene) (PEDOT) films. *Synth. Met.* **2019,** *253*, 26-33.

[250] Ratcliff, E. L.; Jenkins, J. L.; Nebesny, K.; Armstrong, N. R. Electrodeposited, "Textured" Poly(3-hexyl-thiophene) (e-P3HT) Films for Photovoltaic

Applications. *Chem. Mater.* **2008,** *20* (18), 5796-5806.

[251] Bandodkar, A. J.; Jeerapan, I.; Wang, J. Wearable Chemical Sensors: Present Challenges and Future Prospects. *ACS Sens.* **2016,** *1* (5), 464-482.

[252] Lee, B.-L. Electrically conductive polymer composites and blends. *Polymer Engineering & Science* **1992,** *32* (1), 36-42.

[253] Gazotti Jr, W. A.; Casalbore-Miceli, G.; Mitzakoff, S.; Geri, A.; Gallazzi, M. C.; De Paoli, M. A. Conductive polymer blends as electrochromic materials. *Electrochim. Acta* **1999,** *44* (12), 1965-1971.

[254] Riaz, U.; Ashraf, S. M. In *Nanostructured Polymer Blends*; Thomas, S.;Shanks, R.;Chandrasekharakurup, S., Eds.; William Andrew Publishing: Oxford, 2014.

[255] Li, F.-S.; Wu, Y.-S.; Chou, J.; Winter, M.; Wu, N.-L. A Mechanically Robust and Highly Ion-Conductive Polymer-Blend Coating for High-Power and Long-Life Lithium-Ion Battery Anodes. *Adv. Mater.* **2015,** *27* (1), 130-137.

[256] Yu, G.; Gao, J.; Hummelen, J. C.; Wudl, F.; Heeger, A. J. Polymer Photovoltaic Cells: Enhanced Efficiencies via a Network of Internal Donor-Acceptor Heterojunctions. *Science* **1995,** *270* (5243), 1789.

[257] Li, G.; Zhu, R.; Yang, Y. Polymer solar cells. *Nature Photonics* **2012,** *6* (3), 153-161.

[258] Benten, H.; Mori, D.; Ohkita, H.; Ito, S. Recent research progress of polymer donor/polymer acceptor blend solar cells. *Journal of Materials Chemistry A* **2016,** *4* (15), 5340-5365.

[259] Zaumseil, J. In *P3HT Revisited – From Molecular Scale to Solar Cell Devices*; Ludwigs, S., Ed.; Springer Berlin Heidelberg: Berlin, Heidelberg, 2014.

[260] Tietze, U.; Schenk, C.; Gamm, E. In *Electronic Circuits: Handbook for Design and Application*; Tietze, U.;Schenk, C.;Gamm, E., Eds.; Springer Berlin Heidelberg: Berlin, Heidelberg, 2008.

[261] Goffri, S.; Müller, C.; Stingelin-Stutzmann, N.; Breiby, D. W.; Radano, C. P.; Andreasen, J. W.; Thompson, R.; Janssen, R. A. J.; Nielsen, M. M.; Smith, P.et al. Multicomponent semiconducting polymer systems with low crystallization-induced percolation threshold. *Nat. Mater.* **2006,** *5* (12), 950-956.

[262] Yu, X.; Xiao, K.; Chen, J.; Lavrik, N. V.; Hong, K.; Sumpter, B. G.; Geohegan, D. B. High-Performance Field-Effect Transistors Based on Polystyrene-b-Poly(3-hexylthiophene) Diblock Copolymers. *ACS Nano* **2011,** *5* (5), 3559-3567.

[263] Koch, G. In *Trends in Oil and Gas Corrosion Research and Technologies*; El-Sherik, A. M., Ed.; Woodhead Publishing: Boston, 2017.

[264] Koch, G. H.; Brongers, M. P. H.; Thompson, N. G.; Virmani, Y. P.; Payer, J. H. *Corrosion Cost and Preventive Strategies in the United States*; Report by CC Technologies Laboratories, Inc. to Federal Highway Administration (FHWA), Office of Infrastructure Research and Development, McLean, 2001, 2002.

[265] Perez, N. *Electrochemistry and Corrosion Science*; Springer International Publishing: Cham, 2016.

[266] FitzGerald, K. P.; Nairn, J.; Skennerton, G.; Atrens, A. Atmospheric corrosion of copper and the colour, structure and composition of natural patinas on

copper. *Corros. Sci.* **2006,** *48* (9), 2480-2509.

[267] Leygraf, C.; Odnevall Wallinder, I.; Tidblad, J.; Graedel, T. E. *Atmospheric corrosion*; Second edition ed.; Wiley: Hoboken, New Jersey, 2016.

[268] Frankel, G. S. In *Active Protective Coatings*; Hughes, A. E.;Mol, J. M. C.;Zheludkevich, M. L.;Buchheit, R. G., Eds.; Springer Netherlands: Dordrecht, 2016; Vol. 233.

[269] Evans, U. R. *The corrosion of metals*; Longmans, Green, 1924.

[270] Pedeferri, P. In *Corrosion Science and Engineering*; Pedeferri, P., Ed.; Springer International Publishing: Cham, 2018.

[271] Tafel, J. Über die Polarisation bei kathodischer Wasserstoffentwicklung. *Z. Phys. Chem.* **1905,** *50U* (1), 641-712.

[272] Holewinski, A.; Linic, S. Elementary Mechanisms in Electrocatalysis: Revisiting the ORR Tafel Slope. *J. Electrochem. Soc.* **2012,** *159* (11), H864-H870.

[273] Murthy, A. P.; Theerthagiri, J.; Madhavan, J. Insights on Tafel Constant in the Analysis of Hydrogen Evolution Reaction. *J. Phys. Chem. C* **2018,** *122* (42), 23943-23949.

[274] Kelly, R. G. *Electrochemical techniques in corrosion science and engineering*; Marcel Dekker: New York, 2003.

[275] Strehblow, H. H.; Titze, B. The investigation of the passive behaviour of copper in weakly acid and alkaline solutions and the examination of the passive film by esca and ISS. *Electrochim. Acta* **1980,** *25* (6), 839-850.

[276] Strehblow, H. H.; Speckmann, H. D. Corrosion and layer formation of passive copper in alkaline solutions. *Mater. Corros.* **1984,** *35* (11), 512-519.

[277] Maurice, V.; Strehblow, H. H.; Marcus, P. In situ STM study of the initial stages of oxidation of Cu(111) in aqueous solution. *Surf. Sci.* **2000,** *458* (1–3), 185-194.

[278] Szakálos, P.; Hultquist, G.; Wikmark, G. Corrosion of Copper by Water. *Electrochem. Solid-State Lett.* **2007,** *10* (11), C63-C67.

[279] Pourbaix, M. *Atlas of electrochemical equilibria in aqueous solutions*; National Association of Corrosion Engineers: Houston, Tex., 1974.

[280] Zeng, Z.; Chan, M. K. Y.; Zhao, Z.-J.; Kubal, J.; Fan, D.; Greeley, J. Towards First Principles-Based Prediction of Highly Accurate Electrochemical Pourbaix Diagrams. *J. Phys. Chem. C* **2015,** *119* (32), 18177-18187.

[281] Frankel, G. S. Pitting Corrosion of Metals: A Review of the Critical Factors. *J. Electrochem. Soc.* **1998,** *145* (6), 2186-2198.

[282] De Force, B.; Pickering, H. A clearer view of how crevice corrosion occurs. *JOM* **1995,** *47* (9), 22-27.

[283] McMurray, H. N.; Williams, G. In *Shreir's Corrosion*; Cottis, B.;Graham, M.;Lindsay, R.;Lyon, S.;Richardson, T.;Scantlebury, D.;Stott, H., Eds.; Elsevier: Oxford, 2010.

[284] Schreiber, A.; Rosenkranz, C.; Lohrengel, M. M. Grain-dependent anodic dissolution of iron. *Electrochim. Acta* **2007,** *52* (27), 7738-7745.

[285] Takabatake, Y.; Kitagawa, Y.; Nakanishi, T.; Hasegawa, Y.; Fushimi, K. Grain Dependency of a Passive Film Formed on Polycrystalline Iron in pH 8.4 Borate Solution. *J. Electrochem. Soc.* **2017,** *164* (7), C349-C355.

[286] Martinez-Lombardia, E.; Lapeire, L.; De Graeve, I.; Verbeken, K.; Kestens, L. A. I.; Terryn, H. Study of the influence of the microstructure on the corrosion properties of pure copper. *Mater. Corros.* **2016,** *67* (8), 847-856.

[287] Dong, S.; Chen, X.; La Plante, E. C.; Gussev, M.; Leonard, K.; Sant, G. Elucidating the grain-orientation dependent corrosion rates of austenitic stainless steels. *Mater. Des.* **2020,** *191*, 108583.

[288] Garcia, C.; de Tiedra, M. P.; Blanco, Y.; Martin, O.; Martin, F. Intergranular corrosion of welded joints of austenitic stainless steels studied by using an electrochemical minicell. *Corros. Sci.* **2008,** *50* (8), 2390-2397.

[289] Armijo, J. S. Intergranular Corrosion of Nonsensitized Austenitic Stainless Steels. *Corrosion* **2013,** *24* (1), 24-30.

[290] Zhou, Y.; Zuo, Y. The Intergranular Corrosion of Mild Steel in CO2+NaNO2 Solution. *Electrochim. Acta* **2015,** *154*, 157-165.

[291] Bettayeb, M.; Maurice, V.; Klein, L. H.; Lapeire, L.; Verbeken, K.; Marcus, P. Nanoscale Intergranular Corrosion and Relation with Grain Boundary Character as Studied In Situ on Copper. *J. Electrochem. Soc.* **2018,** *165* (11), C835-C841.

[292] Sieradzki, K.; Newman, R. C. Stress-corrosion cracking. *J. Phys. Chem. Solids* **1987,** *48* (11), 1101-1113.

[293] Kip, N.; van Veen, J. A. The dual role of microbes in corrosion. *The ISME journal* **2015,** *9* (3), 542-551.

[294] Parthasarathi, A.; Polan, N. W. Stress corrosion of Cu- Zn and Cu- Zn- Ni alloys: The role of dealloying. *Metall. Trans. A* **1982,** *13* (11), 2027-2033.

[295] Zhou, P.; Erning, J. W.; Ogle, K. Interactions between elemental components during the dealloying of Cu-Zn alloys. *Electrochim. Acta* **2019,** *293*, 290-298.

[296] Williams, D. E.; Zhu, Y. Y. Explanation for Initiation of Pitting Corrosion of Stainless Steels at Sulfide Inclusions. *J. Electrochem. Soc.* **2000,** *147* (5), 1763-1766.

[297] Ryan, M. P.; Williams, D. E.; Chater, R. J.; Hutton, B. M.; McPhail, D. S. Why stainless steel corrodes. *Nature* **2002,** *415* (6873), 770-774.

[298] Martinez-Lombardia, E.; Lapeire, L.; Maurice, V.; De Graeve, I.; Verbeken, K.; Klein, L. H.; Kestens, L. A. I.; Marcus, P.; Terryn, H. In situ scanning tunneling microscopy study of the intergranular corrosion of copper. *Electrochem. Commun.* **2014,** *41*, 1-4.

[299] Martinez-Lombardia, E.; Gonzalez-Garcia, Y.; Lapeire, L.; De Graeve, I.; Verbeken, K.; Kestens, L.; Mol, J. M. C.; Terryn, H. Scanning electrochemical microscopy to study the effect of crystallographic orientation on the electrochemical activity of pure copper. *Electrochim. Acta* **2014,** *116*, 89-96.

[300] Lapeire, L.; Martinez Lombardia, E.; Verbeken, K.; De Graeve, I.; Kestens, L. A. I.; Terryn, H. Effect of neighboring grains on the microscopic corrosion behavior of a grain in polycrystalline copper. *Corros. Sci.* **2013,** *67*, 179-183.

[301] Lapeire, L.; Martinez Lombardia, E.; De Graeve, I.; Terryn, H.; Verbeken, K. Influence of grain size on the electrochemical behavior of pure copper. *J. Mater. Sci.* **2016,** *52* (3), 1501-1510.

[302] Tsuru, T.; Tamiya, K.-I.; Nishikata, A. Formation and growth of micro-droplets during the initial stage of atmospheric corrosion. *Electrochim. Acta* **2004,** *49* (17), 2709-2715.

[303] Tang, X.; Ma, C.; Zhou, X.; Lyu, X.; Li, Q.; Li, Y. Atmospheric corrosion local electrochemical response to a dynamic saline droplet on pure Iron. *Electrochem. Commun.* **2019,** *101*, 28-34.

[304] Telegdi, J.; Shaban, A.; Trif, L. In *Trends in Oil and Gas Corrosion Research and Technologies*; El-Sherik, A. M., Ed.; Woodhead Publishing: Boston, 2017.

[305] Zhang, H.; Lan, H.-q. A review of internal corrosion mechanism and experimental study for pipelines based on multiphase flow. *Corros. Rev.* **2017,** *35* (6), 425-444.

[306] Al-Janabi, Y. T. In *Corrosion Inhibitors in the Oil and Gas Industry*; 1 ed.; Saji, V. S.;Umoren, S. A., Eds.; Wiley, 2020.

[307] Popov, B. N. In *Corrosion Engineering*; Popov, B. N., Ed.; Elsevier: Amsterdam, 2015.

[308] Cui, X.; Zhu, G.; Pan, Y.; Shao, Q.; Zhao, C.; Dong, M.; Zhang, Y.; Guo, Z. Polydimethylsiloxane-titania nanocomposite coating: Fabrication and corrosion resistance. *Polymer* **2018,** *138*, 203-210.

[309] Prasai, D.; Tuberquia, J. C.; Harl, R. R.; Jennings, G. K.; Bolotin, K. I. Graphene: Corrosion-Inhibiting Coating. *ACS Nano* **2012,** *6* (2), 1102-1108.

[310] Riggs, O. L.; Locke, C. E.; Hamner, N. E. *Anodic Protection: Theory and Practice in the Prevention of Corrosion*; Springer US: Boston, MA, 1981.

[311] Antonijevic, M. M.; B., P. M. Copper Corrosion Inhibitors. A review. *Int. J. Electrochem. Sci.* **2008,** *3*, 1-28.

[312] Finšgar, M.; Jackson, J. Application of corrosion inhibitors for steels in acidic media for the oil and gas industry: A review. *Corros. Sci.* **2014,** *86*, 17-41.

[313] Kuznetsov, Y. I. Triazoles as a class of multifunctional corrosion inhibitors. A review. Part I. 1,2,3-Benzotriazole and its derivatives. Copper, zinc and their alloys. *Int. J. Corros. Scale Inhib.* **2018,** *7* (3).

[314] Parkins, R. N. In *Electrochemical Materials Science*; Bockris, J. O. M.;Conway, B. E.;Yeager, E.;White, R. E., Eds.; Springer US: Boston, MA, 1981.

[315] Finšgar, M.; Milošev, I. Inhibition of copper corrosion by 1,2,3-benzotriazole: A review. *Corros. Sci.* **2010,** *52* (9), 2737-2749.

[316] Grillo, F.; Tee, D. W.; Francis, S. M.; Früchtl, H. A.; Richardson, N. V. Passivation of Copper: Benzotriazole Films on Cu(111). *J. Phys. Chem. C* **2014,** *118* (16), 8667-8675.

[317] Jiang, Y.; Adams, J. B. First principle calculations of benzotriazole adsorption onto clean Cu(111). *Surf. Sci.* **2003,** *529* (3), 428-442.

[318] Polewska, W.; Vogt, M. R.; Magnussen, O. M.; Behm, R. J. In Situ STM Study of Cu(111) Surface Structure and Corrosion in Pure and Benzotriazole-

Containing Sulfuric Acid Solution. *J. Phys. Chem. B* **1999,** *103* (47), 10440-10451.

[319] Kosec, T.; Merl, D. K.; Milošev, I. Impedance and XPS study of benzotriazole films formed on copper, copper–zinc alloys and zinc in chloride solution. *Corros. Sci.* **2008,** *50* (7), 1987-1997.

[320] Saavedra-Torres, M.; Escobar, C. A.; Ocayo, F.; Tielens, F.; Santos, J. C. 1,2,3-Benzotriazole derivatives adsorption on Cu(111) surface: A DFT study. *Chem. Phys. Lett.* **2017,** *689*, 128-134.

Chapter 2

General Methods

Since most of the chapters are partially or totally aimed at describing the innovations brought to the electroanalytical possibilities of SECCM, the specific details of the employed protocols (such as the specific SECCM setups or the details of the FEM simulations) are reported in each specific chapter. However, it is useful to describe here the common traits of the employed techniques, especially those that are used in many or all the following chapters, in order to give a broader view of the experimental part of this work.

2.1. MATERIALS

2.1.1. Chemicals

Potassium chloride (KCl, Honeywell, 99.5%), 1,1′-ferrocenedimethanol (FcDM, Sigma Aldrich, 97%), perchloric acid (HClO$_4$, Sigma Aldrich, 70%), hexaammineruthenium(III) chloride ([Ru(NH$_3$)]Cl$_3$, Sigma-Aldrich), dichlorodimethylsilane [Si(CH$_3$)$_2$Cl$_2$, Acros Organics, ≥ 99%], sulphuric acid (H$_2$SO$_4$, Sigma Aldrich, 96%), Cupric sulphate (CuSO$_4$, Sigma Aldrich, 99%), n-dodecane (C$_{12}$H$_{26}$, Sigma Aldrich, 99%), 1-N,N-bis-(2-ethylhexyl)-ARmethyl-benzotriazole-1-methanamine, silicone oil (DC 200, Fluka Analytical), were used as supplied by

the manufacturer. All solutions were prepared with deionized water (Integra HP, Purite, U.K.), which had a resistivity of 18.2 MΩ.cm (25°C).

2.1.2. Electrode materials preparation

Polymer blend electrodes

All the polymeric samples were produced and provided by the Laboratory for Interface Science of Printable Electronic Materials at the University of Arizona, U.S.A.. However, it is useful to give some detail of the preparation, for more clarity.

Indium tin oxide (ITO)-coated glass substrates (Colorado Concept Coatings, sheet resistance < 15 ohm/square) were cleaned by Triton X-100 (Sigma, laboratory grade) diluted with ultrapure water followed by successive sonication in 50:50 deionized water/ethanol, pure ethanol, pure acetone, and pure isopropanol and dried in a stream of nitrogen. Stock solutions of 13 mg/mL of poly(3-hexylthiophene) (P3HT, Rieke, average molecular weight 57,000) and poly(methyl methacrylate) (PMMA, Aldrich, average molecular weight 120,000) were allowed to dissolve overnight in 1,2-dichlorobenzene (Acros, 99%) on a hotplate at 80 °C under constant stirring. Stock solutions were mixed by volume to create, 5:1, 1:1 and 1:5 mixtures of P3HT to PMMA (wt %) and allowed to mix for 15 minutes before casting. Films were filtered using 0.45 μm PTFE filters (Fisherbrand) spin cast at 1000 rpm for 1 minute on Laurell spin coater (500 rpm for acceleration) and annealed at 120°C for 20 minutes.

Note that, together with the blends, also the stock solution of P3HT was employed to produce a polymer electrode sample. Of all the sample produced, however, only the pure P3HT and the 1:5 mixture were subjected to nanoscale electrochemical characterization, as explained in detail in Chapter 3. All the samples were mounted on a SEM aluminium stub, and the conductive surface on the top of the glass was connected to

the stub with conducting silver paint glue (RS Supplies, U.K.). This sample configuration was utilised in every performed analysis.

Glassy Carbon

The glassy carbon (GC) substrate was purchased from HTW-Germany and polished with an aqueous suspension of Al_2O_3 (Buehler, U.S.A.), of particle size 0.05 μm, before use. Subsequently, it was mounted on a SEM aluminium disk stub with conductive silver paint glue (RS Supplies, U.K.) and rinsed with deionized water prior to measurement.

High oriented pyrolytic graphite

The high oriented pyrolytic graphite (HOPG) sample originated from GE Advanced Ceramics (U.S.A.) and was a gift from Prof. R. L. McCreery, University of Alberta, Canada. Full characterization of this material, including the step edge density, has been previously reported.[1] The sample was fixed to an aluminium SEM stub with conductive silver paint glue (RS Supplies, U.K.). Prior to use, the HOPG crystal was gently cleaved using the "scotch tape method"[2] and subsequently left exposed to air for 1 hour, to allow surface "aging", before any electrochemical analysis.

MoS_2

The molybdenite (MoS_2) crystal (semiconducting 2H phase, as previously characterised[3]) was purchased from Manchester Nanomaterials (U.K.). Prior to use as an electrode material, the MoS_2 crystal was fixed on a glass microscope slide with carbon SEM tape and mechanically cleaved using the "scotch tape method".[2] To ensure electrical connection and in order to avoid ohmic resistance through the material, the cleaved MoS_2 surface was electrically connected through a top contact with conductive copper SEM tape, covering most of the material except for a 1 mm diameter exposed circular area.

Polycrystalline copper

The copper (Cu) substrates were prepared from a foil of 3 mm thickness (Goodfellow, U.K., 99.95%), cut into a rectangle of $\approx$ 1 cm × 2 cm. The sample employed in Chapter 5 did not undergo any further thermal process, while the ones used in Chapter 6 and Chapter 7 were annealed under an argon atmosphere for 12 hours at 800° C in a furnace. Subsequently, all the Cu substrates (annealed and non-annealed) were hot mounted at 190° C in cylindrical conductive carbon supports (KonductoMet™, Buehler, U.S.A.) with a SimpliMet™ 3000 Mounting Press (Buehler, U.S.A.) The final samples were roughly 2 cm high and had a diameter of 3 cm.

The mounted Cu substrates were then polished to a mirror finish (roughly $\approx$ 50 nm roughness) on polishing pads with aqueous polishing suspension (Buehler, U.S.A.), as follows: (1) 9 μm MetaDi™ Supreme Diamond suspension on a Texmet™ C polishing pad; (2) 3 μm MetaDi™ Supreme Diamond suspension on a Verdutext™ polishing pad and; (3) 0.02 − 0.06 μm MasterMet™ Colloidal Silica suspension on a ChemoMet™ polishing pad. The polished sample was washed in deionized water and isopropanol and dried with air blowing. Before use as a substrate in SECCM, a *ca.* 3 mm high barrier of chemically-resistant epoxy resin (Sigma Aldrich, Germany) was formed around the Cu foil surface, which served as a well/reservoir for dodecane during scanning (see section 5.2.1).

2.2. NANOPIPETTE PROBES FABRICATION

2.2.1. Nanopipette pulling

All the nanopipettes were fabricated from cylindrical capillaries, that were pulled to a sharp tip with a commercial CO_2 laser puller (P-2000, Sutter Instruments, U.S.A.).
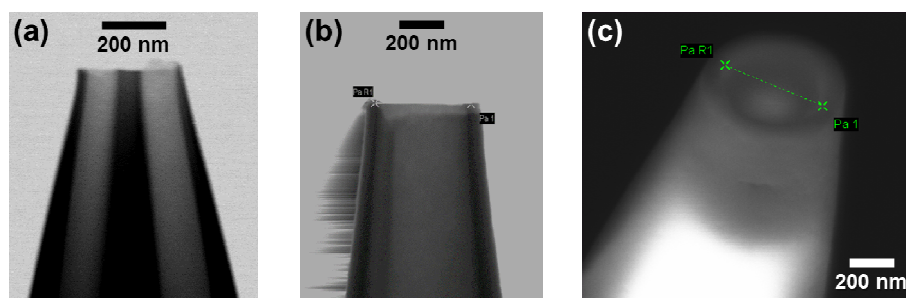
Figure 2.1: **(a-b)** STEM image (bright field) of the tip obtained with **(a)** pulling parameters (i) and a theta quartz capillary, **(b)** pulling parameters (vii) and a borosilicate glass capillary. **(c)** SEM image of the tip obtained with pulling parameters (iv) and a borosilicate glass capillary.

2.2.2. QRCEs fabrication

Double channel pipettes were obtained from quartz theta capillaries (QTF120-90-100, Friedrich & Dimmock Inc., U.S.A.), using the following parameters. (i) For ≈ 200 nm diameter aperture tips (Chapter 3); line 1: HEAT 800, FIL 4, VEL 40, DEL 130, PUL 30; line 2: HEAT 750, FIL 3, VEL 30, DEL 130, PUL 100. (ii) For ≈ 100 nm diameter tips (Chapter 3); line 1: HEAT 850, FIL 4, VEL 20, DEL 130, PUL 80; line 2: HEAT 750, FIL 3, VEL 20, DEL 130, PUL 130.

Single channel pipettes were obtained from filamented borosilicate glass capillaries (GC120F-10, Harvard Apparatus, U.K.), using the following parameters. (iii) For ≈ 800nm tips (Chapter 4); line 1: HEAT 800, FIL 4, VEL 40, DEL 130, PUL 30; line 2: HEAT 750, FIL 3, VEL 20, DEL 130, PUL 100. (iv) For ≈400 nm tips (Chapter 4); line 1: HEAT 350, FIL 3, VEL 40, DEL 220, PUL 0; line 2: HEAT 350, FIL 3, VEL 40, DEL 180, PUL 100. (v) For ≈150 nm tips (Chapter 4); line 1: HEAT 350, FIL 3, VEL 30, DEL 220, PUL 0; line 2: HEAT 350, FIL 3, VEL 40, DEL 180, PUL 120. (vi) For ≈ 400-600 nm aperture tips (Chapter 5); line 1: HEAT 800, FIL 4, VEL 40, DEL 130, PUL 30; line 2: HEAT 750, FIL 3, VEL 20, DEL 130, PUL 100. (vii) For ≈ 400 nm aperture tips (Chapter 6 and Chapter 7); line 1: HEAT 340, FIL 3, VEL 30, DEL 250, PUL −; line 2: HEAT 340, FIL 3, VEL 30, DEL 210, PUL 120.

The scanning electron transmission microscopy (STEM) image of tips obtained with, respectively, program (i) and (vii) and the SEM image of a tip obtained with program (iv) are shown respectively in Figure 2.1a b and c. It needs to be noted that, despite the similarity of the size of tips used in different chapters, slightly different pulling parameters were used due to re-calibrations of the laser puller in between the works.

Ag/AgCl

The Ag/AgCl QRCE was prepared by anodization of an annealed silver wire (0.25 mm diameter, Goodfellow, U.K., 99.99%) in saturated KCl solution for *ca.* 2 minutes. The QRCE potential was potentiometrically calibrated after the SECCM scans by measuring the open circuit potential (OCP) in the solution of interest (either 10 mM KCl + $[Ru(NH_3)_6]Cl_3$, r 0.1M KCl + FcDM or 10 mM H_2SO_4) *versus* a commercial leakless 3.4 M Ag/AgCl electrode (ET072, eDAQ, Australia), that has a theoretical standard potential of + 205 mV vs. the standard hydrogen electrode (SHE).[4] Typically the QRCE has a standard potential that is $\approx$ + 70 − + 80 mV vs commercial Ag/AgCl in the more concentrated chloride solution (5mM FcDM + 0.1M KCl), + 100 mV in the less concentrate (5mM $[Ru(NH_3)_6]Cl_3$ + 0.01M KCl) and $\approx$ +170 − + 260 mV vs commercial Ag/AgCl in the sulphuric acid solution (10 mM H_2SO_4).

Pd/H₂

The Pd/H₂ QRCE was prepared by electrochemical dissolution of H_2 in annealed palladium wire (0.25 mm diameter, Goodfellow, U.K., 99.99%). The Pd wire was held in a 0.1 M $HClO_4$ solution at −3 V vs. Pt wire for 30 mins, and used for experiments immediately after.

2.2.3. Setup of the probe

After pulling, in two specific cases (examined in Chapter 4) the probes were silanized by dipping them into $Si(CH_3)_2Cl_2$ with argon flowing

through the tip (at a pressure of 6 bar) for 1 min (this prevented the silane from entering the tip). This procedure created a hydrophobic surface on the outside of the tip, which aided meniscus cell confinement during scanning. This process was employed only in cases where additional droplet confinement was not already provided by the nature of the sample (such as for very hydrophobic polymer electrodes or mineral oil confined pipettes) and, in any case, only for probes that were >200 nm in diameter. All the other pipettes were employed as produced by the puller.

Each nanopipette was filled with the solution of interest (making sure no bubbles were formed at the tip by optical microscopy examination); for the double channelled ones, each single channel was filled with the same solution. In order to avoid solvent evaporation during prolonged scanning, a silicone oil layer was added on the top of the solution (*i.e.* the back of the nanopipette)[3] and a QRCE was then inserted from the same side into each nanopipette channel. The end of the QRCE was positioned at *ca.* 2 cm from the nanodroplet meniscus formed at the probe tip.[5] The probe was then mounted on the positioning system of the SECCM setup and used for the analysis immediately.

2.3. SECCM

All experiments in the SECCM configuration were carried out on a home-built SEPM workstation, as detailed in previous works.[6,7] While the general setup and principles of the technique are the within all the analysis carried out, within the many chapters there are some differences in the adopted procedures and a few specific parts of the instrumentation. Such differences are highlighted in Table 2.1. In essence, the SECCM platform is comprised of *x-y-z* piezoelectric positioners (details in Table 2.1), homebuilt electrochemical instrumentation (discussed in detail in the respective chapters), a waveform generator and a data collection system. The latter two are both integrated in an FPGA card, used respectively for

applying potential to the system and recording the output from the custom electronic equipment.

The nanopipette probe was mounted on the *z*-piezoelectric positioner and moved to the initial position over the sample using coarse *x-y-z* micropositioners (M-461-XYZ-M, Newport, U.S.A.), in tandem with an optical camera (PLB776U camera equipped with a 4× lens, Pixelink, U.S.A.). The piezoelectric positioners and sensitive components of the electrochemical instrumentation (*i.e.* electrometers heads and galvanostat heads) were placed in an aluminium faraday cage equipped with heat sinks and acoustic foam, equipped with a passive mechanical vibration isolator (specified in Table 2.1). This configuration has previously been shown to minimize electric noise, thermal drift and mechanical vibration.[8-10]

All SECCM measurements were carried out using the "hopping mode" imaging protocol, as previously described[11,12] with the feedback parameters and the employed techniques detailed in the respective chapters. The output signal (*i.e.* either current or potential); was measured at a data acquisition rate (r_{da}) depending on the frequency of measurement (t_m, given in µs per data points) and the number of consecutive measurements averaged for obtaining a digital data point (n_a):

$$r_{da} = t_m (n_a + 1) \tag{2.1}$$

with the +1 arising from the fact that one iteration is necessary for transferring the data to the computer. The specific data are reported in Table 2.1. All data acquisition and instrumental control was carried out with an FPGA card (PCIe-7852R) controlled by a LabVIEW 2016 (National Instruments, U.S.A.) interface running the Warwick Electrochemical Scanning Probe Microscopy software (WEC-SPM, downloadable from the Warwick electrochemistry and interfaces group website, www.warwick.ac.uk/electrochemistry).

Table 2.1: Technical specifications for the SECCM technique employed in each different chapter.

Technical Specific	Customised Setup			
	Chapter 3	Chapter 4	Chapter 5	Chapter 6-7
Piezoelectric positioners (P. I., Germany)	*z*: P-753.1CD *x-y*: P-733.2DD,	*z*: P-753.3CD *x-y*: P-621.2CD	*x-y-z*: P-611.3S,	*z*: P-753.2 *x-y*: P-733.2,
Mechanical vibration isolator	Pneumatic isolation table S-2000A-423.5, (Newport, U.S.A.) supporting the Faraday cage	Mechanical Isolator (Minus K® Technology, Inc. U.S.A.) inside the Faraday cage	Mechanical Isolator (Minus K® Technology, Inc. U.S.A.) inside the Faraday cage	Mechanical Isolator (Minus K® Technology, Inc. U.S.A.) inside the Faraday cage
Main electrochemical technique	Cyclic voltammetry	Chronopotentiometry	Chronopotentiometry	Cyclic voltammetry
Nanopipette channels	Double	Single	Single	Single
Digital acquisition rate	$t_m = 4$ μs pt^{-1} $n_a = 128$ $r_{da} = 516$ μs pt^{-1}	$t_m = 4$ μs pt^{-1} $n_a = 128$ $r_{da} = 516$ μs pt^{-1}	$t_m = 10$ μs pt^{-1} $n_a = 256$ $r_{da} = 2570$ μs pt^{-1}	$t_m = 4$ μs pt^{-1} $n_a = 128$ $r_{da} = 516$ μs pt^{-1}

After collection, all the raw data were processed using the Matlab (Mathworks, U.S.A.) software suite (version R2016b to R2020b depending on the software update). Topographical maps measured with SECCM were further elaborated using the scanning probe image processing (SPIP) software package (v. 6.0.14, Image Metrology, Denmark). Data plotting was performed with the OriginPro 2016 64bit (OriginLab, U.S.A.) software package (version 2016 to 2020 64bit depending on the software update) and Matlab software suite (for the 2D maps). All topographical and electrochemical maps were plotted without any data interpolation.

2.4. MACROSCALE ELECTROCHEMISTRY

2.4.1. Voltammetry

Macroscopic Cyclic voltammetry was performed in a conventional three electrode set-up, with a commercial leakless Ag/AgCl electrode (3.4 M KCl, ET072, eDAQ, Australia) as reference electrode, a coiled platinum wire (0.5 mm diameter, Goodfellow, U.K.) as counter electrode and a working electrode depending on the specific analysis as detailed below:

◆ In Chapter 3, an Au macrodisc electrode (area, A = 0.0201 cm^2, Bioanalytical Systems, U.S.A.) was employed, and the cyclic voltammetry was recorded on a FAS2 Femtostat (Gamry, U.S.A.) potentiostat. Further macroscale analysis discussed in Chapter 3 were performed by the provider of the polymeric samples (at the University of Arizona, U.S.A.) to characterise them after the synthesis. In that case electrochemical measurements were performed with a CH Instruments 920D bipotentiostat with either a gold or ITO counter electrode (area, A = 0.55 cm^2) and Ag/AgCl reference electrode (3.0 M KCl).

◆ In Chapter 6, a 3 mm diameter Cu macrodisc electrode (area 0.071 cm^2, Bioanalytical Systems, U.S.A.) was employed, and the cyclic voltammetry was recorded on a CH Instruments 400 potentiostat. In the case of a de-aerated experiment, the solution was degassed with Ar prior to experimentation, and a blanket of Ar was maintained during the course of the voltammetry.

2.4.2. Chronopotentiometry

Macroscopic electrochemical experiments were performed in a conventional three-electrode format on a commercial FAS2 Femtostat (Gamry, U.S.A.) potentiostat/galvanostat. A commercial Cu macrodisc electrode (3 mm diameter, MF-2110, BASi, U.S.A.), commercial 3.4 M Ag/AgCl reference electrode (*vide supra*) and coiled platinum wire (0.5

mm thickness, $\approx$ 10 cm length) were used as working, reference and counter electrodes, respectively. When needed, the solution of interest was deaerated with nitrogen gas (N_2) for at least 15 minutes, prior to experiments and a blanket of N_2 was maintained during the whole time of measure.

2.5. ELECTRON MICROSCOPY

2.5.1. Scanning Electron Microscopy

SEM was employed to characterise the nanopipette probe geometry and visualise electrode surfaces (HOPG, MoS_2 and Cu surfaces) after SECCM experiments, as previously reported.[3,7,13] The SEM images were obtained on a GeminiSEM Field Emission Scanning Electron Microscope (ZEISS, Germany), at an acceleration voltage of 5 kV using an InLens detector.

2.5.2. Scanning Transmission Electron Microscopy

STEM was employed for the characterization of the probes used in SECCM. The image was collected on a GeminiSEM – Field Emission Scanning Electron Microscope (ZEISS, Germany), equipped with a STEM detector. The image was collected at an acceleration voltage of 30 kV for quartz pipettes and 25 kV for borosilicate ones, employing bright field detection.

2.5.3. Electron Backscattered Diffraction

The EBSD analyses were performed either with a Zeiss SUPRA FE-SEM (Zeiss, Germany), for Chapter 5, or a JEOL JSM-7800F FEG-SEM (Zeiss, Germany) for Chapter 6 and Chapter 7; both instruments were equipped with a Nordlys EBSD detector (Oxford Instruments, U.K.). The EBSD mapping was carried out with an acceleration voltage of 20 keV, with the sample tilted 70º to the detector. EBSD data were pro-

cessed using the HKL CHANNEL5 software (Tango, Oxford Instruments, U.K.) to extract inverse pole figure (IPFz) images for each SECCM scan area, and, in specific cases, disorientation colouring maps (*i.e.* disorientation angle between each couple of neighbouring pixels in the EBSD map) and grain orientation spread (GOS) maps.

2.6.   CONDUCTIVE ATOMIC FORCE MICROSCOPY

Conductive atomic force microscopy (c-AFM) images were obtained using an Asylum research MFP-3D. The measurement was performed in contact mode by applying a constant bias of +2 V between the tip and the sample holder. An OMCL-AC240TM (tip side platinum coating, aluminium reflex coating) ElectriLevers (Olympus, Japan) was employed as the probe. The resulting topography and current maps were analysed with the SPIP software package (version 6.0.14) and reported with no interpolation.

2.7.   OPTICAL MICROSCOPY

Optical microscopy analysis was carried out to verify the absence of air bubbles in the electrolyte-filled pipettes and to characterise the polymer film electrodes. An Olympus BH2 optical microscope, with 500× magnification and top-side illumination (*i.e.* reflection light mode) was employed in all cases.

2.8.   CRYSTALLOGRAPHIC ORIENTATION REPRESENTATION

A 2D projection for representing the orientation of the crystallographic planes in the cubic system was developed, and systematically utilised to represent the analysed grains in Chapters 5 – 7. Here the calculation leading to such projection is described. The orientation of a generic plane, α, in space can be defined by three Euler angles, φ_1, Φ and φ_2. From these angles, it is possible to obtain the Miller indices (h,k,l) of the plane:

$$h = n \sin \Phi \sin \varphi_2 \tag{2.2}$$

$$k = n \sin \Phi \cos \varphi_2 \tag{2.3}$$

$$l = n \cos \Phi \tag{2.4}$$

As it can be seen from Eqs. (2.2) to (2.4), the Miller indices depend only on the latter two Euler angles, with φ_1 corresponding to the rotation of the plane relative to the normal direction.

Due to the symmetry of the cubic system to which Cu belongs (crystal group 225), all the families of the plane $\{h,k,l\}$ have equivalent structures, thus the Miller indexes of planes α (h,k,l) were simply ordered from smallest to largest, so that $h' \leq k' \leq l'$, with h', k' and l' being the rearranged indexes. This was done in order to obtain comparable orientations for the following steps (*vide infra*). For instance, given the aforementioned symmetry, planes (100), (010) and (001) are all equivalent to (001), the one of the three with (h,k,l) sorted from smallest to largest.

Once the Miller indices for each plane α were calculated using Eqs. (2.2) – (2.4), the angle between α and each of the three low-index planes employed for cubic system representation, (001), (011), (111), was calculated, respectively as γ_1, γ_2 and γ_3:

$$\cos \gamma = \frac{h_1' h_2' + k_1' k_2' + l_1' l_2'}{\sqrt{(h_1')^2 + (k_1')^2 + (l_1')^2} \sqrt{(h_2')^2 + (k_2')^2 + (l_2')^2}} \tag{2.5}$$

with (h'_1, k'_1, l'_1) being the Miller index of α and (h'_2, k'_2, l'_2) being the Miller indexes of the considered low index plane. Therefore, each plane α could be described respectively by three coordinates; for example, calculated values for each the low-index planes are shown in Table 2.2. As alluded to above, low-index grains (001), (011) and (111) were chosen to fulfil the requirement of sorting (h,k,l) from smallest to largest. The points representing (001), (011) and (111) planes in the γ_1, γ_2, γ_3 space are called P_1, P_2 and P_3., with coordinates expressed with letters, such as P_1 $(0,a,b)$, P_2 $(a,0,c)$ and P_3 $(b,c,0)$, with $a = 45°$, $b = 54.736°$ and $c = 35.264°$.

Table 2.2: Values of γ_1, γ_2 and γ_3 for the low index planes in the cubic system.

Plane	$\gamma_1^{\ 001}$ (°)	$\gamma_2^{\ 011}$ (°)	$\gamma_3^{\ 111}$ (°)
001	0	45	54.736
011	45	0	35.264
111	54.736	35.264	0

By calculating γ_1, γ_2 and γ_3 for each generic plane α of the cubic system of Miller indices (h',k',l') as defined above, it can be shown that all calculated points, P, lay on a hyperbolic plane that passes through P_1, P_2 and P_3. This can be qualitatively explained by considering that the miller indexes (h,k,l) are not totally independent, being all calculated from the same two Euler angles (Φ and φ_2). Specifically, from the re-elaboration of eq. (2.2), (2.3) and (2.4)

$$k = \sqrt{1-l}\left(1 - \frac{h^2}{1-l}\right) \text{ with } 0 \leq l < 1. \tag{2.6}$$

Therefore, a useful and simple 2D representation of the grains is introduced by calculating the projection of each point in the $(\gamma_1, \gamma_2, \gamma_3)$ space on the plane passing through P_1, P_2 and P_3. Such a plane will be represented by the following equation:

$$u\gamma_1 + v\gamma_2 + w\gamma_3 + k = 0 \,, \tag{2.7}$$

with:

$$u = ac + bc - c^2 \approx 2273.5382^{\circ^2} \,, \tag{2.8}$$

$$v = cb + ab - b^2 \approx 1397.3333^{\circ^2} \,, \tag{2.9}$$

$$w = ac + ab - a^2 = 2025^{\circ^2} \tag{2.10}$$

and

$$k = -2abc = -173719.61^{\circ^3} \,, \tag{2.11}$$

a, b and c correspond to the angles defined above. In order to represent

the points over this plane, two Cartesian coordinates were arbitrary defined as follows: x axis as the line passing through P_1 and P_3, y axis as the line passing through P_1 and orthonormal, to x. The direction of the axis was defined in order for P_2 to have both positive coordinates in this projection. Such coordinates were called C_1 (x-axis) and C_2 (y-axis). Therefore, C_1 and C_2 can be calculated from $\gamma_1, \gamma_2, \gamma_3$ for each considered plane. If the following constants are defined:

$$\mu_1 = \sqrt{c^2 + b^2 + 2a^2 - 2bc} \approx 66.55^{\circ} \tag{2.12}$$

$$\mu_2 = \sqrt{u^2 + v^2 + w^2} \approx 3349.9465^{\circ^2} \tag{2.13}$$

$$\epsilon 1_{\gamma_1} = \frac{a}{\mu_1} \approx 0.6761 \tag{2.14}$$

$$\epsilon 1_{\gamma_2} = -\frac{a}{\mu_1} \approx -0.6761 \tag{2.15}$$

$$\epsilon 1_{\gamma_3} = \frac{c - b}{\mu_1} \approx -0.2926 \tag{2.16}$$

$$\epsilon 2_{\gamma_1} = \frac{w(c-b) + va}{\mu_1 \mu_2} \approx 0.1052 \tag{2.17}$$

$$\epsilon 2_{\gamma_2} = \frac{-u(c-b) + va}{\mu_1 \mu_2} \approx 0.4806 \tag{2.18}$$

$$\epsilon 2_{\gamma_3} = -\frac{a(u+w)}{\mu_1 \mu_2} \approx -0.8676 \tag{2.19}$$

Then for each generic plane, P:

$$C_1^P = \epsilon 1_{\gamma_1}\left(\gamma_1^P\right) + \epsilon 1_{\gamma_2}\left(\gamma_2^P - a\right) + \epsilon 1_{\gamma_3}\left(\gamma_3^P - b\right) \tag{2.20}$$

$$C_2^P = \epsilon 2_{\gamma_1}\left(\gamma_1^P\right) + \epsilon 2_{\gamma_2}\left(\gamma_2^P - a\right) + \epsilon 2_{\gamma_3}\left(\gamma_3^P - b\right) \tag{2.21}$$

The position of some representative planes in coordinates C_1 and C_2 are shown in Figure 2.2. On this plot, in this coordinate system, P_1 (0,0),
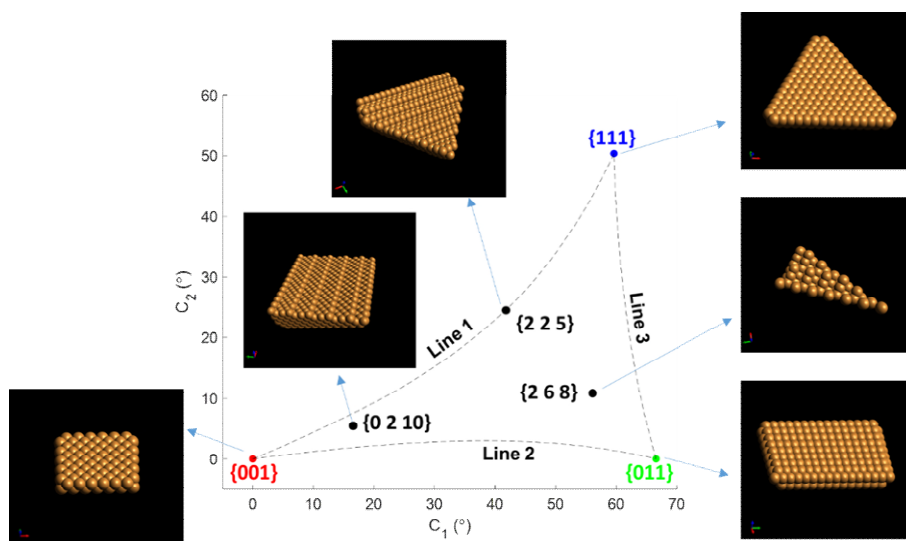
Figure 2.2: Two-dimensional projection of grain orientations in a fcc cubic crystal system, represented in arbitrary coordinates. The black lines delineate the space that contains all possible grain orientations (given the symmetry of the cubic system). The position of the low-index grains is also highlighted, as well as the surface structure of a few exemplar grains indicated on the plot.

P_2 (66.5517°,0), P_3 (59.6074°,50.336°). All generic planes α (*i.e.* all grains) lay in a section delimited by the following three lines, as shown in Figure 2.2: line 1, representing the family of planes with miller indices

2.9.   REFERENCES

[1]   Patel, A. N.; Collignon, M. G.; O'Connell, M. A.; Hung, W. O. Y.; McKelvey, K.; Macpherson, J. V.; Unwin, P. R. A New View of Electrochemistry at Highly Oriented Pyrolytic Graphite. *J. Am. Chem. Soc.* **2012**, *134* (49), 20117-20130.

[2]   Novoselov, K. S.; Geim, A. K.; Morozov, S. V.; Jiang, D.; Zhang, Y.; Dubonos, S. V.; Grigorieva, I. V.; Firsov, A. A. Electric Field Effect in Atomically Thin Carbon Films. *Science* **2004**, *306* (5696), 666-669.

[3]   Bentley, C. L.; Kang, M.; Maddar, F. M.; Li, F.; Walker, M.; Zhang, J.; Unwin, P. R. Electrochemical maps and movies of the hydrogen evolution reaction on natural crystals of molybdenite (MoS2): basal vs. edge plane activity. *Chem. Sci.* **2017**, *8* (9), 6583-6593.

[4]   Spitzer, P.; Wunderli, S.; Maksymiuk, K.; Michalska, A.; Kisiel, A.; Galus, Z.; Tauber, G. In *Handbook of Reference Electrodes*; Inzelt, G.;Lewenstam, A.;Scholz, F., Eds.; Springer Berlin Heidelberg: Berlin, Heidelberg, 2013.

[5]   Bentley, C. L.; Perry, D.; Unwin, P. R. Stability and Placement of Ag/AgCl Quasi-Reference Counter Electrodes in Confined Electrochemical Cells. *Anal. Chem.* **2018**, *90* (12), 7700-7707.

[6]   Ebejer, N.; Güell, A. G.; Lai, S. C. S.; McKelvey, K.; Snowden, M. E.; Unwin, P.

R. Scanning Electrochemical Cell Microscopy: A Versatile Technique for Nanoscale Electrochemistry and Functional Imaging. *Annu. Rev. Anal. Chem.* **2013,** *6* (1), 329-351.

[7]   Snowden, M. E.; Güell, A. G.; Lai, S. C. S.; McKelvey, K.; Ebejer, N.; O'Connell, M. A.; Colburn, A. W.; Unwin, P. R. Scanning Electrochemical Cell Microscopy: Theory and Experiment for Quantitative High Resolution Spatially-Resolved Voltammetry and Simultaneous Ion-Conductance Measurements. *Anal. Chem.* **2012,** *84* (5), 2483-2491.

[8]   Hill, J. W.; Hill, C. M. Directly Mapping Photoelectrochemical Behavior within Individual Transition Metal Dichalcogenide Nanosheets. *Nano Lett.* **2019,** *19* (8), 5710-5716.

[9]   Kang, M.; Perry, D.; Bentley, C. L.; West, G.; Page, A.; Unwin, P. R. Simultaneous Topography and Reaction Flux Mapping at and around Electrocatalytic Nanoparticles. *ACS Nano* **2017,** *11* (9), 9525-9535.

[10] Bentley, C. L.; Unwin, P. R. Nanoscale electrochemical movies and synchronous topographical mapping of electrocatalytic materials. *Faraday Discuss* **2018,** *210* (0), 365-379.

[11] Chen, C.-H.; Jacobse, L.; McKelvey, K.; Lai, S. C. S.; Koper, M. T. M.; Unwin, P. R. Voltammetric Scanning Electrochemical Cell Microscopy: Dynamic Imaging of Hydrazine Electro-oxidation on Platinum Electrodes. *Anal. Chem.* **2015,** *87* (11), 5782-5789.

[12] Bentley, C. L.; Kang, M.; Unwin, P. R. Scanning electrochemical cell microscopy: New perspectives on electrode processes in action. *Curr. Opin. Electrochem.* **2017,** *6* (1), 23-30.

[13] Güell, A. G.; Cuharuc, A. S.; Kim, Y.-R.; Zhang, G.; Tan, S.-y.; Ebejer, N.; Unwin, P. R. Redox-Dependent Spatially Resolved Electrochemistry at Graphene and Graphite Step Edges. *ACS Nano* **2015,** *9* (4), 3558-3571.

Chapter 3

Conductive Polymer Electrodes

Complex blends of conductive and non-conductive polymers are often employed in crucial fields of optoelectronics, as mentioned in Chapter 1 (section 1.4.1), but despite their surface complexity, there is still little comprehension about their nanoscale electrochemical properties. The work presented in this chapter is aimed to prove that SECCM, which so far has had little applications in the field of conductive polymers, due mainly to problems of wettability of the surface and a slow imaging rate for double channel mode of operation, can be successfully applied to the study of this kind of system.

3.1. INTRODUCTION AND BACKGROUND

3.1.1. Conductive polymers in UMEs arrays

Conductive polymer employed in an optoelectronic device is often included in blends with other organic and inorganic, conductive and non-conductive materials; in some cases (given by specific arrangement between the conductive and insulating phases) these materials can effectively act as arrays of UMEs. Traditionally, UMEs arrays are coupled with chemical or optical assays for a number of molecular detection schemes.

97

They necessitate isolated, electronically conductive domains on the order of microns to nanometres surrounded by a contiguous insulating material. Conventional methods of fabrication, however, involving mainly inorganic semiconductors, are generally time and cost intensive and restricted to rigid substrates. On the other hand, the ease of printing polymeric materials enables the development of thin film planar structures that would serve to widen applications, especially in the field of life sciences.[1-3]

Therefore, understanding the microscopic electrochemical behaviour (and specifically the electron transfer properties) of polymeric UME arrays can be of great importance for analytical (linked to the development of assays based on printable conductive polymer electrodes) and optoelectronic applications. Conductive polymers follow a potential-dependent mechanism, whereby the kinetics of electron transfer are associated with the overlap in the density of states (DOS) of the electrode and electrolyte.[4] For semicrystalline polymers such as P3HT, the DOS is strongly connected to the microstructure, with crystalline domains being easier to oxidize than amorphous regions.[5] The fraction of crystallites varies with processing and could hypothetically be altered when the conductive polymer is constrained into a UME configuration. Thus, realization of all-organic electrochemical devices necessitates a detailed understanding both of the nanoscale structure-property relationships governing charge transfer and how these relationships influence measurements on longer length scales.

As a model system for this type of studies, a series of binary conductive/insulating polymers blends was chosen, with the conductive part being the semi-crystalline P3HT, and the insulator part being the amorphous PMMA. P3HT was chosen as the model conductor for organic electrochemical systems as it is well-studied,[6] both structurally and electrochemically (though mostly at the macroscale).[7-9] As the interest of this

chapter is on nanoscale behaviour and how this translates to performance in a UME array, P3HT was blended with PMMA as the system is known to possess microstructural heterogeneity arising from phase segregation.[10,11] Previously, P3HT:PMMA microstructural domains have been used to improve charge transport in organic field effect and electrochemical transistors, to obtain high transmittance while retaining conductivity in opto-electronics, and to alter photoluminescence.[10,12-14] More broadly, blending a conductive polymer with a non-conjugated system is used to acquire new mechanical, optical, morphological and thermal properties, or to introduce strategic intermolecular forces for adhesion/binding, coulombic charge stabilization, or promote desired chemical-electrochemical reactions.[15]

3.1.2. The application of SECCM

Conventional macroscopic electroanalytical methods, notably cyclic voltammetry, are typically used as the main tool to study the properties of conductive polymer electrodes and compare behaviour across materials sets, in order to elucidate electrochemical structure-property relationships. Hence, such relationship can be only probed *indirectly* and with a degree of uncertainty. On the contrary, the SECCM approach can potentially *directly* probe the spatial-heterogeneity arising from phase segregation in polymer blend electrodes, in order to fully understand the relationship between local chemical composition and electrochemical reactivity. Such potentiality, as discussed in Chapter 1 (section 1.3.2) has been previously demonstrated with many classes of (electro)materials but rarely applied for polymer analysis.[16]

Therefore, voltammetric movies from SECCM of the rapid outer-sphere electron transfer process $FcDM^{0/+}$ (where FcDM stands for 1,1′-ferrocenedimethanol) at complex, phase-separated P3HT:PMMA blend electrodes have been correlated with complementary, co-located high-

resolution c-AFM to reveal unambiguously electrical-electrochemical interconnections in the blends, at the nanoscale. The kinetic information extracted from such analysis, then, have been employed, with the aid of FEM simulations, to evaluate the limitations of conventional macroscopic electrochemical analysis in this class of material. With this added understanding, the ambient exposure-induced degradation of the polymeric blend electrodes has been interrogated with SECCM, demonstrating a spatially heterogeneous loss in electrochemical redox behaviour.

3.2. EXPERIMENTAL DETAILS

Details on the employed chemicals, materials and the probe preparation protocols are described in Chapter 2. The specific procedures adopted in this work involved nanoscale electrochemical measurement with SECCM, followed by the analysis of such measures for extracting kinetical data, which then were employed in numerical simulations for describing the system's behaviour. Therefore, this section will describe, in order, these three specific procedures.

3.2.1. SECCM Experiments

In this work, a double channel SECCM setup has been employed in a potential controlled (voltammetric) mode to measure the characteristics of ITO supported polymer blend films, in a solution containing 4.5 mM FcDM as electrochemical mediator and 100 mM KCl as supporting electrolyte. The main setup of the technique is shown in Figure 3.1a. The sample (produced by the University of Arizona with the procedure highlighted in Chapter 2) was mounted on a custom sample holder (surrounded by a moat of water in order to maintain a constant humidity), placed on the *x-y* piezoelectric positioner, while the probe was mouthed on the *z* piezo. The two QRCEs and the sample were connected to a bi-potentiostat, that was responsible for applying the two different potentials E_1 and E_2, as shown in Figure 3.1a.
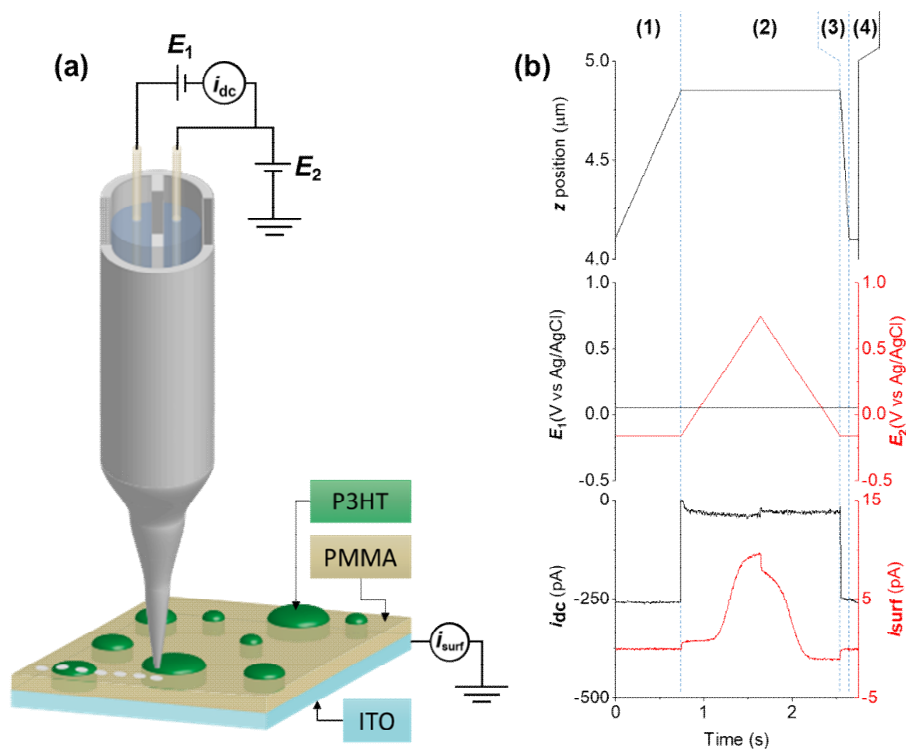
Figure 3.1: **(a)** Scheme of the double channel voltammetric SECCM setup employed herein, specifically for the 1:5 P3HT:PMMA blend electrode. The probe was translated across the substrate (working electrode) surface through the use of piezoelectric positioners in a "hopping mode" configuration. All the potential (E_1 and E_2) and current (i_{dc} and i_{surf}) parameters are indicated on the appropriate point of the scheme. **(b)** Example plots of z-position (top plot), E_1 and E_2 (middle plot), and i_{dc} and i_{surf} (bottom plot) as a function of time, recorded simultaneously during a single approach to a P3HT domain within a 1:5 P3HT:PMMA blend electrode, with a nanopipette (diameter $\approx$ 200 nm) containing 4.5 mM FcDM + 100 mM KCl.

The voltammetric SECCM was carried out in hopping mode, as previously described.[17] This protocol involves approaching the probe to the surface of interest at a series of predefined grid points, and carrying out a single electrochemical experiment on each landing. In this context, the term "landing" refers to droplet (meniscus) contact; the probe itself does not make physical contact with the surface. During the approach, a *dc* ion current (indicated by i_{dc} in Figure 3.1), induced by applying a bias of 50 mV (indicated by E_1 in Figure 6) between the QRCEs located in the two channels of the nanopipette probe, served as a feedback signal to detect

each landing (*i.e.* meniscus-surface contact), at which time the z-approach was halted. Cyclic voltammetry was performed by sweeping the potential of one of the QRCEs (indicated by E_2 in Figure 3.1), which determined the substrate potential (E_{surf}) together with E_1, as discussed in Chapter 1 (section 1.3.2) and described by eq. (1.57), and the surface current (i_{surf}) was measured. In this way, a surface dependent electrochemical movie of the surface current in function of potential and special coordinates was collected.

Figure 3.1b shows representative examples of the z-extension, applied potentials (E_1, E_2) and the measured currents (i_{dc} and i_{surf}) for a single "hop" of a scanning experiment. During approach [Figure 3.1b, (1)], i_{dc} adopts a fixed value ("non-contact" value) which depends on the electrolyte composition, tip geometry and bias potential.[18] Landing is detected by a large spike (several hundreds of pA) in i_{dc} as the meniscus is deformed due to surface contact [Figure 3.1b, (2)], which serves as a feedback signal to halt the z-approach. Once on the surface [Figure 3.1b, (3)], the z-position is fixed, and cyclic voltammetry is performed by sweeping E_2, as i_{surf} is measured. After the measurement [Figure 3.1b, (4)], the probe is retracted and translated in x/y space, while i_{dc} returns to its non-contact value for the next "hop". Note that to accommodate for drift in i_{dc}, the feedback threshold was defined relative to the non-contact value on each and every hop in a self-referencing regime.[19,20]

The use of i_{dc} as feedback signal represents the main innovation brought to the double channel SECCM technique. So far, due to the susceptibility of the i_{dc} signal to drift, a different signal has typically been employed in conventional double channel SECCM, *i.e.* the amplitude of an *ac* component of i_{dc} generated by a sine wave distance modulation of the z-piezo position, applied through the use of a DSP lock-in amplifier (SR830, Stanford Research Systems, U.S.A.); more details regarding this

method can be found in Appendix, Section A.2. Despite its high sensitivity for the surface detection, because of intrinsic time limitations in the response of the lock-in amplifier the use of this *ac* parameter limits the approach rate of the pipette to approximately 1/10 of the pipette diameter per second (in this case $v_{appr} \leq 0.02$ μm s^{-1}, since the employed pipettes were 100 nm to 200 nm dimeter),[18,21] making impossible the collection of the number of points needed in the analysis of a high number of micrometric features ($\approx 9000 - 11000$) in a reasonable amount of time (*i.e.* less than a day). Since i_{dc} has a faster response to the surface contact, it was possible to employ an approach rate of 1 μm s^{-1}, which, together with a lateral scan rate of 25 μm s^{-1} and an electrochemical perturbation time of about 1.8s, allowed each scan to be collected in approximately 8 to 12 hours. The issues deriving by the substantial shift in i_{dc} during such amount of time were overcome by employing a "self-referencing" feedback mode, which consisted in stopping the approach when an absolute variation of i_{dc} (± 100 pA) was detected compared to the value of i_{dc} measured before each single approach.

Note that the area of contact between the droplet and the surface during the voltammetric analysis, and therefore the active working electrode area, depends on the geometry of the probe and the characteristics of the electrolyte and the surface (*i.e.* wettability of the surface). The usual method for determining the wetted area, *i.e.* observing the droplet "footprints", that is the mark left on the surface due to surface modification or electrolyte residue, post-measurement using SEM,[22] as shown in the next chapters, was not applicable in this case, due to the damage caused on the polymer surface by the electron beam. Thus, in order to determine the dimensions of the droplet cell, the constant-distance mode of SECCM was deployed,[23,24] measuring the footprint by translating the probe over the boundary separating a conductive P3HT domain from a non-conductive PMMA domain, as outlined in Appendix, Section A.2. The wetted

area was determined to be ≈ 1.5 times the diameter of the probe, consistent with previous studies in this configuration.[25]

3.2.2. Kinetic analysis with steady state voltammetry

The standard heterogeneous electron-transfer rate constant (k^0) and transfer coefficient (a) associated with the FcDM$^{0/+}$ process were calculated using a well-used numerical method proposed to treat steady state voltammetric data.[26] Due to the conical shape of the nanopipette probe used in SECCM, there is a radial contribution to mass-transport, which results in a flux that is *ca.* 10% of an inlaid disk electrode of the same size, as discussed in Chapter 1 (section 1.3.2).[18] However, the confined geometry of the meniscus (droplet) cell in SECCM tends to suppress the enhanced flux (*i.e.* higher current density) normally expected at the edge of conventional UMEs; therefore, a uniformly accessible electrode condition was hypothesized to a first approximation. The validity of such hypothesis is discussed, with the support of FEM simulation of a typical SECCM setup, in Appendix, section A.3.1.

In order to calculate k^0 and a values, the steady state limiting current (i_{ss}) and voltammetric half-wave ($E_{1/2}$) and quarter-wave ($E_{1/4}$ and $E_{3/4}$) potentials were extracted from each voltammetric transient, as shown in Figure 3.2. These parameters were used to firstly determine a, based on the difference between $|E_{1/2}-E_{1/4}|$ and $|E_{1/2}-E_{3/4}|$, and subsequently k^0, which depends on a, $|E_{1/2}-E_{1/4}|$, the formal potential ($E^{0\prime}$) and the mass-transport coefficient (k_m). $E^{0\prime}$ was estimated from macroscale voltammetry, under conditions of electrochemical reversibility (on an Au electrode, *vide infra*), and k_m was calculated as follows:

$$k_m = \frac{i_{ss}}{nFAC^*} \qquad (3.1)$$

where C^* is the bulk concentration of FcDM. For comparison, under con-
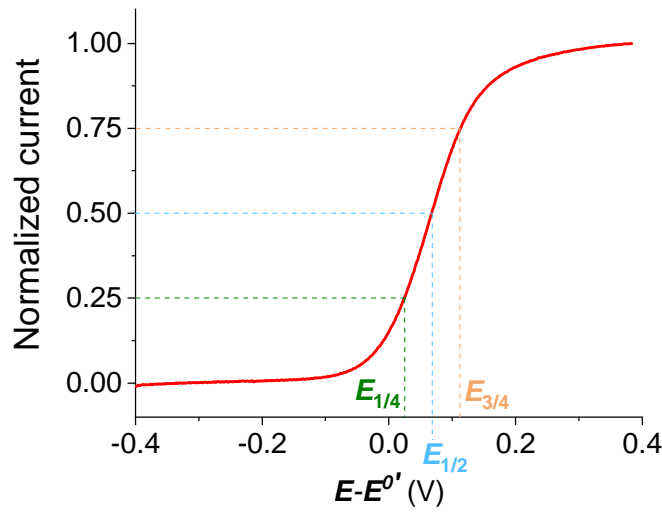
Figure 3.2: Example of a normalized steady state voltammogram, with the main parameters required for microscopic kinetic analysis, i_{ss}, $E_{1/4}$, $E_{1/2}$ and $E_{3/4}$ labelled. The potential scale is referred to the standard potential of the FcDM$^{0/+}$ process, $E^{0\prime}$.

ditions of planar diffusion (*i.e.* at a macroscopic electrode), k_m is calculated from the voltammetric peak current as follows:

$$k_{\mathrm{m}} = 0.4663 \left(\frac{nFvD}{RT} \right)^{\frac{1}{2}} \tag{3.2}$$

3.2.3. FEM simulations of a P3HT macroscopic response.

FEM simulations were carried out in two different configurations, depending on the electrode system under consideration, either an Au electrode, a pure P3HT film or a 1:5 P3HT:PMMA blend electrode. In all cases, a one electron electron-transfer reaction (FcDM → FcDM$^+$ + e^-) governed by the Butler-Volmer formalism of electrode kinetics was assumed. The homogeneously active electrodes, that is the Au (*i.e.* reversible case) and pure P3HT film electrodes were simulated using the DigiElch software package (v.8.FD, Gamry, U.S.A.), employing a planar geometry and semi-infinite one-dimensional (1D) diffusion regime. In the simulations, the bulk concentration of FcDM was set at 4.5 mM, E^0 was experimentally determined from macroscale voltammetry on gold (*vide infra*), the diffusion coefficient of FcDM^0 and FcDM$^+$ were set to 8×10^{-6} cm^2 s^{-1} and the electrode area was set at 0.021 and 0.55 cm^2 for the Au
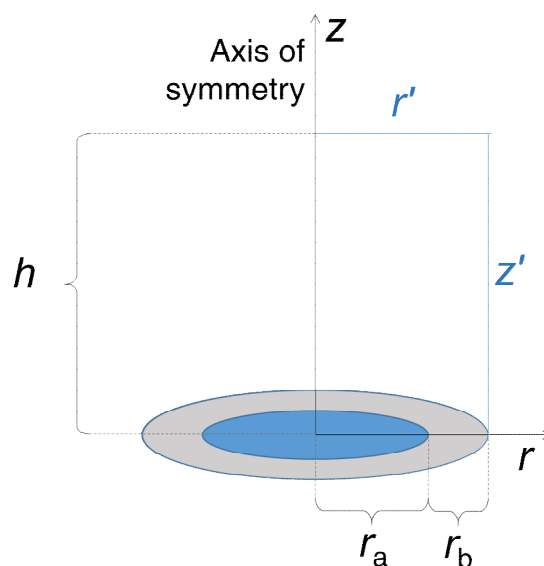
Figure 3.3: Schematic of the 2D axisymmetric geometry built in COMSOL Multiphysics to represent the 1:5 P3HT:PMMA blend electrode. Boundaries r_a and r_b represent the active (conductive) P3HT and inactive (insulating) PMMA domains, respectively.

and P3HT electrode, respectively. The kinetic parameters, k^0 and a, were set to be 1 cm s^{-1}, 0.5 (electrochemically reversible) for the Au, and extracted from experimental data (employing the method described in the previous section) for the P3HT film electrodes. Note that unless explicitly stated, R_u was set to 0 Ω in all simulations.

In the case of the heterogeneously active 1:5 P3HT:PMMA blend electrode, FEM simulations were performed using the COMSOL Multiphysics software package (v.5.1, COMSOL Inc., Sweden). A bi-dimensional axisymmetric simulation set up was employed, using a rectangular cell with edges named r (bottom), z (left), r' (top) and z' (right), as shown in Figure 3.3. The cell dimensions were set to 1.61 μm width (corresponding to $r_a + r_b$, see Figure 3.3) and 500 μm height (corresponding to h), with z set as the symmetry axis. On both the left (z) and right (z') edges, the condition of zero flux was imposed, as well as on the bottom edge (r) along r_b (*i.e.* the insulating PMMA domain).

On the top edge (r'), both zero flux and constant concentration conditions were imposed (with $C_{r'}$ = 4.5 mM). No concentration condition

was imposed on z'. On the P3HT simulation domain (all over r_a), a potential-dependent flux, governed by Butler-Volmer electrode kinetics was employed, with k^0 and a extracted from experimental data (employing the method described in the previous section). As above, the bulk concentrations of FcDM^0 and FcDM$^+$ were set to 4.5 and 0 mM, respectively.

3.3. RESULTS AND DISCUSSION

3.3.1. Compositional surface characterisation

As noted above, this work has been carried out in collaboration with the Laboratory for Interface Science of Printable Electronic Materials at the University of Arizona, where the polymeric samples were fabricated and initially characterised by spectroscopic, crystallographic and macroscopic electrochemical analysis. With the exception of the macroscopic electrochemistry, these results are beyond the scope of this thesis, but are available in published reference originated from the work.[27] Nevertheless, it is useful to list the main highlights of such characterisation:

◆ In the sample presenting both P3HT and PMMA (respectively in 5:1, 1:1 and 1:5 weight ratio) the two phases are completely separated; however, a very small fraction of the PMMA could be intercalated within the conductive P3HT domains.

◆ The microstructure depends on the ratio between the two polymers: the 5:1, 1:1 have islands of insulating PMMA within continuous P3HT, while the opposite is observed for the 1:5 sample (*i.e.* islands of P3HT within continuous PMMA). In any case, the conductive P3HT domains are always in contact with the underlying ITO support.

◆ No chemical interaction between the P3HT and the PMMA phase was observed in any of the blends, neither were microstructural change in interchain packing of the P3HT between the pure P3HT sample and the P3HT domains in the blends.

Given these results, the pure P3HT and the 1:5 blend samples were chosen as suitable substrates for the nanoscale multi-microscopy analysis.

3.3.2. Correlative electrochemical multi-microscopy for nanoscale kinetic analysis.

The spatially-dependent electron-transfer characteristics of pure P3HT and 1:5 P3HT:PMMA blend films were probed at the nanoscale using double channel voltammetric SECCM.[22,23,28] The nanopipette probes had a diameter of 100 – 200 nm, (Figure 2.1a) and were filled with 4.5 mM FcDM and 100 mM KCl. The dual barrels were equipped with Ag/AgCl QRCEs which possess a stable potential of *ca.* 0.070 to 0.080 V (measured to 1 mV) vs Ag/AgCl (3.4 M KCl).[29] Note that unless otherwise stated, all potentials herein are corrected to the Ag/AgCl (3.4 M KCl) reference scale. During operation, a small potential bias (50 mV) was applied between the identical QRCEs located in the two channels of the probe, inducing a *dc* ion current ($i_{dc} \approx 250$ pA), which was used as a feedback signal, as highlighted above. Note that this i_{dc} feedback is independent of the substrate conductivity and thus can be used to position the probe on both the P3HT and PMMA domains of the polymer blend electrode.[23,30]

SECCM was initially performed on freshly prepared films of P3HT and 1:5 P3HT:PMMA by performing cyclic voltammetry in the potential range *ca.* − 0.14 to 0.75 V vs Ag/AgCl (*i.e.* − 0.2 to 0.6 V vs Ag/AgCl QRCE) to observe the FcDM$^{0/+}$ redox process. The FcDM$^{0/+}$ electron transfer reaction is a rapid, mechanistically simple, outer-sphere process on most conventional (*e.g.,* metal and carbon) electrode materials:[31]

$$\text{FcDM} \rightleftharpoons \text{FcDM}^+ + e^- \tag{3.3}$$

As the nanopipette probes used in SECCM possess a conical geometry, mass-transport is predominantly governed by quasi-radial diffusion, , resulting in relatively high rates of mass-transport that allow (near)

steady state conditions to be established on the voltammetric timescale explored herein (*i.e.* ms timescale at voltammetric scan rate, $v = 1$ V s^{-1}).[18,32] The heterogeneous electron-transfer rate constant (k^0) and transfer-coefficient (a) were calculated numerically from the experimentally derived formal ($E^{0'}$), half-wave ($E_{1/2}$) and quarter-wave ($E_{1/4}$ and $E_{3/4}$) potentials, with the method discussed in section 3.2.2.[26]

A spatially resolved electrochemical flux movie for the FcDM$^{0/+}$ process on an area of the pure P3HT film electrode is shown in Appendix, Movie A1. A single frame from the movie, obtained at a potential where FcDM$^{0/+}$ is mass-transport limited (*i.e.* 0.65 V vs Ag/AgCl) is shown in Figure 3.4a. Evident from Movie A1 and Figure 3.4a, the P3HT film exhibits relatively uniform electrochemical activity towards the FcDM$^{0/+}$ process throughout the entire potential range, with the exception of a few non-conductive areas of ≈ 2 μm size. Comparison with the synchronously obtained topographical (z-height) map (Figure 3.4b) reveals no correlation between the physical structure and electrochemical activity, with the film possessing a surface roughness on the same scale (*ca.* 15 nm RMS) as the underlying ITO support.

For comparison of these sample with conventional electrodes (*i.e.* metals), a classical Nernstian behaviour and underlying Butler-Volmer mechanism was assumed; the limitations of these assumptions for conductive polymer electrodes have been detailed previously,[33] but regardless, provide an initial point of comparison. The uniform electrochemical activity of the P3HT film is reflected in the spatially resolved k^0 map shown in Figure 3.4c, from which surface average (9567 individual measurements) values of $k^0 \approx 3 \times 10^{-2}$ cm s^{-1} and $a \approx 0.6$ are derived (see section 3.3.3 for the discussion about the statistical distribution of these values). Note that this k^0 value is orders-of-magnitude lower than that usually measured for the oxidation of ferrocene and derivatives at conventional metal or carbon electrodes, which are on the order of $1-10$ cm s^{-1}.[31]

(a) Steady state current

(b) SECCM topography

(c) Calculated k^0
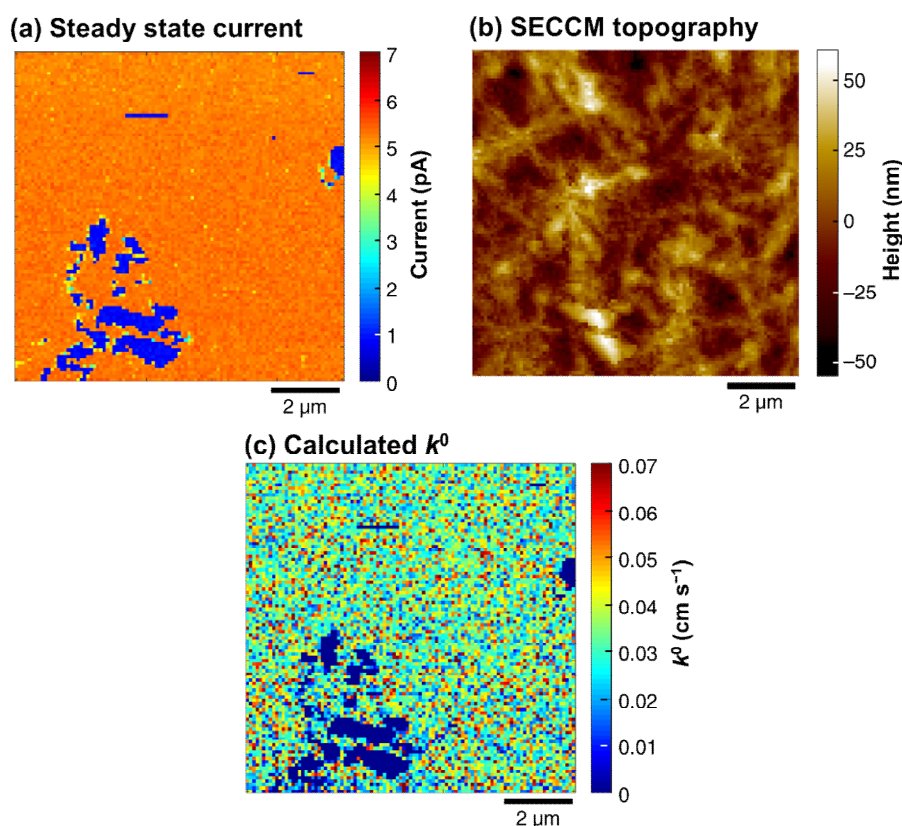
Figure 3.4: (**a**) Electrochemical activity and (**b**) corresponding topographical map recorded in the SECCM configuration (101 by 101 pixels, hopping distance 100 nm), visualizing the FcDM$^{0/+}$ process on a fresh P3HT film deposited on ITO coated glass. (a) Single frame of Movie A1, taken at 0.74 V vs Ag/AgCl. (**c**) Map of k^0 values associated with the FcDM$^{0/+}$ process, calculated numerically from the spatially resolved $i-E$ measurements from SECCM. k^0 was calculated only where a full steady state voltammogram was obtained within the potential window, and set to 0 otherwise. The nanopipette probe used for SECCM was $\approx$ 100 nm in diameter and contained 4.5 mM FcDM + 100 mM KCl.

This is expected based on the significantly lower intrinsic DOS of polymeric electrode materials (P3HT) compared to conventional metallic conductors. However, these average results are much larger than previously reported macroscale cyclic voltammetry measurements of the FcDM$^{0/+}$ process on electrodeposited P3HT ($k^0 \approx 7 \times 10^{-4}$ cm s^{-1}), which exhibited clear (electrochemical) irreversibility.[33]

As anticipated above, the 1:5 P3HT:PMMA blend electrode is structurally heterogeneous, with segregated P3HT and PMMA domain; this

is further illustrated by c-AFM imaging in Figure 3.5a and b. The c-AFM revealed the elevated islands (*ca.* 10 nm in height, Figure 3.5a) in such blend to be conductive P3HT domains (conductance current of *ca.* +10 pA above the non-conducting baseline, at +2 V), within a "sea" of insulating PMMA, shown in Figure 3.5b. The individual P3HT:PMMA domains also contrast optically, as shown in Figure 3.5c. From Figure 3.5a-c, the roughly circular P3HT domains (islands) are on average *ca.* 2.3 μm in diameter and separated by an average distance of *ca.* 2.9 μm.

Voltammetric SECCM performed on the same scanned area using the protocol outlined above; the synchronously obtained topographical map is shown in Figure 3.5d. The morphology (*i.e.* height, shape and diameter) of the individual P3HT domains in Figure 3.5d is qualitatively similar to the co-located AFM map in Figure 3.5a, demonstrating the high-fidelity of SECCM topographical mapping.[24] The corresponding spatially resolved electrochemical movie for the $FcDM^{0/+}$ process on the blend electrode is shown in Appendix, Movie A2. A single frame from the movie, obtained at a potential where the $FcDM^{0/+}$ process is mass-transport limited on the individual P3HT domains (*i.e.* 0.74 V vs Ag/AgCl) is also shown in Figure 3.5e. Evident from MovieA2 and Figure 3.5e, the polymer blend electrode possesses highly heterogeneous electrochemical activity, with the P3HT domains (*i.e.* red areas in Figure 3.5e) supporting the $FcDM^{0/+}$ process, while only non-faradaic current arising predominantly from stray capacitance (*ca.* 0.8 pA) was measured on the insulating PMMA domains (*i.e.* blue areas in Figure 3.5e).

Considering potentials where the $FcDM^{0/+}$ process is kinetically limited (*i.e.* at $E < E_{1/2}$, *ca.* 0.2 to 0.4 V vs Ag/AgCl) in Movie A2, it is clear that the individual P3HT domains are not uniformly active. The larger domains on average show higher electrochemical activity (*i.e.* higher currents at a given potential) than the smaller domains, explored further below.
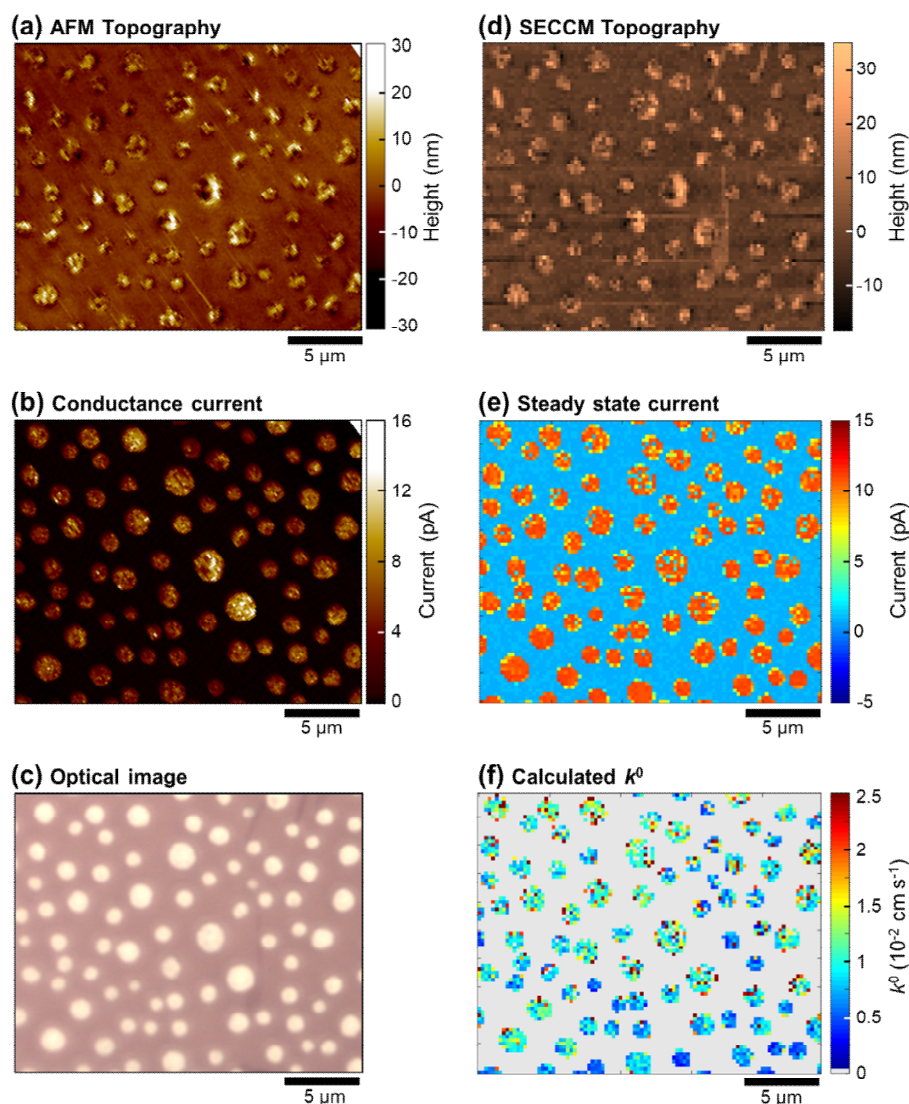
Figure 3.5: Correlative multi-microscopy analysis of the surface of a 1:5 P3HT:PMMA blend electrode, deposited on an ITO support. (**a**) Topographical and (**b**) corresponding electrical conductivity maps, measured using c-AFM (bias potential = + 2.0 V). (**c**) Optical microscopy image (reflected light, 500x magnification). (**d**) Topographical and corresponding (**e**) electrochemical activity map recorded in the SECCM configuration (97 by 79 pixels, hopping distance = 0.25 μm, 2.85 s pixel^{-1}), extracted as a single frame of Movie A2, taken at 0.74 V vs Ag/AgCl. (**f**) Map of k^0 values for the FcDM$^{0/+}$ process, calculated numerically from spatially resolved $i–E$ data from SECCM (Movie A2). In (f), the colour scheme was applied only where full steady state voltammograms were measured (*i.e.* on the P3HT domains); otherwise, it was assigned no colour, coinciding with the insulating PMMA domains. The nanopipette probe used for SECCM, (d – f), was ≈ 200 nm in diameter and contained 4.5 mM FcDM + 100 mM KCl.

112
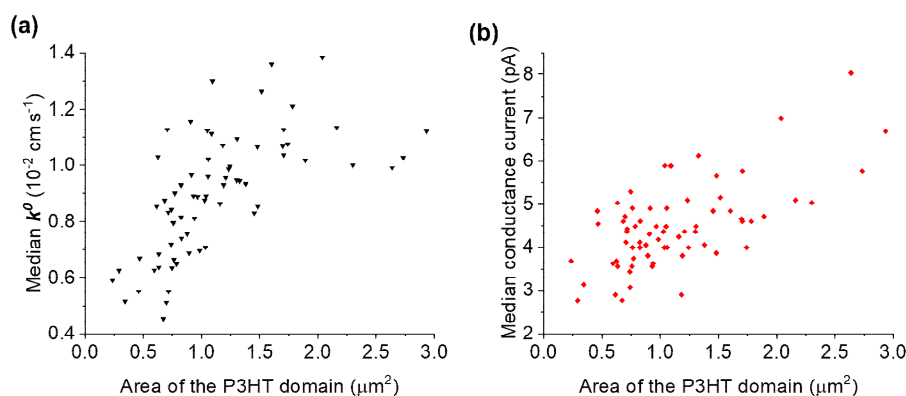
Figure 3.6: Plots of (**a**) the median value of k^0 from each P3HT domain from a fresh 1:5 P3HT:PMMA blend electrode, both as a function of the area of the individual domain and (**b**) the median conductance current measured with c-AFM. The conductance current and k^0 values were extracted from Figure 3.5b and f, respectively, while the area of the domains was extracted by the analysis of the optical microscopy image shown in Figure 3.5c.

Upon sweeping to more positive potentials (*i.e.* $E > 0.6$ V, Figure 3.5e), all P3HT domains attain a mass-transport limited current of *ca.* 11 pA. This limiting current is approximately 10% of what is expected at a conventional inlaid metal disc electrode of the same diameter as the used nanopipette probe (*ca.* 200 nm in Figure 3.5, see Figure 2.1a), in agreement with theoretical predictions of SECCM mass transport.[18] Note that in Figure 3.5e, pixels located at the edges of the islands exhibit currents that are smaller than the mass-transport limit due to the co-contribution of conductive P3HT and non-conductive PMMA within the area probed by the meniscus cell (*i.e.* only a fraction of the probed area is conductive/active).

Using the numerical approach outlined in section 3.2.2, pixel-resolved electrode kinetic parameters (*i.e.* k^0 and a values) were extracted, as illustrated by the spatially resolved k^0 map in Figure 3.5f. Considering all of the active P3HT domains (1826 individual measurements), average k^0 and a values of 8×10^{-3} cm s^{-1} and 0.4 were calculated, corresponding to a *ca.* 4-fold decrease in the FcDM$^{0/+}$ electrode kinetics compared to the pure P3HT case above (Figure 3.4c).
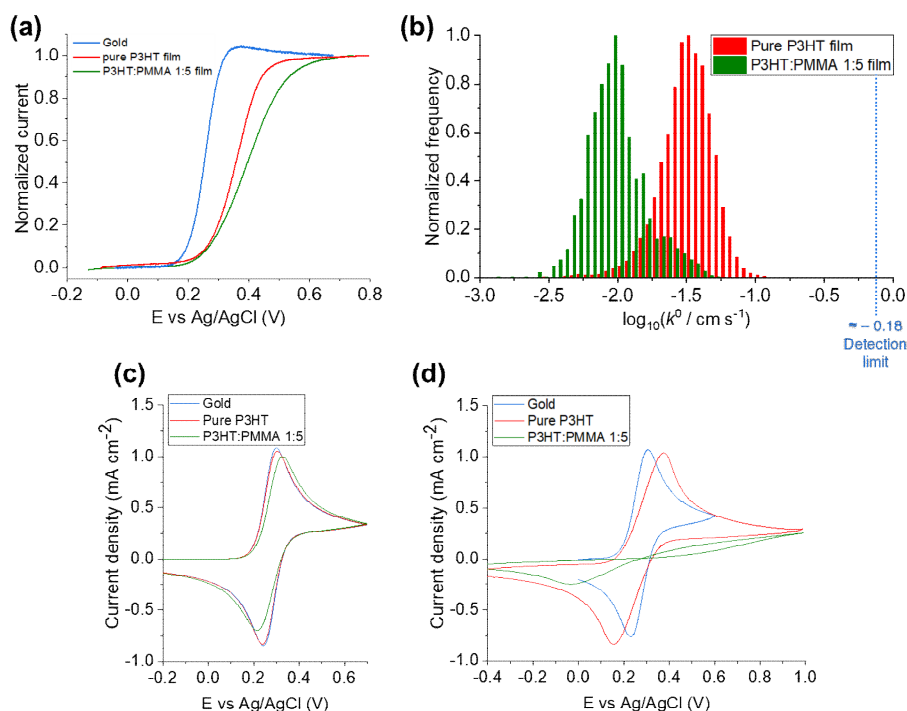
Figure 3.7: (**a**) Normalized near steady state voltammograms ($v = 1$ V s^{-1}) obtained from the FcDM$^{0/+}$ process in the SECCM configuration (probe diameter ≈ 200 nm) on Au, P3HT and 1:5 P3HTPMMA blend electrodes. The curves were obtained by averaging 278, 9567 and 1826 individual measurements respectively on the Au, P3HT and P3HT domains of the 1:5 P3HT:PMMA blend electrode. (**b**) Histograms of measured k^0 values for P3HT and 1:5 P3HT:PMMA blend electrodes (logarithmic scale), with an indication of the maximum k^0 that can be calculated (limit of detection) with the employed method (dotted blue line).(**c**) Simulated and (**d**) experimental macroscopic CVs ($v = 0.1$ V s^{-1}). In all plots, the blue, red and green curves refer to the Au, P3HT and 1:5 P3HT:PMMA blend electrodes, respectively. All experiments were performed with a 4.5 mM FcDM + 100 mM KCl solution. In (c), the reversible case was employed to determine E0' for the process, whose value was calculated to be 0.271 V vs Ag/AgCl (3.4M KCl).

Evidently, the electrode kinetics associated with the FcDM$^{0/+}$ process is P3HT domain-dependent, with the intra-domain variation being smaller than the inter-domain variation. In general, the k^0 values measured on an individual P3HT domain (island) are relatively homogeneous and also tend to be larger on the largest islands (Figure 3.6a). Larger islands also coincide with the largest conductance currents in the solid state (Figure 3.6b). This effect may be due to the geometry of the conducting

and electrochemical probe arrangements; particularly, if the conductivity within the film were highly anisotropic laterally and perpendicular to the ITO substrate, with the lateral conductivity was much greater than the perpendicular one. Usually in c-AFM of conductive polymer films, such effects are not considered,[34] with the local conductivity cell dimensions ascribed to the tip contact area.

Given the lateral domain size extremely larger than the film thickness, however the lateral conductivity here would need to be orders of magnitude higher than that perpendicular for a purely geometrical effect based on domain size to be an important factor; therefore, other effects between individual domains cannot be ruled out, including localized differences in sample thickness, small differences in domain composition, and spatial variations in potential and charge density distributions.[35] In particular, regarding the composition, the fact that the k^0 values tend towards those recorded on the pure P3HT film at high domain sizes could indicate that the domains become increasingly like pure P3HT as they increase in size (even though the variation in composition would have to be very small, according to the characterisation carried out after the electrode preparation). Most likely, such effect is caused by a coexistence of all these factors.

3.3.3. Predicting the macroscopic voltammetric response of polymer blend electrodes.

Steady state voltammograms from the pure P3HT film and 1:5 P3HT:PMMA blend electrodes obtained by averaging all of the active "pixels" in Movie A1 and A2, respectively, are shown in Figure 3.7a. A relatively high mass-transport coefficient is achieved in the SECCM configuration with the nanoscale probes employed herein,[18] with a value $k_m \approx 8 \times 10^{-2}$ cm s^{-1}, estimated from the mass-transport-limited current calculation detailed in section 3.2.2 [eq. (3.1)]. Kinetically, from the analysis of Figure 3.7a, both the pure P3HT film (red trace, $k^0 \approx 3 \times 10^{-2}$ cm s^{-1}) and

1:5 P3HT:PMMA polymer blend (green trace, $k^0 \approx 8 \times 10^{-3}$ cm s^{-1}) can be statistically distinguished from one another, as well as from the electrochemically reversible case (as measured on a nanocrystalline Au electrode, blue trace, $k^0 > 1$ cm s^{-1}).[31] The numerically derived k^0 values for both the pure P3HT and 1:5 P3HT:PMMA electrodes both follow log-normal distributions, as shown in Figure 3.7b.

Log(k^0) is proportional to the standard free energy of activation for a heterogeneous electron-transfer reaction, which, in this case, will be composed of the reorganization energy and work terms (as per Marcus theory),[36] and the energetic barrier of the actual electron transfer event, which is dependent, among other factors, on the DOS.[37] As FcDM$^{0/+}$ is a well-known outer sphere redox couple, the electron transfer rate is most likely to be limited by the relatively low DOS of P3HT (which is why the kinetics of FcDM$^{0/+}$ is slow enough to be measurable). Note that the apparent energy barriers observed (inferred from k^0) are averages over the area probed during each SECCM measurement (*e.g.*, Figure 3.5e and Movie A2), comprising a multitude of sites with different properties (*e.g.*, local DOS). It is the distribution in electrochemical activities between these elementary sites of P3HT that gives rise to the log-normal distributions in Figure 3.7b. This also explains why the distributions in Figure 3.7b are of the same width (*i.e.* standard deviation of 0.3 in both cases), as the electrode material (P3HT) and redox process (FcDM$^{0/+}$) under investigation are analogous in the two cases.

In order to predict the macroscopic electrochemical response from the nanoscale measurements for the three different electrodes considered, FEM simulations were conducted, with the setup described in section 3.2.3. The Au ($k^0 = 1$ cm s^{-1}, $a = 0.5$, essentially reversible) and pure P3HT film ($k^0 = 3 \times 10^{-2}$ cm s^{-1}, $a = 0.6$) cases were simulated assuming mass-transport occurred solely by planar (1D) diffusion to a homogeneously active electrode surface. The 1:5 P3HT:PMMA blend electrode

case was simulated with a 2D axisymmetric geometry (Figure 3.3), where the central area represents a conductive P3HT domain ($k^0 = 8 \times 10^{-3}$ cm s^{-1}, $a = 0.4$) while the surrounding ring represents a non-conductive PMMA domain (set as a no flux boundary). The radius of the P3HT domain (r_a in Figure 3.3) was set to be 1.19 μm while the extension of the PMMA ring around it (r_b in Figure 3.7c) was set to be 0.22 μm, both values being averages calculated from the topographical/optical images shown in Figure 3.5. A condition of no flux was imposed at the cylindrical surface defined by $r = r_a + r_b$, in order to approximate the conditions of an infinite close-packed array of microelectrodes (*e.g.*, Figure 3.5e). Note that the simulation domain represented by Figure 3.3 is a simplified representation, but will give a good guide as to the general shape of a macroscopic CV curve.[38]

Simulated cyclic voltammograms (CVs) obtained at a scan rate of 0.1 V s^{-1} are shown in Figure 3.7c. A relatively low mass-transport coefficient is obtained at this moderate scan rate, $k_m \approx 2 \times 10^{-3}$ cm s^{-1}, estimated from the voltammetric peak current, as detailed in section 3.2.2 [eq. (3.2)]. In addition, a minimum diffusion layer thickness on the order of 40 μm ($\approx D / k_m$) is estimated, meaning the diffusion fields from the individual active P3HT domains of the 1:5 P3HT:PMMA blend (≈ 2.3 μm in diameter and separated by ≈ 2.9 μm, see Figure 3.5a) overlaps fully on this timescale, and thus planar diffusion can be assumed (which has been incorporated into the model described by Figure 3.3).

Note that due to the relatively low k_m value, the macroscopic voltammetric response simulated for the pure P3HT film is indistinguishable from the Au electrode (*i.e.* both are electrochemically reversible, compare red and blue curves), while the 1:5 P3HT:PMMA blend electrode shows a larger voltammetric peak-to-peak separation ($\Delta E_p = 118$ mV, compared to 56 mV of the other two, reversible cases). In other words, despite the

different properties of the three electrode materials, the simulations predict that macroscopic cyclic voltammetry can only distinguish between the pure P3HT and 1:5 P3HT:PMMA cases, but not the Au and the pure P3HT cases (electrochemically reversible).

Thus, a major reason why conventional cyclic voltammetric methods of analysis alone are not suitable for benchmarking the quality of conductive polymer films as electron conductors (*i.e.* electrodes) is susceptibility to ohmic resistance (*iR* drop), particularly at the high scan rates required to probe the kinetics of rapid electron-transfer processes (explored below). In addition, even if the complications from *iR* drop were to be avoided, in the absence of spatial-information on electrochemical reactivity (*i.e.* obtained from SECCM mapping), a number of assumptions would need to be made (*i.e.* uniform size, spacing and reactivity of the P3HT domains, see Figure 3.3) to quantitatively interpret macroscopic electrochemical data, as in Figure 3.7c.

For comparison with the simulations, macroscopic cyclic voltammetry was carried out on an Au macrodisc electrode, a P3HT film electrode and a 1:5 P3HT:PMMA blend electrode, shown in Figure 3.7d. Evidently, while the experimentally measured CV on the Au macrodisc is in excellent agreement with theory, the CVs obtained on the pure P3HT and 1:5 P3HT:PMMA blend are vastly different to those predicted by simulation. Both polymer electrodes exhibit dramatic shifts in peak potential (towards more positive values for the oxidation peak and more negative for the reduction peak) and decreases in the peak current density compared to the reversible case (Au). In particular, the 1:5 P3HT:PMMA blend does not exhibit classical peak shaped current-potential behaviour during the forward potential scan, rather showing a flattened, plateau-type response that gives rise to a positive hysteresis on the reverse sweep. Naive interpretation of these data may indicate that the electrochemical activity of P3HT can be dramatically influenced by

blending with PMMA, with the k^0 value associated with the FcDM$^{0/+}$ process decreasing by several orders of magnitude between pure P3HT electrode and the 1:5 P3HT:PMMA blend.

As alluded to above, the large discrepancy between the experimental (Figure 3.7d) and simulated CVs predicted from analysis with SECCM (Figure 3.7c) is reasonably attributed to the presence of uncompensated resistance (R_u). For conventional metallic electrodes, R_u is typically a small fraction of the solution resistance (R_s) arising from the finite separation between working and reference electrodes and is included in the measured potential as an ohmic drop term (iR_u). In the present case, it is assumed that an additional resistance arising from the finite electrical conductivity of the polymer films (as well as the P3HT-ITO interface), R_{film}, also contributes to R_u. Such resistive components can be considered to be in series, *i.e.* their effect is summed. While R_s is constant in all experiments, R_{film} is a macroscopic property that depends on the composition of the polymer electrode, increasing with PMMA content in the blend.

Therefore, simulations that incorporate R_u can emulate the general shape of the experimental CVs for the pure P3HT electrode, with R_u = 115 Ω, as shown in Figure 3.8a, and 1:5 P3HT:PMMA blend electrode, with $R_u \approx$ 5000 Ω, as shown in Figure 3.8b. Note that in the simulations, R_u (and therefore R_{film}) is assumed to be independent of potential, which is likely to be an oversimplification, as P3HT is known to exhibit potential-dependent conductivity (*i.e.* R_{film} is potential-dependent).[39] In any case, as R_u is the predominant factor controlling the potential-dependent electron transfer rate, the macroscopic CVs (Figure 3.7d) cannot be analysed straightforwardly to reveal the structure-dependent k^0 values, as previous studies on similar materials would seem to suggest.[40-42]

As detailed above, k_m value calculated for a fully active surface (*i.e.* pure P3HT) at the macroscale (v = 0.1 V/s) is *ca.* 2×10^{-3} cm s^{-1}. When corrected for the fact that only $\approx$ 10% of the 1:5 P3HT:PMMA surface is ac-
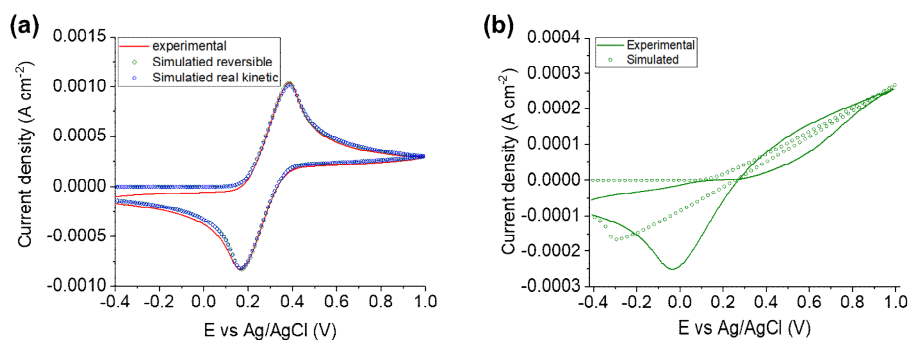
Figure 3.8: (**a**) Comparison between experimental voltammetric curve of FcDM oxidation for pure P3HT (continuous line) and simulations obtained with an added uncompensated resistance of 115 Ω, both considering the reversible case ($k^0 = 1$ cm s^{-1}, $a = 0.5$, green circles) and the measured kinetic parameters on the P3HT film ($k^0 = 0.03$ cm s^{-1}, $a = 0.6$, blue circles). (**b**) Comparison between the experimental voltammetric curve for the 1:5 P3HT:PMMA blend (continuous line) and a simulated curve (circles), obtained for a fully reversible system ($k^0 = 1$ cm s^{-1}, $a = 0.5$), with the addition of an uncompensated resistance of 5000 Ω. All simulations and experiment were performed with a 1D geometry and planar diffusion, at a sweep rate of 0.1 V s^{-1} and in 5 mM FcDM concentration.

tive (from the chemical characterisation and the c-AFM), a k_m value of *ca.* 1×10^{-2} cm s^{-1} is calculated on the individual P3HT domains (UMEs), which is approximately 10% of that in the SECCM configuration ($k_m \approx 8 \times 10^{-2}$ cm s^{-1}). Based on this, in the absence of iR_u effects, one would expect that the macroscopic CV would be closer to reversible than that measured in the SECCM configuration, which, when comparing Figure 3.7a and d, is contrary to what is observed experimentally. Thus, the differences between the experimental and simulated macroscopic CVs in Figure 3.7d and e are solely attributable to iR_u (predominantly R_{film} in the case of the 1:5 P3HT:PMMA blend), and the SECCM-averaged CVs (Figure 3.7a) reflects the iR_u-free response of the P3HT domains. The two different diffusion regimes can be illustrated schematically, in the case of 1:5 P3HT:PMMA blend electrode, as shown in Figure 3.9.

At the macroscale, the diffusion layer is orders of magnitude larger than the size of the individual P3HT domains (UMEs), thus mass trans-
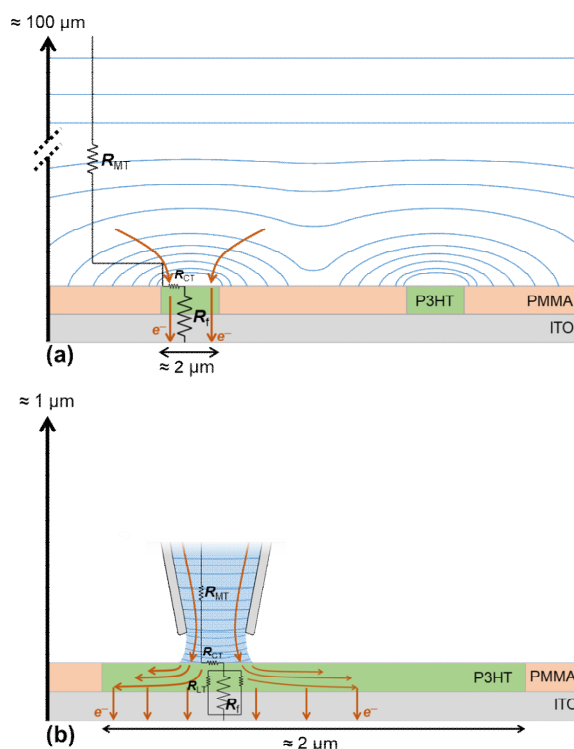
Figure 3.9: Scheme of the mass-transport to (*i.e.* diffusion layers) and the charge-transfer within individual P3HT domains (UMEs) of the 1:5 P3HT:PMMA blend, at the **(a)** macroscale and **(b)** in the SECCM droplet-cell configuration. All of the involved resistances are highlighted in the scheme, with R_{MT} being the mass-transport resistance, R_{CT} the charge-transfer resistance, R_f the film resistance and R_{LT} the lateral charge-transfer resistance.

port in solution and charge-transfer in the P3HT film (to the underlying ITO support) are predominantly planar, as illustrated in Figure 3.9a.

By contrast, in the SECCM droplet-cell configuration, mass-transport within the pipette occurs radially (see section 3.2.2 and Appendix, section A.3.1), and because the electrode area probed by the nanopipette (commensurate with the pipette dimensions, *ca.* 200 nm) is considerably smaller than individual P3HT domains, charge-transfer through the film occurs in the perpendicular and lateral directions, as illustrated in Figure 3.9b. In effect, the additional charge-transfer pathways act to lower the effective resistance of the film. This, in addition to the small currents (*i.e.* < 20 pA, herein) measured in SECCM render this technique relatively
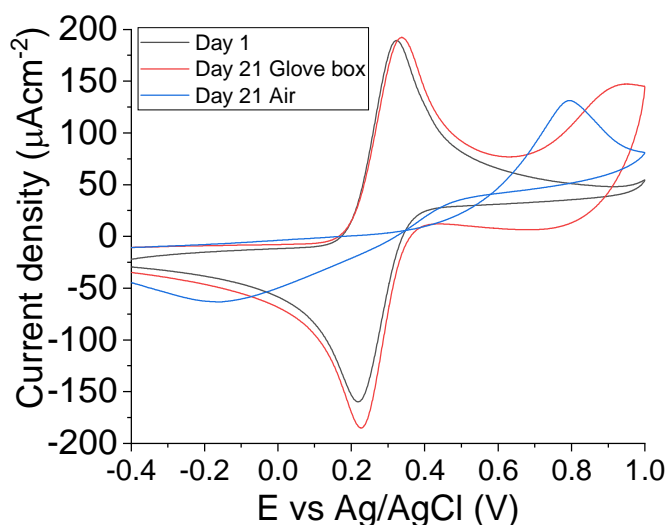
Figure 3.10: Cyclic voltammogram of pristine and aged P3HT films in 1 mM FcDM in 0.1 M KCl (v = 0.1 V s^{-1}). All three P3HT samples were prepared in the same day. One sample was measured immediately after preparation (black line), while the other two were kept for 21 days, respectively, in the glove box filled with Ar gas (red line) and in ambient atmosphere (blue line) before the measurement.

immune to iR_u effects,[22] meaning that it can be applied to study the electrochemical properties of relatively resistive materials such as conductive polymer blends (herein) and semiconductors in general.[24,43]

3.3.4. Sample aging at microscopic level.

P3HT is known to undergo chemical degradation upon prolonged exposure (*i.e.* on the days to weeks' timescale) to ambient conditions (*i.e.* light and atmospheric oxygen).[44,45] The chemical degradation is expected to alter the electrochemical performance, as demonstrated from macroscale CVs on the pure material, shown in Figure 3.10. Briefly, any chemical reaction can degrade the film and alter the local density of states and thus the rate of electron transfer. Therefore, shown below, local electrochemical activity may serve as a far more sensitive probe to spatial degradation effects than what can currently be measured chemically.

The spatial instability of the polymer electrode was explored using voltammetric SECCM, employing the protocol outlined above (for the
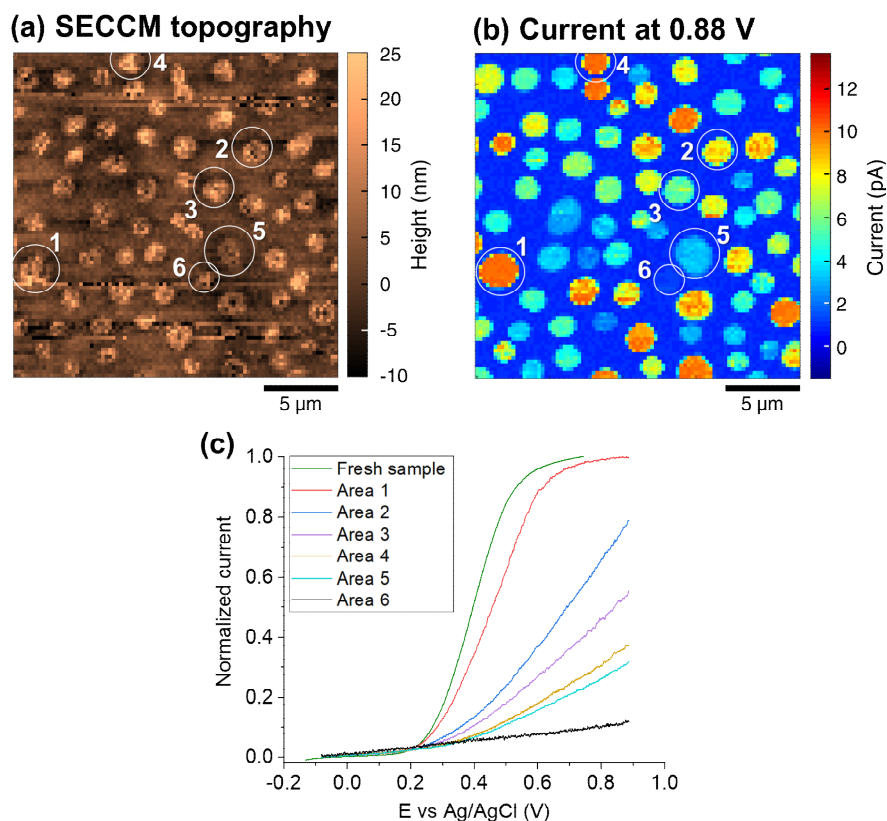
Figure 3.11: (**a**) Topographical and corresponding (**b**) electrochemical activity map recorded in the SECCM configuration (89 by 89 pixels, hopping distance = 0.25 μm, 2.38 s pixel^{-1}), visualizing the FcDM$^{0/+}$ process on an aged 1:5 P3HT:PMMA blend electrode. (b) is a single frame of Movie A3, taken at 0.88 V vs Ag/AgCl. (**c**) Normalized near steady state voltammograms (υ = 1 V s^{-1}) extracted from the six P3HT domains labelled in (a) and (b), alongside the one extracted from a fresh 1:5 P3HT:PMMA blend electrode (see Figure 3.5). The curves were obtained by averaging all "active" pixels within the individual P3HT domains. The nanopipette probe was ≈ 200 nm in diameter and contained 4.5 mM FcDM + 100 mM KCl.

"fresh" samples) to scan the 1:5 P3HT:PMMA blend electrode after "aging" under ambient conditions for a period of three weeks. Evident from the SECCM topography map in Figure 3.11a, the area scanned on the aged blend electrode is structurally analogous to that of the fresh electrode (see above, Figure 3.5d), with μm-sized islands of conductive P3HT within a matrix of insulating PMMA. However, when viewing the spatially resolved current-potential data, shown in Appendix, Movie A3, it is clear that the "aged" blend electrode exhibits a significantly different

pattern of nanoscale reactivity compared to the "fresh" electrode above. There are statistical differences between the current measured at the individual P3HT domains at the aged surface, with only a single domain attaining a mass-transport limited current for the FcDM$^{0/+}$ process within the examined potential window (– 0.11 to 0.88 V vs Ag/AgCl), as shown in Figure 3.11b. This indicates that k^0 varies significantly from domain-to-domain (*i.e.* orders-of-magnitude differences), which contrasts the fresh sample where all P3HT domains attained an identical mass-transport limited current within the scanned potential window (Figure 3.5e) and relatively small inter-domain variations in k^0 were observed.

Figure 3.11c shows the averaged steady state voltammograms extracted from individual P3HT domains. As noted above, only a single domain supported a mass-transport limited current, labelled **1** in Figure 3.11b and c, from which a k^0 value of *ca.* 5×10^{-3} cm s^{-1} was calculated, which is approximately half of that measured at the fresh electrode surface (*vide supra*). The absence of a mass-transport limited current plateau (within the investigated potential window) precludes quantitative analysis for the other domains, but it is clear that the k^0 value progressively decreases from curve **2** to **6**. The slowest response is barely distinguishable from the (stray) capacitive response obtained on the insulating PMMA areas (normalized to 0 in the plot). Evidently, exposure to the ambient atmosphere on the weeks' timescale significantly affects the electron-transfer properties of P3HT, whether pure (Figure 3.10) or blended with PMMA (Movie A3 and Figure 3.5c).

While the chemical mechanism leading to these observed changes is beyond the scope of this proof-of-concept, it can be postulated that variations in the local chemical environment arising from differences in composition/structure (*i.e.* PMMA content) or oxygen diffusion rates at the individual P3HT domain level could alter degradation rates at the (sub)microscale. Such non-uniform (spatially-dependent) degradation

rates would be "invisible" in a conventional macroscopic CV, which is controlled by electrode-film resistance (*i.e.* R_{film} contributing to R_u) rather than redox reactions (*i.e.* the $FcDM^{0/+}$ process), as highlighted by the schemes in Figure 3.9. SECCM clearly serves as a more sensitive screening tool for (electro)chemical degradation of semiconductor materials, with broader applicability beyond just organic electronics.

3.4. CONCLUSION

This study advocates the use of *correlative electrochemical multi-microscopy* to understand the underlying structural factors governing electron-transfer in complex, structurally-heterogeneous electrode materials from the nanoscale to macroscale. Correlation of topographical, compositional and conductance mapping with quantitative, nanoscale resolution electrochemical flux movies from SECCM revealed only a slightly reduced electron-transfer rate constant (*i.e.* k^0 value) for the $FcDM^{0/+}$ process in the isolated P3HT domains in a 1:5 P3HT:PMMA blend, if compared to pure P3HT electrodes at a commensurate length scale. Combining these data with complementary FEM simulations, macroscopic electrochemical behaviour was predicted and further compared to experiment, demonstrating that electrode-film resistance, rather than redox reaction kinetics (*i.e.* $FcDM^{0/+}$), controls the measured macroscopic electrochemistry of these polymer blend electrodes. These results suggest that conventional bulk voltammetric measurements should be used with caution to assess the quality of conductive polymers as electrodes. With this additional knowledge, the ambient exposure-induced degradation of P3HT:PMMA blend electrodes was interrogated with SECCM to reveal a spatially-heterogeneous loss of P3HT electroactivity, with individual P3HT domains affected to dramatically different extents.

Overall, this study highlights the great strength of SECCM for resolving structure-property (*e.g.*, electrochemical activity or degradation) relationships in complex (electro)materials such as conductive polymer

blends and for predicting the factors that control electrochemistry across length scales. The possibility of performing large and highly resolved maps (implemented thank to the use of i_{dc} as feedback parameter), opens up the possibility to systematically examine complex blends of conducting and insulating materials. The presented approaches should be generally applicable to any class of conductive polymer (or polymer blend), and offers the possibility for re-evaluating and optimizing materials that were previously discarded due to apparently poor macroscopic electrochemical properties.

3.5.   REFERENCES

[1]   Green, R. A.; Lovell, N. H.; Wallace, G. G.; Poole-Warren, L. A. Conducting polymers for neural interfaces: Challenges in developing an effective long-term implant. *Biomaterials* **2008,** *29* (24), 3393-3399.

[2]   Abidian, M. R.; Corey, J. M.; Kipke, D. R.; Martin, D. C. Conducting-Polymer Nanotubes Improve Electrical Properties, Mechanical Adhesion, Neural Attachment, and Neurite Outgrowth of Neural Electrodes. *Small* **2010,** *6* (3), 421-429.

[3]   Cui, X.; Lee, V. A.; Raphael, Y.; Wiler, J. A.; Hetke, J. F.; Anderson, D. J.; Martin, D. C. Surface modification of neural recording electrodes with conducting polymer/biomolecule blends. *Journal of Biomedical Materials Research* **2001,** *56* (2), 261-272.

[4]   Neelamraju, B.; Rudolph, M.; Ratcliff, E. L. Controlling the Kinetics of Charge Transfer at Conductive Polymer/Liquid Interfaces through Microstructure. *J. Phys. Chem. C* **2018,** *122* (37), 21210-21215.

[5]   Tsoi, W. C.; Spencer, S. J.; Yang, L.; Ballantyne, A. M.; Nicholson, P. G.; Turnbull, A.; Shard, A. G.; Murphy, C. E.; Bradley, D. D. C.; Nelson, J.et al. Effect of Crystallization on the Electronic Energy Levels and Thin Film Morphology of P3HT:PCBM Blends. *Macromolecules* **2011,** *44* (8), 2944-2952.

[6]   Kleinschmidt, A. T.; Root, S. E.; Lipomi, D. J. Poly(3-hexylthiophene) (P3HT): fruit fly or outlier in organic solar cell research? *Journal of Materials Chemistry A* **2017,** *5* (23), 11396-11400.

[7]   Ratcliff, E. L.; Jenkins, J. L.; Nebesny, K.; Armstrong, N. R. Electrodeposited, "Textured" Poly(3-hexyl-thiophene) (e-P3HT) Films for Photovoltaic Applications. *Chem. Mater.* **2008,** *20* (18), 5796-5806.

[8]   Shallcross, R. C.; Stubhan, T.; Ratcliff, E. L.; Kahn, A.; Brabec, C. J.; Armstrong, N. R. Quantifying the Extent of Contact Doping at the Interface between High Work Function Electrical Contacts and Poly(3-hexylthiophene) (P3HT). *J. Phys. Chem. Lett.* **2015,** *6* (8), 1303-1309.

[9]   Sirringhaus, H.; Brown, P. J.; Friend, R. H.; Nielsen, M. M.; Bechgaard, K.; Langeveld-Voss, B. M. W.; Spiering, A. J. H.; Janssen, R. A. J.; Meijer, E. W.; Herwig, P.et al. Two-dimensional charge transport in self-organized, high-mobility conjugated polymers. *Nature* **1999,** *401* (6754), 685-688.

[10]   Wang, X.; Lee, W. H.; Zhang, G.; Wang, X.; Kang, B.; Lu, H.; Qiu, L.; Cho, K. Self-stratified semiconductor/dielectric polymer blends: vertical phase separation for facile fabrication of organic transistors. *Journal of Materials Chemistry C* **2013,** *1* (25), 3989-3998.

[11]   Zhang, X.; Wang, B.; Huang, W.; Wang, G.; Zhu, W.; Wang, Z.; Zhang, W.; Facchetti, A.; Marks, T. J. Oxide–Polymer Heterojunction Diodes with a Nanoscopic Phase-Separated Insulating Layer. *Nano Lett.* **2019,** *19* (1), 471-476.

[12]   Bae, S.; Kim, H.; Lee, Y.; Xu, X.; Park, J.-S.; Zheng, Y.; Balakrishnan, J.; Lei, T.; Ri Kim, H.; Song, Y. I.et al. Roll-to-roll production of 30-inch graphene films for transparent electrodes. *Nature Nanotechnology* **2010,** *5* (8), 574-578.

[13]   Wu, M.-C.; Liao, H.-C.; Lo, H.-H.; Chen, S.; Lin, Y.-Y.; Yen, W.-C.; Zeng, T.-W.; Chen, C.-W.; Chen, Y.-F.; Su, W.-F. Nanostructured polymer blends (P3HT/PMMA): Inorganic titania hybrid photovoltaic devices. *Sol. Energy Mater. Sol. Cells* **2009,** *93* (6), 961-965.

[14]   Kergoat, L.; Battaglini, N.; Miozzo, L.; Piro, B.; Pham, M.-C.; Yassar, A.; Horowitz, G. Use of poly(3-hexylthiophene)/poly(methyl methacrylate) (P3HT/PMMA) blends to improve the performance of water-gated organic field-effect transistors. *Org. Electron.* **2011,** *12* (7), 1253-1257.

[15]   Janasz, L.; Marszalek, T.; Zajaczkowski, W.; Borkowski, M.; Goldeman, W.; Kiersnowski, A.; Chlebosz, D.; Rogowski, J.; Blom, P.; Ulanski, J.et al. Ultrathin film heterojunctions by combining solution processing and sublimation for ambipolar organic field-effect transistors. *Journal of Materials Chemistry C* **2018,** *6* (29), 7830-7838.

[16]   McKelvey, K.; O'Connell, M. A.; Unwin, P. R. Meniscus confined fabrication of multidimensional conducting polymer nanostructures with scanning electrochemical cell microscopy (SECCM). *Chem. Commun.* **2013,** *49* (29), 2986-2988.

[17]   Chen, C.-H.; Jacobse, L.; McKelvey, K.; Lai, S. C. S.; Koper, M. T. M.; Unwin, P. R. Voltammetric Scanning Electrochemical Cell Microscopy: Dynamic Imaging of Hydrazine Electro-oxidation on Platinum Electrodes. *Anal. Chem.* **2015,** *87* (11), 5782-5789.

[18]   Snowden, M. E.; Güell, A. G.; Lai, S. C. S.; McKelvey, K.; Ebejer, N.; O'Connell, M. A.; Colburn, A. W.; Unwin, P. R. Scanning Electrochemical Cell Microscopy: Theory and Experiment for Quantitative High Resolution Spatially-Resolved Voltammetry and Simultaneous Ion-Conductance Measurements. *Anal. Chem.* **2012,** *84* (5), 2483-2491.

[19]   Bentley, C. L.; Unwin, P. R. Nanoscale electrochemical movies and synchronous topographical mapping of electrocatalytic materials. *Faraday Discuss* **2018,** *210* (0), 365-379.

[20]   Page, A.; Perry, D.; Young, P.; Mitchell, D.; Frenguelli, B. G.; Unwin, P. R. Fast Nanoscale Surface Charge Mapping with Pulsed-Potential Scanning Ion

Conductance Microscopy. *Anal. Chem.* **2016,** *88* (22), 10854-10859.

[21]   Liu, D.-Q.; Chen, C.-H.; Perry, D.; West, G.; Cobb, S. J.; Macpherson, J. V.; Unwin, P. R. Facet-Resolved Electrochemistry of Polycrystalline Boron-Doped Diamond Electrodes: Microscopic Factors Determining the Solvent Window in Aqueous Potassium Chloride Solutions. *ChemElectroChem* **2018,** *5* (20), 3028-3035.

[22]   Bentley, C. L.; Edmondson, J.; Meloni, G. N.; Perry, D.; Shkirskiy, V.; Unwin, P. R. Nanoscale Electrochemical Mapping. *Anal. Chem.* **2019,** *91* (1), 84-108.

[23]   Ebejer, N.; Güell, A. G.; Lai, S. C. S.; McKelvey, K.; Snowden, M. E.; Unwin, P. R. Scanning Electrochemical Cell Microscopy: A Versatile Technique for Nanoscale Electrochemistry and Functional Imaging. *Annu. Rev. Anal. Chem.* **2013,** *6* (1), 329-351.

[24]   Bentley, C. L.; Kang, M.; Unwin, P. R. Nanoscale Structure Dynamics within Electrocatalytic Materials. *J. Am. Chem. Soc.* **2017,** *139* (46), 16813-16821.

[25]   Guell, A. G.; Meadows, K. E.; Dudin, P. V.; Ebejer, N.; Macpherson, J. V.; Unwin, P. R. Mapping nanoscale electrochemistry of individual single-walled carbon nanotubes. *Nano Lett.* **2014,** *14* (1), 220-224.

[26]   Mirkin, M. V.; Bard, A. J. Simple analysis of quasi-reversible steady-state voltammograms. *Anal. Chem.* **1992,** *64* (19), 2293-2302.

[27]   Daviddi, E.; Chen, Z.; Beam Massani, B.; Lee, J.; Bentley, C. L.; Unwin, P. R.; Ratcliff, E. L. Nanoscale Visualization and Multiscale Electrochemical Analysis of Conductive Polymer Electrodes. *ACS Nano* **2019,** *13* (11), 13271-13284.

[28]   Bentley, C. L.; Kang, M.; Unwin, P. R. Scanning electrochemical cell microscopy: New perspectives on electrode processes in action. *Curr. Opin. Electrochem.* **2017,** *6* (1), 23-30.

[29]   Bentley, C. L.; Perry, D.; Unwin, P. R. Stability and Placement of Ag/AgCl Quasi-Reference Counter Electrodes in Confined Electrochemical Cells. *Anal. Chem.* **2018,** *90* (12), 7700-7707.

[30]   Ebejer, N.; Schnippering, M.; Colburn, A. W.; Edwards, M. A.; Unwin, P. R. Localized High Resolution Electrochemistry and Multifunctional Imaging: Scanning Electrochemical Cell Microscopy. *Anal. Chem.* **2010,** *82* (22), 9141-9145.

[31]   Sun, P.; Mirkin, M. V. Kinetics of Electron-Transfer Reactions at Nanoelectrodes. *Anal. Chem.* **2006,** *78* (18), 6526-6534.

[32]   Momotenko, D.; Byers, J. C.; McKelvey, K.; Kang, M.; Unwin, P. R. High-Speed Electrochemical Imaging. *ACS Nano* **2015,** *9* (9), 8942-8952.

[33]   Rudolph, M.; Ratcliff, E. L. Normal and inverted regimes of charge transfer controlled by density of states at polymer electrodes. *Nat. Commun.* **2017,** *8* (1), 1048.

[34]   Lee, H. J.; Lee, J.; Park, S.-M. Electrochemistry of Conductive Polymers. 45. Nanoscale Conductivity of PEDOT and PEDOT:PSS Composite Films Studied by Current-Sensing AFM. *J. Phys. Chem. B* **2010,** *114* (8), 2660-2666.

[35]   Reid, O. G.; Munechika, K.; Ginger, D. S. Space Charge Limited Current Measurements on Conjugated Polymer Films using Conductive Atomic Force

Microscopy. *Nano Lett.* **2008,** *8* (6), 1602-1609.

[36] Bard, A. J.; Faulkner, L. R. *Electrochemical Methods: Fundamentals and Applications*; John Wiley and Sons Inc., 2001.

[37] Marcus, R. A.; Sutin, N. Electron transfers in chemistry and biology. *Biochim. Biophys. Acta, Rev. Bioenerg.* **1985,** *811* (3), 265-322.

[38] Davies, T. J.; Ward-Jones, S.; Banks, C. E.; del Campo, J.; Mas, R.; Muñoz, F. X.; Compton, R. G. The cyclic and linear sweep voltammetry of regular arrays of microdisc electrodes: Fitting of experimental data. *J. Electroanal. Chem.* **2005,** *585* (1), 51-62.

[39] Harris, J. K.; Neelamraju, B.; Ratcliff, E. L. Intersystem Subpopulation Charge Transfer and Conformational Relaxation Preceding in Situ Conductivity in Electrochemically Doped Poly(3-hexylthiophene) Electrodes. *Chem. Mater.* **2019,** *31* (17), 6870-6879.

[40] Wijeratne, K.; Ail, U.; Brooke, R.; Vagin, M.; Liu, X.; Fahlman, M.; Crispin, X. Bulk electronic transport impacts on electron transfer at conducting polymer electrode-electrolyte interfaces. *Proc. Natl. Acad. Sci. U.S.A.* **2018,** *115* (47), 11899-11904.

[41] Milner, D. F.; Weaver, M. J. The influence of uncompensated solution resistance on the determination of standard electrochemical rate constants by cyclic voltammetry, and some comparisons with a.c. voltammetry. *Anal. Chim. Acta* **1987,** *198*, 245-257.

[42] Gennett, T.; Weaver, M. J. Reliability of standard rate constants for rapid electrochemical reactions. *Anal. Chem.* **1984,** *56* (8), 1444-1448.

[43] Bentley, C. L.; Kang, M.; Maddar, F. M.; Li, F.; Walker, M.; Zhang, J.; Unwin, P. R. Electrochemical maps and movies of the hydrogen evolution reaction on natural crystals of molybdenite (MoS2): basal vs. edge plane activity. *Chem. Sci.* **2017,** *8* (9), 6583-6593.

[44] Schafferhans, J.; Baumann, A.; Deibel, C.; Dyakonov, V. Trap distribution and the impact of oxygen-induced traps on the charge transport in poly(3-hexylthiophene). *Appl. Phys. Lett.* **2008,** *93* (9), 093303.

[45] Rivaton, A.; Chambon, S.; Manceau, M.; Gardette, J.-L.; Lemaître, N.; Guillerez, S. Light-induced degradation of the active layer of polymer-based solar cells. *Polym. Degrad. Stab.* **2010,** *95* (3), 278-284.

Chapter 4

SECCM Chronopotentiometry

T he work presented in this chapter is not directly related to either of the two important fields of applications described in Chapter 1 (*i.e.* studies on conductive polymers and corrosion). In fact, this chapter is entirely dedicated to the development of SECCM itself, in order to address the technical and theoretical nuances arising from its application in current-controlled mode, *i.e.* with chronopotentiometry. This development is critical for many fields of research (some of which are explored herein), and it will be fundamental for the corrosion studies carried out in the next chapter.

4.1. INTRODUCTION AND BACKGROUND

Despite being less used than potential-controlled methods in modern electrochemical science, current-controlled or galvanostatic techniques still play an important role in diverse fields, including coatings (*i.e.* electroplating)[1] and battery research,[2] where constant-current conditions are usually applied to allow fine control over the rate of (electro)chemical processes. For instance, a notable advantage of galvanostatic techniques in electroplating is that the charge passed, and hence the amount of material electrodeposited can be controlled precisely, which generally makes

it easier to obtain a uniform deposition compared to constant-potential conditions.[3] Another interesting application of galvanostatic methods can be found in the field of electrocatalysis, where a commonly adopted metric for benchmarking the activity of a material is the overpotential required to achieved a given current density (*e.g.*, 10 mA cm^{-2}, η_{10});[4,5] as explored herein, this kind of determination is conceptually easier under current-controlled conditions, rather than controlled-potential.

For all these reasons, and other that will be discussed further herein, it would be interesting to expand the applicability of SECCM in order to include galvanostatic techniques on a routine basis. Some steps have already been done in this direction: galvanostatic SECCM has recently been used as part of studies to map the charge/discharge characteristics of battery electrodes,[6-8] even though the galvanostatic characterisation represented only a small and complementary part of the work. In order to improve the use of chronopotentiometric SECCM in these and further applications, it is necessary to understand in more detail the electrochemical response of different kinds of system with this unique (galvanostatic) mode of application.

Therefore, in this chapter chronopotentiometric SECCM has been applied for the study of three model electrochemical systems, in order to verify the validity and liability of the method by comparing results in current-controlled mode with previous results on similar systems in the potential-controlled mode. Firstly, the outer-sphere $[Ru(NH_3)_6]^{3+/2+}$ process was characterised at a polished GC surface, where ideal electrochemical reversibility (*i.e.* "Nernstian" behaviour) is expected, given the scale of the nanopipette used (*ca.* 500 nm) compared to the structural heterogeneity in GC (*i.e.* it is microstructurally isotropic).[9] These measurements sought to confirm the stability of the meniscus (droplet) cell and demonstrate the reproducibility of the electrochemical potential (E) - time (t) curves at the different pixels among the thousands of an SECCM

scan. Secondly, the same process was investigated on an aged HOPG surface, which has previously been shown to exhibit complex, structure-dependent (*i.e.* step edge, vs. basal plane) electron-transfer properties under these conditions.[10] Finally, the technique was employed in the context of electrocatalysis to probe the HER activity of bulk MoS_2, demonstrating enhanced catalytic activity at macroscopic defect sites where the step edge is exposed.

4.2. SECCM SETUP

Details about the experimental SECCM setup (*i.e.* common instrumentation, probes and electrode materials preparation and data analysis) and the electron microscopy technique employed in this work are provided in Chapter 2. The custom setup employed in this chapter includes a home-built low current galvanostat, employed to apply the current (i_{app}) at the QRCE present in the single-channel nanopipette probe and measure the potential (E_{surf}) at the substrate. A schematic representation of the setup for galvanostatic SECCM and chronopotentiometric measurements is given at the start of the results and discussion section (Figure 4.1).

The chronopotentiometric SECCM experiments were performed with a "hopping mode" imaging protocol, as previously described.[11,12] This protocol involved approaching the nanopipette probe to the substrate surface at a series of predefined locations in a grid and, upon each meniscus landing (note that the pipette itself did not contact the surface), a chronopotentiometric measurement was made, allowing the creation of time-dependent 2-dimensional electrochemical potential "maps" of the substrate. In addition, the *z*-position of the probe was recorded synchronously on every approach, and the contact *z*-coordinate was plotted as a function of *x-y* coordinate to create a topographical map of the substrate surface. During approach of the tip, the potential measured in the galvanostat circuit was employed for positional feedback in order to detect

meniscus contact with the surface. A change of 6 V from the 'overload' value ($\pm$10 V) experienced when the tip was at open circuit (tip away from the surface) was set as the feedback threshold to indicate meniscus contact and to immediately stop the nanopipette movement on each approach. The nanopipette speeds were 3 μm s^{-1} on approach, 20 μm s^{-1} on retract (by 4 μm) and 5 μm s^{-1} for lateral movement. The distance between each pixel depended on the tip size and sample; pixel densities are specified for each data set presented.

After collection, all the raw data were processed using the Matlab software suite. "False approach" points, *i.e.* where the nanopipette was triggered to stop but subsequent analysis revealed that meniscus contact had not been made (evident from a 'spike' in the synchronously obtained topographical map, not shown in the results), were discarded. These events were rare, *e.g.* amounting to 12 out of the 6561 pixels for $[Ru(NH_3)_6]^{3+/2+}$ process on GC, discussed below.

4.3.   RESULTS AND DISCUSSION

4.3.1.   Chronopotentiometric SECCM: working principles.

A general scheme of the technique and typical data for a single pixel are shown in Figure 4.1. As the single channel nanopipette (Figure 4.1a) was moved across the surface in the "hopping-mode" regime, the measured galvanostat output potential (E_{output}) was used for positional feedback (*vide supra*). Figure 4.1b shows representative examples of the *z*-position of the probe, current applied by the galvanostat (i_{app}) and E_{output} for a single "hop" with a single pulse chronopotentiometry measurement (preceded by a landing at OCP), as used for the $Ru(NH_3)_6^{3+/2+}$ case discussed below. When i_{app} of a specific magnitude and polarity is set at the galvanostat, the instrument tunes E_{output} (equivalent to E_{surf} during meniscus contact) until the set current is reached. If the electrochemical cell has not been formed (*i.e.* meniscus contact has not been made with the surface, 'non-contact'), E_{output} will be in the "overload" state [$\pm$10 V for the
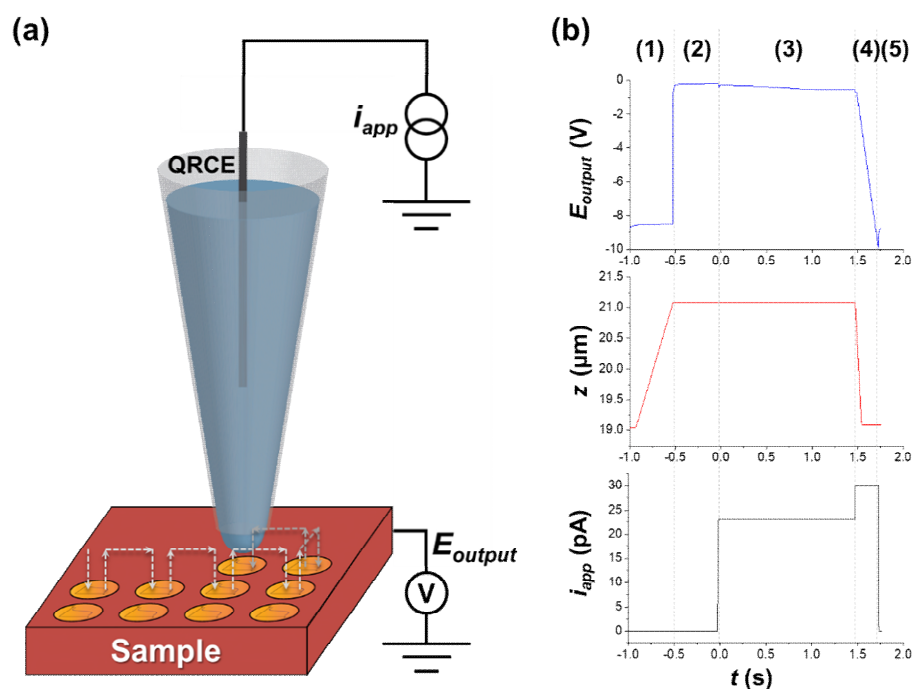
Figure 4.1: (**a**) Schematic of the SECCM configuration deployed in the galvanostatic mode with a single channel pipette probe. The arrows indicate the movement of the probe across substrate (working electrode) surface during a typical scanning protocol. (**b**) Plots showing the variation of three main parameters (z-position of the tip, applied current i_{app}, and output potential of the galvanostat, E_{output}) recorded synchronously during a single hop of a typical scanning experiment. Each individual operation is marked with a number: (**1**) approach; (**2**) meniscus contact; (**3**) current pulse to desired value; (**4**) retract (second current pulse to establish 'overload condition' and; (**5**) movement to the next point. These data were collected under the following experimental conditions: tip diameter *ca.* 400 nm (tip orifice area *ca.* $1.2 \cdot 10^{-9}$ cm², example shown in Figure 2.1c), electrolyte solution 5 mM $[Ru(NH_3)_6]Cl_3$ in 10 mM KCl, performing the $[Ru(NH_3)_6]^{3+/2+}$ process on a GC substrate.

employed instrument, with the sign dependent on the polarity of i_{app}, *i.e.* Figure 4.1b, (**1**)]. E_{output} remains constant at the 'overload' value until the probe makes meniscus contact with the surface (note that the probe itself does not make physical contact with the surface). This is true even when the current is set to 0 pA during the nanopipette approach, as in Figure 4.1b, (**1**) and (**2**).

Once meniscus contact was sensed, E_{output} quickly transitioned to E_{surf} [*i.e.* Figure 4.1b, (**2**)]. This dramatic potential change (several volts) was

135

set as the "feedback threshold" for stopping the *z*-approach of the probe, and starting the chronopotentiometric pulse experiment at a time 0.5 s later. The probe was kept standing at that fixed distance from the surface for the whole duration of the chronopotentiometric analysis, with no feedback during the contact period, as the thermal drift of the system (approximately 0.1 nm/s) was considered to be negligible on the time scale of a single hop of the scan, as assessed in our previous work.[13]

In Figure 4.1b, (**3**) the current was pulsed to 23 pA (see next section for clarifications about the amplitude of the current) and the corresponding potential measured as a function of time. After the chronopotentiometric pulse (duration 1.5 s in Figure 4.1b), the probe was retracted a fixed distance (2 µm) from the surface [*i.e.* Figure 4.1b, (**4**)], before being moved to the next point and E_{output} again adopted the 'overload' condition [*i.e.* Figure 4.1b, (**5**)]. During the retraction, i_{app} was pulsed to a larger value [*e.g.*, 30 pA in Figure 4.1, (**4**)], in order to minimize the time taken for E_{output} to reset to the non-contact or 'overload' value (*i.e.* ±10 V) for the next hop [*i.e.* $dE_{output}/dt \propto i_{app}$ in Figure 4.1, (**4**)].

This methodology, combined with the use of nanopipettes of different sizes (ranging from 150 nm to 800 nm in diameter) has been employed to perform spatially resolved chronopotentiometric measurements in a range of electrochemical systems (*vide supra*) in order to demonstrate the versatility and wide applicability of the chronopotentiometric SECCM technique.

4.3.2. $[Ru(NH_3)_6]^{3+/2+}$ process on glassy carbon

This first system was chosen in order to verify the stability and reproducibility of the confined electrochemical cell in chronopotentiometric conditions, as well as compare the SECCM case with the general theory of controlled current analysis. The $[Ru(NH_3)_6]^{3+/2+}$ electron transfer reaction is a rapid, mechanistically simple, outer-sphere process:[14]

$$[\text{Ru}(\text{NH}_3)_6]^{3+} + e^- \rightleftharpoons [\text{Ru}(\text{NH}_3)_6]^{2+}, \tag{4.1}$$
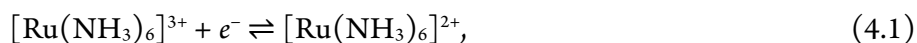
The process has an $E^0 = -\,0.208\text{V}$ vs. Ag/AgCl (sat. KCl) and is well-known to exhibit the characteristics of an ideal, reversible process at most electrode materials, including GC under 'typical' cyclic voltammetric conditions.[15] Thus, this Nernstian process was investigated first at a GC electrode in order to examine the reproducibility of galvanostatic SECCM.

As introduced in Chapter 1, a typical chronopotentiometric curve for a Nernstian process would present a plateau at a potential close to $E^{0'}$ followed by a dramatic change of E at a time $t = \tau$, described by the Sand equation [eq. (1.53)],[16] rearranged here in order to explicit τ:

$$\tau = \pi D \left(\frac{nFC^*}{2I_{app}} \right)^2 \tag{4.2}$$

where C^* is the bulk concentration of $[\text{Ru}(\text{NH}_3)_6]^{3+}$, D is the diffusion coefficient and I_{app} is the applied current density[‡] It has previously been established that radial diffusion makes a significant contribution to mass-transport in the SECCM configuration, with the diffusional flux in SECCM being *ca.* 10% of that expected at the same size microdisc electrode,[17] confirmed herein by performing linear sweep voltammetric experiments, as shown in Figure 4.2. A near steady state voltammogram was obtained at a scan rate of 100 mV s^{-1}, with the steady state limiting cathodic current (i_{ss}) determined to be 24 pA ($I_{ss} = 13.3$ mA cm^{-2}, given a radius of SECCM contact, a, of 2.5×10^{-5} cm estimated by the cross-sectional area of the tip end), which is approximately 15 times smaller than the value expected at the same sized microdisc [given by eq. (1.51)].[18]

[‡] Note that, while i denotes the current, I always refers to the current density ($I = i/A$)
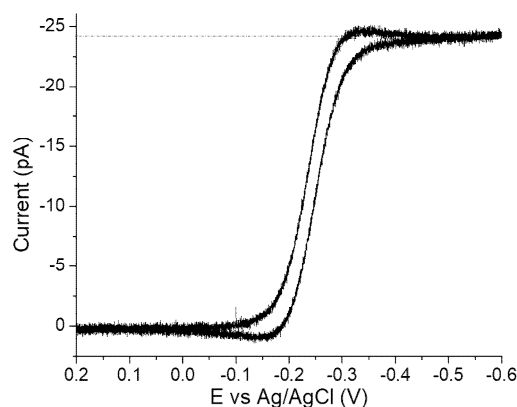
Figure 4.2: Cyclic voltammogram (CV) obtained from a solution of $Ru(NH_3)_6Cl_3$ (5 mM in 10 mM KCl) at a glassy carbon surface in the SECCM format with a 480 nm diameter probe. The CV was recorded in the range $+0.2V \rightarrow -0.6V \rightarrow +0.2V$, at a sweep rate of 100 mVs^{-1}, with a procedure analogous to that described for a single point voltammetric SECCM measure in Chapter 3 (albeit with a single channel probe)

As discussed in section 1.2.2, for a microdisc electrode, if $i_{app}/i_{ss} \gg 1$, the approximate solution for τ can be obtained from eq. (4.2), whereas if i_{app} approaches i_{ss}, the transition time will tend to infinity (see Figure 1.7b).[19-21] This predicted behaviour was verified also in the SECCM configuration by performing chronopotentiometric experiments at a series of increasing i_{app}, as shown in Figure 4.3. In all cases, the current was pulsed from an initial value $i_{app} = 0$ pA (*i.e.* close to OCP) to a particular cathodic current value (ranging in magnitude from 25 to 31pA), always larger than $i_{ss} = 24$ pA in order to see the transition. Typical chronopotentiometric curves are shown in Figure 4.3a. For clarity, the meniscus landing response with 0 pA current is set to negative times and the cathodic pulses start at $t = 0$ s. Immediately after the cathodic current pulse, in all curves, E_{surf} presents a very sharp negative 'spike', before settling at the expected value for the reduction process (assuming a reversible process, justified above) on the millisecond timescale. This potential 'spike' can be attributed to double layer charging and stray capacitance as i_{app} is changed abruptly. As shown in Figure 4.3b, τ becomes much extended as i_{app} approaches i_{ss}, analogous to the case with microdisc electrodes.[19-21] Conversely, τ approaches a more linear behaviour with respect to I_{app}^{-2} at
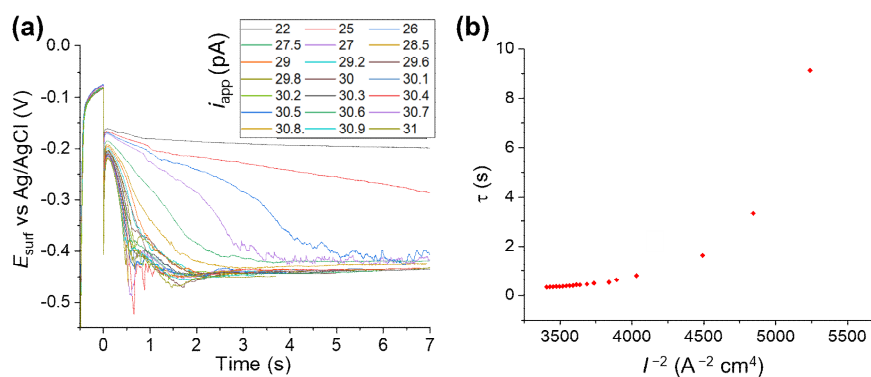
Figure 4.3: (**a**) Single-pulse galvanostatic curves obtained in the SECCM configuration with a solution containing 5 mM $Ru(NH_3)_6^{3+}$ and 10 mM KCl at a GC substrate. For times, $t < 0$ s, $i_{app} = 0$ pA and the current transient corresponds to the landing of the meniscus. At $t = 0$ s, i_{app} was jumped to a value in the range 22 to 31 pA for the cathodic pulse (positive times, indicated on the plot). (**b**) Plot of transition time, τ [calculated from the data in (**a**)] *versus* I_{app}^{-2}. The vertical dotted line in (b) indicates the inverse square of the steady state current density (*i.e.* I_{ss}^{-2}), for $I_{ss} = 13.3$ mA cm^{-2}. In these experiments, the diameter of the nanopipette probe was *ca.* 480 nm.

higher values of i_{app} (shown in Figure 4.3b), analogous to the case with macroscale electrodes (*vide supra*).

It should be noted that the transition becomes broader and less well-defined with decreasing i_{app} (see Figure 4.3a), making it difficult to accurately determine τ. In addition, comparison with theory[19-21] reveals that the values of i_{app} employed herein (up to 31 pA) are too low to observe fully linear τ vs. I_{app}^{-2} behaviour (*i.e.* as predicted by the Sand equation), but it was difficult to apply higher current values, as τ becomes too small in comparison to the timescale of double layer and stray capacitance charging (*vide supra*). For this reason, no further attempt was made to treat the τ vs. I_{app}^{-2} data quantitatively. Finally, it is interesting to note that after the transition, as shown in Figure 4.3a, the $E-t$ curves obtained in the SECCM configuration become relatively noisy and unstable, if compared to the corresponding ones obtained on a macrodisc electrode (not shown). This is probably due to slight instability of the droplet (meniscus) cell during the cathodic process to which the potential transitions (*i.e.* ORR and/or HER).
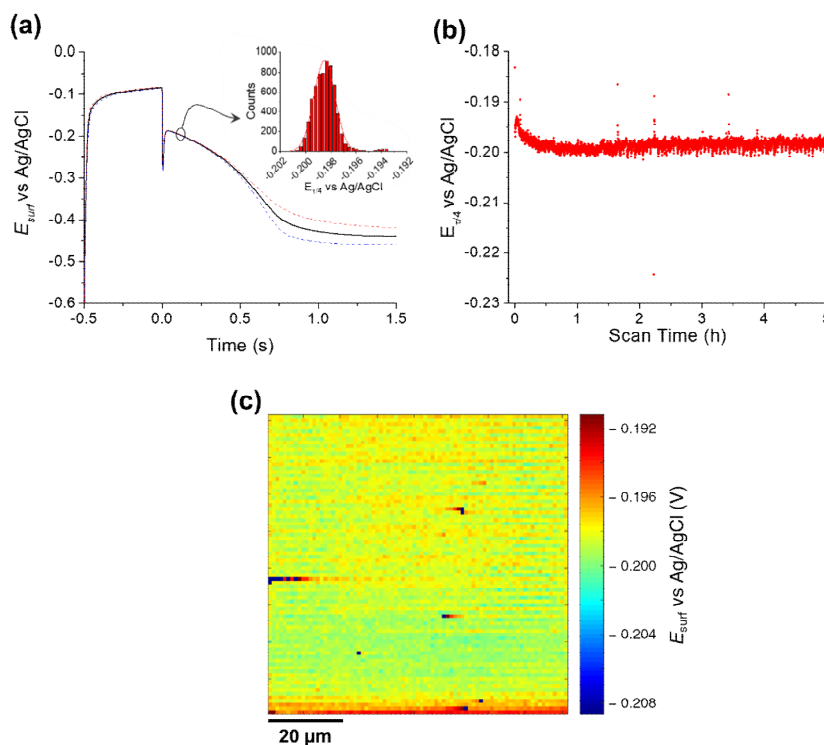
Figure 4.4: (**a**) Average $E-t$ curve ($N = 6561$) obtained from an 81×81 pixel galvanostatic SECCM scan. At each pixel, meniscus landing was achieved with $i_{app} = 0$ pA (OCP) and the current was stepped to $i_{app} = 23$ pA during the cathodic current pulse (set at $t = 0$ s). The standard deviation from measurements at all points is also shown (dotted lines), as well as the statistical analysis of $E_{\tau/4}$ (inset). (**b**) Variation of $E_{\tau/4}$ measured over the *ca.* 5 hour scan time. In these experiments, the diameter of the nanopipette probe was *ca.* 400 nm. (**c**) SECCM surface potential map showing E_{surf} at a time of 0.125 s of the chronopotentiometric transient. The 12 blue spots in (c) correspond to the "false approach" points of the SECCM scan (discussed in section 4.2).

In order to test the reproducibility of the galvanostatic method for long timescale imaging (≈ 5 hours), a scan consisting of 6561 individual $E-t$ experiments (81×81 points, square grid, hopping distance of 1 μm) was carried out on a polished GC electrode. A cathodic chronopotentiometry pulse with $i_{app} = 23$ pA ($I_{app} \approx 15$ mA cm^{-2}) was performed at every point, preceded by 0 pA applied current for meniscus landing on the surface (*i.e.* OCP), with i_{app} chosen to be high enough in relation to i_{ss} to observe the transition (note, the probe used in these experiments was smaller than that used above in Figure 4.3, around 450 nm of diameter, and i_{ss} was lower than the previous probe).

Figure 4.4a plots the average of all recorded *E-t* curves, with a representation of the statistical tolerance at every point. Evidently, the curves are very reproducible prior to the transition ($0 < t < \tau$, *i.e.* during the $[\mathrm{Ru(NH_3)_6}]^{3+/2+}$ process), confirming that the meniscus cell (footprint) is very stable and consistent on this timescale. The first section of the curve ($0 < t < \tau$) was fitted with a typical macroscale potential profile for a Nernstian process [eq. (1.55)] to give values of τ and $E_{\tau/4}$ [equal to $E^{0'}$, assuming $D_{[\mathrm{Ru(NH_3)_6}]^{3+}} = D_{[\mathrm{Ru(NH_3)_6}]^{2+}}$, as shown by eq. (1.56)], of 0.502s $\pm$ 0.001 s and -0.199 V $\pm$ 0.002 V vs. Ag/AgCl (3.4 M KCl), respectively.

In particular, $E_{\tau/4}$ exhibits a very narrow normal distribution, with a standard variation of just $\sigma = 0.002$ V, a testament to the reproducibility of this methodology and the meniscus contact at thousands of different points across the working electrode surface. This is further evident from an analysis of the drift of $E_{\tau/4}$ over the scan time (Figure 4.4b), which changes by only *ca.* -5 mV over the 5 hour timescale, likely attributable to slight drift in the QRCE potential, as previously reported.[22] Finally, an analysis of the $E_{\tau/4}$ map and topography image does not indicate any substantial variation during the scan, as shown in Figure 4.4c. Overall, these results verify the general applicability and reproducibility of SECCM chronopotentiometry, which is expanded to more complex electrochemical systems in the following sections.

4.3.3. $[\mathrm{Ru(NH_3)_6}]^{3+/2+}$ process on aged HOPG

Previous work employing SECCM in tandem with complementary microscopy/spectroscopy techniques has shown that for the $[\mathrm{Ru(NH_3)_6}]^{3+/2+}$ process on "aged" HOPG (exposed to the ambient atmosphere for an extended period before measurements), there was a difference in the $[\mathrm{Ru(NH_3)_6}]^{3+}$ reduction potential between the basal surface and step edge sites, with enhanced electrochemical activity at step edges.[10] Thus, the $[\mathrm{Ru(NH_3)_6}]^{3+/2+}$ process on aged HOPG was investigated as a model system to demonstrate the capability of SECCM
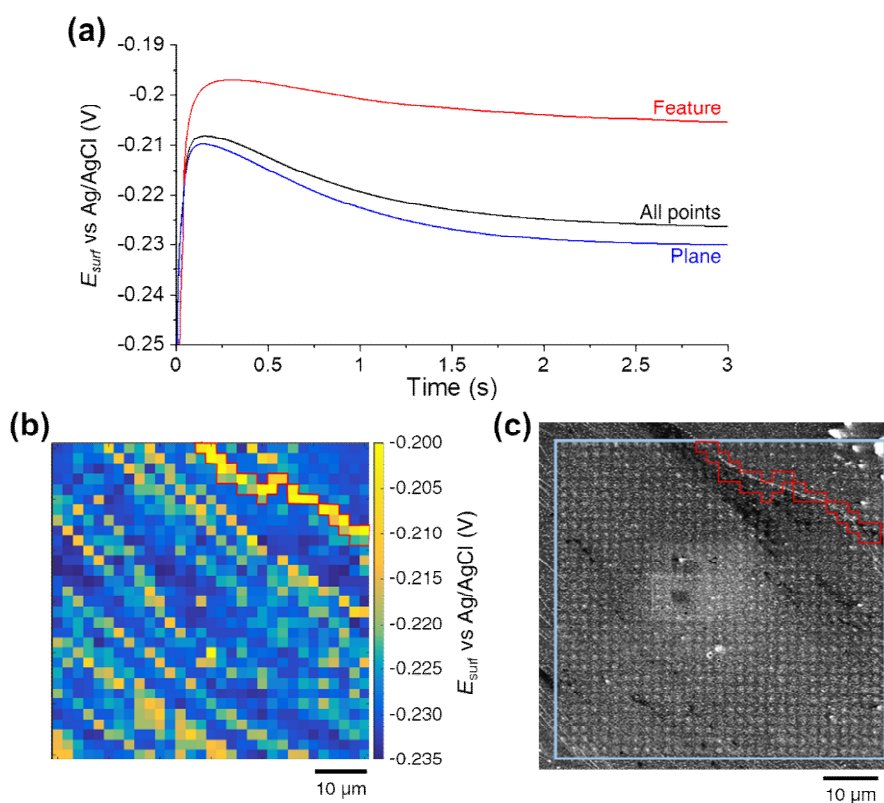
Figure 4.5: **(a)** *E-t* plots for the reduction scan of 5 mM $[Ru(NH_3)_6]^{3+}$ (10 mM KCl supporting electrolyte) on an aged HOPG surface. The plots were obtained by averaging: all points of the scan (black trace); points obtained on the step edge feature [red trace, indicated by the red boxes in **(b)** and **(c)**]; and points obtained at the basal surface (blue trace). All curves were measured with i_{app} = 10 pA, which was maintained consistently throughout the experiment (*i.e.* during each approach and landing). In these experiments, the diameter of the pipette probe was *ca.* 800 nm. **(b)** Map showing E_{surf} at t = 3s. **(c)** SEM image of the same area, with the scan area marked by the blue square.

higher values of i_{app} (shown in Figure 4.3b), analogous to the case with macroscale electrodes (*vide supra*).

A chronopotentiometric scan (961 individual experiments, 31 × 31 points in a square grid, with a hopping distance of 2 μm) was performed on a mechanically exfoliated HOPG substrate that had been aged for 1 hour prior to use. In these experiments the cathodic current, I_{app} = 1.5 mA cm^{-2} (i_{app} = 10 pA), was selected to be only *ca.* 15% of I_{ss} ($I_{ss} \approx$ 10 mA cm^{-2}) as the aim was to quantify the activity for the $[Ru(NH_3)_6]^{3+/2+}$ process, and so measuring τ was not necessary. In addition, a relatively long

pulse time of 3 s was employed in order to ensure the electrochemical process achieved steady state (*vide supra*).

A summary of key results is shown in Figure 4.5. Figure 4.5a shows the average of all the galvanostatic curves ($N = 961$) collected on the aged HOPG surface. In agreement with the results above, the *E-t* curve initially exhibits a sharp negative spike on the millisecond timescale (charging) before settling on the expected waveshape for this kind of system, *i.e.* a plateau with an E_{surf} value close to (but not equal to) E^0, as discussed earlier. A spatially resolved electrode potential map of the HOPG surface was constructed by plotting E_{surf} measured after 3 s vs. *x-y* position, as shown in Figure 4.5b. Clearly, the basal surface possesses relatively uniform activity (blue areas in the map), with a series of "high activity" features running diagonally across the scan area, revealed to be step edges through co-located imaging with scanning electron microscopy, SEM (image shown in Figure 4.5c). Note that these features were too small to identify from the SECCM topographical map recorded synchronously with the electrochemical data, which just appeared as a relatively flat and featureless surface (not shown), due to the size of the pipette probe used (*vide supra*). The most prominent feature (likely the largest multilayer step edge), set in the top right corner of the scan area exhibits a potential that is, on average, 21 mV more positive than the one of the surrounding plane (ranging from +13 mV at the beginning to +24 mV at the end of the pulse), indicating that the electrochemical reaction proceeds more readily at the step edge, for reasons outlined in detail elsewhere.[10]

4.3.4. HER on MoS₂ natural crystals

MoS$_2$ is a promising low-cost, earth-abundant electrocatalyst for HER.[23,24] The sample used herein was naturally occurring molybdenite (2H phase), a layered crystalline semi-conductor with a surface consisting of extended basal planes interrupted by step edge defects of variable

height (monoatomic to several multi-layer, tens of nm in size). It is generally accepted that the basal plane of MoS_2 (2H phase) is a relatively inactive HER catalyst, while the step edge possesses high catalytic activity, established from theoretical and experimental standpoints.[4,25] Recent voltammetric SECCM studies mapped the electrocatalytic activity of molybdenite, revealed uniform electrocatalytic activity at the basal plane (on the μm length scale) and enhanced activity at the step edge.[26-28]

As alluded to above, chronopotentiometry presents a very facile route for benchmarking catalytic materials *(i.e.* determining the overpotential required for a given current density, at particular locations of the surface, with high spatial-resolution). Besides, it allows the measurement to be carried out at a very small current density *(i.e.* the "foot of the wave", where the reaction is purely surface-controlled) compared to the current densities that are generally measured in potential-controlled methods, thus opening up a new dynamic (lower current density) range for electrocatalytic imaging, as will be demonstrated here. For these measurements a current density of 2 mA cm^{-2} (i_{app} = 0.628 pA, with a 150 nm diameter probe, assuming that the wetted area is the same size as the probe dimensions, as previously reported[27]) was used on a mechanically exfoliated MoS_2 crystal in 0.1 M $HClO_4$; a pulse of 0.5s was applied to every point, giving an average rate of acquisition of 0.75s per point (taking into account the time of approach, retract and lateral movement), which is comparable with the scan rate achieved in potential-controlled SECCM work on the same system.[26]

The main results of the chronopotentiometric scan are shown in Figure 4.6. The topographical map shown in Figure 4.6a, constructed directly from the *z*-approach data collected during the SECCM experiment, reveals that the scan area is predominantly on the basal plane, with large, multilayer step edges (tens of nm in size) present in the top-left and top-right corners. Comparing the topographical map with the spatially
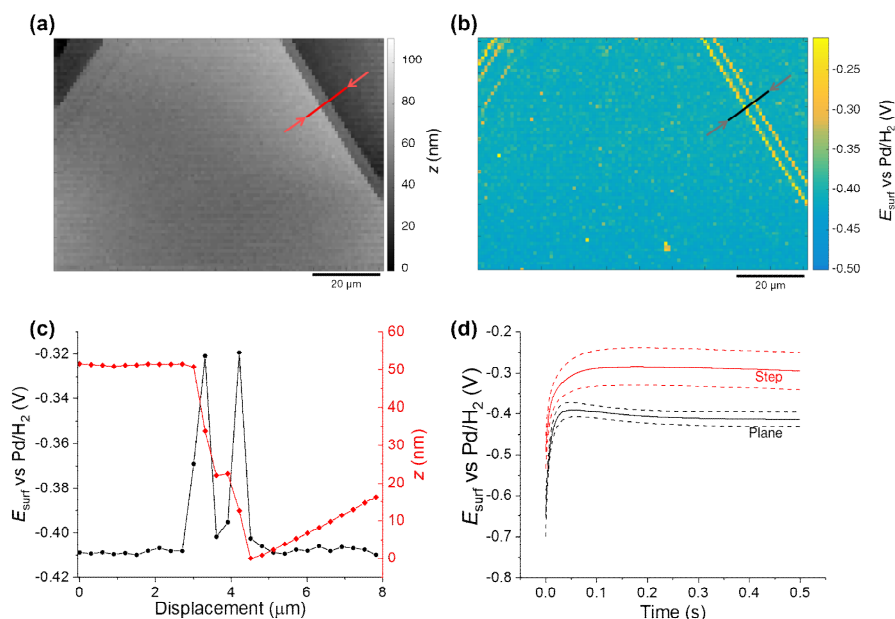
Figure 4.6: SECCM **(a)** topographical and **(b)** galvanostatic (E_{surf} at 0.3 s) electrochemical activity maps obtained from 0.1 M HClO$_4$ solution, visualizing HER activity at the surface of MoS$_2$. **(c)** Line scan profiles of topography (red trace) and E_{surf} (black trace), obtained at the lines indicated in **(a)** and **(b)**, respectively. **(d)** Average E–t curves obtained at the basal plane (black trace) and two step-edge features located in the top-right corner of the scan area (red trace). Standard deviations are also represented (dashed lines). In these experiments, the diameter of the nanopipette probe was *ca.* 150nm.

resolved chronopotentiometric map (constructed at 0.3 s, where the curve stabilizes) in Figure 4.6b confirms the aforementioned heterogeneity between the basal plane and step edges, with more positive potentials (*i.e.* smaller overpotentials) measured at the latter. As shown in Figure 4.6c, line-scan profiles of z-height and E_{surf} further demonstrate that the sites of enhanced activity are located on the multistep surface features (*i.e.* defects sites where the step edge is exposed).

Average E–t curves shown in Figure 4.6d reveal that the basal plane possesses a uniform activity on this length scale, with an average E_{surf} of −413 mV ± 18 mV vs. Pd/H$_2$ at the end of the pulse. In addition, the average E_{surf} taken from the two large features located on the top-right of the map (see Figure 4.6d, red solid line) is − 295 mV ± 46 mV vs. Pd/H$_2$, again demonstrating accelerated HER kinetics at the exposed step edge.
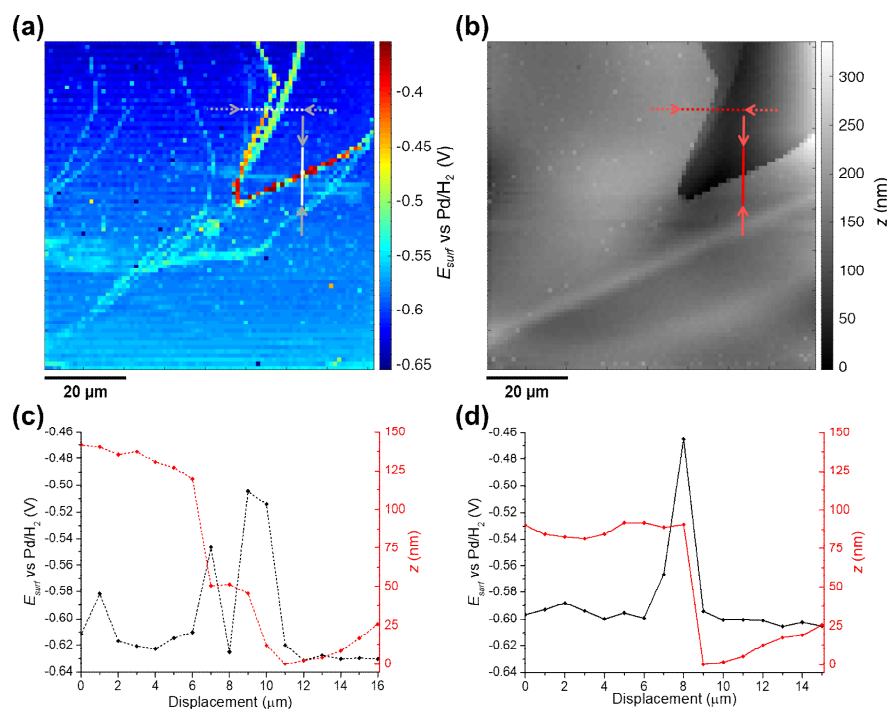
Figure 4.7: Chronopotentiometric scan of an MoS_2 surface, performed with a probe of 820 nm diameter filled with 0.1M $HClO_4$ solution. A chronopotentiometric current i_{app}=10.6 pA was employed. (**a**) Surface potential (E_{surf}) map at 0.2s after the pulse current application. (**b**) Synchronously recorded SECCM topographical map. (**c,d**) Line scan profiles of topography (red traces) and E_{surf} (black trace), obtained at the lines indicated in (a) and (b), as either dotted lines (plotted in **c**) or continuous lines (plotted in **d**).

It is worth noting that the red $E{-}t$ curve arises from an area comprised of both basal and step edge, with the size of the feature determining the basal:edge ratio in the probed area (*i.e.* the step edge activity was not measured in isolation). This is why the activity enhancement (evidenced by the shift in E_{surf}) scales with step size, with bigger steps appearing to be being more active than the smaller ones, down to levels below the sensitivity of SECCM topography, as shown in Figure 4.7 for a scanned area with multiple sized steps (see comparison between Figure 4.7a and b). Given that the geometry of the step-edge features are known from the topographical map, step edge activity could be estimated directly, following the procedure similar to that outlined in previous work,[27] although this was beyond the scope of this proof of concept.

It is worth remarking that the analysis carried out above has allowed catalytic activity to be probed directly by simply applying a current of 0.628 pA (*ca.* 2 mA cm^{-2}), which is considerably lower than the average currents measured with the voltammetric (*e.g.,* potential-controlled) techniques utilized in previous studies (up to – 1 V VS RHE and 60pA with a 50 nm diameter tip).[7,27,29,30] Compared to a typical SECCM LSV experiment , such current and potentials will fall in the very early foot of the reduction wave, where the distinction between the activity of planes and edges is quite difficult due to the current being very close to noise level of the electrochemical instrumentation. This is one major advantage of the galvanostatic approach, as this and similar analyses can be carried out without significantly polarizing the substrate (working electrode) surface.

4.4. CONCLUSIONS

SECCM was deployed in the current-controlled (galvanostatic or chronopotentiometric) mode to interrogate electrochemical systems of increasing complexity. Firstly, the analysis of the electrochemically reversible $[Ru(NH_3)_6]^{3+/2+}$ process at a homogeneous surface (on the scale of the SECCM probe), polished GC, demonstrated that the meniscus cell configuration is sufficiently stable when operated in the current-controlled mode, with a consistent electrochemical response ($E_{\tau/4} = -0.210 \pm 0.002$ V vs. Ag/AgCl) recorded over an extended experimental timescale (over 5 hours, and over 6000 individual points). Further analysis of the same process on an aged HOPG surface revealed that subtle differences in activity, enhanced at the step edge relative to the basal plane (*ca.* 20 mV difference in E_{surf}), could be detected readily with high sensitivity. Finally, the optimized setup was applied to study the activity of an electrocatalytic surface, proving the efficacy of galvanostatic techniques for "benchmarking" catalytic activity by measuring the overpotential at a given current density. Enhanced catalytic activity towards the HER was

measured at the step edge of MoS_2 relative to the basal plane, revealed directly by comparing the synchronously obtained E_{surf} and topographical "maps".

Remarkably, high sensitivity and resolution were achieved in both the topographical and electrochemical images, despite the application of a very small current (< 1 pA), avoiding significant polarization or damage of the sample. It follows that this approach should allow the study of the surface dependency of processes that would be difficult to examine in potential-controlled mode, due to the occurrence of other higher current processes at nearby potentials, such as for example, the ubiquitous interference of the HER with electrochemical CO_2 reduction (ECR) in aqueous electrolytes.[31,32] This is also an important consideration, for example, in the study of corrosion-related processes, where small changes in potential can change the active dissolution current by orders of magnitude, resulting in significant damage to the material under examination.[33] The use of chronopotentiometric SECCM in corrosion studies will be the main topic of the next chapter. Overall, the work presented here opens up promising new applications of galvanostatic techniques at the nanoscale level, including to fields where current-controlled methods are typically applied, such as electroplating or energy storage materials characterization, and where the high spatial resolution of SECCM could be very powerful in elucidating structure-activity correlations.

4.5. REFERENCES

[1] Ali, G. A. M.; Yusoff, M. M.; Ng, Y. H.; Lim, H. N.; Chong, K. F. Potentiostatic and galvanostatic electrodeposition of manganese oxide for supercapacitor application: A comparison study. *Curr. Appl. Phys.* **2015,** *15* (10), 1143-1147.

[2] Talaie, E.; Bonnick, P.; Sun, X.; Pang, Q.; Liang, X.; Nazar, L. F. Methods and Protocols for Electrochemical Energy Storage Materials Research. *Chem. Mater.* **2017,** *29* (1), 90-105.

[3] Martínez-Paredes, G.; González-García, M. B.; Costa-García, A. In situ electrochemical generation of gold nanostructured screen-printed carbon electrodes. Application to the detection of lead underpotential deposition. *Electrochim. Acta* **2009,** *54* (21), 4801-4808.

[4]   Benck, J. D.; Hellstern, T. R.; Kibsgaard, J.; Chakthranont, P.; Jaramillo, T. F. Catalyzing the Hydrogen Evolution Reaction (HER) with Molybdenum Sulfide Nanomaterials. *ACS Catal.* **2014,** *4* (11), 3957-3971.

[5]   Anantharaj, S.; Ede, S. R.; Karthick, K.; Sam Sankar, S.; Sangeetha, K.; Karthik, P. E.; Kundu, S. Precision and correctness in the evaluation of electrocatalytic water splitting: revisiting activity parameters with a critical assessment. *Energy Environ. Sci.* **2018,** *11* (4), 744-771.

[6]   Tao, B.; Yule, L. C.; Daviddi, E.; Bentley, C. L.; Unwin, P. R. Correlative Electrochemical Microscopy of Li-Ion (De)intercalation at a Series of Individual LiMn2 O4 Particles. *Angew. Chem. Int. Ed.* **2019,** *58* (14), 4606-4611.

[7]   Takahashi, Y.; Kumatani, A.; Munakata, H.; Inomata, H.; Ito, K.; Ino, K.; Shiku, H.; Unwin, P. R.; Korchev, Y. E.; Kanamura, K.et al. Nanoscale visualization of redox activity at lithium-ion battery cathodes. *Nat. Commun.* **2014,** *5*, 5450.

[8]   Snowden, M. E.; Dayeh, M.; Payne, N. A.; Gervais, S.; Mauzeroll, J.; Schougaard, S. B. Measurement on isolated lithium iron phosphate particles reveals heterogeneity in material properties distribution. *J. Power Sources* **2016,** *325*, 682-689.

[9]   Harris, P. J. F. Fullerene-related structure of commercial glassy carbons. *Philos. Mag.* **2004,** *84* (29), 3159-3167.

[10]   Güell, A. G.; Cuharuc, A. S.; Kim, Y.-R.; Zhang, G.; Tan, S.-y.; Ebejer, N.; Unwin, P. R. Redox-Dependent Spatially Resolved Electrochemistry at Graphene and Graphite Step Edges. *ACS Nano* **2015,** *9* (4), 3558-3571.

[11]   Chen, C.-H.; Jacobse, L.; McKelvey, K.; Lai, S. C. S.; Koper, M. T. M.; Unwin, P. R. Voltammetric Scanning Electrochemical Cell Microscopy: Dynamic Imaging of Hydrazine Electro-oxidation on Platinum Electrodes. *Anal. Chem.* **2015,** *87* (11), 5782-5789.

[12]   Bentley, C. L.; Kang, M.; Unwin, P. R. Scanning electrochemical cell microscopy: New perspectives on electrode processes in action. *Curr. Opin. Electrochem.* **2017,** *6* (1), 23-30.

[13]   McKelvey, K.; Kinnear, S. L.; Perry, D.; Momotenko, D.; Unwin, P. R. Surface charge mapping with a nanopipette. *J. Am. Chem. Soc.* **2014,** *136* (39), 13735-13744.

[14]   Bard, A. J.; Faulkner, L. R. *Electrochemical Methods: Fundamentals and Applications*; John Wiley and Sons Inc., 2001.

[15]   Schmickler, W.; Santos, E. *Interfacial Electrochemistrty*; 2 ed.; Springer, Berlin, Heidelberg, 2010.

[16]   Sand, H. J. S. III. On the concentration at the electrodes in a solution, with special reference to the liberation of hydrogen by electrolysis of a mixture of copper sulphate and sulphuric acid. *Philos. Mag.* **1901,** *1* (1), 45-79.

[17]   Snowden, M. E.; Güell, A. G.; Lai, S. C. S.; McKelvey, K.; Ebejer, N.; O'Connell, M. A.; Colburn, A. W.; Unwin, P. R. Scanning Electrochemical Cell Microscopy: Theory and Experiment for Quantitative High Resolution Spatially-Resolved Voltammetry and Simultaneous Ion-Conductance Measurements. *Anal. Chem.* **2012,** *84* (5), 2483-2491.

[18]   Saito, Y. A Theoretical Study on the Diffusion Current at the Stationary
       Electrodes of Circular and Narrow Band Types. *Rev. Polarogr.* **1968,** *15* (6),
       177-187.

[19]   Aoki, K.; Akimoto, K.; Tokuda, K.; Matsuda, H.; Osteryoung, J.
       Chronopotentiometry at very small stationary disk electrodes. *J. Electroanal.
       Chem. Interf. Electrochem.* **1985,** *182* (2), 281-294.

[20]   Fleischmann, M.; Pons, S. The behavior of microdisk and microring electrodes.
       Mass transport to the disk in the unsteady state: Chronopotentiometry. *J.
       Electroanal. Chem. Interf. Electrochem.* **1988,** *250* (2), 257-267.

[21]   Abrantes, L. M.; Fleischmann, M.; Li, L. J.; Hawkins, M.; Pons, J. W.;
       Daschbach, J.; Pons, S. The behavior of microdisk electrodes:
       Chronopotentiometry and linear sweep voltammetric experiments. *J.
       Electroanal. Chem. Interf. Electrochem.* **1989,** *262* (1), 55-66.

[22]   Bentley, C. L.; Perry, D.; Unwin, P. R. Stability and Placement of Ag/AgCl
       Quasi-Reference Counter Electrodes in Confined Electrochemical Cells. *Anal.
       Chem.* **2018,** *90* (12), 7700-7707.

[23]   Hinnemann, B.; Moses, P. G.; Bonde, J.; Jørgensen, K. P.; Nielsen, J. H.; Horch,
       S.; Chorkendorff, I.; Nørskov, J. K. Biomimetic Hydrogen Evolution: MoS2
       Nanoparticles as Catalyst for Hydrogen Evolution. *J. Am. Chem. Soc.* **2005,** *127*
       (15), 5308-5309.

[24]   Jaramillo, T. F.; Jørgensen, K. P.; Bonde, J.; Nielsen, J. H.; Horch, S.;
       Chorkendorff, I. Identification of Active Edge Sites for Electrochemical
       H_2 Evolution from MoS_2 Nanocatalysts. *Science*
       2007, *317* (5834), 100.

[25]   Seh, Z. W.; Kibsgaard, J.; Dickens, C. F.; Chorkendorff, I.; Nørskov, J. K.;
       Jaramillo, T. F. Combining theory and experiment in electrocatalysis: Insights
       into materials design. *Science* **2017,** *355* (6321).

[26]   Bentley, C. L.; Kang, M.; Unwin, P. R. Nanoscale Structure Dynamics within
       Electrocatalytic Materials. *J. Am. Chem. Soc.* **2017,** *139* (46), 16813-16821.

[27]   Bentley, C. L.; Kang, M.; Maddar, F. M.; Li, F.; Walker, M.; Zhang, J.; Unwin,
       P. R. Electrochemical maps and movies of the hydrogen evolution reaction on
       natural crystals of molybdenite (MoS2): basal vs. edge plane activity. *Chem. Sci.*
       2017, *8* (9), 6583-6593.

[28]   Tao, B.; Unwin, P. R.; Bentley, C. L. Nanoscale Variations in the
       Electrocatalytic Activity of Layered Transition-Metal Dichalcogenides. *J. Phys.
       Chem. C* **2020,** *124* (1), 789-798.

[29]   Bentley, C. L.; Andronescu, C.; Smialkowski, M.; Kang, M.; Tarnev, T.; Marler,
       B.; Unwin, P. R.; Apfel, U.-P.; Schuhmann, W. Local Surface Structure and
       Composition Control the Hydrogen Evolution Reaction on Iron Nickel
       Sulfides. *Angew. Chem. Int. Ed.* **2018,** *57* (15), 4093-4097.

[30]   Mariano, R. G.; McKelvey, K.; White, H. S.; Kanan, M. W. Selective increase in
       CO_2 electroreduction activity at grain-boundary surface terminations. *Science*
       2017, *358* (6367), 1187.

[31]   Ooka, H.; Figueiredo, M. C.; Koper, M. T. M. Competition between Hydrogen
       Evolution and Carbon Dioxide Reduction on Copper Electrodes in Mildly

Acidic Media. *Langmuir* **2017,** *33* (37), 9307-9313.

[32] Cave, E. R.; Shi, C.; Kuhl, K. P.; Hatsukade, T.; Abram, D. N.; Hahn, C.; Chan, K.; Jaramillo, T. F. Trends in the Catalytic Activity of Hydrogen Evolution during CO2 Electroreduction on Transition Metals. *ACS Catal.* **2018,** *8* (4), 3035-3040.

[33] Esmaily, M.; Svensson, J. E.; Fajardo, S.; Birbilis, N.; Frankel, G. S.; Virtanen, S.; Arrabal, R.; Thomas, S.; Johansson, L. G. Fundamentals and advances in magnesium alloy corrosion. *Prog. Mater Sci.* **2017,** *89*, 92-193.

Chapter 5

Grain Dependent Cu Corrosion

T his is the first of the three chapters dedicated to the study of the corrosion and corrosion protection of copper within a nanoscale droplet cell. The discussion initiated in Chapter 4 opened up interesting possibilities for the use of chronopotentiometric SECCM in corrosion measurements. The present contribution is a direct evolution of such discussion. Besides, this work does not have chronopotentiometry as a sole innovation, but is aimed at expanding nanoscale electrochemical studies to a metal/aqueous nanodroplet/oil three-phase system, and further visualise the grain dependent corrosion processes on a wider range of grains, thus gaining a more comprehensive view of the critical process(es). This latter innovation will be further expanded during the voltammetric studies described in Chapter 6 and Chapter 7.

5.1. INTRODUCTORY REMARKS

The impact and importance of corrosion studies has been broadly discussed in Chapter 1 (section 1.4.2), highlighting how electrochemical techniques, allied to complementary analytical and microscopy methods, play a central role in unveiling corrosion and corrosion protection mechanisms.[1-5] However, a limitation of many experimental approaches is that

the electrochemical perturbation (and measurement) is applied globally at a macroscopic electrode immersed in a bulk solution,[6] but most corrosion processes are initiated and perpetuated at (sub)microscopic surface sites (*e.g.*, grain boundaries, inclusions, microscratches etc.).[7-12] Mismatch between the scale of key corrosion phenomena and conventional electrochemical methods makes it difficult to unambiguously identify the key anodic/cathodic sites driving corrosion. This issue is compounded for the case of atmospheric corrosion,[13] or corrosion in certain automotive/industrial environments (*vide infra*),[14,15] which take place due to the action of small droplets on the surface in a confined system.

The possibility of SECCM of mapping electrochemistry locally and directly *via* a nanoscale electrochemical meniscus cell,[16-20] and its combination with co-located crystallographic orientation measurements (EBSD), has permitted the study of various electrochemical processes at a range of polycrystalline materials, with some important corrosion applications.[21-25] As exemplified in Chapter 1, section 1.4.2 for Ref. [22], the analysis of polycrystalline surfaces has involved, so far, mainly the specific comparison of selected grains, usually representative of the low index gains of the crystallographic system of the material of interest. This approach, despite producing very interesting and important results, is relatively limiting of the capabilities of SECCM, which is able to perform analysis on a wide range of surface orientations within a single analysis. Besides, sometimes the most active and interesting grains in electrochemistry are far from the low-energy planar structures of low index grains, so it would be interesting to gain a full spectrum view of the electrochemical activity/surface structure relationship.

In addition to its high spatiotemporal resolution in surface/electrochemistry characterisation, the meniscus cell configuration of SECCM facilitates rapid reactant/product exchange with the surrounding environment, mimicking a gas diffusion electrode, with an enhanced flux of

gases into the meniscus cell (*i.e.* at the three-phase boundary).[26-28] When operated in air, SECCM emulates the configuration of atmospheric corrosion, with gas exchange (*e.g.*, oxygen, O_2) taking place across the liquid/gas interface of the meniscus in contact with a surface of interest. As recently reported, and expanded upon herein, SECCM can also be operated under oil immersion,[24,25] which not only aids in confinement of the meniscus cell during prolonged measurements,[25] but also opens up the possibility of studying the effect of oil-soluble species (*e.g.*, corrosion inhibitors, organic contaminants, redox mediators etc.) on local reactions at the solid/liquid/liquid interface with high spatial-resolution. This configuration is regaining interest for fundamental studies,[29,30] as well as being of great practical importance (*e.g.*, phase-transfer reactions in industrial chemical processes, biology etc.).[31]

In Chapter 4, the versatility of chronopotentiometry in the confines of the meniscus cell of the SECCM configuration was demonstrated; here that knowledge is translated into local corrosion measurement. First, it is possible to make meniscus contact at zero applied current, corresponding to OCP, which is measured. This corresponds to the corrosion (mixed) potential, where the rate of anodic dissolution of the metal (forming metal ions) and the rate of reduction of oxygen are balanced. Surface ion release under this condition is then analysed by subsequent "electrochemical titration" of a portion of the released metal ions, by applying a cathodic current and recording the resulting chronopotentiometric curve. This allows the evaluation of intrinsic corrosion susceptibility, *in situ*, with high spatial-resolution, for the entire range of crystallographic orientations of a polycrystalline metal (co-located EBSD analysis). Chronopotentiometry measurements with and without O_2 present, and the use of an anodic pulse to induce the anodic dissolution (as well as the cathodic measurements mentioned) allow all the key electrochemical processes underpinning localised corrosion to be studied. The patterns

of surface reactivity establish the intimate link between corrosion susceptibility, electrochemical kinetics and surface structure at the nanoscale.

5.2. EXPERIMENTAL DETAILS

All techniques employed in this work are commonly used in SECCM studies and shared between chapters in this thesis, therefore their main setup description is included in the General Methods (Chapter 2). However, since the use of SECCM in triple-phase environment and the cross-correlation between SECCM and EBSD is firstly introduced, it is useful to give some specifics about such methods for the present work.

5.2.1. Triple-phase SECCM

The SECCM setup employed in this work is shown in Figure 5.1. All SECCM experiments were carried out with a single channelled pipette filled with a 10 mM H_2SO_4 solution (pH $\approx$ 1.9) and equipped with an Ag/AgCl QRCE, on a polycrystalline Cu sample (preparation described in section 2.1.2). After positioning the sample and the probe on the instrument (such as the probe tip was at $\approx$ 1 mm form the surface) a layer of dodecane was placed onto the Cu substrate to a thickness that also covered the tip of the SECCM probe, and confined using a chemically-resistant epoxy resin well, as schematised in Figure 5.1 (the two elements are labelled *e* and *f,* respectively). Unless otherwise stated, the dodecane layer was exposed to the ambient air, meaning that O_2 was present in the SECCM droplet cell. In the limited cases where an O_2-free environment was needed, an environmental cell was used, through which Argon was flowed for at least an hour before and during experiment, as outlined in previous contributions[24,32] and described more in detail in Chapter 6.

The SECCM experiments were performed in the chronopotentiometric mode, with a "hopping mode" imaging protocol, employing a home-built sensitive galvanostat with an ultralow input bias current, as introduced in the last chapter. The pipette was approached with a current set
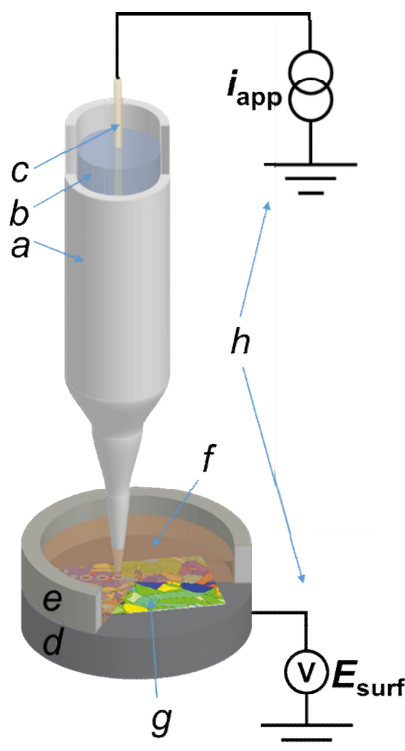
Figure 5.1: Scheme (not to scale) of the SECCM three-phase (Cu/aqueous/dodecane) setup employed in this work. The main components of the system are: **a** nanopipette probe; **b** electrolyte solution (H₂SO₄ 10 mM); **c** QRCE connected to the galvanostat; **d** conductive carbon mounting for the sample, connected to the voltage measuring device; **e** epoxy resin well to contain dodecane; **f** dodecane layer covering **g** the polycrystalline copper (working electrode) surface and; **h** homebuilt galvanostat and potential measuring device.

to be zero (within the sensitivity range of the galvanostat, which had an instrumental error of ± 6 fA) so that upon meniscus contact, the recorded potential was effectively the mixed corrosion potential, measured in conditions of net zero-current. This potential approximates closely to the OCP and it will be referred to as such, for brevity, noting its equivalence to the mixed corrosion potential. After the OCP measurement step, a chronopotentiometric pulse measurement was then performed to a desired value of applied current and the potential-time profile recorded for a defined period. Subsequently, the nanopipette probe was retracted from the surface and moved laterally to begin the approach to the next point. The nanopipette translation speeds were 5 μm s⁻¹ on approach, 20

μm s^{-1} on retract (by 1.5 μm) and 30 μm s^{-1} during lateral movement. The distance between each pixel (*i.e.* the hopping distance) was 1 μm, larger than the diameter of the area wetted by the meniscus cell (*vide infra*), so as to ensure that each point measurement was independent of the last. At the beginning of each approach, the potential was set to the "overload" value of the FPGA card (+10 V). A detectable decrease of more than 5 V from this value was set as the threshold to indicate when the meniscus had made contact with the surface.

The chronopotentiometric pulse data collected at each position were organised in order to create time-dependent two-dimensional maps (Movies A4 to A6) of the recorded local working electrode potential as a function of time (*i.e.* an electrochemical movie of E_{surf} in the imaged region as a function of time, where E_{surf} is the surface potential measured during SECCM). The current (i_{app}) was applied at the QRCE and E_{surf} was measured at the substrate (working electrode). The transition time (τ) was calculated at each pixel of Movies A5 and A6 by finding the time of the inflection point of the chronopotentiometric curve during the cathodic pulse. Each electrochemical movie was collected on different spots of the same Cu sample. Two different nanopipette probes were employed for the anodic scan (Movie A4) and the cathodic scans (Movies A5 and A6, collected subsequently).

5.2.2. Correlated electron microscopy characterisation

SEM imaging was employed to measure the contact area of the meniscus cell with polycrystalline Cu, by evaluating the size the of footprints left on the surface after the measurements; the measured diameters (precision better than ± 50 nm) were ≈ 600 nm (wetted area ≈ 1.6 × 10^{-9} cm^2) for the anodic pulse experiments herein and ≈ 900 nm (wetted area ≈ 6.4 × 10^{-9} cm^2) for the cathodic pulse experiments (Appendix, section A.4.1). These aerial values were used to calculate applied current densities. Importantly, there was no noticeable influence of surface microstructure on

the degree of wetting (Appendix, section A.4.1) for any particular experimental run. Furthermore, the consistency of SECCM potential data within areas of the same surface structure, and for different times within an imaging run, indicates the consistency of the meniscus contact.

EBSD mapping was carried out as reported in section 2.5.3, on the same areas of the SECCM analysis, after the electrochemical experiment was performed. The raw data were elaborated in order to obtain the average orientation parameters for each considered grain, and the grain boundary map extracted from EBSD mapping was employed for identify each grain activity on the electrochemical maps. This correlation allowed to divide each electrochemical image into subsets corresponding to each single grain measured by EBSD (except the ones that corresponded to less than 1 pixel in the SECCM map), and carry statistical analysis on them.

5.3. RESULTS AND DISCUSSION

5.3.1. Copper electrochemistry in H_2SO_4 (pH 2): macroscale vs microscale.

Consulting the phase stability (potential/pH) diagram for copper,[33] only one anodic reaction is possible at pH $\approx$ 2: the oxidation of Cu to form the soluble cupric ion (Cu^{2+}):

$$Cu_{(s)} \rightarrow Cu^{2+} + 2e^{-} \tag{5.1}$$
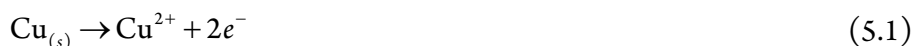
which has a standard electrode potential $E^0 = 0.134$ V vs Ag/AgCl (3.4 M KCl). This process in eq. (5.1) is referred to as the Cu/Cu^{2+} process, herein. Note that although eq. (5.1) shows an overall 2 electron process, this is an oversimplification of the Cu oxidation process, which under most conditions occurs through the intermediate, $Cu(I)_{ads}$, formed through coupled interfacial (electro)chemical reactions with complexing agents (*e.g.* Cl^- or SO_4^{2-}) or O_2, in solution.[34-37] An example of such reaction is the oxidation of the Cu(I) intermediate by the dissolved oxygen:

$$\text{Cu(I)}_{ads} + \frac{1}{2}\text{O}_2 \rightarrow \text{Cu}^{2+} + \frac{1}{2}\text{H}_2\text{O}_2 \,, \tag{5.2}$$
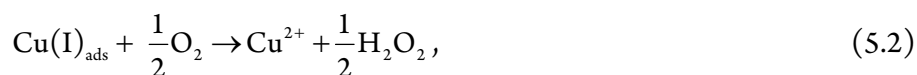
which is thought to play a fundamental role in Cu dissolution in aerated acidic conditions.[37,38] Indeed, stable Cu(I)_{ads} intermediates can be observed at pH > 5,[33] in copper oxides, hydroxides or oxyhydroxides (collectively referred to as CuO_x, herein), but these species are not thermodynamically stable at pH 2, given the following reaction:

$$\text{CuO}_x + (2x)\text{H}^+ \rightarrow \text{Cu}^{2+} + x\text{H}_2\text{O} \tag{5.3}$$

although they may well play a role in multi-step Cu electrodissolution.

A few cathodic processes need to be considered for the defined conditions, the most obvious being the ORR [eq. (5.4)] and the HER [eq. (5.5)]:

$$\text{O}_2 + 2\text{H}^+ + 2e^- \rightarrow \text{H}_2\text{O}_2 \tag{5.4}$$

$$2\text{H}^+ + 2e^- \rightarrow \text{H}_2 \tag{5.5}$$
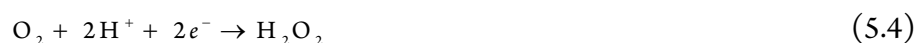
which have an E^0 of, respectively, + 0.322 V and − 0.323 V vs Ag/AgCl (3.4 M KCl) at pH = 2. Note that in acidic media, the ORR reportedly follows the $2e^-$ pathway to form H_2O_2 as the main product.[37,39] From the E^0 values of Eqs. (5.1) and (5.4), Cu dissolution occurs spontaneously upon immersion in aerated solution (pH ≈ 2), as per the following equation:

$$\text{Cu} + \text{O}_2 + 2\text{H}^+ \rightarrow \text{Cu}^{2+} + \text{H}_2\text{O}_2 \tag{5.6}$$

Eq. (5.6) is the Cu corrosion reaction that occurs at the OCP. Thus, for the conditions of the present measurements, a third cathodic process that needs to be considered is the electrodeposition of Cu^{2+} [liberated during eq. (5.6)] to $\text{Cu}_{(s)}$ [*i.e.* the reverse of eq. (5.1)], referred to as the Cu^{2+}/Cu process, herein. The important role of $\text{HSO}_4^-/\text{SO}_4^{2-}$ through surface complexation, as well as the intercalation of these ions within Cu adlayers during the deposition process, has been previously highlighted.[40-43]

Constant current chronopotentiometry is a powerful approach for separating electrochemical processes that occur at similar potentials [*e.g.*, Eqs. (5.1), (5.4) and (5.5)].[44] As highlighted in Chapter 1 and Chapter 4, when the constant current condition is imposed, the working electrode (Cu herein) adopts the potential necessary to drive the most favourable redox reaction at the rate necessary to support i_{app}. At the transition time (τ), when the i_{app} can no longer be supported by such reaction, the working electrode potential shifts to the value necessary to carry out the next most favourable reaction at the imposed rate. By plotting the measured potential as a function of time, closely spaced redox processes can be resolved as distinct potential plateaus.[45]

To demonstrate the merit of the technique for resolving the Cu/Cu^{2+}, ORR and HER processes [Eqs. (5.1), (5.4) and (5.5), respectively], a comparative chronopotentiometry study was carried out at the macroscale (*i.e.* in bulk solution) and microscale (*i.e.* in the SECCM configuration, Figure 5.1), as shown respectively in Figure 5.2a and b. Note that all current pulses were preceded by an equilibrium pulse at the OCP (*i.e.* i_{app} set to zero), which is represented on the resulting $E–t$ plots at "negative times". The anodic current pulse in bulk (Figure 5.2a, green dashed line) and the SECCM configuration (Figure 5.2b, green dashed line) results in a constant potential plateau corresponding to Cu oxidation *via* the reaction shown in eq. (5.1). For electrodissolution, the potential remains at a constant value (*i.e.* no transition is observed) because of the constant supply of reactant (*i.e.* Cu).

During the cathodic current pulse in bulk aerated solution (Figure 5.2a, red line), three processes (plateaus) are observed at the following potentials: (*1*) $\approx - 0.1$ V, (*2*) $\approx - 0.4$ V and (*3*) $\approx - 0.75$ V vs Ag/AgCl. Thus, the three cathodic processes discussed above are easily discriminated using chronopotentiometry. By performing control experiments in deaerated solution, where only the HER is possible (Figure 5.2a, black
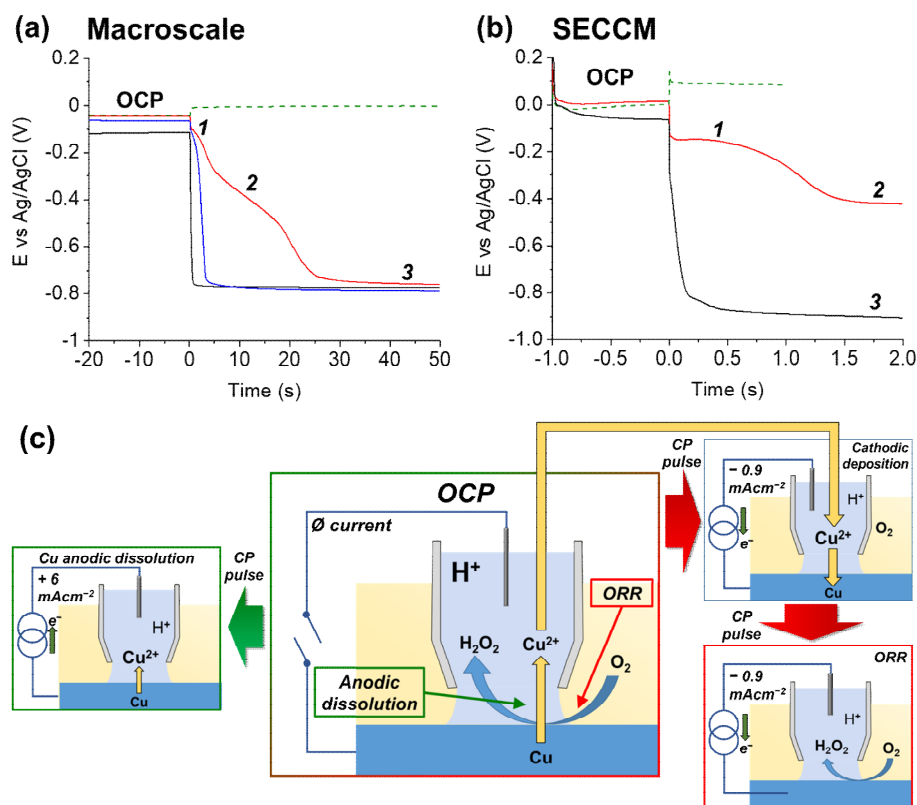
Figure 5.2: Anodic and cathodic chronopotentiometric (E–t) curves obtained from polycrystalline Cu (10 mM H_2SO_4, pH = 2) at **(a)** a Cu macrodisc electrode (area, A = 0.071 cm^2) and **(b)** in the three-phase SECCM configuration. In (a), transients are shown for anodic (green) and cathodic (red, blue and black traces) I_{app} pulses of 0.1 mA cm^{-2} magnitude preceded by 20 s OCP pre-equilibrium. The experiments were carried out in aerated H_2SO_4 (red and green curves), deaerated H_2SO_4 (black curve) and de-aerated H_2SO_4 containing 0.2 mM $CuSO_4$ (blue curve). In (b), anodic (green trace) and cathodic (red trace) I_{app} pulses of 6 and 0.88 mA cm^{-2}, respectively at a polycrystalline Cu foil electrode (immersed in dodecane) were preceded by 1 s OCP pre-equilibrium. The contact area ("footprint") of the meniscus cell was 1.6×10^{-9} and 6.4×10^{-9} cm^2 for the anodic and cathodic I_{app} pulse, respectively. The anodic and cathodic E_{surf}–t curves were obtained by averaging 10,287 and 11,556 individual measurements, respectively. The numbers on the curves in (a) and (b) define the specific cathodic processes described in the text. **(c)** Schematics of the reactions portrayed in both the anodic (represented by the green arrows) and cathodic (represented by the red arrows) potentiometric analyses in the SECCM configuration. The Cu^{2+} released during the OCP step (mixed potential due to the Cu/Cu^{2+} reaction and ORR) is redeposited during the first part of the cathodic pulse (with the connection between the two processes represented by the yellow arrow).

line) and deaerated solution spiked with 0.3 mM CuSO₄, where both
Cu^{2+}/Cu and the HER are possible (Figure 5.2a, blue line), plateaus (**1**),
(**2**) and (**3**) are assigned to Cu^{2+}/Cu [reverse of eq. (5.1)], ORR [eq.
(5.4)] and HER [eq. (5.5)], respectively. It should be re-iterated, that in
bulk aerated solution (*i.e.* Figure 2a, red line), the Cu^{2+} that gives rise to
plateau (**1**) is released into solution during the OCP pre-pulse, from the
acid etching of Cu(s) in the presence O₂ [*i.e.* eq. (5.6)]. These results are
consistent with previous work on chronopotentiometric Cu deposition
in H_2SO_4 at the macroscale.[46]

The corresponding SECCM chronopotentiometric pulse experiment
carried out on a polycrystalline Cu surface (immersed in dodecane) (Fig-
ure 5.2b) produced some different features to the macroscopic case. Each
individual E_{surf}–t experiment was limited to 3 seconds (1 second OCP, 2
seconds current pulse) to maintain meniscus cell stability (*i.e.* minimise
surface wetting) and ensure reasonable imaging times when creating sur-
face arrays of data (up to a few hours, as shown in the previous two chap-
ters). Taking into consideration that $\tau \propto I_{app}^{-2}$ [as described in Chapter 1
and Chapter 4, Eqs. (1.53) and (4.2)], a larger applied current density
(I_{app}) value of 0.88 mA cm⁻² (i_{app} = 5.65 pA, see Appendix, section A.4.1,
for the measured wetting area) had to be employed in the SECCM con-
figuration (*c.f.* 0.1 mA cm⁻² in the macroscale experiment) to observe
both the Cu^{2+}/Cu and ORR processes on this timescale. A typical E_{surf}–t
curve obtained by averaging 11556 individual measurements, each at sep-
arate locations across a polycrystalline Cu surface, is shown in Figure 5.2b
(red line). Analogous to the case in bulk solution (*vide supra*), plateau
(**1**), the Cu^{2+}/Cu process, occurs at *ca.* – 0.15 V, which undergoes a tran-
sition (at time $\tau \approx 1.1$ s) to plateau (**2**), the ORR, at *ca.* – 0.42 V.

In order to verify the nature of such plateaus, a comparison with an
SECCM analysis in de-aerated atmosphere (Figure 5.2b, black curve, av-
erage of 625 individual measurements across a Cu surface), obtained by

applying I_{app} = 0.95 mA cm^{-2} (i_{app} = 30 pA, note the larger wetting radius of the SECCM meniscus cell under these conditions, Appendix, Figure A.7). As in the macroscopic case, in the absence of O$_2$, E_{surf} shifts rapidly and settles directly on a plateau compatible with process (**3**) (≈ -0.85 V), *i.e.* the HER. Note that in the aerated SECCM configuration, the final transition to the HER was not observed, even when a longer pulse time was applied (*i.e.* tens of seconds timescale). As explored in detail through FEM simulations in Appendix, section A.3.2, this is due to the high flux of O$_2$ into the SECCM droplet from the oil phase. In fact, the oil phase acts as an infinite reservoir of O$_2$ (with a saturating concentration of 2.02 mM compared to 0.26 mM in the aqueous phase[47]), compressing the diffusion layer and effectively reaching a steady state where the condition for the transition (O$_2$ concentration at the electrode being zero) is never met;[48,49] this happens because I_{app} (0.88 mA cm^{-2}) is *ca.* 100 times smaller than the stationary state current for the ORR (84 mA cm^{-2}, as calculated in Appendix).

Note that the absence of a plateau (**1**) in the de-aerated case (Figure 5.2b, black curve) indicates that the amount of Cu^{2+} released by oxide dissolution, eq. (5.3), is negligible (undetectable) compared to that released from the corrosion of Cu, [eq. (5.6)], in aerated solution (Figure 5.2b, red curve). Although this is inferred from the surface average behaviour (Figure 5.2b, black curve), under de-aerated conditions a rapid transition is consistently observed during all single point measurements, with no significant variation in the transition time (< 0.1 s) between the individual grains examined. Hence it is assumed that the amount of Cu^{2+} released from oxide dissolution is negligible on all grains. Thus, as explored below, by 'titrating' the Cu^{2+} released during eq. (5.6), by application of a cathodic current, τ can effectively serve an *in situ* indicator of the extent of the Cu corrosion that occurs with zero applied current (*i.e.* at OCP). To illustrate this, and further emphasise all of the processes relevant to Cu

corrosion in acid media (*i.e.* Cu/Cu²⁺, Cu²⁺/Cu and the ORR), a schematic is presented in Figure 5.2c of the key processes that may occur in SECCM at OCP and during the cathodic and anodic pulses.

As discussed in the previous chapter, the transition time (τ), *i.e.* the time at which the concentration of the reactant (Cu^{2+} in this case) reaches zero at the electrode surface, can be approximated by the Sand equation [eq. (4.2)] when the magnitude of I_{app} is several times larger than the magnitude of the steady state limiting current density (which, as explored above, is not the case for the ORR reaction). In the present case, all the parameters of the Sand equation do not vary significantly over the different grains, with $D_{Cu^{2+}} \approx 7.2 \cdot 10^{-6}$ cm² s⁻¹ (Ref. [50]), $n = 2$ (reasonably assumed independent of grain orientation) and $I_{app} \approx 0.88$ mA cm⁻² (as stated above, there is no significant variation in the meniscus cell wetting from point-to-point within the scan). Therefore, any variation in τ between grains reflects variation in the effective concentration of solubilised Cu^{2+}, arising from the corrosion of $Cu_{(s)}$ during the OCP pre-equilibrium step [*i.e.* eq. (5.6)], effectively functioning as an indirect method of titration of the released ions. Herein, the relationship between τ and the relevant corrosion reactions (*vide supra*) is used, qualitatively, to fingerprint regions of the surface where corrosion is most facile (longer τ); eq. (4.2) does not apply quantitatively, as the Cu^{2+} concentration is transient and local.

In reference to Eqs. (5.1) and (5.4), the key factor for evaluating the ease of a reaction on a certain point of the surface is E_{surf}, which is dependent on both thermodynamic and kinetic factors:[45]

$$E_{surf} = E^{0'} + Q \tag{5.7}$$

where $E^{0'}$ ($\approx E^0$) is the formal potential of the main involved electrochemical step, and Q is dependent on I_{app} and the interplay of electrochemical kinetics (rate constant, concentration)-mass transport. As I_{app}, and mass

transport conditions are constant throughout an SECCM scan, variations in the measured E_{surf} informs on the local thermodynamics and kinetics of the processes, analogous to chronopotentiometry at ultramicroelectrodes.[48]

5.3.2. Grain-dependent copper anodic (electro)dissolution.

To map the grain-dependence of the Cu/Cu^{2+} process (*i.e.* copper electrodissolution) an anodic waveform comprising of OCP for 1 second, followed by $I_{app} \approx +6.25$ mA cm^{-2} (with an applied current of 10 pA and an average wetting area of 1.6×10^{-9} cm^2, determined from the SEM image of the scanned area, Appendix Figure A.6) for 1.5 second was used at each position of the surface of polycrystalline Cu. A spatiotemporally-resolved electrochemical movie of Cu/Cu^{2+} activity (maps of potential as a function of time) is included in Appendix, Movie A4 (details in Appendix, section A.1.2). A single frame of Movie A4, taken at a time of 0.2 s into the anodic pulse, is shown in Figure 5.3a.

Comparison of these data with the co-located crystallographic orientation (EBSD) map in Figure 5.3b reveals the strong crystallographic dependence of the Cu/Cu^{2+} process. As part of the measurement protocol (*vide supra*) OCP data were collected at the same locations, and a strong grain dependency was also observed, as shown in Appendix (Figure A.13). A discussion of the grain-dependent OCP characteristics is presented for data collected with the cathodic pulse SECCM scan (*vide infra*).

Due to the large number of independent $E_{surf}-t$ measurements made on individual grains (*e.g.,* see Figure 5.3a), structure-dependent distributions of electrochemical activity can be extracted and statistically analysed. For example, a comparison between the distribution of E_{surf} extracted from the significant grains marked α and β in Figure 5.3b, is shown in Figure 5.3c. Grains α and β possess orientations within a few degrees
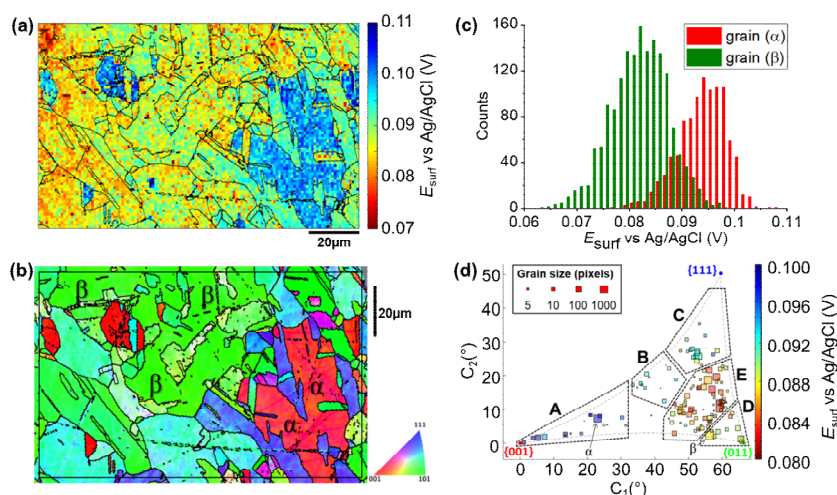
Figure 5.3: (**a**) E_{surf} map of the Cu/Cu^{2+} (Cu oxidation) process on a polycrystalline Cu foil electrode immersed in dodecane, obtained in the three-phase SECCM configuration with I_{app} = + 6.25 mA cm^{-2}. The nanopipette probe contained aerated 10 mM H$_2$SO$_4$ and contacted an area of the surface of 1.6×10^{-9} cm^2. The map was extracted at time 0.2 s of Movie A4. (**b**) Crystallographic orientation map, IPFz (Inverse Pole Figure normal to the z axis) obtained with EBSD. Grains marked α and β are representative of {001} and {011} orientations, respectively. The grain boundaries in (b) are overlaid on the E_{surf} map in (a). (**c**) Statistical distribution of E_{surf} extracted from grains α and β, marked in (b). (**d**) Full grain orientation correlation analysis of E_{surf} at 0.2 s, extracted from (a), *versus* the average grain orientation, extracted from (b), projected onto a 2D plot, as explored in Chapter 2, section 2.8. The labels are used to group particular regions for the textual discussion. Details of the data extracted for each single grain can be found in Appendix, Section A.5.1 (Figure A.12 and Table A.1).

of the {001} and {011} orientations, respectively, and possess average E_{surf} values (taken at the maximum of the normal distributions in Figure 5.3c) of + 0.095 V (std. dev. = 0.010 V) and + 0.082 V (std. dev. = 0.012 V). Despite this relatively high variance, and the resulting partial overlapping of the two distributions, there is a clear difference in Cu oxidation susceptibility (of ≈ 13 mV) between the two grains, highlighting the strength of SECCM for resolving even small differences in nanoscale structure-activity.[16,20]

Comparing representative grains, such as α and β in Figure 5.3b, provides insight into the structure-dependent electrochemical activity of a surface.[22,24] It should be noted, however, that even these "representative

grains" are not perfectly coincident with the ideal low-index grains, {001}, {011} and {111}, which are often the subject of macroscopic single-crystal experiments and theoretical studies.[51-54] To gain a more complete view of structure-dependent Cu oxidation susceptibility, a two-dimensional (2D) representation of the crystallographic-orientation was developed, analogous to the inverse pole figure in the z direction (IPFz) colour key (*e.g.,* see Figure 5.3b). Details of the development and implementation of this 2D projection are given in the General Methods (Chapter 2, section 2.8).

In essence, the crystallographic orientations within a scan area, determined by EBSD analysis, are plotted in Cartesian space (*x-y* coordinates denote the orientation of the grain relative to the ideal low-index orientations) and the electrochemical activity (*i.e.* E_{surf}), determined by SECCM analysis, is plotted on a separate colour scale. In this way, the crystallographic orientation and electrochemical activity can be readily visualised and compared for many surface orientations of a polycrystalline surface. As pointed in section 5.1, this kind of extended analysis has never been performed on such a wide range of crystallographic orientations mainly involving, so far, specific comparison of selected grains, usually representative of the low index gains of the crystallographic system of the material of interest.[7,8,12,21,23,24,26,55,56] Therefore, this work represents a significant advance in the use of SECCM to study the relationship between electrode surface structure and activity.

A correlative plot of E_{surf} *versus* grain orientation, constructed from the SECCM and EBSD datasets (Figure 5.3a and b, respectively), is shown in Figure 5.3d. In order to compare to the corrosion-related processes, five distinct areas within which the activities are broadly similar are demarcated A to E in Figure 5.3d: A) Grains close to the {001} plane, 0.096 < E_{surf} < 0.1 V; B) the band of grains around the {225} grain, 0.09 < E_{surf} < 0.094 V; C) grains toward the {111} orientation, 0.09 < E_{surf} < 0.094 V; D) grains close to the {011} orientation, 0.088 < E_{surf} < 0.09 V and; E) the

band of grains located between B, C and D, $E_{surf} < 0.088$ V. Notably, area E, of intermediate orientation, is the most susceptible to oxidation and is in an area of the plot that is closest to the $\{011\}$ plane. Note that the grains that lay at the boundaries of the distinct areas of activity, such as grain β (Figure 5.3b), which is between areas D and E, tend to show intermediate electrochemical behaviours, making the transition between neighbouring areas of the plot relatively smooth.

5.3.3. Grain-dependent cathodic processes: ORR

The SECCM chronopotentiometric cathodic waveform comprised of OCP for 1 second, followed by $I_{app} = -0.88$ mA cm^{-2} for 2 seconds (consisting in an applied current of 0.565 pA over an average wetting area of 6.4×10^{-9} cm^2, measured from the SEM image of the scanned area, Appendix Figure A.8 and Figure A.9). Spatiotemporal-resolved electrochemical movies of cathodic activity are included in Appendix, Movie A5 and A6 (obtained for two different areas of the Cu working electrode surface). A single frame of Movie A5, taken at a time when E_{surf} is dictated by the energetics (*i.e.* thermodynamics/kinetics) of the ORR (*i.e.* $t = 2$ s in Figure 5.2b), is shown in Figure 5.4a (note that the Cu^{2+}/Cu process is explored separately, below).

Comparison of Figure 5.4a with the co-located EBSD map presented in Figure 5.4b reveals a clear correlation between E_{surf} and crystallographic orientation. To illustrate this, three grains were selected from Figure 5.4b, labelled γ, δ and ε. γ is representative of the $\{011\}$ family, with an average orientation of $\{0.03\ 0.67\ 0.73\}$; δ is representative of the $\{001\}$ family, with an average orientation of $\{0.067\ 0.042\ 1.0\}$; and ε is representative of the $\{111\}$ family, with an average orientation of $\{0.54\ 0.53\ 0.66\}$. Comparing the statistical distribution of the E_{surf} associated with the ORR process measured at each position within these grains (Figure 5.4c) gives the following values: $E_{surf,\gamma} = -0.439$ V (st. dev. 0.008 V), $E_{surf,\delta} = -0.424$ V (st. dev. 0.007 V) and $E_{surf,\varepsilon} = -0.401$ V (st. dev. 0.007 V). The inter-grain
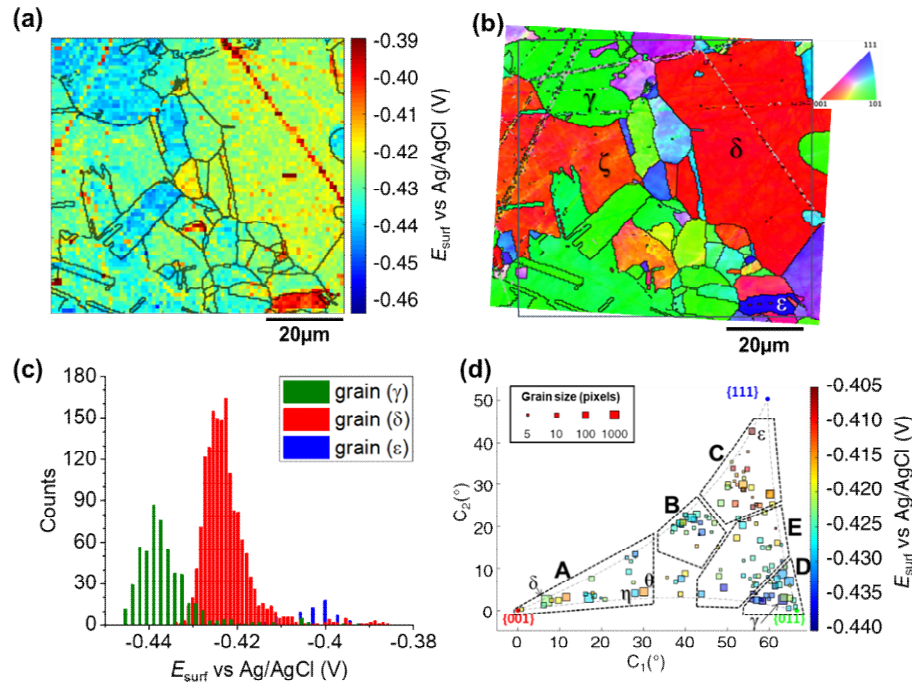
Figure 5.4: (**a**) Surface potential (E_{surf}) map of the ORR process on a polycrystalline Cu foil electrode immersed in dodecane, obtained in the SECCM configuration with I_{app} = − 0.88 mA cm⁻². During these measurements, the nanopipette probe contained aerated 10 mM H_2SO_4 and contacted an area of 6.4×10^{-9} cm². The map was extracted at time 2 s of Movie A5. (**b**) Crystallographic orientation map, IPFz obtained with EBSD. Grains marked γ, δ and ε are representative of {011}, {001} and {111} orientations, respectively. The grain boundaries from Figure 5.4b are overlaid on the E_{surf} map in (a). (**c**) Statistical distribution of E_{surf} in three representative grains, designated γ, δ and ε in Figure 5.4b. (**d**) Full grain orientation correlation analysis of E_{surf} at 2 s, extracted from (a) and Figure A.14a (Appendix, section A.5.1), respectively for Movie A5 and A6, *versus* the average grain orientation, extracted, respectively, from (b) and Figure A.14b (Appendix, section A.5.1), and projected onto a 2D plot. Details of the data extracted for each single grain can be found in Appendix, Section A.5.1 (Figure A.15 and Table A.2).

variation in E_{surf} (*ca.* 0.05 V) is similar to that measured for the Cu/Cu²⁺ process (*ca.* 0.04 V, Figure 5.3a) while the intra-grain variation is around three times smaller, making clearer the difference between these example grains.

Considering the E_{surf} − crystallographic orientation correlation plot (Figure 5.4d), a highly complex grain dependence can be observed. For

sake of comparison with the Cu/Cu²⁺ process analysed earlier, five activity areas (named A to E) are highlighted in Figure 5.4d, in the same positions as the ones in Figure 5.3d. Area C, comprising the grains that are closest to the {111} orientation (*e.g.*, grain ε) possess the highest ORR activity ($-0.420 < E_{surf} < -0.405$ V), while area D, with the grains that are closest to the {011} orientation (*e.g.*, grain γ) possess the lowest ORR activity ($E_{surf} < -0.430$, with a couple of exceptions). The other three areas have intermediate values of E_{surf}, with areas B and E having $-0.430 < E_{surf} < -0.420$ V, and area A in the range -0.430 V to -0.415 V. It is worth noting that the lowest-activity grains in area D are not exactly coincident with {011}, but rather in a group lying at lower values of C_1 ($\approx 58°$ instead of $\approx 66°$ of the {011}).

For comparison with literature studies on single crystals, comparing grains γ, δ and ε, ORR kinetics increases in the order Cu{011} < Cu{001} < Cu{111}. The relative ORR rates on the Cu{111} and Cu{001} facets are in agreement with previous voltammetric studies on macroscopic single crystal electrodes,[52,57] which ascribed variations in the ORR kinetics and/or reaction pathway with grain structure to the adsorption of spectator species, specifically (bi)sulphate (*i.e.* HSO_4^- and SO_4^{2-}) in aqueous H_2SO_4. In other words, the structure (and potential) dependent adsorption of (bi)sulphate anions blocks catalytic active sites for the adsorption of O_2 molecules, inhibiting the ORR in a grain-dependent manner. While analogous experimental literature is not available on Cu{011}, it is worth noting that this crystal plane is considered to have strongest binding for dissociated oxygen.[58-60] As Cu is on the descending branch of the classical Volcano plot for the ORR (noting that the literature focuses more on the $4e^-$ reduction; studies of Cu amalgams suggest the same trend for the $2e^-$ process),[61, 62] it follows that an increased binding strength would result in more sluggish ORR kinetics, consistent with the present measurements, and highlighting the value of SECCM-EBSD pseudo-single crystal studies in being able to investigate a wide range of surface structures well be-

yond what is possible with classical single crystal studies. According to previous STM and theoretical studies,[54,59,63-65] the interaction of oxygen with Cu{001} and Cu{011} happens at significantly lower temperatures and coverage than on {111} surfaces. This may also explain why grains that are closer to the {111} orientation appear to possess the fastest ORR kinetics, by lowering the binding strength (*i.e.* towards the peak of the Volcano plot).

It is also interesting to note that individual high-index grains shown in Figure 5.4d can present reactivity that is distinct from neighbouring grains of similar structure. For instance, consider the two grains labelled η and θ in Figure 5.4d, area A. While these grains differ by only 2.12° in the 2D projection (their average Miller indexes are {0.306 0.036 0.951} and {0.329 0.040 0.944}, respectively), grain θ possesses significantly higher activity (E_{surf} = − 0.415 V) compared to η (E_{surf} = − 0.427 V) and the surrounding grains (E_{surf} average of neighbouring grains with less than 10° difference in orientation being also − 0.427 V). Such a difference, which is found in two grains that are relatively big and of comparable size (thus relatively immune to random statistical variations), demonstrates that the grain dependency of surface electrochemical reactions cannot be interpreted simply in terms of a surface structure that is a composite of individual low-index grains. A more detailed analysis of this phenomenon will be carried out in the next chapter.

5.3.4. Grain-dependent cathodic processes: Cu deposition

The analysis of the part of the cathodic chronopotentiometric pulse transient concerning the Cu^{2+}/Cu process [plateau (*1*) in Figure 5.2b] focuses on two fundamental parameters, E_{surf} and τ. These parameters carry different and complementary information, with E_{surf} indicating on the energetics (kinetics/thermodynamics) of the reaction, and τ indicating on the amount of Cu^{2+} released into solution during the OCP stage [*i.e.* due to corrosion, as per eq. (5.6)]. Figure 5.5a reproduces a single

Figure 5.5. (a) E_{surf} map for the Cu^{2+}/Cu process (Cu electrodeposition) on a polycrystalline Cu foil electrode immersed in dodecane, obtained with SECCM with I_{app} = − 0.88 mA cm^{-2}. The nanopipette probe contained aerated 10 mM H_2SO_4 and contacted an area of 6.4×10^{-9} cm^2. The map was extracted at time 0.25 s of Movie S2. **(b)** Map of $\tau_{Cu^{2+}/Cu}$, extracted from Movie A5. The grain areas determined from Figure 5.4b are overlaid on the maps in (a) and (b). **(c – d)** Full grain orientation correlation analysis of (c) E_{surf} at 0.25 s and (d) $\tau_{Cu^{2+}/Cu}$, extracted from (a) and Figure A.14c, and (b) and Figure A.14d, respectively, with the average grain orientation extracted from Figure 5.4b and Figure A.14b. The insets in (c) and (d) show the distributions of E_{surf} and $\tau_{Cu^{2+}/Cu}$, extracted from grains γ, δ and ε, marked in Figure 5.4b. Details of the data extracted for each grain can be found in Appendix, section A.5.1 (Figure A.15 and Table A.2).

frame of Movie A5, taken at a relatively early time, *t* = 0.25 s when I_{app} is solely supplied by the Cu^{2+}/Cu process, while Figure 5.5b shows a spatially resolved map of $\tau_{Cu^{2+}/Cu}$ (derived from the E_{surf} data in Movie A5).

Comparing Figure 5.5a and b (and Movie A5) with the co-located EBSD map in Figure 5.4b, shows that there is a clear correlation between electrochemical activity (as reflected in both E_{surf} and τ) and surface crystallographic orientation. This is also clear from the 2D plots of E_{surf} and τ *versus* crystallographic orientation, shown in Figure 5.5c and d, respectively.

Focusing on the grain-dependent E_{surf} characteristics (Figure 5.5c), two distinct areas can be identified on the plot, marked F and G, listed below in order of decreasing ease of reduction. F) Grains with orientations between the {011} and {111} low-index planes, $-0.13 < E_{surf} < -0.09$ V and; G) grains close to the {001} orientation (specifically the ones with $C_1 < 50°$ and $C_2 < 30°$), $-0.19 < E_{surf} < -0.15$ V. Notably, grains close to the {001} orientation result in both the highest anodic (Cu/Cu^{2+}, Figure 5.3d) and the lowest cathodic potentials (Cu^{2+}/Cu, Figure 5.5c), and thus the multistage Cu dissolution and Cu^{2+} deposition processes are not simply related.

As introduced above, the intermediate $Cu(I)_{ads}$ species on the surface play a fundamental role in the dissolution process, with its subsequent oxidation to $Cu(II)$ considered to be the rate determining step,[34,35] and being highly affected by the presence of O_2 in solution.[38,66,67] Conversely, for the re-deposition process [*i.e.* Cu^{2+}/Cu] sulphate complexation and intercalation is poised to play a major role.[40-43] The difference in mechanism may explain the different grain dependencies of the dissolution and deposition processes.

E_{surf} associated with the Cu^{2+}/Cu process also shows significantly higher range of values between grains (≈ 0.15 V difference) compared to 0.04 V (for Cu/Cu^{2+}) and 0.05 V (ORR); compare Figure 5.5a, Figure 5.3a and Figure 5.4a, respectively. Comparing the statistical distribution of the E_{surf} associated with the Cu^{2+}/Cu process measured at each position within the three grains highlighted in Figure 5.4b, γ, δ and ε, (Figure 5.5d, inset) gives the following values: $E_{surf,\gamma} = -0.132$ V (st. dev. 0.014 V), $E_{surf,\delta} = -0.164$ V (st. dev. 0.026 V) and $E_{surf,\varepsilon} = -0.082$ V (st. dev. 0.020 V). It is worth noting that although there is significant inter-grain variations in E_{surf} (*i.e.* compare γ, δ and ε in Figure 5.5c, inset), the intra-grain variation, measured by the standard deviation, is comparable for both the Cu^{2+}/Cu and Cu/Cu^{2+} processes (Figure 5.3c).

As stated above, τ depends on the amount of Cu^{2+} released into the solution during the OCP step ($t < 0$, Figure 5.2b), therefore the analysis presented in Figure 5.5b and d (extracted from Movie A5 and A6) can give an insight on the relationship between the two half reactions contributing to Cu corrosion [*i.e.* Cu oxidation and ORR, Eqs. (5.1) and (5.4)]. The variation in τ within a single grain is generally relatively high, for example, comparing the τ distributions of grains γ, δ and ε (inset in Figure 5.5d), differences in the maximum value of the three distributions are evident (*e.g.*, β has the longest transition time), but the distributions overlap more than in the equivalent E_{surf} distributions (inset in Figure 5.5d). Nevertheless, due to the large number of $E_{surf}-t$ measurements made in each individual grain, differences in the mean τ values are readily distinguished, with $\tau_\gamma = 1.101$ s (st. dev. = 0.059 s), $\tau_\delta = 1.197$ s (st. dev. = 0.097 s) and $\tau_\varepsilon = 1.138$ s (st. dev. = 0.096 s).

More broadly, Figure 5.5d presents very clear trends in τ with crystallographic orientation, evident by considering the same five distinct areas (named A to E), discussed above. Area B, in particular, is the one with the smallest τ values ($\tau \leq 1$ s), corresponding to the lowest amount of Cu^{2+} released at OCP, which is consistent with the energetically unfavourable Cu/Cu^{2+} (*i.e.* most positive values of E_{surf}) and ORR (*i.e.* most negative values of E_{surf}) processes on these planes (consult Figure 5.3d and Figure 5.4d, respectively). In contrast, area E possesses relatively large τ values ($\tau \geq 1.2$ s), which may be explained by the relatively favourable Cu/Cu^{2+} process on these planes (although the ORR remains relatively unfavourable). Area C also possesses relatively large τ values ($\tau \geq 1.1$ s), which may be the result of a favourable ORR that overcomes the moderately unfavourable Cu oxidation. Area D, where ORR is unfavourable but the Cu/Cu^{2+} is moderately favourable, possesses intermediate τ values ($\tau \approx 1.1$ s). The response in area A is more complex, possessing relatively variable τ values, *e.g.*, grains closer to the {001} orientation possess $\tau \geq 1.2$ s

Figure 5.6: (**a**) SECCM E_{surf} map at OCP on a polycrystalline Cu foil electrode immersed in dodecane. The nanopipette probe contained aerated 10 mM H_2SO_4 and contacted an area of 6.4×10^{-9} cm^2 at each location in the map. The map was extracted at time $- 0.01$ s of Movie A5 (negative times are used for indicating the pre-cathodic OCP step). The grain boundaries from Figure 5.4b are overlapped on the map. (**b**) Full grain orientation correlation analysis of E_{surf} at $- 0.01$ s from (a) and Figure A.14e *versus* the average grain orientation, extracted from Figure 5.4b and Figure A.14b. Details of the data extracted for each single grain can be found in Appendix, section A.5.1 (Figure A.15 and Table A.2). Relevant orientation areas are marked on the graph. (**c**) Plot of the general correlation between $\tau_{Cu^{2+}/Cu}$ from Figure 5.5b and Figure A.14d, *versus* the E_{surf} in the OCP step for each point measurement (from Figure 5.6a and Figure A.14e). τ is represented as the median values of τ for each recorded value of OCP (with a step size of 0.31 mV, corresponding to the sensitivity of the measurement), with an error bar representing the standard deviation for the same set of data. Only the OCP points with at least 10 τ values are represented.

(*c.f.* area E), while those with higher C_1 values ($\geq 25°$) possess $\tau \leq 1$ s (*c.f.* area B). Nevertheless, area A is largely an exception, and the relative ease of the two half reactions, Cu/Cu^{2+} and ORR (from E_{surf}), is a predictor of the amount of Cu^{2+} released during corrosion at OCP (from τ) on the grains situated in areas B - E.

5.3.5. Grain-dependent open circuit potential step.

A map of the OCP extracted from Movie A5 (0.01 s before the application of the cathodic pulse) is shown in Figure 5.6a. It is clear that OC!P is grain dependent, as shown in the OCP/crystallographic orientation correlation plot, presented in Figure 5.6b. Most clearly by visual inspection, area B, which shows the most negative OCP values (with a median value $E_{surf,B} = 0.0046$ V, compared to an overall median of 0.0116 V), also have the smallest τ values, corresponding to the least amount of Cu^{2+} released in the OCP step (*vide supra*), indicating that the least anodic OCP corresponds to a surface with the highest corrosion resistance. Although the deduction of corrosion susceptibility from OCP measurements may be complicated due to the different surface structural dependences of the kinetics and thermodynamics of the Cu/Cu^{2+} and ORR processes, and the involvement of O_2 in the Cu/Cu^{2+} process, there is a positive relationship between τ (from Figure 5.5b and Figure A.14d) and the OCP (from Figure 5.6b, and Figure A.14e), as shown in Figure 5.6c. Thus, while there maybe outliers (note the error bars on τ in Figure 5.6c), nanoscale OCP measurements provide a guide to metal corrosion susceptibility/resistance, particularly if large datasets can be collected (*i.e.* on the order of a few thousand points, Figure 5.6).

5.3.6. Electrochemical activity of microscopic surface defects.

Physical deformation, in particular scratches, are unavoidably introduced during the manufacturing and the finishing (polishing) processes of any metal surface. It is accepted that, in most cases, a macroscopic scratch will possess increased corrosion susceptibility compared to the rest of the metallic surface, predominantly due to induced micro-fractures in the material that act as initiation sites for corrosion-related processes.[68,69] Although the corrosion-action of several different kinds of physical deformation have been the subject of macroscopic electrochem-
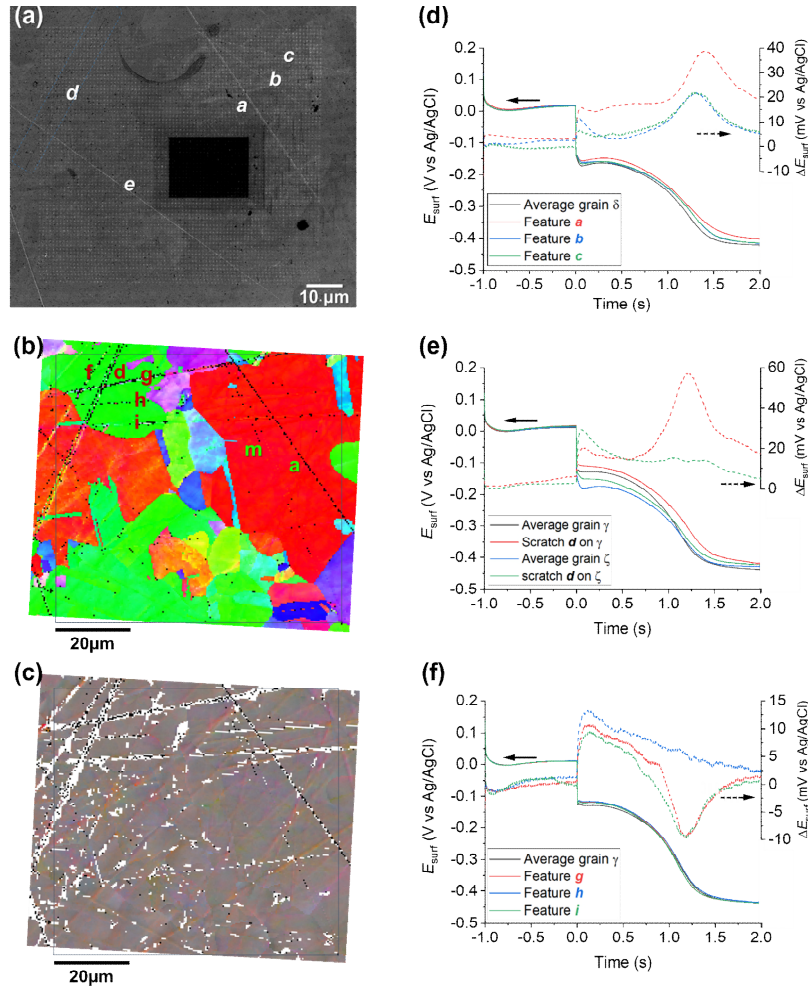
Figure 5.7: (**a**) SEM image of the scanned area of Figure 5.4 and Figure 5.5 (Movie A5), with main surface scratches labelled with the letters *a-e*. (**b**) Raw EBSD map (*i.e.* without grain boundaries drawn) of the area scanned in the ESI, Movie A5. Five main surface defects (scratches), labelled *f – i*, are identified. Note that scratches can be generally identified as a black zone in EBSD images, due to the fact that the "shadow effect" of the scratches walls generally do not allow the underlying crystallographic orientation to be determined. (**c**) EBSD misorientation colouring map of the same area. The colours in this map indicate inter-pixel misorientation, such that a visible colour difference between any two adjacent points within a given grain represents the misorientation angle between such points. (d-f) Comparison of the average chronopotentiometric ($E-t$) curves recorded on the scratches to the surrounding grain(s), identified on the corresponding EBSD image, Figure 5.4b. In (**d**), scratches *a*, *b* and *c* are compared to grain δ and in (**e**), scratch *d* is compared to grains γ and ζ, which are identified on the corresponding EBSD image, Figure 5.4b. In (**f**), scratches *g*, *h* and *i* are compared to grain γ. Also shown are plots of the difference between the $E_{surf}-t$ curves recorded on the scratches and the surrounding grain, ΔE_{surf}.

ical investigation and surface analysis techniques,[70-72] the role of micro-scopic defects, such as scratches introduced by fine polishing, is still largely unknown. SECCM enables electrochemical activity to be probed at a commensurate scale to microscopic surface defects.

A number of microscopic scratches were observed in the mirror-finished Cu surface employed in this work, as indicated by the SEM and EBSD images shown in Figure 5.7a-c, respectively. Five major scratches can be identified within the cathodic scan area shown in Figure 5.4 and Figure 5.5 and labelled *a* to *e* in Figure 5.7a. Additionally, at least other 6 features can be identified in the IPFz map (Figure 5.7b) and *ca.* 20 minor defects can be identified if the disorientation colour map is analysed (Figure 5.7c). The discussion here focuses mainly on the features identified under cathodic polarisation, but a few scratches were also identified within anodic polarisation, identified and briefly discussed in Appendix, Figure A.16 .

Electrochemical analysis of these scratches, achieved by correlating the SECCM and SEM/EBSD maps, reveals that microscopic surface deformations often have a pronounced effect on the (cathodic) surface activity. As an example, Figure 5.7d compares the E_{surf}–t pulses obtained from scratches *a*, *b* and *c* of Figure 5.7a to the average E_{surf}–t from the surrounding grain, in which they are located (*i.e.* grain δ in Figure 5.4b). Evidently, all three features exhibit enhanced cathodic activity compared to the grain average, with feature *a* being the most active. It is important to note that the area probed by the nanopipette ($\approx$ 900 nm diameter for the cathodic pulse, Figure A.8a) is much larger than the topographical deformation ($\approx$ 50 nm width, as can be seen from the SEM image, Figure 5.7a; commensurate with the size of the polishing particles; it can be assumed the depth of the scratch would be similar). Notably, while the scratch is a minor component of the probed area, there is evidently considerably more Cu^{2+} released at OCP in these locations, lengthening the transition

time between the Cu^{2+}/Cu and ORR processes.

A fascinating aspect of this analysis is that the activity of the scratch seems to be highly dependent on the grain in which it is located. As an example, the results over feature *d* are analysed in Figure 5.7e. The section of scratch *d* that is located on grain γ behaves very similarly to that of scratch *a* on grain δ (*i.e.* $\Delta E_{surf} \approx + 20$ mV for both the cathodic processes and a longer transition between the Cu/Cu^{2+} and ORR plateaus). Conversely, on the section of scratch *d* that is located on grain ζ, ΔE_{surf} for the Cu^{2+}/Cu process is $\approx + 20$ mV, compared to ≈ 0 mV for the ORR.

In addition, despite the very similar orientation of grains δ and ζ, the two scratches located on them, *a* and *d*, exhibit a completely different behaviour, shown in Figure 5.7d and e, respectively. Similar observations can also be made for the several scratches, besides *d*, found on grain γ, as shown in Figure 5.7f. It should also be noted that some surface defects have no apparent effect on E_{surf}, such as scratch *e* in Figure 5.7a. Evidently, the electrochemical activity induced by surface deformation must depend on the orientation of the underlying grain that is exposed within the defect, in addition to other factors such as the increased surface area resulting from surface roughening, and/or the increased surface strain.

Interestingly, while such variety of enhanced activity is observed for mechanically induced defects in the structure, the same is not generally observed in the present conditions, for the grain boundaries, as can be seen from the reproduction of the anodic and cathodic E_{surf} maps without the boundaries overlaid (Figure 5.8a-c). It has previously been shown that SECCM possesses sufficient sensitivity to detect the activity of atomic scale defects such as step edges,[73] grain boundaries[28,74] and point defects,[75] with the caveat that these sites need to be highly active (*ca.* orders-of-magnitude) compared to the surrounding basal surfaces, in order to be detected.[76] While the lack of electrochemical contrast at grain boundaries may indicate that they do not serve as anodic/cathodic sites
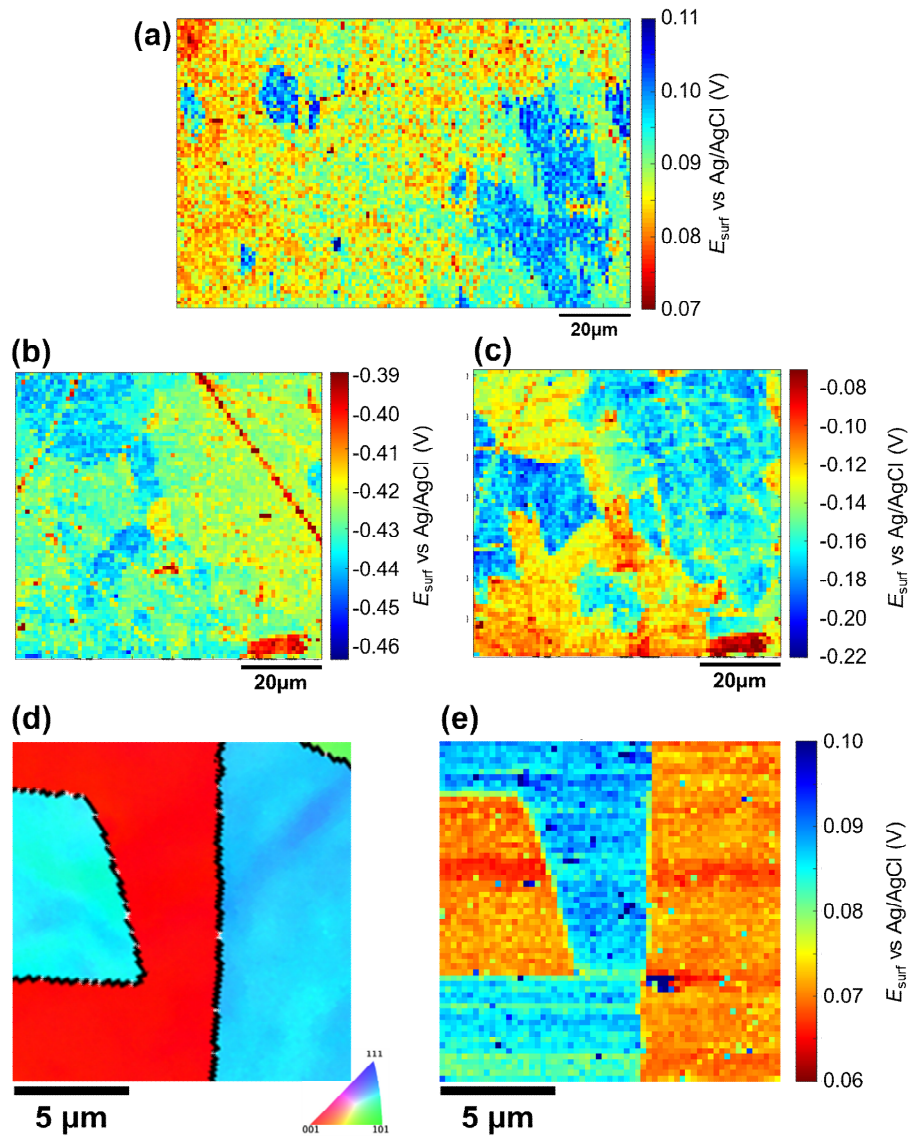
Figure 5.8: (**a-c**) Reproduction of, respectively, (**a**) Figure 3a, (**b**) Figure 4a and (**c**) Figure 5a, all without the grain boundaries overlaid on the electrochemical map. (**d**) EBSD map (IPFz) of a polycrystalline Cu surface and (**e**) corresponding SECCM E_{surf} map, collected with the following method: a chronopotentiometric pulse of 0.3s at a current of 1pA ($\approx$ 4 mA cm^{-2}, given a contact area of $\approx$ 180 nm diameter with a probe of $\approx$ 150 nm diameter), preceded by an OCP step of 0.2s. The map was extracted a time 0.1 s of the anodic pulse.

in the present case, the large size of the droplet footprint (800 – 900 nm diameter) relative to the grain boundary (*i.e.* the majority of the measurement area is grain rather than grain boundary) needs to be noted.

To better target grain boundaries, an analogous anodic chronopoten-tiometric SECCM experiment was carried out with a smaller nanopipette probe (*ca.* 150 nm diameter) and higher spatial resolution (250 nm), but from the comparison between the EBSD map (Figure 5.8d) with the E_{surf} map (Figure 5.8e) it is evident that in this case the grain boundary activity still appears to be roughly the average of the two adjacent grains. Thus, while enhanced anodic/cathodic activity at the grain boundary termina-tions cannot be totally ruled out at this lateral resolution, it is concluded that these sites are not orders-of-magnitude more active than the sur-rounding grains. Nevertheless, these results still clearly demonstrate that the microscopic features can play an important role as initiation sites for corrosion-related processes, and further underline the great power of SECCM for identifying and characterising them. Further analysis of scratches and defects by SECCM could be very valuable towards devel-oping a holistic view of metal reactivity and corrosion.

5.4. CONCLUSION

SECCM was successfully adapted to map grain-dependent electrochem-ical activity at an aqueous nanodroplet/oil/metal three-phase interface, emulating the conditions encountered during corrosion in industrial/au-tomotive environments, and opening up new prospects for fundamental electrochemical studies at the (sub)microscale. Application of a *correla-tive multi-microscopy approach*, in which electrochemistry at a polycrystal-line copper surface, from SECCM, was combined with co-located struc-tural information from EBSD, allowed full elaboration of the structure-activity relationship for three corrosion-related processes and their inter-correlation: Cu/Cu^{2+}, Cu^{2+}/Cu and ORR, and the combination of Cu/Cu^{2+} and ORR during a pre-equilibrium OCP (mixed potential) step.

This in-depth analysis method has revealed unique, process-depend-ent patterns of reactivity for the full spectrum of surface crystallographic

orientations, for which the electrochemical activity of high-index surface facets cannot be predicted simply through combination of the {001}, {011} and {111} response(s). Within the full spectrum of surface orientations, it was possible to identify those where the two reactions contributing to Cu corrosion (*i.e.* Cu/Cu^{2+} and ORR) are most favoured. Nanoscale OCP (mixed potential) measures were furtherly introduced, outlying a procedure to detect Cu^{2+} released into solution at OCP as a marker of the extent of corrosion, as reflected in the chronopotentiometric transition time. This analysis highlights the value of both kinetic mapping and OCP measurements for revealing local corrosion susceptibility with SECCM.

In addition, it was also possible to probe the electrochemical activity of individual (micro)scratches, revealing that these nanoscopic surface defects can serve as cathodic "hot-spots" for corrosion-related processes. Moreover, this work sets a new standard for surface structure-activity studies in (electro)materials and corrosion science, and additionally provides a new configuration for the study of multiphase environments at the nanoscale. As mentioned at the beginning, such configuration will be valuable, in the next two chapters, for characterising the effect of two important factors involved in corrosion at the nanoscale: the presence of atmospheric O_2 and the presence of a corrosion inhibitor.

5.5. REFERENCES

[1]   Marcus, P.; Mansfeld, F. B. *Analytical Methods In Corrosion Science and Engineering*; CRC Press, 2005.

[2]   Herl, T.; Matysik, F.-M. Recent Developments in Electrochemistry–Mass Spectrometry. *ChemElectroChem* **2020**, *7* (12), 2498-2512.

[3]   Ogle, K.; Weber, S. Anodic Dissolution of 304 Stainless Steel Using Atomic Emission Spectroelectrochemistry. *J. Electrochem. Soc.* **2000**, *147* (5), 1770.

[4]   Gewirth, A. A.; Niece, B. K. Electrochemical Applications of in Situ Scanning Probe Microscopy. *Chem. Rev.* **1997**, *97* (4), 1129-1162.

[5]   Jensen, M. B.; Tallman, D. E. In *Electroanalytical Chemistry A Series of Advances*; Bard, A. J.;Zosky, C., Eds.; CRC Press: Boca Raton, 2012; Vol. 24.

[6]   Andreatta, F.; Fedrizzi, L. The use of the electrochemical micro-cell for the investigation of corrosion phenomena. *Electrochim. Acta* **2016,** *203*, 337-349.

[7]   Martinez-Lombardia, E.; Gonzalez-Garcia, Y.; Lapeire, L.; De Graeve, I.; Verbeken, K.; Kestens, L.; Mol, J. M. C.; Terryn, H. Scanning electrochemical microscopy to study the effect of crystallographic orientation on the electrochemical activity of pure copper. *Electrochim. Acta* **2014,** *116*, 89-96.

[8]   Martinez-Lombardia, E.; Lapeire, L.; De Graeve, I.; Verbeken, K.; Kestens, L. A. I.; Terryn, H. Study of the influence of the microstructure on the corrosion properties of pure copper. *Mater. Corros.* **2016,** *67* (8), 847-856.

[9]   Renner, F. U.; Stierle, A.; Dosch, H.; Kolb, D. M.; Lee, T. L.; Zegenhagen, J. Initial corrosion observed on the atomic scale. *Nature* **2006,** *439* (7077), 707-710.

[10]   Bettayeb, M.; Maurice, V.; Klein, L. H.; Lapeire, L.; Verbeken, K.; Marcus, P. Nanoscale Intergranular Corrosion and Relation with Grain Boundary Character as Studied In Situ on Copper. *J. Electrochem. Soc.* **2018,** *165* (11), C835-C841.

[11]   Reformatskaya, I. I.; Rodionova, I. G.; Beilin, Y. A.; Nisel'son, L. A.; Podobaev, A. N. The Effect of Nonmetal Inclusions and Microstructure on Local Corrosion of Carbon and Low-alloyed Steels. *Prot. Met* **2004,** *40* (5), 447-452.

[12]   Luo, J.; Hein, C.; Pierson, J.-F.; Mücklich, F. Localised corrosion attacks and oxide growth on copper in phosphate-buffered saline. *Mater. Charact.* **2019,** *158*, 109985.

[13]   Tang, X.; Ma, C.; Zhou, X.; Lyu, X.; Li, Q.; Li, Y. Atmospheric corrosion local electrochemical response to a dynamic saline droplet on pure Iron. *Electrochem. Commun.* **2019,** *101*, 28-34.

[14]   Lejre, K. H.; Kiil, S.; Glarborg, P.; Christensen, H.; Mayer, S. In *ASME 2017 Internal Combustion Engine Division Fall Technical Conference*, 2017.

[15]   Migahed, M. A. Corrosion inhibition of steel pipelines in oil fields by N,N-di(poly oxy ethylene) amino propyl lauryl amide. *Prog. Org. Coat.* **2005,** *54* (2), 91-98.

[16]   Bentley, C. L.; Edmondson, J.; Meloni, G. N.; Perry, D.; Shkirskiy, V.; Unwin, P. R. Nanoscale Electrochemical Mapping. *Anal. Chem.* **2019,** *91* (1), 84-108.

[17]   Kang, M.; Momotenko, D.; Page, A.; Perry, D.; Unwin, P. R. Frontiers in Nanoscale Electrochemical Imaging: Faster, Multifunctional, and Ultrasensitive. *Langmuir* **2016,** *32* (32), 7993-8008.

[18]   Ebejer, N.; Güell, A. G.; Lai, S. C. S.; McKelvey, K.; Snowden, M. E.; Unwin, P. R. Scanning Electrochemical Cell Microscopy: A Versatile Technique for Nanoscale Electrochemistry and Functional Imaging. *Annu. Rev. Anal. Chem.* **2013,** *6* (1), 329-351.

[19]   Bentley, C. L.; Kang, M.; Unwin, P. R. Scanning electrochemical cell microscopy: New perspectives on electrode processes in action. *Curr. Opin. Electrochem.* **2017,** *6* (1), 23-30.

[20]   Bentley, C. L.; Kang, M.; Unwin, P. R. Nanoscale Surface Structure–Activity in Electrochemistry and Electrocatalysis. *J. Am. Chem. Soc.* **2019,** *141* (6), 2179-2193.

[21]   Yule, L. C.; Bentley, C. L.; West, G.; Shollock, B. A.; Unwin, P. R. Scanning electrochemical cell microscopy: A versatile method for highly localised corrosion related measurements on metal surfaces. *Electrochim. Acta* **2019,** *298,* 80-88.

[22]   Yule, L. C.; Shkirskiy, V.; Aarons, J.; West, G.; Shollock, B. A.; Bentley, C. L.; Unwin, P. R. Nanoscale electrochemical visualization of grain-dependent anodic iron dissolution from low carbon steel. *Electrochim. Acta* **2020,** *332,* 135267.

[23]   Yule, L. C.; Shkirskiy, V.; Aarons, J.; West, G.; Bentley, C. L.; Shollock, B. A.; Unwin, P. R. Nanoscale Active Sites for the Hydrogen Evolution Reaction on Low Carbon Steel. *J. Phys. Chem. C* **2019,** *123* (39), 24146-24155.

[24]   Shkirskiy, V.; Yule, L. C.; Daviddi, E.; Bentley, C. L.; Aarons, J.; West, G.; Unwin, P. R. Nanoscale Scanning Electrochemical Cell Microscopy and Correlative Surface Structural Analysis to Map Anodic and Cathodic Reactions on Polycrystalline Zn in Acid Media. *J. Electrochem. Soc.* **2020,** *167* (4).

[25]   Li, Y.; Morel, A.; Gallant, D.; Mauzeroll, J. Oil-Immersed Scanning Micropipette Contact Method Enabling Long-term Corrosion Mapping. *Anal. Chem.* **2020,** *92* (18), 12415-12422.

[26]   Chen, C.-H.; Meadows, K. E.; Cuharuc, A.; Lai, S. C. S.; Unwin, P. R. High resolution mapping of oxygen reduction reaction kinetics at polycrystalline platinum electrodes. *Phys. Chem. Chem. Phys.* **2014,** *16* (34), 18545-18552.

[27]   Ustarroz, J.; Ornelas, I. M.; Zhang, G.; Perry, D.; Kang, M.; Bentley, C. L.; Walker, M.; Unwin, P. R. Mobility and Poisoning of Mass-Selected Platinum Nanoclusters during the Oxygen Reduction Reaction. *ACS Catal.* **2018,** *8* (8), 6775-6790.

[28]   Mariano, R. G.; McKelvey, K.; White, H. S.; Kanan, M. W. Selective increase in CO_2 electroreduction activity at grain-boundary surface terminations. *Science* **2017,** *358* (6367), 1187.

[29]   Terry Weatherly, C. K.; Ren, H.; Edwards, M. A.; Wang, L.; White, H. S. Coupled Electron- and Phase-Transfer Reactions at a Three-Phase Interface. *J. Am. Chem. Soc.* **2019,** *141* (45), 18091-18098.

[30]   Terry Weatherly, C. K.; Glasscott, M. W.; Dick, J. E. Voltammetric Analysis of Redox Reactions and Ion Transfer in Water Microdroplets. *Langmuir* **2020,** *36* (28), 8231-8239.

[31]   Marken, F.; Watkins, J. D.; Collins, A. M. Ion-transfer- and photo-electrochemistry at liquid|liquid|solid electrode triple phase boundary junctions: perspectives. *Phys. Chem. Chem. Phys.* **2011,** *13* (21), 10036-10047.

[32]   Ornelas, I. M.; Unwin, P. R.; Bentley, C. L. High-Throughput Correlative Electrochemistry–Microscopy at a Transmission Electron Microscopy Grid Electrode. *Anal. Chem.* **2019,** *91* (23), 14854-14859.

[33]   Beverskog, B. Revised Pourbaix Diagrams for Copper at 25 to 300°C. *J. Electrochem. Soc.* **1997,** *144* (10), 3476.

[34]   Cordeiro, G. G. O.; Barcia, O. E.; Mattos, O. R. Copper electrodissolution mechanism in a 1M sulphate medium. *Electrochim. Acta* **1993,** *38* (2), 319-324.

[35]   Wong, D. K. Y.; Coller, B. A. W.; MacFarlane, D. R. A kinetic model for the

dissolution mechanism of copper in acidic sulfate solutions. *Electrochim. Acta* **1993,** *38* (14), 2121-2127.

[36]   Kanzaki, Y.; Bruckenstein, S. Anodic Dissolution of Copper in Oxygenated Sulfuric Acid Solution as Examined by Rotating Ring-Disk Electrode. *Electrochemistry* **2013,** *81* (7), 547-552.

[37]   Andersen, T. N.; Ghandehari, M. H.; Eyring, H. A Limitation to the Mixed Potential Concept of Metal Corrosion: Copper in Oxygenated Sulfuric Acid Solutions. *J. Electrochem. Soc.* **1975,** *122* (12), 1580-1585.

[38]   Gray, R. D. Kinetics of oxidation of copper(I) by molecular oxygen in perchloric acid-acetonitrile solutions. *J. Am. Chem. Soc.* **1969,** *91* (1), 56-62.

[39]   Colley, A. L.; Macpherson, J. V.; Unwin, P. R. Effect of high rates of mass transport on oxygen reduction at copper electrodes: Implications for aluminium corrosion. *Electrochem. Commun.* **2008,** *10* (9), 1334-1336.

[40]   Magnussen, O. M.; Hotlos, J.; Nichols, R. J.; Kolb, D. M.; Behm, R. J. Atomic structure of Cu adlayers on Au(100) and Au(111) electrodes observed by in situ scanning tunneling microscopy. *Phys. Rev. Lett.* **1990,** *64* (24), 2929-2932.

[41]   Madry, B.; Wandelt, K.; Nowicki, M. Deposition of copper multilayers on Au(111) in sulfuric acid solution: An electrochemical scanning tunneling microscopy study. *Surf. Sci.* **2015,** *637-638*, 77-84.

[42]   Madry, B.; Wandelt, K.; Nowicki, M. Deposition of copper and sulfate on Au(111): New insights. *Appl. Surf. Sci.* **2016,** *388*, 678-683.

[43]   Yoshioka, T.; Matsushima, H.; Ueda, M. In situ observation of Cu electrodeposition and dissolution on Au(100) by high-speed atomic force microscopy. *Electrochem. Commun.* **2018,** *92*, 29-32.

[44]   Berzins, T.; Delahay, P. Theory of Electrolysis at Constant Current in Unstirred Solution. II. Consecutive Electrochemical Reactions. *J. Am. Chem. Soc.* **1953,** *75* (17), 4205-4213.

[45]   Bard, A. J.; Faulkner, L. R. *Electrochemical Methods: Fundamentals and Applications*; John Wiley and Sons Inc., 2001.

[46]   Hinatsu, J. T.; Foulkes, F. R. Electrochemical kinetic parameters for the cathodic deposition of copper from dilute aqueous acid sulfate solutions. *Can. J. Chem. Eng.* **1991,** *69* (2), 571-577.

[47]   Battino, R.; Seybold, P. G. The O2/N2 Ratio Gas Solubility Mystery. *J. Chem. Eng. Data* **2011,** *56* (12), 5036-5044.

[48]   Aoki, K.; Akimoto, K.; Tokuda, K.; Matsuda, H.; Osteryoung, J. Chronopotentiometry at very small stationary disk electrodes. *J. Electroanal. Chem. Interf. Electrochem.* **1985,** *182* (2), 281-294.

[49]   Abrantes, L. M.; Fleischmann, M.; Li, L. J.; Hawkins, M.; Pons, J. W.; Daschbach, J.; Pons, S. The behavior of microdisk electrodes: Chronopotentiometry and linear sweep voltammetric experiments. *J. Electroanal. Chem. Interf. Electrochem.* **1989,** *262* (1), 55-66.

[50]   Hinatsu, J. T. Diffusion Coefficients for Copper (II) in Aqueous Cupric Sulfate-Sulfuric Acid Solutions. *J. Electrochem. Soc.* **1989,** *136* (1), 125.

[51]   Wilms, M.; Broekmann, P.; Stuhlmann, C.; Wandelt, K. In-situ STM

investigation of adsorbate structures on Cu(111) in sulfuric acid electrolyte. *Surf. Sci.* **1998,** *416* (1), 121-140.

[52] Brisard, G.; Bertrand, N.; Ross, P. N.; Marković, N. M. Oxygen reduction and hydrogen evolution–oxidation reactions on Cu(hkl) surfaces. *J. Electroanal. Chem.* **2000,** *480* (1), 219-224.

[53] Bodappa, N.; Su, M.; Zhao, Y.; Le, J. B.; Yang, W. M.; Radjenovic, P.; Dong, J. C.; Cheng, J.; Tian, Z. Q.; Li, J. F. Early Stages of Electrochemical Oxidation of Cu(111) and Polycrystalline Cu Surfaces Revealed by in Situ Raman Spectroscopy. *J. Am. Chem. Soc.* **2019,** *141* (31), 12192-12196.

[54] Gattinoni, C.; Michaelides, A. Atomistic details of oxide surfaces and surface oxidation: the example of copper and its oxides. *Surf. Sci. Rep.* **2015,** *70* (3), 424-447.

[55] Krawiec, H.; Szklarz, Z. Combining the Electrochemical Microcell Technique and the Electron Backscatter Diffraction method to study the electrochemical behaviour of polycrystalline aluminium in sodium chloride solution. *Electrochim. Acta* **2016,** *203*, 426-438.

[56] Yule, L. C.; Daviddi, E.; West, G.; Bentley, C. L.; Unwin, P. R. Surface microstructural controls on electrochemical hydrogen absorption at polycrystalline palladium. *J. Electroanal. Chem.* **2020,** *872*, 114047.

[57] Jiang, T.; Brisard, G. M. Determination of the kinetic parameters of oxygen reduction on copper using a rotating ring single crystal disk assembly (RRDCu(hkl)E). *Electrochim. Acta* **2007,** *52* (13), 4487-4496.

[58] Duan, X.; Warschkow, O.; Soon, A.; Delley, B.; Stampfl, C. Density functional study of oxygen on Cu(100) and Cu(110) surfaces. *Phys. Rev. B* **2010,** *81* (7), 075430.

[59] Liu, Q.; Li, L.; Cai, N.; Saidi, W. A.; Zhou, G. Oxygen chemisorption-induced surface phase transitions on Cu(110). *Surf. Sci.* **2014,** *627*, 75-84.

[60] Jensen, F.; Besenbacher, F.; Laegsgaard, E.; Stensgaard, I. Surface reconstruction of Cu(110) induced by oxygen chemisorption. *Phys. Rev. B* **1990,** *41* (14), 10233-10236.

[61] Nørskov, J. K.; Rossmeisl, J.; Logadottir, A.; Lindqvist, L.; Kitchin, J. R.; Bligaard, T.; Jónsson, H. Origin of the Overpotential for Oxygen Reduction at a Fuel-Cell Cathode. *J. Phys. Chem. B* **2004,** *108* (46), 17886-17892.

[62] Hansen, H. A.; Viswanathan, V.; Nørskov, J. K. Unifying Kinetic and Thermodynamic Analysis of 2 e– and 4 e– Reduction of Oxygen on Metal Surfaces. *J. Phys. Chem. C* **2014,** *118* (13), 6706-6718.

[63] López-Moreno, S.; Romero, A. H. Atomic and molecular oxygen adsorbed on (111) transition metal surfaces: Cu and Ni. *J. Chem. Phys.* **2015,** *142* (15), 154702.

[64] Matsumoto, T.; Bennett, R. A.; Stone, P.; Yamada, T.; Domen, K.; Bowker, M. In *Stud. Surf. Sci. Catal.*; Iwasawa, Y.;Oyama, N.;Kunieda, H., Eds.; Elsevier, 2001; Vol. 132.

[65] Besenbacher, F.; Nørskov, J. K. Oxygen chemisorption on metal surfaces: General trends for Cu, Ni and Ag. *Prog. Surf. Sci.* **1993,** *44* (1), 5-66.

[66] González-Dávila, M.; Santana-Casiano, J. M.; González, A. G.; Pérez, N.; Millero, F. J. Oxidation of copper(I) in seawater at nanomolar levels. *Mar. Chem.* **2009,** *115* (1-2), 118-124.

[67] Navon, N.; Cohen, H.; van Eldik, R.; Meyerstein, D. Effect of fumarate on the kinetics and reaction mechanism of Cu+aq with dioxygen. *J. Chem. Soc., Dalton Trans.* **1998,** *21*, 3663-3666.

[68] Meng, F.; Han, E.-H.; Wang, J.; Zhang, Z.; Ke, W. Localized corrosion behavior of scratches on nickel-base Alloy 690TT. *Electrochim. Acta* **2011,** *56* (4), 1781-1785.

[69] Blanc, C.; Creus, J.; Touzet-Cortina, M. In *Mechanics - Microstructure - Corrosion Coupling*; Blanc, C.;Aubert, I., Eds.; Elsevier, 2019.

[70] Tang, X.; Cheng, Y. F. Localized dissolution electrochemistry at surface irregularities of pipeline steel. *Appl. Surf. Sci.* **2008,** *254* (16), 5199-5205.

[71] Kleber, C.; Schreiner, M. Multianalytical in-situ investigations of the early stages of corrosion of copper, zinc and binary copper/zinc alloys. *Corros. Sci.* **2003,** *45* (12), 2851-2866.

[72] Kong, D.; Dong, C.; Ni, X.; Li, X. Corrosion of metallic materials fabricated by selective laser melting. *NPJ Mater. Degrad.* **2019,** *3* (1).

[73] Bentley, C. L.; Kang, M.; Maddar, F. M.; Li, F.; Walker, M.; Zhang, J.; Unwin, P. R. Electrochemical maps and movies of the hydrogen evolution reaction on natural crystals of molybdenite (MoS2): basal vs. edge plane activity. *Chem. Sci.* **2017,** *8* (9), 6583-6593.

[74] Aaronson, B. D. B.; Chen, C.-H.; Li, H.; Koper, M. T. M.; Lai, S. C. S.; Unwin, P. R. Pseudo-Single-Crystal Electrochemistry on Polycrystalline Electrodes: Visualizing Activity at Grains and Grain Boundaries on Platinum for the Fe2+/Fe3+ Redox Reaction. *J. Am. Chem. Soc.* **2013,** *135* (10), 3873-3880.

[75] Byers, J. C.; Güell, A. G.; Unwin, P. R. Nanoscale Electrocatalysis: Visualizing Oxygen Reduction at Pristine, Kinked, and Oxidized Sites on Individual Carbon Nanotubes. *J. Am. Chem. Soc.* **2014,** *136* (32), 11252-11255.

[76] Güell, A. G.; Cuharuc, A. S.; Kim, Y.-R.; Zhang, G.; Tan, S.-y.; Ebejer, N.; Unwin, P. R. Redox-Dependent Spatially Resolved Electrochemistry at Graphene and Graphite Step Edges. *ACS Nano* **2015,** *9* (4), 3558-3571.

Chapter 6

Triple-Phase Cu Dissolution and O$_2$ effect

Now that a wide spectrum method of analysis of the correlation between electrochemical properties and surface crystallographic orientation has been established for Cu corrosion studies (Chapter 5), it is time to start to see the effect of some specific environmental variables on it. The first obvious variable that can affect corrosion processes at this triple-phase Cu/H$_2$SO$_4$/Oil interphase, especially at the nanoscale, is the presence of O$_2$ in the system. Therefore, the analysis of O$_2$ action on this specific nanoscale corrosion system is the main topic of this chapter.

6.1. INTRODUCTION AND BACKGROUND

SECCM is based on the confinement of an electrochemical cell into a nanodroplet meniscus, and it is important to underline that, aside of the peculiar electrochemical setup of this specific technique, nanodroplets themselves present unique physical/chemical environments that influence the properties of the species confined inside. Indeed, the kinetics of many reactions are dramatically accelerated when confined to micro- or nanodroplets[1-6] due to the high droplet area-to-volume ratio and surface

tension, which can cause charge accumulation at the droplet-edge, local pH variations, fast de-solvation and rapid interfacial reactant/product exchange with the surrounding environment.[6-8] Beyond nanodroplets, interfacial exchange across nanometric phase boundaries takes place in many technologically and biologically important (electro)chemical reactions, including H_2/O_2 redox in fuel cells, chemical synthesis/polymerization, metabolic processes, electrodeposition and corrosion.[9,10] Reactions involving O_2 are particularly important due to its high natural abundance and ease of diffusion through hydrophilic and hydrophobic media.[11-13] In particular, as already underlined in the previous chapter, the flux of O_2 at the boundary of an aqueous nanodroplet is of fundamental interest for studying corrosion processes in automotive environment (*e.g.* in engine oil) and in specific occurrences in the oil industry.[14-16]

While homogeneous reactions in (sub)microdroplets have been widely explored,[17] there is a comparative lack of understanding on heterogeneous (*i.e.* inter-phase) reactions, *e.g.*, (electro)chemical processes that take place at the triple-phase interface formed with an electrode surface. Therefore, the specific setup of SECCM introduced in the previous chapter,[18-20] with the nanometric droplet (meniscus) cell formed at the end of the fluidic probe immersed in a layer of dodecane and in contact with a Cu polycrystalline surface, can serve as a model system for developing this kind of triple-phase studies. In order to study the role of O_2 in such condition, herein SECCM has been performed in potential-controlled mode, comparing voltammetric movies from polycrystalline Cu in the presence (i.e. in contact with air) and absence (i.e. in Ar atmosphere) of O_2, through the use of a sealed environmental cell. These data are rationalised through the use of FEM simulations of the nanodroplet environment. Furthermore, the possibility of multi-microscopic electrochemical analysis given by the co-use of SECCM and EBSD on the same sampled surface can bring this kind of electrochemical analysis to a higher level, where not only the effect of O_2 on the Cu corrosion reactions is

studied, but also the influence of the Cu crystallographic structure on such effect can be directly determined.

6.2. EXPERIMENTAL DETAILS

6.2.1. SECCM

The SECCM configuration employed in this chapter is completely analogous to that employed in Chapter 5 (with technical setup described in Chapter 2). A single channel pipette of diameter $\approx$ 400 nm (Figure 2.1b) filled with a 10 mM H_2SO_4 and equipped with an Ag/AgCl QRCE was approached to a polycrystalline Cu sample, with the surface of the metal and the nanodroplet meniscus immersed in dodecane layer. Nonetheless, some peculiarity of the work carried in this chapter need to be noted. Firstly, measurements were carried out both in presence and in absence of O_2, in order to compare the two cases. For measurements with O_2 present, the entire set up (*i.e.* SECCM probe and immersed Cu substrate) was exposed to the ambient air (as in the previous chapter). For measurements with O_2 absent, the tip of the SECCM probe and the dodecane covered Cu substrate were contained in a custom-built environmental cell,[21] which was mounted on the *x-y* piezoelectric positioner. The environmental cell was purged with high-purity Ar at a flow rate of 80 mL min^{-1} for at least 1 hour prior to use, which was also maintained for the duration of all SECCM scanning experiments.

Secondly, all SECCM experiment were carried out in potential-controlled regime, *i.e.* applying constant potential pulses and LSV to the system (voltammetric hopping mode).[22-24] Specifically the pipette was approached to the surface until meniscus contact, with the positional feedback achieved by monitoring the current flowing between the Cu working electrode and Ag/AgCl QRCE (termed the surface current, i_{surf}); the *z*-approach was halted upon detection of an absolute current threshold of 1.5 pA, (indicating the formation of a 2-electrode electrochemical cell).

During approach, an initial potential (E_i) of – 0.7 V vs Ag/AgCl QRCE (*ca.* – 0.45 V vs Ag/AgCl 3.4 M KCl) was applied at the Cu substrate. After landing, E_i was held for 0.25 s, before sweeping the potential positively at scan rate (v) = 1 V s^{-1}. After reaching the final potential (E_f) values of *ca.* + 0.24 V and + 0.61 V vs Ag/AgCl under aerated and de-aerated conditions, respectively, the direction of the potential sweep was reversed back towards E_i to produce a CV. Note that although a full CV was recorded, only the forward sweep is presented as an LSV. As CV curves were measured for each point of the scan area, i_{surf}, electrochemical movies were created, as previously reported.[22,25] During scanning, the nanopipette was approached at a speed of 3 μm s^{-1}, retracted at 10 μm s^{-1} (for a distance of 2 μm) and moved laterally at a speed of 20 μm s^{-1} between each point. The distance between each landing point (*i.e.* the hopping distance) was set to be 2 μm in every scan, in order to avoid overlapping of the areas wetted by the meniscus, and therefore keeping each CV measurement independent of the others.

6.2.2. FEM simulations

FEM simulations were performed with the COMSOL Multiphysics 5.4 software suite employing the geometry detailed in Figure 6.1. The simulation was carried out to reproduce the anodic dissolution of Cu in the controlled potential mode, sweeping the potential from the initial value of 0 V to the final value E_f (+ 0.24 V and + 0.61 V vs Ag/AgCl under aerated and de-aerated conditions, respectively). As discussed in detail below, two different cases were considered: (**1**) with no O₂ present in the system and Cu(I) is a surface adsorbed species; (**2**) with O₂ present in both the oil and aqueous solution and Cu(I) is a surface adsorbed species (*i.e.* reaction between Cu(I) and O₂ takes place heterogeneously). In all cases, a single channelled pipette was simulated, through a 2D axisymmetric geometry.
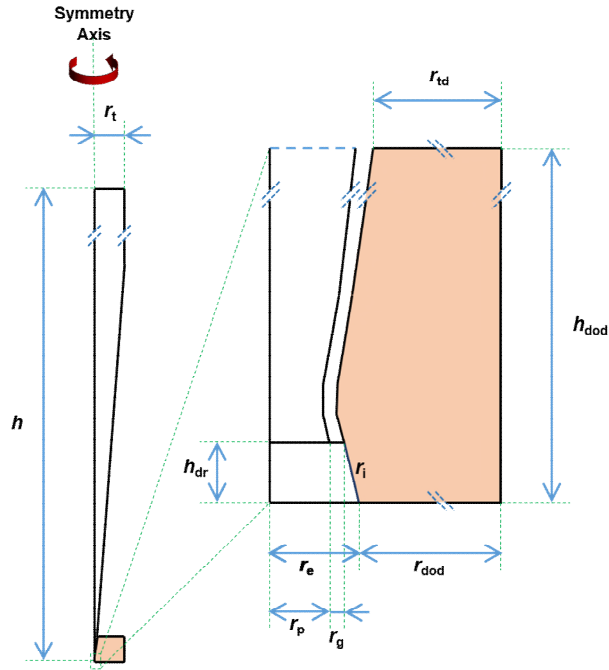
Figure 6.1: Scheme of the geometry employed in the FEM simulations. The whole geometry is represented on the left, while a magnification of the meniscus (droplet) cell area is schematized on the right. In all cases, $h = 5 \cdot 10^{-2}$ m, $h_{dr} = 200$ nm, $h_{dod} = 3 \cdot 10^{-4}$ m, $r_t = 3.5 \cdot 10^{-4}$ m, $r_{td} = 2.77 \cdot 10^{-4}$ m, $r_g = 37.5$ nm. In case (1), $r_p = 300$ nm and $r_e = 500$ nm and r_i was set as a no-flux boundary. In case (2), the aerated dodecane layer, coloured in orange, was added. $r_p = 225$ nm, $r_e = 350$ nm and r_i was set as the O_2 phase transfer boundary. In all cases r_{dod} was adjusted such as $r_{dod} + r_e = 3 \cdot 10^{-4}$ m. The values of r_e were chosen to be a reasonable approximation of the values extracted from the experimental wetting areas (Figure A.10, and the values of r_p were adjusted subsequently to be approximately 1.5 times smaller).

The mass-transport of all species in the aqueous and the oil phase was assumed to be governed solely by diffusion, and modelled using the Transport of Diluted Species module within COMSOL. The bottom boundary of the meniscus probe (labelled r_e in Figure 6.1), represents the electrode (*i.e.* the dissolving Cu surface), while the boundary marked as r_i represents the aqueous solution / dodecane interface. The following simulation conditions were employed:

Case 1: As the Cu/Cu(I) is assumed to be Nernstian (*vide infra*), and Cu(I) is a surface-adsorbed species, the Cu electrode is considered to be

fully covered with Cu(I)* in the range of potentials considered (*i.e. E >* 0.4 V vs. Ag/AgCl in de-aerated solution). Thus, the simulations were performed by considering a nominally "Cu(I)* electrode", where the rate determining step (RDS) is the Cu(I)/Cu(II) process. The flux, *J* for this sluggish 1 *e⁻* oxidation was therefore expressed as follows, assuming Butler-Volmer kinetics:

$$J_{Cu^{2+}} = k^{et} \exp\left[(1-\alpha) \frac{nF}{RT} \left(E - E^{0'} \right) \right]$$

(6.1)

where k^{et} is a generic heterogeneous standard rate constant for the electrode dissolution process [*i.e.* Cu(I)/Cu(II)], α is the transfer coefficient, E is the applied potential, $E^{0'}$ is the formal potential, n is the number of electrons exchanged, F is the Faraday constant, R is the Universal gas constant and T is the absolute temperature. The reaction is electrochemically irreversible, and thus the reverse reaction was not considered. Within these simulations, $T = 298.15$ K, $n = 1$ and $E^{0'} = -0.015$ V [see section 6.3.1, reaction (6.9)]. E was swept from 0 V to $E_f = +0.61$ V. k^{et} and α were adjusted heuristically to fit the experimental data. Cu^{2+} was the only species present in solution, and the current was obtained by integration over the whole electrode boundary, considering the rotational symmetry:

$$i_{surf} = \int_0^{2\pi} r d\phi \int_0^{r_e} nFD_{Cu^{2+}} \frac{\partial [Cu^{2+}]}{\partial z} dr$$

(6.2)

with $\partial[Cu^{2+}]/\partial z$ is the concentration gradient in the z direction, Φ is the rotation angle and $D_{Cu^{2+}}$ is the diffusion coefficient. $D_{Cu^{2+}}$ was set equal to $8 \cdot 10^{-6}$ cm² s⁻¹ (Ref. [26]) and the bulk concentration $C_{Cu^{2+}}$ was set equal to 0. Note that n was set equal to 2 when calculating i_{surf} through eq. (6.2), taking into account the overall stoichiometry of the Cu/Cu(II) process.

Case 2: As alluded to above, the Cu/Cu(I) process [reaction (6.8), see below] is assumed to be Nernstian. Thus, in the range of potentials considered (*i.e.* 0 < E < 0.24 V vs. Ag/AgCl in aerated solution), Cu(I)* only

partially covers the Cu surface, with activity described by the Nernst Equation:

$$a_{Cu(I)^*} = \exp\left[\frac{nF}{RT}\left(E - E^{0'}\right)\right] \tag{6.3}$$

With $n = 1$ and $E^{0'} = 0.315$ V. O_2 was added to the homogeneous solution, both in the aqueous and the oil phase, and its reaction with $Cu(I)^*$ was limited to the electrode surface, giving rise to the following flux:

$$J_{Cu^{2+}} = k_{O_2} a_{Cu(I)^*} \left[O_2\right]_{z=0} \tag{6.4}$$

The current was calculated with the same integration as in eq. (6.2), but with $n = 1$ in order to account for the fact that only 1 e^- was electrochemically exchanged.

Two different diffusion coefficients (D) and bulk concentrations (C) were employed for O_2 in the aqueous phase (*i.e.* in the nanopipette probe) and the dodecane phase, with $D_{aq} = 2 \cdot 10^{-5}$ cm^2 s^{-1} (Ref. [27]), $D_{dodec} = 4.11 \cdot 10^{-5}$ cm^2 s^{-1} (Ref. [28]), $C_{aq} = 0.26$ mM and $C_{dodec} = 2.02$ mM.[29] For the species Cu^{2+}, the same diffusional parameters of case (1) were employed. The relative initial concentrations were imposed as boundary conditions both at the top of the tip (labelled r_t in Figure 6.1) and at the top of the dodecane layer (labelled r_{td} in Figure 6.1). An equilibrium partition flux was imposed at the edge of the nano-droplet meniscus (labelled r_i in Figure 6.1):

$$J_{O_2, dodec}^{r_i} = -k_{in}\left[O_2\right]_{dodec} + k_{out}\left[O_2\right]_{aq} \tag{6.5}$$

$$J_{O_2, aq}^{r_i} = +k_{in}\left[O_2\right]_{dodec} - k_{out}\left[O_2\right]_{aq} \tag{6.6}$$

with

$$K_{part} = \frac{k_{out}}{k_{in}} \tag{6.7}$$

where K_{part} is the partition coefficient between the two phases. From literature data, $K_{part} = 7.8$ (Ref. [30]), while k_{out} was set to be a high value

(k_{out} = 10 cm s^{-1}), such that the system could be considered at equilibrium on the time scale of the calculation, as explored in the previous chapter (and detailed in Appendix, section A.3.2). Unless otherwise stated, all boundaries were set to have a no-flux condition. All simulations were carried out with a time dependent calculation of time $\boldsymbol{t} = (E_f - E_i)/v$, with v being the sweep rate, set to 1 V s^{-1}. The time was divided into 1000 time-steps, with a relative tolerance of 0.01. PARDISO solver was employed in all cases.

6.3. RESULTS AND DISCUSSION

6.3.1. Average effect of O$_2$ on the voltammetric curve.

As introduced above, SECCM was deployed to investigate the effect of O$_2$ on the electrochemical reactions of Cu within an acidic nanodroplet (pH $\approx$ 2) immersed in dodecane. On the surface, a constant potential pulse was carried out at – 0.45 V vs. Ag/AgCl, followed by local voltammetric analysis (starting at – 0.45 V vs. Ag/AgCl and sweeping positively at voltammetric scan rate, v = 1 V s^{-1}) under ambient and argon-purged conditions (in an environmental cell)[21] to isolate the effect of O$_2$. The average curves measured in the two different conditions, as well as the average pre-LSV pulses, are shown in Figure 6.2.

The first, obvious distinction between the aerated and the de-aerated case is given by the possibility of O$_2$ of being reduced at the electrode, within the cathodic side of the LSV, therefore distinguishing between ORR [reaction (5.4)] and HER [reaction (5.5)] as the main cathodic process. Based on thermodynamic considerations [*e.g.*, Eqs. (5.4) and (5.4)], the cathodic wave would be expected to shift negatively from the aerated to the de-aerated case, with the HER place at more negative potentials than the ORR. However, as shown in Figure 6.2a, the current density of the cathodic wave is very similar in the two cases, with the de-aerated one being, in fact, slightly larger.
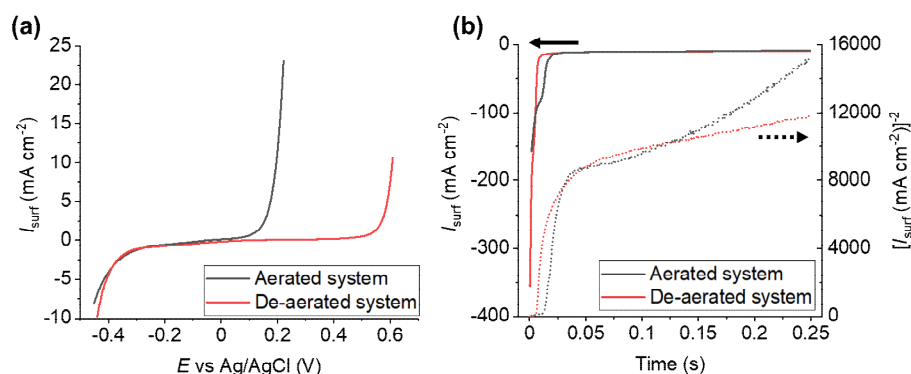
Figure 6.2: (**a**) Average LSVs (v = 1 V s^{-1}) obtained with the voltammetric SECCM configuration in a Cu/H$_2$SO$_4$/dodecane triple-phase system. (**b**) Average constant potential pulse, performed at the initial potential of the LSV (– 0.45 V) for 0.25 s before the start of the LSV, with the solid curve representing the current density (I_{surf}) and the dotted one representing (I_{surf})$^{-2}$. In both (a) and (b) the red curves were obtained in deaerated conditions (averaging 5200 single measurements) and the grey curves were obtained in aerated conditions (averaging 5100 single measurements). The E scale is referred to a leakless Ag/AgCl electrode with a 3.4 M KCl solution.

Interestingly, the same effect is also observed during the pre-LSV pulse (Figure 6.2b). Consulting the phase stability diagram of Cu,[31] the HER is the only possible reaction in de-aerated acidic solution, corroborated by the shape of the i–t curve, which is essentially Cotrellian beyond 0.05 s [Figure 6.2b, with the "Cottrell" behaviour defined by eq. (1.44)], as well as the Tafel slope obtained from the LSV ($\approx$ 120 mV/dec, going from 10 mA cm^{-2} to 1 mA cm^{-2}, Figure 6.2a). By contrast, in the aerated case, the i–t curve is non-Cotrellian (Figure 6.2b) and the Tafel slope is significantly larger (Figure 6.2a), indicating that a different reaction (*i.e.* ORR) is taking place.

Therefore, it appears that the HER occurs at a significantly smaller overpotential than would be expected for Cu, which is reportedly a relatively poor HER catalyst in bulk.[32,33] The exact cause of this phenomenon is unknown and is presently under investigation. One possibility is that it arises from unique reactivity, charge accumulation and/or H$_2$ mass-transport at the aqueous/oil/metal interface. The cathodic branch of the LSV will not be further discussed in this chapter, rather the anodic

197

branch, which can also give more insights on the properties of the corrosion process in the two cases, will be considered.

6.3.2. Effect of O₂ on Cu electro-dissolution.

The anodic dissolution of (electro)dissolution of metallic copper can follow several different pathways, visually schematised, both in the deaerated and aerated case, in Figure 6.3. The first reaction is the oxidation of Cu to Cu(I):

$$Cu_{(s)} \rightarrow Cu(I) + e^- \quad E^0 = 0.315 \text{ V vs Ag/AgCl}^{34} \tag{6.8}$$

This process is assumed to be fast (*i.e.* at equilibrium) on the timescale of the reactions considered.[35-37] Due to very low thermodynamic stability in aqueous media, Cu(I) is assumed to exist as a complexed surface-adsorbed species [denoted Cu(I)* hereafter] on the voltammetric timescale (*vide infra*), as per previous studies.[36-38] In the absence of O₂ (Figure 6.3a), Cu(I)* is furtherly electro-oxidized to Cu(II):

$$Cu(I) \rightarrow Cu(II) + e^- \quad E^0 = -0.015 \text{ V vs Ag/AgCl}^{34} \tag{6.9}$$
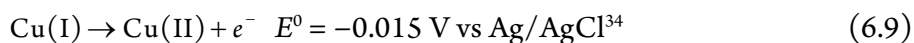
Even though the reaction is extremely favoured thermodynamically [such that Cu(I) can rarely form stable complexes in aqueous solution], it is subject to severe kinetic limitations.[35,37] In the presence of O₂, additional Cu oxidation pathways have been proposed,[39,40] involving O₂ as an electron acceptor from the Cu(I)* species, *e.g.*, in acidic solution:

$$Cu(I)^* + O_2 \rightarrow CuO_2^+ \tag{6.10}$$

$$CuO_2^+ + H^+ \rightarrow Cu(II) + HO_2 \tag{6.11}$$

where HO₂ is the protonated form of the superoxide (O₂⁻) ion.

Naturally, due to the existence of distinct aerobic [Eqs. (6.8), (6.10) and (6.11)] and anaerobic [Eqs. (6.8) and (6.9)] pathways, O₂ perturbs the electro-dissolution of Cu, readily demonstrated with conventional macroscopic (bulk) voltammetry, displayed in Figure 6.4. In particular,
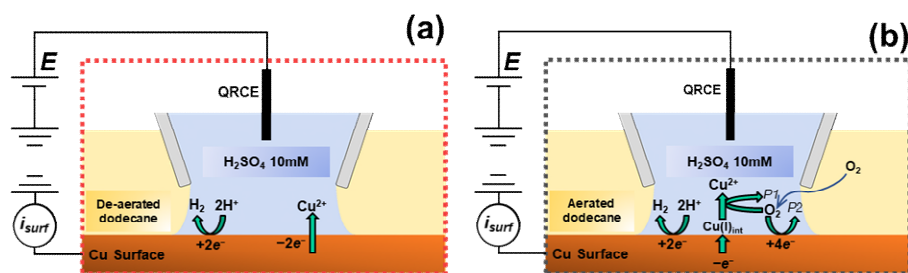
Figure 6.3: Schematic of SECCM set up (nanopipette tip filled with 0.01 M H_2SO_4 and equipped with an Ag/AgCl, immersed in dodecane and contacted with the Cu surface) and the possible related cathodic and anodic processes in (**a**) the de-aerated or (**b**) the aerated system.
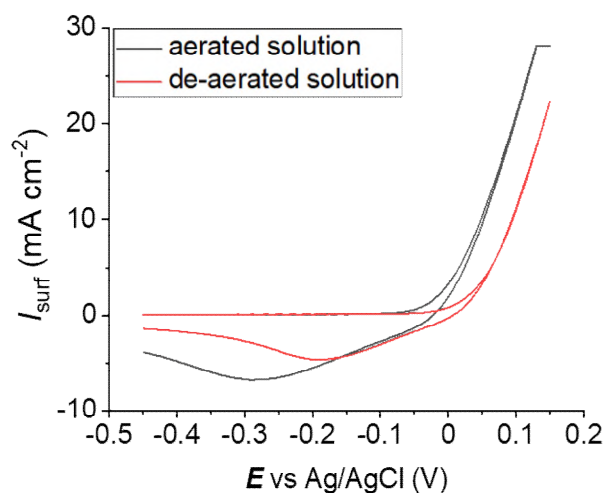
Figure 6.4: Macroscopic CVs obtained from a 3 mm diameter Cu macrodisc electrode in aerated (black curve) and de-aerated (red curve) 1 M H_2SO_4. The potential was swept from -0.45 V to $+0.15$ V vs Ag/AgCl, at a sweep rate of 1 V s^{-1}. In both cases, a potential pulse of 60s was applied at the initial potential prior to the start of the sweep. The two curves present a difference in the onset potential for Cu electro-dissolution of approximately ≈ 50 mV. Unlike the SECCM experiments, all the macroscopic electro-chemistry reported here was carried out in a 1 M H_2SO_4 solution, in order to avoid interference by solution resistance. Such problems can be neglected in the SECCM environment due to the extremely small current measured.

the oxidation wave is shifted *ca.* $+50$ mV in aerated H_2SO_4 (grey curve) compared to de-aerated (red curve). Other differences can be seen in the position and the magnitude of the Cu re-deposition peak, indicating a possible complex and a-symmetric influence of O_2 on the two processes, as also observed in the previous chapter.

As alluded to above, due to the unique nanodroplet configuration of SECCM (*i.e.* large surface area-to-volume and rapid interfacial exchange), the effect of O_2 is dramatically enhanced, as demonstrated in Figure 6.2a. Evidently, in the SECCM configuration the Cu electro-oxidation wave is shifted *ca.* +400 mV in the presence of O_2, highlighting the significance of high O_2 influx in the nanodroplet configuration. Interestingly, while both curves in Figure 6.2a are shifted anodically compared to their bulk counterparts (Figure 6.4), this effect is more significant under de-aerated conditions, increasing the "potential gap" between the two curves. This may stem from the fact that (electro-)dissolution involves the removal of Cu atoms from active step sites,[41,42] which are expected to be readily annihilated from the nanometric probed (working electrode) area.

In other words, during Cu electro-oxidation, the active step sites would "move" to the boundaries of the nanometric SECCM meniscus cell on a very short timescale, thereby forcing the reaction to take place on the less active basal surface. Other explanations could take into account the surface modification caused by the enhanced HER described above (if the HER hinders the reduction of the native oxide layer), as well as local pH variation caused by such reaction in the cathodic branch of the LSV. While these effects make Cu electro-oxidation more difficult in de-aerated conditions [Eqs. (6.8) and (6.9)], this effect is partially offset by the high flux of O_2 under aerated conditions, which effectively forces the reaction through an alternative pathway [Eqs. (6.10) and (6.11)].

6.3.3. FEM simulations of O₂ action in Cu dissolution

The mechanism of action of O_2 on Cu electro-dissolution was further explored semi-quantitatively by FEM simulations, whose geometry is schematized in Figure 6.5a and described in more details in section 6.2.2. The oil behaves as an O_2 reservoir through a partition equilibrium at the dodecane/nanodroplet interface. As stated above, Cu(I) was assumed to

exist solely as a complexed surface-adsorbed species [*i.e.* Cu(I)*],[36-38] and thus disproportionation in solution and homogeneous reactions with O_2 were not considered. In addition, since eq. (1) is assumed fast, at low driving force (*i.e. E < E*[0], as in the aerated case) the surface concentration of Cu(I)* is governed by the Nernst equation,[38] while at high driving force (*i.e. E >> E*[0], as in the de-aerated case) the surface is fully covered in Cu(I)*. Note that the E^0 values are reported under standard conditions[34] and have not been modified to take surface adsorption of Cu(I) into account, thus the kinetic parameters derived below are apparent values and may not be physically meaningful.

In the de-aerated case (Figure 6.5b), the electro-dissolution was assumed to proceed *via* eq. (6.8) followed by eq. (6.9). As eq. (6.8) is Nernstian (*vide supra*), the experimental data were simulated by considering a nominally "Cu(I)* electrode" undergoing electro-oxidation *via* eq. (6.9) , governed by Butler-Volmer kinetics with the charge-transfer coefficient (*a*) and electron-transfer coefficient (k^{et}) treated as variables. In the aerated case, shown in Figure 6.5c, the electro-dissolution was assumed to proceed *via* eq. (6.8) followed by eq. (6.10). Evidently, Cu electro-oxidation is highly sensitive to the kinetic constant of eq. (6.10), owing to the unique configuration of the nanodroplet cell, with a high contact surface between the aqueous and oil phase, the latter effectively acting as an O_2 reservoir. This is clear in the simulated concentration profile (Figure 6.5d), where at E_{5mA} (defined as the onset potential required to achieve a current density of 5 mA cm^{-2}, *ca.* 0.17 V in the best-fit simulation), O_2 is most depleted at the centre of the meniscus cell (*i.e.* at the point furthest from the aqueous-oil interface).

Note that the FEM simulations predict that O_2 becomes the limiting factor at high driving force, limiting *I* to a steady state value of *ca.* 50 mA cm^{-2}, as shown in Figure 6.5e, but this is not observed experimentally (see Figure 6.2b). This is because in reality there are many follow up reactions
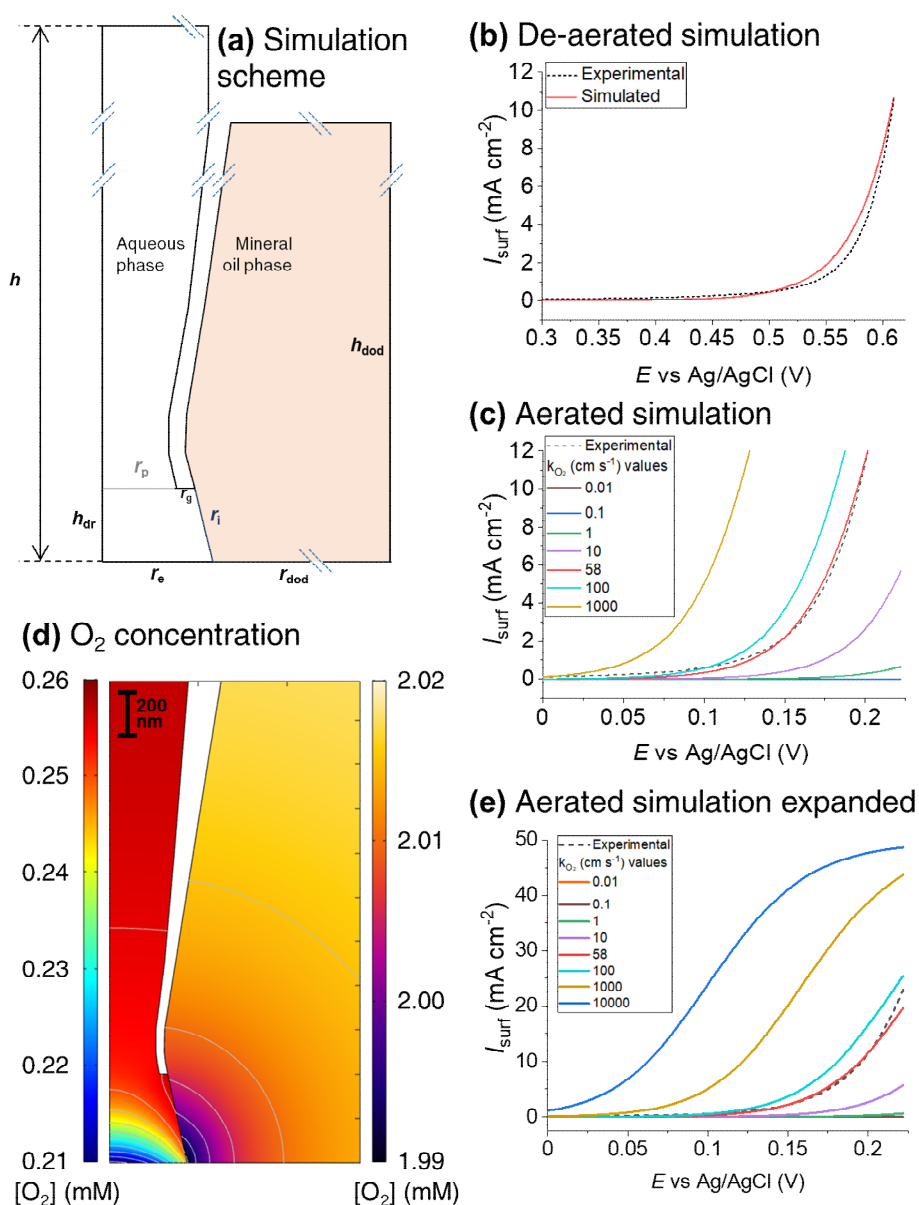
Figure 6.5: (**a**) Scheme of the geometry employed in the FEM simulations, adapted from Figure 6.1. (**b**) Simulation-experiment comparison ($\alpha = 0.25$, $k^{et} = 2.3 \cdot 10^{-16}$ mol cm^{-2} s^{-1}) under de-aerated conditions. (**c**) Simulation-experiment comparisons (with different values of the kinetic constant, k_{O2}) under aerated conditions. (**d**) Simulated O₂ concentration profile ($k_{O2} = 58$ cm s^{-1}) obtained at E_{5mA} ($E = 0.17$ V, $I = 5$ mA cm^{-2}). (**e**) Reproduction of (c) over a wider current density scale and with the curve obtained at $k_{O_2} = 10\,000$ cm s^{-1} added to the plot.

that would serve to regenerate O₂ (*e.g.*, local pH changes due to eq. (6.11) , electro-oxidation of O₂⁻ to O₂ and other parasitic processes) and further release/oxidize Cu(I) in solution [*e.g.*, reverse of eq. (6.10), eq. (6.11),

and disproportionation], which play prominent roles in the electro-dissolution process.[39,40,43] As such, the simplified model presented in Figure 6.5, which is in excellent agreement with the experimental data at low driving force (*i.e. E* < 0.24 V vs. Ag/AgCl, Figure 6.5c), represents the minimum possible influence of O_2 on Cu electro-dissolution within an aqueous nanodroplet environment.

6.3.4. Multi-microscopy grain activity analysis

So far, the "representative" LSVs considered (Figure 6.2a) were obtained by averaging *ca.* 5000 independent measurements on polycrystalline Cu under each condition. Their analysis provides a general idea of the effect of O_2 on Cu electro-dissolution (Figure 6.5), but ignores the possible influence of the underlying surface structure. Beyond its unique nanodroplet cell configuration (*vide supra*), SECCM enables the construction of spatially-resolved electrochemical activity movies (Appendix, Movie A7 to A10), which can be readily correlated to co-located structural information (*i.e.* crystallographic orientation from electron backscattered diffraction, EBSD) to resolve nanoscale structure-activity *directly* and *unambiguously*, as specifically shown in Chapter 4.[20,22,44]

The results of this *correlative multi-microscopy approach* are shown in Figure 6.6. The comparison of the E_{5mA} map under de-aerated and aerated conditions (Figure 6.6 and b, respectively) with the co-located crystallographic orientation maps (Figure 6.6c and d, respectively) reveals that Cu electro-dissolution is a highly grain-dependent process. Interestingly, compiling these data into electrochemistry/structure correlation plots (Figure 6.6e and f, with the construction of such graphs described in Chapter 2, section 2.8) reveals that the grain-dependency of the Cu electro-dissolution process is different in the de-aerated and aerated cases, again supporting the initial assumption that the Cu(I)-O_2 interaction takes place heterogeneously [*i.e.* at the electrode surface, eq. (6.10)].
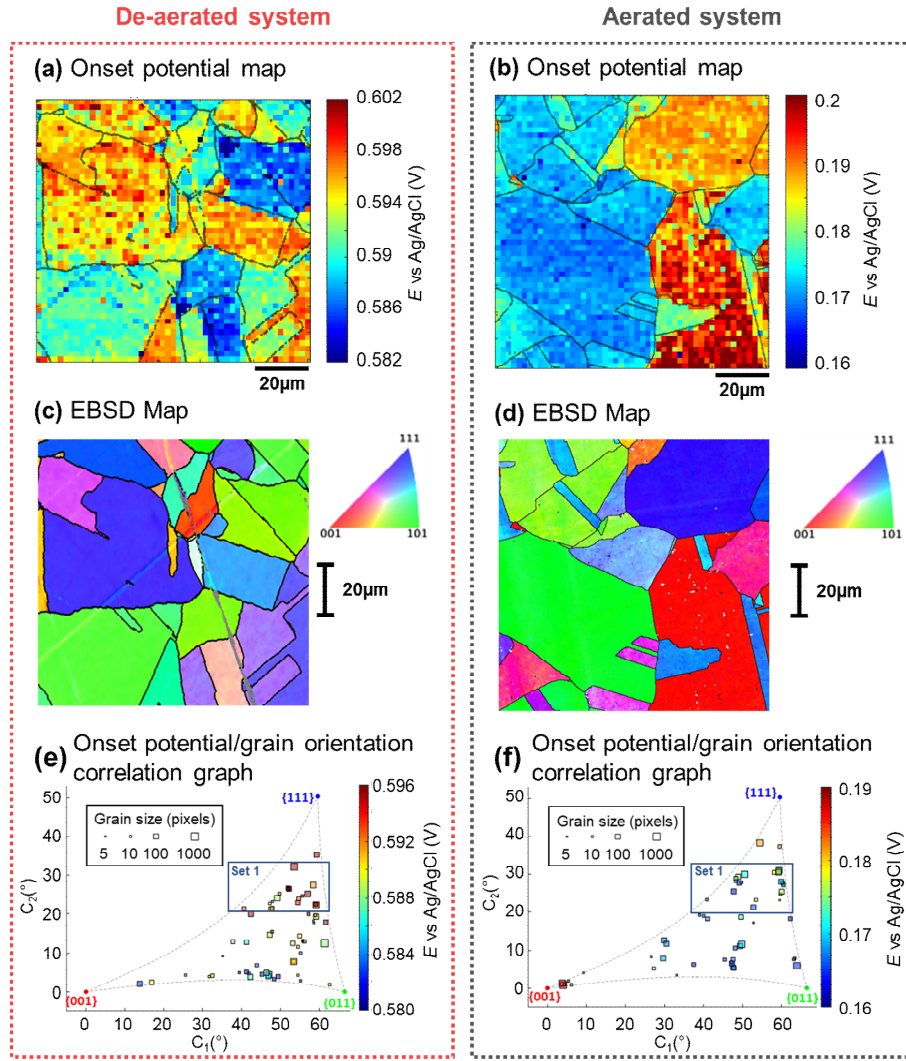
Figure 6.6: **(a,b)** Maps of E_{5mA} obtained under **(a)** de-aerated (extracted from Movie A7) and **(b)** aerated (extracted from Movie A9) conditions. **(c,d)** Corresponding crystallographic orientation maps, IPFz obtained with EBSD are shown in **(c)** and **(d)**, respectively. **(e,f)** Electrochemistry (E_{5mA}) vs. structure (average grain orientation) correlation plots, shown in **(e)** and **(f)**, respectively. E_{5mA} was extracted from Movies A7 and A8 [de-aerated, *i.e.* from (a) and Figure A.17a] in (e) and Movies A9 and A10 [aerated, *i.e.* from (b) and Figure A.17b] in (f). (a,b) were obtained in the SECCM configuration with a nanopipette probe containing 0.01 M H₂SO₄. The grain boundaries extracted from (c) and (d) were overlaid to (a) and (b), respectively.

Under de-aerated conditions (Figure 6.6e), the grains with the lowest susceptibility to oxidation are close to the {111} orientation (*i.e.* with C_2 ≥ 20°, E_{5mA} > 0.59 V), while grains with low C_2 values, in particular those

close to the {012} and {035} planes possess the highest susceptibility (*i.e.* E_{5mA} < 0.58 V). This difference may be attributable to the intrinsically lower surface energy of the {111} plane[45] and/or grain-dependent surface stabilization brought on by the adsorption of (bi)sulfate.[46-48]

Further, the E_{5mA} values for the two grains that are closest to the {001} orientation (*i.e.* the two grains that lay at 10° < C_1 < 20° in Figure 6.6e) tentatively indicate an increase in electro-oxidation susceptibility towards the {001} (although no definitive conclusions can be drawn since this family of grains is generally under-represented in the de-aerated data). By contrast, under aerated conditions (Figure 6.6f), grains close to the {100} orientation (C_1 < 10°, E_{5mA} > 0.18 V) possess the lowest oxidation susceptibility, followed by those very close to the {111} orientation ($C_2 \geq 35°$, $E_{5mA} \approx 0.18$ V). In addition, grains with orientations in the 20° $\leq C_2 \leq 35°$ range now possess relatively high oxidation susceptibility, with $E_{5mA} \approx 0.17$ V.

Aside from specific areas of activity, qualitatively comparing Figure 6.6e and f it is possible to note a general trend of decreasing E_{5mA} by decreasing C_2 [*i.e.* moving away from the {111} orientation], with then a steep increase in the aerated case once the {001} orientation is reached (corresponding to the left side of the graph presented in Figure 6.6f). However, this decreasing trend has a much steeper drop-off in the aerated case, particularly for the grains that are around 20° $\leq C_2 \leq 30°$ (called Set 1 for brevity, identified in Figure 6.6e and f).

Therefore, the presence of O_2 tends to strongly facilitate the anodic dissolution process on the grains of Set 1, if compared to the {001} oriented grains, which instead pass from being relatively active in the de-aerated case to be the most resistance. To be clear, actually O_2 strongly facilitate the oxidation process on both these sets of grains, but it seems to be much more efficient at doing so on Set 1.

6.3.5. Probing heterogeneity within similarly oriented grains

Expanding further on the structure-dependent electrochemical analysis, it is useful step aside from the examination of the general trend of electrochemical activity within the whole spectrum of orientation and give a closer look to the variability within groups of grains with similar orientation. As already observed in the previous chapter, some grains with very similar orientation (adjacent in the correlation plot), can present very different electrochemical behaviour, with one generally be an exception compared to the surrounding grains. This is also the case for the sets of grains collected herein.

Examining the statistical distribution of E_{5mA}, over all the single point measurements performed with SECCM in Movies A7-A10, shown in Figure 6.7a, it is clear that there is a higher variability in the aerated data (*e.g.*, standard deviations of *ca.* 9 and 4 mV in the aerated and de-aerated cases, respectively). While this may be partly due to the fact that two different sets of grains were examined [*e.g.*, as stated above, in the de-aerated case, there is a substantial lack of $\{001\}$ oriented grains, that are instead well represented in the other case], these data strongly suggest that the presence of O_2 causes the anodic dissolution process to become more strongly structure-sensitive, and therefore present a higher degree of variability with subtle variations of crystallographic orientation.

This intrinsic variability is also evident in the electrochemistry (E_{5mA}) vs. structure (average grain orientation) correlation plots (Figure 6.6e and f), where there are several exceptions to the general trends described above, as highlighted in the reproductions shown respectively, in Figure 6.7b and c. For example, as noted above, in the de-aerated case E_{5mA} tends to increase with C_2, with grains close to $\{111\}$ orientation being less susceptible to electro-oxidation. However, there are several exceptions to this trend, such as grains 16 (Figure A.18 and Table A.3, highlighted in
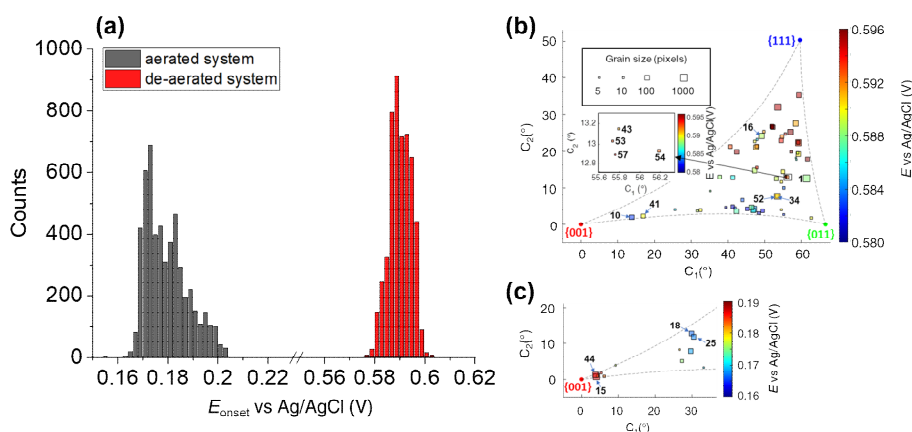
Figure 6.7: (**a**) Statistical distribution of E_{5mA} calculated for each measured point, respectively in aerated (grey distribution) and de-aerated (red distribution) conditions. The calculated standard deviations are 0.0085 V for the aerated condition and 0.0043 V for the de-aerated. (**b-c**) Reproduction of (**b**) Figure 6.6e (**c**) part Figure 6.6f with identified critical areas and grains. The grains are numbered according to the lists presented in Appendix, section A.5.2.

Figure 6.7b), with an orientation close to {358}, that possesses significantly lower E_{5mA} values than its neighbours. By contrast, some specific groups of grains, such as grains 34 and 52 (Figure A.18 and Table A.3, highlighted in Figure 6.7b) that have an orientation close to {168}, and 43, 53, 54 and 57 (Figure A.18 and Table A.3, highlighted in Figure 6.7b), that have an orientation close to {268}, possess higher E_{5mA} values than the surrounding ones.

Such local variations were observed also in the aerated case. Specifically, it is worth to examine a small subset of grains that exhibited unique Cu electro-dissolution activities despite nominally similar orientations. The grains were named α to δ for more clarity, but they numbered, respectively, 46, 51, 52 and 54, in Figure A.19 and Table A.4. Figure 6.8a reports an extract of the E_{5mA} map extracted from Movie A10 (shown entirely in Figure A.17b)[§] containing such grains, compared to the co-located EBSD map in Figure 6.8b (shown entirely in Figure A.17d).

[§] Figure A.17b, together with Figure 6.6b, was used to construct the electrochemistry/orientation correlation map for the aerated case.
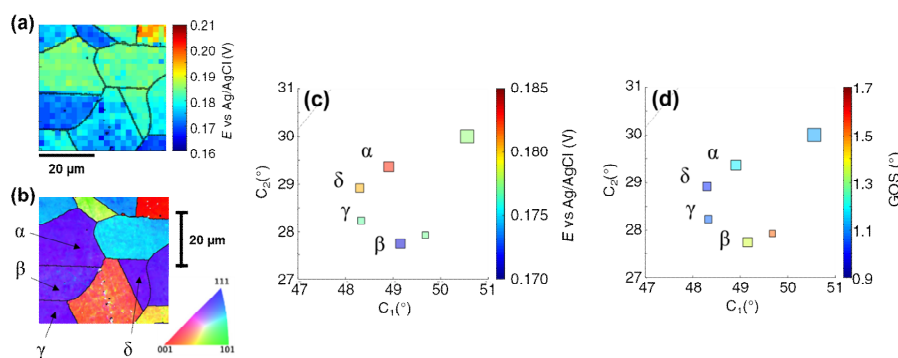
Figure 6.8: **(a)** Extract of E_{5mA} maps from Movie A10 (aerated conditions) and **(b)** the corresponding EBSD map (extract of Figure A.17d). **(c-d)** Extracts of (c) E_{5mA} and (d) GOS vs. structure (average grain orientation) correlation plots, respectively from Figure 6.6f and Figure 6.9.

The selected group of grains presents near-identical average crystallographic orientations, as shown by the electrochemistry/structure correlation map in Figure 6.8c (they differ from each other by < 2° in the projection), and yet the Cu electro-dissolution process is significantly easier on grain β, if compared to the others (E_{5mA} is *ca.* 20 mV more negative). The difference can be visualised also on the map (Figure 6.8a) since the grains are adjacent on the surface. This data clearly indicates that the grain average orientation cannot be taken as the sole descriptor of Cu oxidation susceptibility.[49]

Delving further into the EBSD data, grain β possesses a higher grain orientation spread (abbr. GOS, corresponding to the intra-grain standard deviation in crystallographic orientation) than the others, as shown in Figure 6.8d. Interestingly, for grain β the additional surface disorder induced by the larger grain orientation spread translates to higher activity (consistent with the discussion on stepped vs basal surface activity, above). As shown in Figure 6.9, (portraying the complete GOS map), the GOS itself is grain dependent, being remarkably higher for grains in the lower part of the graph, *i.e.* towards the grains [{001} and {011}], which are less thermodynamically stable.[45] This may indicate that the more stable planes, such as {111}, tend to form more pristine (*i.e.* less defective)
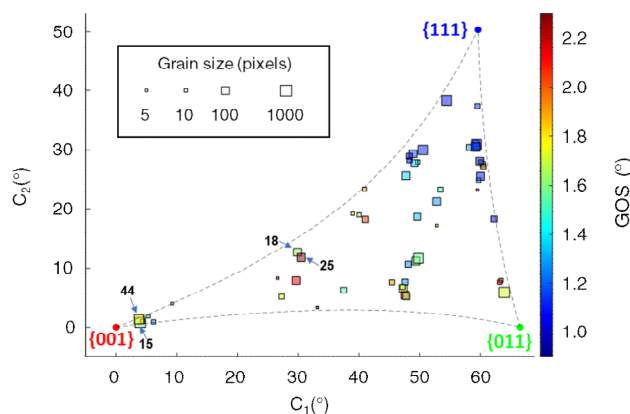
Figure 6.9: Correlation plot for the GOS and the crystallographic orientation for the aerated case, obtained by data extracted form Figure 6.6d and Figure A.17d. Significant grains mentioned in the text are highlighted on the plot.

surfaces, but the presence of defects can nonetheless be extremely important in dictating the electrochemical activity of the grain.[50]

However, in other cases of high GOS variability within families of grains that are very close in orientation, a corresponding significant change of E_{5mA} was not observed. For example, consider grains 18 and 25 (Figure A.19, Table A.4, highlighted in Figure 6.7 and Figure 6.9), that in the projection differ only by 1.07°, but with a ΔGOS of 0.82°; or grains 15 and 44, (Figure A.19, Table A.4, highlighted in Figure 6.7 and Figure 6.9), that are only 0.58° apart but have a ΔGOS of 0.46° (for comparison, the ΔGOS between grain α and β in Figure 4 of the main text is 0.47°). In both cases, as highlighted in Figure 6.7c, the electrochemical activity of the grains in the couple is all but similar ($\Delta E_{5mA} < 1$ mV). Therefore, the orientation of the specific planes and the nature of the steps (defects) interrupting the regularity of each specific grain, rather than just the amount of them, appears to be a fundamental factor affecting the grain dependency of the considered reaction(s).

6.4. CONCLUSION

The work presented in this chapter took advantage of the unique three-phase configuration of SECCM, introduced in Chapter 5 to study

how rapid interfacial exchange can influence (electro)chemical pathways in an aqueous nanodroplet environment. In particular, the effect of O_2 on Cu electro-dissolution was studied employing voltammetric SECCM coupled with co-locate crystallographic orientation analysis (EBSD), comparing de-aerated (Ar fluxed) and aerated cases. O_2 flux across the nanodroplet-dodecane interface was observed to have a dramatic effect on the rection, shifting E_{5mA} by *ca.* – 400 mV compared to the de-aerated case. Such effect was associated with the different Cu dissolution mechanism in presence of O_2 and the possibility of the oil phase to be an infinite reservoir of O_2 during the scale of the experiment. The Cu electro-dissolution presented complex grain dependent characteristics in both de-aerated and aerated conditions (as partially explored in Chapter 5), but the effect of oxygen was found to affect such dependency, with grains in some areas of the orientation spectrum (e.g. a specific band of grains relatively close to the {111} orientation) being more sensitive to the reaction with O_2.

Furthermore, the grain dependent analysis revealed how some grains of similar orientation can present different electrochemical behaviour, possibly due to "contamination" of the crystallographic planes themselves (which , in a polycrystalline surface, are often far from ideality), with slightly different oriented planes and steps. This finding also highlights the importance of a comprehensive whole-spectrum analysis on a wide range of grains for distinguishing the general behaviour from local variations. As inter-phase reactions involving interfacial reactant/product exchange at complex surfaces play a pivotal role not only in corrosion studies, as highlighted by this and the previous chapter and further discussed in Chapter 7, but also in renewable energy generation/storage applications (*e.g.,* batteries and fuel cells), materials synthesis (*e.g.,* electrodeposition) and biological processes (*e.g.,* cellular metabolism), one may envisage that SECCM will play a significant role in future high-throughput studies in these important areas.

6.5.   REFERENCES

[1]   Girod, M.; Moyano, E.; Campbell, D. I.; Cooks, R. G. Accelerated bimolecular reactions in microdroplets studied by desorption electrospray ionization mass spectrometry. *Chem. Sci.* **2011,** *2* (3), 501-510.

[2]   Yan, X.; Cheng, H.; Zare, R. N. Two-Phase Reactions in Microdroplets without the Use of Phase-Transfer Catalysts. *Angew. Chem. Int. Ed.* **2017,** *56* (13), 3562-3565.

[3]   Banerjee, S.; Gnanamani, E.; Yan, X.; Zare, R. N. Can all bulk-phase reactions be accelerated in microdroplets? *Analyst* **2017,** *142* (9), 1399-1402.

[4]   Nam, I.; Lee, J. K.; Nam, H. G.; Zare, R. N. Abiotic production of sugar phosphates and uridine ribonucleoside in aqueous microdroplets. *Proc. Natl. Acad. Sci. U.S.A.* **2017,** *114* (47), 12396.

[5]   Koga, S.; Williams, D. S.; Perriman, A. W.; Mann, S. Peptide–nucleotide microdroplets as a step towards a membrane-free protocell model. *Nat. Chem.* **2011,** *3* (9), 720-724.

[6]   Mortensen, D. N.; Williams, E. R. Ultrafast (1 μs) Mixing and Fast Protein Folding in Nanodrops Monitored by Mass Spectrometry. *J. Am. Chem. Soc.* **2016,** *138* (10), 3453-3460.

[7]   Mashaghi, S.; van Oijen, A. M. External control of reactions in microdroplets. *Sci. Rep.* **2015,** *5* (1), 11837.

[8]   Mondal, S.; Acharya, S.; Biswas, R.; Bagchi, B.; Zare, R. N. Enhancement of reaction rate in small-sized droplets: A combined analytical and simulation study. *J. Chem. Phys.* **2018,** *148* (24), 244704.

[9]   Terry Weatherly, C. K.; Ren, H.; Edwards, M. A.; Wang, L.; White, H. S. Coupled Electron- and Phase-Transfer Reactions at a Three-Phase Interface. *J. Am. Chem. Soc.* **2019,** *141* (45), 18091-18098.

[10]   Kumar, A.; Ciucci, F.; Morozovska, A. N.; Kalinin, S. V.; Jesse, S. Measuring oxygen reduction/evolution reactions on the nanoscale. *Nat. Chem.* **2011,** *3* (9), 707-713.

[11]   Gu, C.; Nie, X.; Jiang, J.; Chen, Z.; Dong, Y.; Zhang, X.; Liu, J.; Yu, Z.; Zhu, Z.; Liu, J.et al. Mechanistic Study of Oxygen Reduction at Liquid/Liquid Interfaces by Hybrid Ultramicroelectrodes and Mass Spectrometry. *J. Am. Chem. Soc.* **2019,** *141* (33), 13212-13221.

[12]   Subbaraman, R.; Strmcnik, D.; Paulikas, A. P.; Stamenkovic, V. R.; Markovic, N. M. Oxygen Reduction Reaction at Three-Phase Interfaces. *ChemPhysChem* **2010,** *11* (13), 2825-2833.

[13]   Yan, X.; Lai, Y.-H.; Zare, R. N. Preparative microdroplet synthesis of carboxylic acids from aerobic oxidation of aldehydes. *Chem. Sci.* **2018,** *9* (23), 5207-5211.

[14]   Jardine, F. Engine Corrosion - its Causes and Avoidance. *SAE Tech. Pap. 250030* **1925**.

[15]   Lejre, K. H.; Kiil, S.; Glarborg, P.; Christensen, H.; Mayer, S. In *ASME 2017 Internal Combustion Engine Division Fall Technical Conference*, 2017.

[16]   Zhang, H.; Lan, H.-q. A review of internal corrosion mechanism and

experimental study for pipelines based on multiphase flow. *Corros. Rev.* **2017,** *35* (6), 425-444.

[17] Lach, S.; Yoon, S. M.; Grzybowski, B. A. Tactic, reactive, and functional droplets outside of equilibrium. *Chem. Soc. Rev.* **2016,** *45* (17), 4766-4796.

[18] Ebejer, N.; Güell, A. G.; Lai, S. C. S.; McKelvey, K.; Snowden, M. E.; Unwin, P. R. Scanning Electrochemical Cell Microscopy: A Versatile Technique for Nanoscale Electrochemistry and Functional Imaging. *Annu. Rev. Anal. Chem.* **2013,** *6* (1), 329-351.

[19] Bentley, C. L.; Kang, M.; Unwin, P. R. Nanoscale Surface Structure–Activity in Electrochemistry and Electrocatalysis. *J. Am. Chem. Soc.* **2019,** *141* (6), 2179-2193.

[20] Wahab, O. J.; Kang, M.; Unwin, P. R. Scanning electrochemical cell microscopy: A natural technique for single entity electrochemistry. *Curr. Opin. Electrochem.* **2020,** *22*, 120-128.

[21] Ornelas, I. M.; Unwin, P. R.; Bentley, C. L. High-Throughput Correlative Electrochemistry–Microscopy at a Transmission Electron Microscopy Grid Electrode. *Anal. Chem.* **2019,** *91* (23), 14854-14859.

[22] Bentley, C. L.; Kang, M.; Unwin, P. R. Nanoscale Structure Dynamics within Electrocatalytic Materials. *J. Am. Chem. Soc.* **2017,** *139* (46), 16813-16821.

[23] Yule, L. C.; Daviddi, E.; West, G.; Bentley, C. L.; Unwin, P. R. Surface microstructural controls on electrochemical hydrogen absorption at polycrystalline palladium. *J. Electroanal. Chem.* **2020,** *872*, 114047.

[24] Shkirskiy, V.; Yule, L. C.; Daviddi, E.; Bentley, C. L.; Aarons, J.; West, G.; Unwin, P. R. Nanoscale Scanning Electrochemical Cell Microscopy and Correlative Surface Structural Analysis to Map Anodic and Cathodic Reactions on Polycrystalline Zn in Acid Media. *J. Electrochem. Soc.* **2020,** *167* (4).

[25] Bentley, C. L.; Kang, M.; Maddar, F. M.; Li, F.; Walker, M.; Zhang, J.; Unwin, P. R. Electrochemical maps and movies of the hydrogen evolution reaction on natural crystals of molybdenite (MoS2): basal vs. edge plane activity. *Chem. Sci.* **2017,** *8* (9), 6583-6593.

[26] Quickenden, T. I.; Jiang, X. The diffusion coefficient of copper sulphate in aqueous solution. *Electrochim. Acta* **1984,** *29* (6), 693-700.

[27] Xing, W.; Yin, M.; Lv, Q.; Hu, Y.; Liu, C.; Zhang, J. In *Rotating Electrode Methods and Oxygen Reduction Electrocatalysts*; Xing, W.;Yin, G.;Zhang, J., Eds.; Elsevier: Amsterdam, 2014.

[28] Kowert, B. A.; Dang, N. C. Diffusion of Dioxygen in n-Alkanes. *J. Phys. Chem. A* **1999,** *103* (7), 779-781.

[29] Battino, R.; Seybold, P. G. The O2/N2 Ratio Gas Solubility Mystery. *J. Chem. Eng. Data* **2011,** *56* (12), 5036-5044.

[30] Abraham, M. H.; Acree Jr, W. E. Correlation and prediction of partition coefficients between the gas phase and water, and the solvents dodecane and undecane. *New J. Chem.* **2004,** *28* (12), 1538-1543.

[31] Beverskog, B. Revised Pourbaix Diagrams for Copper at 25 to 300°C. *J. Electrochem. Soc.* **1997,** *144* (10), 3476.
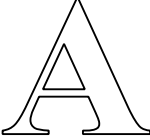
[32] Trasatti, S. Work function, electronegativity, and electrochemical behaviour of metals: III. Electrolytic hydrogen evolution in acid solutions. *J. Electroanal. Chem. Interf. Electrochem.* **1972,** *39* (1), 163-184.

[33] Kulkarni, A.; Siahrostami, S.; Patel, A.; Nørskov, J. K. Understanding Catalytic Activity Trends in the Oxygen Reduction Reaction. *Chem. Rev.* **2018,** *118* (5), 2302-2312.

[34] Rumble, J. R. *CRC Handbook of Chemistry and Physics, 100th Edition*; Rumble; John R. ed.; CRC press, 2019.

[35] Cordeiro, G. G. O.; Barcia, O. E.; Mattos, O. R. Copper electrodissolution mechanism in a 1M sulphate medium. *Electrochim. Acta* **1993,** *38* (2), 319-324.

[36] Jardy, A.; Legal Lasalle-Molin, A.; Keddam, M.; Takenouti, H. Copper dissolution in acidic sulphate media studied by QCM and rrde under ac signal. *Electrochim. Acta* **1992,** *37* (12), 2195-2201.

[37] Wong, D. K. Y.; Coller, B. A. W.; MacFarlane, D. R. A kinetic model for the dissolution mechanism of copper in acidic sulfate solutions. *Electrochim. Acta* **1993,** *38* (14), 2121-2127.

[38] Mattsson, E.; Bockris, J. O. M. Galvanostatic studies of the kinetics of deposition and dissolution in the copper + copper sulphate system. *Trans. Faraday Soc.* **1959,** *55* (0), 1586-1601.

[39] Gray, R. D. Kinetics of oxidation of copper(I) by molecular oxygen in perchloric acid-acetonitrile solutions. *J. Am. Chem. Soc.* **1969,** *91* (1), 56-62.

[40] Navon, N.; Cohen, H.; van Eldik, R.; Meyerstein, D. Effect of fumarate on the kinetics and reaction mechanism of Cu+aq with dioxygen. *J. Chem. Soc., Dalton Trans.* **1998,** *21*, 3663-3666.

[41] Polewska, W.; Vogt, M. R.; Magnussen, O. M.; Behm, R. J. In Situ STM Study of Cu(111) Surface Structure and Corrosion in Pure and Benzotriazole-Containing Sulfuric Acid Solution. *J. Phys. Chem. B* **1999,** *103* (47), 10440-10451.

[42] Magnussen, O. M.; Behm, R. J. Atomic-Scale Processes in Cu Corrosion and Corrosion Inhibition. *MRS Bull.* **1999,** *24* (7), 16-23.

[43] Pacioni, N. L.; Filippenko, V.; Presseau, N.; Scaiano, J. C. Oxidation of copper nanoparticles in water: mechanistic insights revealed by oxygen uptake and spectroscopic methods. *Dalton Trans.* **2013,** *42* (16), 5832-5838.

[44] Bentley, C. L.; Edmondson, J.; Meloni, G. N.; Perry, D.; Shkirskiy, V.; Unwin, P. R. Nanoscale Electrochemical Mapping. *Anal. Chem.* **2019,** *91* (1), 84-108.

[45] Duan, X.; Warschkow, O.; Soon, A.; Delley, B.; Stampfl, C. Density functional study of oxygen on Cu(100) and Cu(110) surfaces. *Phys. Rev. B* **2010,** *81* (7), 075430.

[46] Bodappa, N.; Su, M.; Zhao, Y.; Le, J. B.; Yang, W. M.; Radjenovic, P.; Dong, J. C.; Cheng, J.; Tian, Z. Q.; Li, J. F. Early Stages of Electrochemical Oxidation of Cu(111) and Polycrystalline Cu Surfaces Revealed by in Situ Raman Spectroscopy. *J. Am. Chem. Soc.* **2019,** *141* (31), 12192-12196.

[47] Li, W. H.; Ye, J. H.; Li, S. F. Y.; Nichols, R. J. In situ scanning tunneling microscopy investigation of restructuring and anodic dissolution of Cu(111)

electrode in sulphuric acid solution. *Surf. Sci.* **2000,** *449* (1), 207-217.

[48]   Maurice, V.; Klein, L. H.; Strehblow, H.-H.; Marcus, P. In Situ STM Study of the Initial Stages of Anodic Oxidation of Cu(111) in the Presence of Sulfates. *J. Electrochem. Soc.* **2003,** *150* (7), B316.

[49]   Lapeire, L.; Martinez Lombardia, E.; Verbeken, K.; De Graeve, I.; Kestens, L. A. I.; Terryn, H. Effect of neighboring grains on the microscopic corrosion behavior of a grain in polycrystalline copper. *Corros. Sci.* **2013,** *67*, 179-183.

[50]   O'Mullane, A. P. From single crystal surfaces to single atoms: investigating active sites in electrocatalysis. *Nanoscale* **2014,** *6* (8), 4012-4026.

Chapter 7

Corrosion Inhibition by Benzotriazole

As introduced and developed in the previous two chapters, the SECCM configuration can be easily adapted to study anodic and cathodic electrochemical processes at nanoscale at a $Cu/H_2SO_4/$dodecane triple-phase interface. In Chapter 6, in particular, it was demonstrated how the presence of O_2 in the oil phase dramatically affects such processes, in a grain dependent fashion. The purpose of this chapter is to understand if other species dissolved in the oil phase can have an impact on what happens in the nanodroplet. In order to do that, the best strategy is to add the desired species to the oil phase (dodecane), repeat the LSVs measures of Chapter 6 and then compare the two sets of data. In this chapter, such strategy is applied to study the effect of a corrosion inhibitor on Cu corrosion reactions.

7.1. INTRODUCTION AND CONTEXT

7.1.1. Cu corrosion in automotive and oil industry

Cu is widely used in the automotive and oil refinery industries, and its corrosion, together with other metals', is viewed as an extremely expensive issue, as pointed in Chapter 1. Specifically, in these fields the active

corrosion agents are typically water-soluble (or partially oil-soluble) acids (*e.g.*, sulfonic, sulphuric and/or carboxylic acids and their salts) dissolved in the small amount of water that contaminates all oil products.[1,2] In particular for the automotive industry, waste products (*e.g.*, carbon, nitrogen and sulphur oxides and water) originating from the combustion chamber generate acidic nanodroplets within the oil phase, which can induce localized corrosion upon contact with the metallic (*e.g.*, Cu) surfaces of the engine.[3,4] For this reason, the previous two chapters have been dedicated to the study of corrosion reactions in a system aimed to reproduce, with a model experiment, such triple-phase nanoscale system in an electrochemical configuration.

The concept of corrosion inhibitor has been also introduced, as a species that is able to slow down the process by interfering with the involved electrochemical reactions. The most studied and arguably the most important corrosion inhibitor for Cu surfaces is 1,2,3 - Benzotriazole (BTAH, Figure 7.1a), which has been known since the late 1940s and applied as a corrosion suppressor since the 1960s.[5] The action of BTAH in suppressing and controlling Cu degradation is mainly due its ability to strongly interact with metal surfaces, predominantly through the nitrogen atoms present in the heterocyclic ring (especially when it is in the deprotonated form, BTA^-), as well as the π electrons of the aromatic ring (Figure 7.1a). This strong interaction results in the formation of supramolecular structures, which effectively act as physical barrier to the surrounding environment.[6-8] In the years since its inception, many BTAH derivatives have been synthesized in order to adapt its use to different conditions;[9-11] for example, oil-soluble derivatives are used in the oil and automotive industries to suppress the aforementioned Cu degradation.[12]

Due to the great potential of BTAH and derivatives for suppressing corrosion in a wide range of applications, many studies have attempted to characterise the interaction between the BTAH molecule and Cu sur-
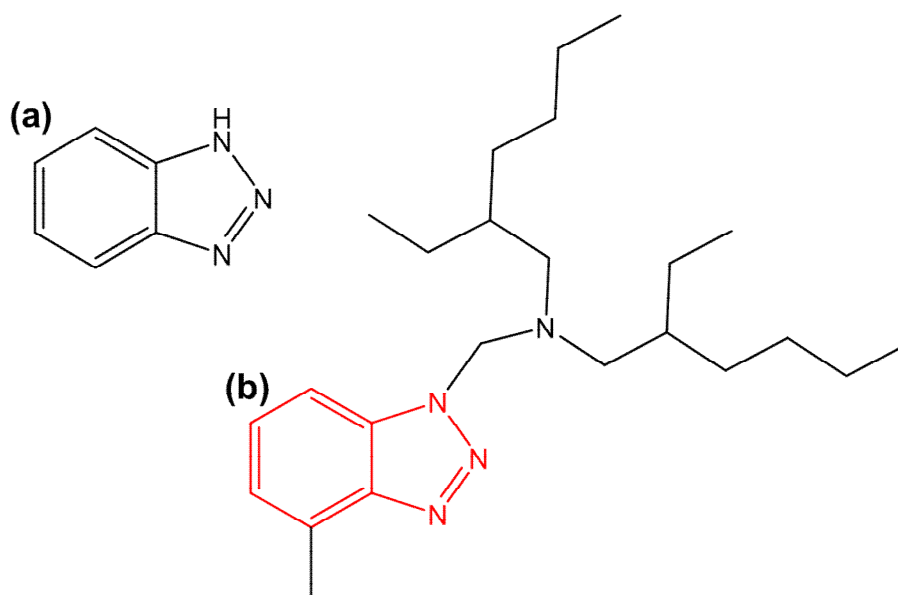
Figure 7.1: Chemical structures of (**a**) 1,2,3-Benzotriazole and (**b**) 1-N,N-bis-(2-ethylhexyl)-ARmethyl-benzotriazole-1-methanamine (BTA−R), the oil soluble derivative considered in this contribution. The red structure in (b) highlights the part of the molecule in common between (a) and (b).

faces, both experimentally, with surface characterization techniques, such as STM,[13-17] XPS or electrochemical impedance spectroscopy (EIS),[6,18] and theoretically, with quantum chemical calculations [*e.g.* with density functional theory (DFT)].[19-23] These investigations have revealed that the nature of adsorbed BTAH is sensitive to Cu surface structure, primarily the crystallographic orientation, with different interaction energies and unique structures and aggregates formed only on specific planes.[13,14,22,23]

As an example, calculations showed that BTAH is more prone to lose the acidic proton upon interaction with the {001} plane, as well as to have stronger π electron interactions, if compared to more densely packed surfaces such as the {111} plane.[22,23] The observation of such heterogeneity of action, couple with the heterogeneity of corrosion properties (*e.g.* Cu dissolution or ORR) of the different grains on a polycrystalline surface (widely discussed in the previous two chapters),[24-27] naturally raises the

question of what is the grain dependent specific interaction of BTAH derivative on each of these processes.

7.1.2. SECCM possibilities in corrosion inhibition studies

As demonstrated by the work presented in Chapter 5 and Chapter 6, as well as in previous contributions,[28-31] the multi-microscopy approach involving SECCM and co-located EBSD allowed to gain an holistic view of the electrochemical reactions involved in corrosion across the whole spectrum of crystallographic orientations. In Chapter 6, in particular, SECCM was deployed to perform voltammetry on polycrystalline copper in both aerated and de-aerated conditions, highlighting a dramatic difference in the susceptibility of the surface to anodic dissolution in the two conditions, as well as in the grain dependency of the process.

A natural extension of these works is to study the grain-specific action and inhibition efficiency of BTAH, which up until now, as is evident from the works mentioned above, has almost exclusively been carried out on the well-defined, low index crystallographic planes of Cu (*i.e.* {001}, {011} and {111}). The previous chapters demonstrated clearly that the electrochemical activity of high-index surface facets, which are a substantial component of a polycrystalline surface, cannot be predicted simply through combination of such low index grains response(s). Hence it is worth asking if that observation is valid also for the inhibitor's action. Besides, given the relevance of the triple phase system (Cu/aqueous nanodroplet/oil) in oil and automotive industry, it is worth asking if the addition of a corrosion inhibitor in the oil phase can affect the grain dependent corrosion processes happening in the aqueous acidic nanodroplet.

Therefore, the work presented in this chapter exploits the power of the SECCM/EBSD combined multi microscopy approach for understanding the activity of an oil soluble BTAH derivative, 1-N,N-bis-(2-

ethylhexyl)-ARmethyl-benzotriazole-1-methanamine (Figure 7.1b, from now on called BTA−R for compactness), by comparing the anodic SECCM voltammetric results of Chapter 6 with the analogous analysis conducted in presence of the inhibitor in the oil phase. In order to do so, besides recalling the details analysis of the grain dependency of the anodic processes, also the cathodic processes, that was only barely touched in the previous chapter, will be examined in detail. This work can demonstrate how such methodology can help to disclose the grain dependent action of benzotriazole on the Cu surface, giving a clear path for closing the gap of knowledge between the surface science and theoretical studies of BTAH surface interaction, that give insights on the specificity of the interaction on each different surface, and the testing of its effect on corrosion in an industry-relevant system, which normally does not include grain dependent analysis, thus paving the way for a multiscale comprehension of the phenomenon.

7.2. EXPERIMENTAL DETAILS

All the SECCM experiment, as well as the intercorrelation with the EBSD results have been carried out with the same methods described in Chapter 6 (the general setup instead is detailed in Chapter 2), with the only difference of employing a 100 ppm (in weight) solution of BTA−R in dodecane as mineral oil phase, instead of pure dodecane.

7.2.1. Contact angle measurements

All the contact angle measurements were carried out with Krüss DSA30 goniometer and embedded software. The Cu sample was placed in a quartz cuvette filled with the mineral oil solution (either dodecane or 100 ppm BTA−R in dodecane), and the droplet placed on it subsequently. All the employed droplets had a volume of 300 µL and were mechanically laid on the Cu surface. The contact angle was monitored every 0.5 s for 100 s and reported as average between the left and the right angle.

7.3. RESULTS AND DISCUSSION

7.3.1. Grain dependent corrosion reactions with BTA–R

SECCM was performed in a triple-phase aqueous nanodroplet/oil/ metal interface configuration, whereby the Cu surface was immersed in a mineral oil model medium, consisting in a 100 ppm solution of BTA–R in dodecane. Such BTAH derivative (whose structure is shown in Figure 7.1b), is obtained by methylating the aromatic ring and substituting the protonated nitrogen in the azole ring with a tertiary amine alkyl chain. This renders the molecule soluble in dodecane, while unmodified BTAH itself is not.

Although the added alkyl chains are not expected to interact strongly with the Cu surface, they may indirectly influence the adsorption of BTA–R through: (i) steric hindrance, possibly putting an obstacle to the formation of the most packed supramolecular structures and; (ii) preventing the formation of a negative charge on the azole ring (as in BTA^-). However, it has been suggested that in certain specific conditions the inhibitor could lose the tertiary amine chain thus releasing BTA^- to react on the surface;[32-34] furthermore, the Wan-der-Waals interactions with the polarised heterocyclic ring, as well as the interaction with the π electrons system (as briefly mentioned above) is thought to play an important role in the formation of specific structures on the Cu surface.[16,35] Therefore, none of the different types of interaction reported for BTAH on Cu can be excluded *a priori* due to such hydrophobic additions to the molecule.

SECCM was employed to collect voltammetric electrochemical movies of this triple phase system,(Cu surface, H_2SO_4 solution in the nanopipette and BTA–R solution in dodecane) both for the de-aerated system (Movies A11-A13) and the aerated one (Movies A14-A15). As an example, a set of data obtained by multi-microscopy correlation from Movie A11 and co-located EBSD analysis is shown in Figure 7.2.

Figure 7.2: **(a-b)** SECCM current maps extracted from Movie A11, respectively at **(a)** the beginning (E = − 0.45 V) and **(b)** the end (E = + 0.64 V) of the LSV sweep. **(c)** Crystallographic orientation map (IPFz) measured with EBSD on the same area. The grain boundaries extracted from (c) were overlaid on (a) and (b). **(d)** Exemplar average LSV curves extracted from selected grains marked in (c) and magnification of respectively the cathodic wave **(e)** and the anodic wave **(f)**. The overall average curve was also added in (d-f). **(g-h)** Statistical distribution of the current measured (a) and (b), respectively in **(g)** for the cathodic current and **(h)** for the anodic current, for the specific grains highlighted in (c).

After the approach at a cathodic potential (− 0.45 V vs Ag/AgCl) a 0.25s chronoamperometric pulse was applied, followed by potential sweep towards positive potentials at 1 V s^{-1}. As shown in Figure 7.2, from the comparison of the i_{surf} maps at the initial (Figure 7.2a) and final potential (Figure 7.2b) of the LSV with the EBSD performed on the same area (Figure 7.2c), the electrochemical processes present a clear grain de-

pendency, analogous to what was observed for the same system in absence of the corrosion inhibitor (Figure 6.6). To demonstrate this clearly, average LSVs were extracted from four specific grains, labelled α, β, γ and δ in Figure 7.2c, and plotted in Figure 7.2d.

All LSVs are qualitatively similar to the average of all the LSVs over this scan area (green line), but exhibit differences in the magnitude of the anodic and cathodic current, shown clearly in the magnified curves presented respectively in Figure 7.2e and f. From their comparison, it is evident that the HER, which is the main cathodic reaction in absence of O_2 (as briefly discussed in the previous chapter for the uninhibited case), has an activity that varies, in the selected grains, with the trend δ > β >> γ > α, while for the anodic reaction (Cu oxidation) the trend is δ > β > α ≈ γ.

An easier way to visualize such differences, and clear advantage of the use of SECCM for this kind of system, is to compare the distribution histograms for the current in all cases, shown respectively in Figure 7.2g and h for the cathodic an anodic c current. Such plots show that despite the random variation of the electrochemical properties within the grains (which, in term of standard deviation, for the selected grains is *ca.* 1.4 pA for the cathodic current and *ca.* 33 pA for the anodic current), significantly different average behaviour can be detected in each case, however, in some cases, grains that in average have different behaviour in fact present a high degree of overlapping (such as grain β with δ and α with γ in Figure 7.2g). Therefore, the intergrain differences can be sometimes more shaded than an average measure would suggest, because of several different factors contributing to the corrosion reaction, as well as the non-ideality of the planes present in a polycrystalline sample.

In all the cases examined in this and the previous chapter (*i.e.* aerated and de-aerated case, with or without BTA–R in the oil phase) both cathodic and anodic waves of the LSV analysis resulted in some sort of grain

dependency, highlighting the fact that BTA−R, added in this specific concentration (100 ppm) in the oil, does not cause the complete homogenization of the surface behaviour, *i.e.* the grain orientation plays a role in the corrosion process also in the presence of an inhibitor. Higher concentration of BTA−R may trigger a level of electrochemical processes depression that could lead to a decrease of current such that he intergrain differences would not be detectable, hence a relatively low employed concentration of inhibitor can be particularly useful to give insights on which grains are more or less susceptible to the inhibitor activity. Therefore, the action of BTA−R was analysed by comparing the different grain dependency, in absence and presence of the inhibitor, of all the major electrochemical processes examined, ranging from the anodic dissolution to the cathodic processes in presence and in absence of O_2.

7.3.2. Evaluating the general effect of the corrosion inhibitor on the voltammetric response.

Figure 7.3 shows the comparison, with the average LSVs measured both in deaerated and aerated atmosphere (respectively in Figure 7.3a and b), between the case with the oil phase composed only of dodecane (grey lines) *versus* a 100 ppm BTA−R dodecane solution (red lines). It is clear that the inhibitor has an effect in both cases. First of all, according to complementary SEM imaging of the area of scan (Appendix, Figure A.11), the contact area of the droplet is always decreased when the inhibitor is added. This is compatible with BTA−R forming a uniform layer on the surface, exposing the aqueous droplet to a layer of organic molecules; such layer can therefore increase the hydrophobicity, decreasing the extent of the nanodroplet spread during the contact with the surface.

Such property can be verified, although in relatively different condition (*i.e.* a macroscale droplet and no electric stimulus applied, and only in the aerated case) with a contact angle measure, as shown in Figure 7.3c. The contact angle measure was conducted in a triple-phase environment

(a) CV average, deaerated

(b) CV average, aerated

(c) Contact angle

Figure 7.3: (**a-b**) comparison of the average LSV curves before and after the addition of BTA−R to the oil layer, respectively in (**a**) the de-aerated case (comparing the averages obtained from Movies A7-A8, with those obtained from Movies A11-A13, averaging respectively 5200 and 7440 single measurements) and (**b**) the aerated case (comparing the averages obtained from Movies A9-A10 with those obtained from Movies A14-A15, averaging respectively 5100 and 5200 single measurements). (**c**) Contact angle measurement obtained with a 10 mM H2SO4 solution droplet (300 μL) deposited on a mirror polished polycrystalline Cu surface covered in pure dodecane (black spots) or a 100 ppm solution of BTA−R in dodecane. In each case the uninhibited case is represented by black colour and inhibited case by red colour.

similar to that used for the SECCM measures, with a 10 mM H_2SO_4 solution droplet immersed in mineral oil and in contact with a mirror polished Cu surface. The contact angle increases of about $\approx 20°$ when the inhibitor is added in the dodecane, with a considerable decrease in the interfacial tension between the droplet and the metal. This behaviour is compatible with the formation of a hydrophobic coating, caused by the interaction with BTA−R. Besides, based on the SEM imaging of the wetted areas (Appendix, Figure A.11) the increased hydrophobicity does not

seem to depend on the grain orientation itself, since no difference can be qualitatively observed in the footprint of the SECCM droplet on different grains in either cases. Therefore, it is possible to exclude the effect of the decreased area just by calculating the current density in each case.

The current density decrease shown with the addition of the inhibitor in Figure 7.3a and b is effective for both cathodic and anodic processes, although with different extents, in both the aerated and de-aerated case. While BTA−R seems to have a high efficiency in decreasing the cathodic current (at $E = -0.45$ V) in the de-aerated case and the anodic current ($E = +0.62$ V) in the aerated case (with, respectively, a decrease of 72% and 74%), it shows a more modest effect with the cathodic wave in the aerated case (37% decrease at $E = -0.45$ V) and for the anodic current in the de-aerated case (34% decrease at $E = +0.22$ V).

Despite the differences in affecting the average response from the surface, in each considered electrochemical wave the presence of the inhibitor significantly affects the reaction at a surface level (*vide infra*). The power of the multi-microscopy approach employed in this work is to unveil such influence over all the spectrum of crystallography orientation. In order to do such comparison, the 2D correlation plot between the electrochemical characteristics and the crystallographic orientation, introduced in Chapter 2 (section 2.8), and already employed in Chapter 5 and 6, is used here, correlating data extracted from Movies A7-A15 with colocated EBSD images. In order to have a parameter useful to uniformly compare the 2D correlation plots for the cathodic and anodic processes with and without the inhibitor, the 2 mA cm^{-2} onset potential (*i.e.* the potential needed to achieve a cathodic current of 2 mA cm^{-2} indicated as E_{2mA}) was used as a meter of comparison between the inhibited and uninhibited case.

All average data extracted from each single grain in presence of BTA−R are listed in Table A.5 for the de-aerated case (with grain IDs vis-

ualised in Figure A.24) and in Table A.6 for the aerated one (with grain IDs visualised in Figure A.25). Such data can be compared with the ones from the un-inhibited case, obtained in the previous chapter and listed in Table A.3 for the de-aerated case (with grain IDs visualised in Figure A.18) and in Table A.4 for the aerated one (with grain IDs visualised in Figure A.19).

7.3.3. BTA–R action on the cathodic process in a de-aerated system.

As discussed earlier, the cathodic current is dramatically decreased in presence of the inhibitor in the de-aerated case. In these conditions of atmosphere and pH the only feasible reaction that can be carried out cathodically is the HER [reaction (5.5)], and it is clear from the average curves shown in Figure 7.3a that the presence on the inhibitor considerably affects the conversion of H^+ at the surface. Figure 7.4 shows the comparison between the E_{2mA}/crystallographic orientation correlation plots in the absence (Figure 7.4a) and the presence (Figure 7.4a) of BTA–R. All the data in the projections were extracted from the comparison between SECCM electrochemical movies (Movies A7-A8 for the uninhibited case and Movies A11-A13 for the inhibited one, with all the maps reported in Appendix, Figure A.20b and d and Figure A.22b,d and f) and the EBSD maps collected in the same areas (respectively Figure 6.6c and Figure A.17c for the uninhibited case and Figure 7.2c, Figure A.22g and h for the inhibited one).

In the inhibitor-free case two grain orientation areas possess particularly high activity, marked as area A and B in Figure 7.4a: area A comprises the three grains the closest to the {001} orientation, whereas area B includes grains with intermediate orientation, laying over the highly stepped grains area in the centre of the graph, but closer to the {011} plane. Conversely, the areas with the lowest HER activities are the ones marked as C and D, respectively at high values of C_2 (*i.e.* closer to the
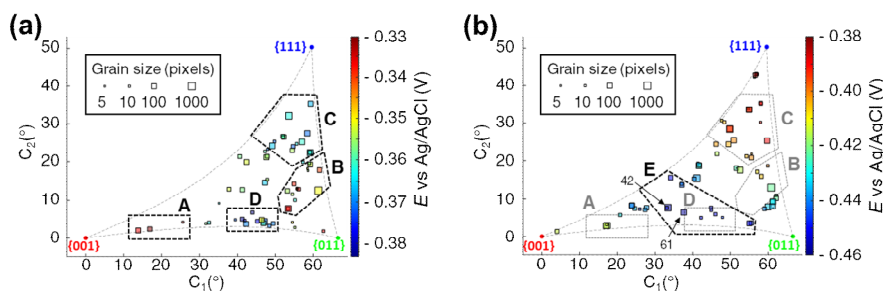
Figure 7.4: 2D correlation plots between the crystallographic orientation and E_{2mA} of the cathodic process in de-aerated condition, respectively (**a**) in absence and (**b**) in presence of BTA–R dissolved in the dodecane phase. The plot shown in (a) was obtained from correlation of Movies A7-A8 (Figure A.20b and d) and IPFz EBSD maps reported in Figure 6.6c and Figure A.17c The plot shown in (b) was obtained from correlation of Movies A11-A13 (Figure A.22b,d and f) and IPFz EBSD maps reported in Figure 7.2c and Figure A.22g and h . Relevant areas of the plot are marked with the letters A-E. In two grains marked in (b), respectively grain 42 and 61 (Table A.5), the value of E_{2mA} was set at −0.458 V, because most points of those grains do not reach the current of − 2 mA cm^{-2} in the examined potential range, as shown in Figure A.22b. Given the points for which E_{2mA} could be measured within such grains, it is reasonable to think that their average E_{2mA} would be nonetheless close to such value.

{111} orientation) and over the grains around the {012} and {035} orientation, as shown in Figure 7.4a. Even though such differences are not easy to rationalize, the HER reactivity difference between the {001} and the {111} grain in H_2SO_4 was previously theorized to be due to higher adsorption coverage of sulphate or bi-sulphate species on the {111}, causing the inhibition of HER activity on such plane.[36]

With the addition of BTA–R , the average onset potential is shifted of about 50 mV more negative, however such shift does not apply to all the areas of the spectrum of orientation with the same intensity, as it is clear from the comparison of the two correlation maps (Figure 7.4a and b). Unlike the un-inhibited case, the most active grains are undoubtfully the ones at high values of C_2, *i.e.* tending towards the {111} orientation (including area C examined earlier), with $E_{2mA} \geq -0.39$ V for $C_2 \geq 35°$, while the HER activity gradually decreases with such coordinate, to reach a

minimum of $E_{2mA} \approx -0.45$ V in area D and neighbouring grains (identified as area E) with a small gain to ≈ -0.42 V toward the {001} orientation (including area A and other 2 grains the closest to the {001}).

The influence of BTA−R on the HER reaction grain dependency is therefore very complex, but it is clear that the grains of area C (and, generalising, the grains closer to the {111} orientation) are the ones where the inhibitor has the least effect. A possible explanation is that the higher affinity of Cu{111} with the (bi)sulphate complexing agents in solution may be an obstacle to the interaction with BTA−R. Therefore, the competition between BTA−R and (bi)sulphate complexing agents could cause a part of the inhibitor layer to be removed during the contact with the H_2SO_4 droplet, reducing the inhibition efficiency. On the other hand area A, which showed a relatively high HER susceptibility without the inhibitor ($E_{2mA} \approx -0.33$ V), in the presence of BTA−R has a relatively low activity; since the (bi)sulphate complexation was theorized to be almost absent over Cu{001}, in this case the interaction with the BTA−R is possibly more efficient, having to depend less on the competition between the two complexing agents.

As noted in the previous chapters, some grains tend to manifest properties that are peculiarly different from the ones of very similar orientation. As it can be qualitatively observed from Figure 7.4, this is the case for the inhibitor free case (Figure 7.4a), particularly regarding the grains in area B, as well as one grain in area D (grain 55 in Table A.3). In the inhibited case (Figure 7.4b), instead, such behaviour is not observed. This may be an indication that the interaction BTA−R reduces the chances that a specific surface will expose particularly active sites. In fact, at the centre of the spectrum of orientation are situated the grains that are more likely to expose unusual combination of steps for a large portion of their surface. Such steps, as demonstrated for several materials for HER (especially Pt),[37] can be important sites of initiation of the reaction.[38,39]

The "smoothing" of the grain dependency curve seems to suggest that such steps might not play such important role when the inhibitor is present, with BTA−R annihilating the reaction from these sites (which, being more active, are also more subject to the interaction with the inhibitor) and allowing it only at the various combinations of basal planes composing the grains.

7.3.4. BTA−R action on the cathodic process in aerated conditions.

Nature of the cathodic process

The voltammetric behaviour of the system in presence of O_2 presents several complex peculiarities. In particular, in the un-inhibited case the cathodic current is similar in magnitude to that measured in the de-aerated case, even though with a completely different Tafel slope. As discussed in the previous chapter, it is reasonable to assume that the cathodic current is mostly originated by ORR [reaction (5.4)], even though the presence of HER, given the low overpotential observed in de-aerated conditions, cannot be completely ruled out.[**] However, as it can be seen from a qualitative comparison of the E_{2mA}/Crystallographic orientation correlation plots in the two un-inhibited cases (de-aerated in Figure 7.4a and aerated in Figure 7.5a), the grain dependency is significantly different in the two cases, with the grain toward the {111} orientation (including area C highlighted in the two plots) being among the least active in the de-aerated case (HER) and the most active in the aerated one (ORR). On the contrary, the grains closer to the {001} orientation observe the opposite trend, being more active in absence of O_2 and less in its presence. These results are consistent with previous works comparing HER and ORR on Cu {111} and {001} surfaces.[36,40]

[**] As pointed in Chapter 6, this phenomenon is still under investigation and will not be further discussed in this thesis; it will just be assumed that the contribution of ORR in the aerated case is overwhelming on the cathodic branch of the LSV.
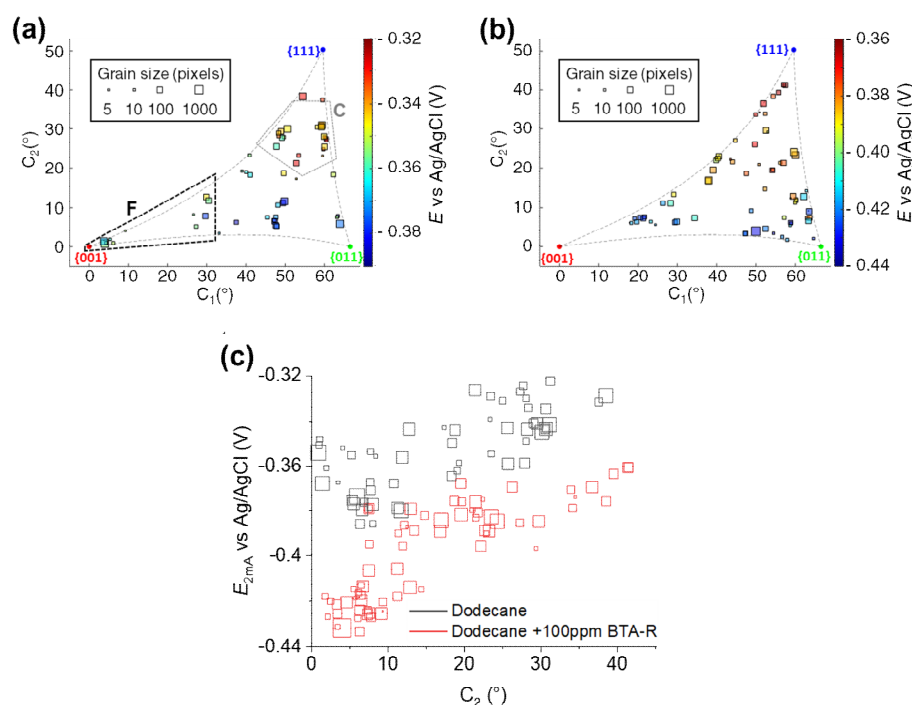
Figure 7.5: (**a-b**) 2D correlation plots between the crystallographic orientation and E_{2mA} of the cathodic process in aerated condition, respectively (**a**) in absence and (**b**) in presence of BTA–R in the dodecane phase. The plot shown in (a) was obtained from correlation of Movies A9-A10 (Figure A.21b and d) and IPFz EBSD maps reported in Figure 6.6d and Figure A.17d The plot shown in (b) was obtained from correlation of Movies A14-A15 (Figure A.23b and d) and IPFz EBSD maps reported in Figure A.23e and f. (**c**) Correlation plot of E_{2mA} in function of the sole C_2 coordinate, extracted from both (a) (grey scatters) and (b) (red scatters).

Furthermore, the results shown in Figure 7.5a can be compared with the ORR E_{surf}/crystallographic orientation correlation map obtained with chronopotentiometric cathodic pulse in Chapter 5 (Figure 5.4d, p. 170) In that case, in fact, due to the nature of the measure, the measured potential is most likely uninfluenced by HER rate. Interestingly, despite the physiological differences due to the compositions of the set of examined grains (the projection in Figure 7.5a has considerably less grains in the {011} orientation area) the trends of the potential in the two projections are qualitatively very similar, with the highest susceptibility being with the grains closest to the {111} orientation, and the area of lowest susceptibility being around the bottom right of the graph. In both cases the

grains closest to the {001} plane (area A in Figure 5.4d, corresponding to area F in Figure 7.5a) have an intermediate behaviour This brings another confirmation that the ORR makes up most of the electrochemical contribution in the cathodic wave.

Effect of BTA–R addition

With the addition of the inhibitor, the decrease in cathodic current is in average more modest than in the de-aerated case, as described in the previous section. Comparing the average increase in onset potential caused by BTA–R, ΔE_{2mA} is *ca.* 45 mV in the aerated system (Figure 7.3b), compared to $\approx$ 60 mV in the de-aerated case (Figure 7.3a). Thus, it appears that the inhibitor is less efficient at forming a barrier to O_2 than H^+, possibly because of the less hydrophilicity of the molecule, and therefore the higher capability of penetrating the BTA–R layer. Furthermore, since O_2, unlike H^+, is present in high concentration in the oil phase (the saturation concentration is roughly 10 times higher than in the aqueous nanodroplet), it is reasonable to assume that it is already interacting with the inhibitor layer on the surface before the analysis is performed.

Interestingly, unlike the de-aerated case, the grain dependency of the process does not have drastic changes with the addition of the inhibitor. If the un-inhibited (Figure 7.5a) and the inhibited (Figure 7.5b) case are compared, the general trend of high activity at high values of C_2, towards the {111} orientation, and less favourable reaction at the bottom of the plot (between {001} and {011} orientation), is substantially verified. This leads to the assumption that the higher efficiency of HER suppression by the BTA–R is due to the high efficiency showed on the most active grains, while in the case of O_2 related cathodic reactions the inhibition is more uniform and less grain dependent. This suggests that the inhibition mechanism in aerated conditions may be more related to the capability of the BTA–R adsorbed layer of offering a physical barrier to the passage of O_2 rather than the competition for active sites on the surface.

Nonetheless, some grain dependent properties of the inhibitory action can be identified also in this case, in particular in an intermediate band of grains, those indicatively situated at $10° < C_2 < 25°$, as it can be better visualised by the 1D plot of E_{2mA} *versus* C_2 (Figure 7.5c). E_{2mA} increases fairly regularly with C_2 in the un-inhibited case, whereas in presence of BTA−R not only the whole plot is shifted cathodically of about 45 mV, as discussed above, but E_{2mA} presents a sharp rise at $C_2 \approx 10°$, to values that in some cases are comparable to the ones of the un-inhibited case (such grains, however, are not at the same C_1 coordinate), with a following plateau until $C_2 \approx 25°$, which leads again to a regular increase. Therefore, the inhibition effect on these grains is slightly less pronounced then on the others of the orientation spectrum. This is an evidence that, despite the action of BTA−R is less grain dependent in this case than in de-aerated conditions (i.e. with HER), the grain difference is not completely erased by the presence of oxygen. Remarkably, this property is not observable unless a consistent sample of the full spectrum of orientations is investigated, reiterating the usefulness of conducting this kind of wide range correlations, made possible on this case by the use of SECCM.

7.3.5. BTA−R action on the anodic processes.

As detailed in the previous chapter, the presence of O_2 has a dramatic effect on the anodic dissolution of Cu in the employed triple-phase environment, depending mostly on the slow kinetics of the electrochemical reaction $Cu(I)/Cu(II)$ [eq. (6.9)] and the high reactivity of O_2 at the surface with $Cu(I)$. As shown herein, such dramatic effect can be seen also in the grain dependent activity of BTA−R. As anticipated earlier, the decrease in anodic current due to the addition of the inhibitor is more pronounced in aerated conditions (74 % instead of 34% in de-aerated conditions), leading to the assumption that the inhibitor is more efficient in the presence of O_2. In term of onset potential shift, $\Delta E_{2mA} \approx 40$ mV in aerated conditions and ≈ 15 mV in the de-aerated one. Given the high difference
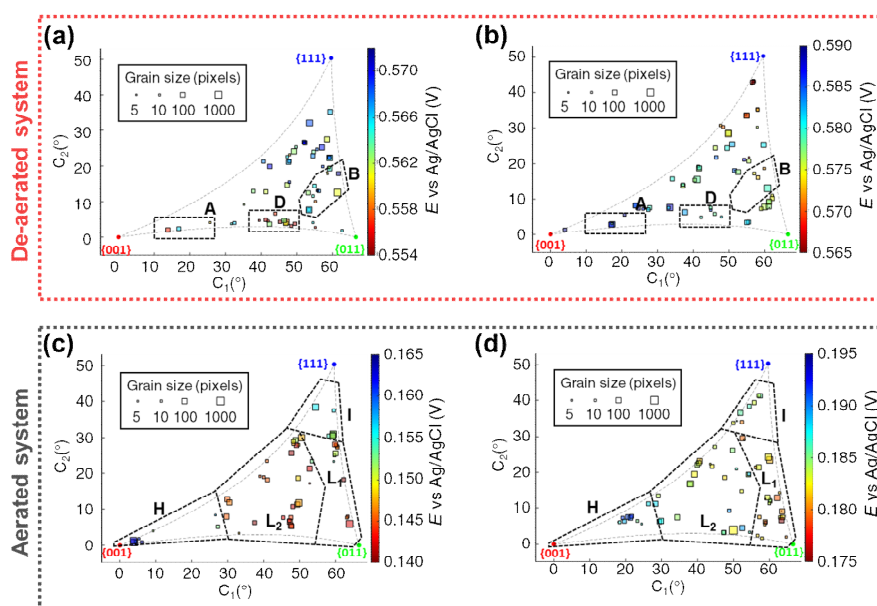
Figure 7.6: E_{2mA}/crystallographic orientation 2D correlation plots for the anodic processes. **(a-b)** Plots in de-aerated conditions, respectively **(a)** in absence and **(b)** in presence of BTA−R in the dodecane phase. **(c-d)** Plots in aerated conditions, respectively **(c)** in absence and **(d)** in presence of BTA−R in the dodecane phase. The plot shown in (a) was obtained from correlation of Movies A7-A8 (Figure A.20a and c) and IPFz EBSD maps reported in Figure 6.6d and Figure A.17d The plot shown in (b) was obtained from correlation of Movies A11-A13 (Figure A.22a,c and e) and IPFz EBSD maps reported in Figure 7.2c and Figure A.22g and h. The plot shown in (c) was obtained from correlation of Movies A9-A10 (Figure A.21a and c) and IPFz EBSD maps reported in Figure 6.6d and Figure A.17d The plot shown in (d) was obtained from correlation of Movies A14-A15 (Figure A.23a and c) and IPFz EBSD maps reported in Figure A.23e and f.

in the mechanism in de-aerated and aerated conditions, it is reasonable to expect BTA−R to manifest a different grain dependent behaviour in the two cases; the 2D E_{2mA}/crystallographic orientation correlation plots for the anodic dissolution for the four considered cases (uninhibited and inhibited in both de-aerated and aerated conditions), shown in Figure 7.6, seem to confirm this hypothesis.

Inhibition of Cu oxidation in de-aerated conditions

When O_2 is absent, in the un-inhibited case (Figure 7.6a) the trend of Cu oxidation susceptibility presents some peculiar hotspots, in particular

around the grains of orientation close to the {012} and {035} planes (corresponding to area D, Figure 7.6a), as described in Chapter 6. Interestingly, while these grains seem to be the most active for the anodic dissolution, with $E_{2mA} \approx 0.558$ V, they are instead the least active for the HER reaction (Figure 7.4a, area D). It would seem that in Figure 7.6a E_{2mA} increases towards the {001} plane, although the data are not conclusive, given that the two grains closest to such plane (identified as n. 41 an 10 in Figure A.18 and Table A.3) have different onset potential (0.566 V and 0.557 V respectively, with the second more similar to the average of area D) and they are, anyway, at least 10° far from the {001} itself. Overall, the oxidation susceptibility decreases by moving towards the {111} plane (*i.e.* increasing the coordinate C_2). As well as for the cathodic wave, several grains can be qualitatively observed to have very different E_{2mA} despite having similar orientation (such as in the example just described). Interestingly, in most cases the outstanding grains are not the same for the cathodic and the anodic process; this observation, together with the shift of the most active grains from area A and B for HER to area D for the anodic dissolution, highlights the fact that different steps in the surface are more active for the two different reactions.

The addition of the inhibitor, despite causing a relatively modest decrease in anodic current density in average (the average E_{2mA} increases of ≈ 15 mV, as discussed above) causes a drastic change in the grain dependency of the process. Similar to the cathodic process (Figure 7.4b), the grains closer to the {111} orientation (*i.e.* with $C_2 > 30°$) pass from being the least susceptible to oxidation (without BTA−R) to be the most active (with BTA−R), showing a very marginal increase in the onset potential ($\Delta E_{2mA} < 5$ mV in average). On the other hand, the set of grains at the bottom of the spectrum (area D, highlighted in both Figure 7.6a and b) shows a higher rate of inhibition ($\Delta E_{2mA} \approx 20$ mV in average), even though such area is not the least active in presence of the inhibitor, as for the cathodic processes.

In this case (*i.e.* de-aerated and in presence of BTA−R) the most re-sistant grains are the ones closest to {001} (C1 ≤ 25°, comprising also area A, as indicated in Figure 7.6b). Even though very few grains were measured in this part of the spectrum in the un-inhibited case to have a definitive comparison between Figure 7.6a and b, it is reasonable to think that the efficiency of BTA−R on this group of grains (closer to the {001} orientation) is relatively high.

Therefore, as a general behaviour, while the inhibition of the cathodic process (HER) seems to depend on the possibility of competition for ac-tive sites on the surface between BTA−R an (bi)sulphate ions, for the an-odic dissolution the grains with a higher dissolution rate in the un-inhib-ited case are also those that interact the most proficiently with the inhib-itor.

Inhibition of Cu oxidation in aerated conditions

In the aerated case (Figure 7.6c and d) the situation is significantly dif-ferent. As discussed in Chapter 6, the presence of O_2 drastically changes the mechanism of the Cu depletion, in particular the conversion between Cu(I) and Cu^{2+} [see Eqs. (6.10) and (6.11)], affecting the grain depend-ence of the process. In both cases (un-inhibited, Figure 7.6c, and inhib-ited, Figure 7.6d) the grains with the lowest oxidation susceptivity are the ones closer to the {001} orientation, indicated as area H in Figure 7.6c and d, with average $E_{2mA} \approx 0.161$V for the un-inhibited case and 0.190 V for the inhibited; however, due to the different sets of grains present in this areas in the two cases, the comparison needs to be taken cautiously. The following area in term of E_{2mA} (marked as area I in Figure 7.6c and c) comprehends the grains closer to the {111} orientation, that have an E_{2mA} approximately 10 mV more negative than area H; this trend is verified both in the un-inhibited and inhibited case. Therefore, the efficiency of BTA−R is similar on these group of grains, area H and I, with an increase of about 30 mV in E_{2mA} when the inhibitor is added.

Conversely, the grains that lay at coordinates that are between these two groups (area L), *i.e.* all the highly stepped grains and the grains toward the {011} orientation, show a more complicated pattern when it comes to BTA–R inhibition. While these grains present a rather uniform activity in the un-inhibited case, higher than area H and I, (albeit with some differences, as pointed out in Chapter 5, which, however, implied different experimental conditions, such as the use of galvanostatic condition and the pre-conditioning OCP pulse) their susceptibility is quite variable in presence of BTA–R. Generalizing, the grains that are closer to the {n11} line, on the right of the graph, (sub-area L_1) present a relatively low value of E_{2mA} in both the un-inhibited and inhibited case, with a change of *ca.* 30 mV (from *ca.* 0.143 V in the un-inhibited case to 0.180 V in the inhibited one), slightly higher of the change of grains in areas H and I. Conversely, the other grains, tending towards the middle of the graph (the highest stepped surfaces, area L2) present a more severe increase in E_{2mA} (*ca.* 45 mV, from *ca.* 0.142 V in the un-inhibited case to $\approx$ 0.185 V in the inhibited one, with high variability), therefore the action of the inhibitor is more pronounced. This observation could suggest that, unlike in the case of ORR, the inhibition of the Cu oxidation process in aerated conditions is affected more by specific surface interactions, rather than just the capability of repelling O_2 from the surface.

7.4.   CONCLUSION

In this chapter the multi-microscopy approach, involving electrochemical data from SECCM and cross-correlated crystallographic orientation data from EBSD in a triple phase Cu/aqueous nanodroplet/mineral oil system was applied to study the action of an oil soluble benzotriazole derivative (BTA–R) against Cu corrosion. In order to do so, the grain dependent data obtained in absence of the inhibitor in the oil (already partially discussed in the previous chapter) were compared with analogous data collected with the inhibitor added to the mineral oil

phase. Interestingly, the efficiency of the inhibition is highly dependent on the specific process (HER, ORR, Cu oxidation in aerated and de-aerated conditions), in a complex grain dependent pattern. In general, while the action of BTA−R in de-aerated conditions is highly dependent on the crystallographic orientation, in presence of O_2 the inhibitor shows a more homogeneous behaviour, suggesting that in the former case its mechanism of action is more related to the interaction with specific active sites on the surface, while in the latter to the capability of creating a barrier to the passage of O_2 to the surface.

In de-aerated condition, in particular, for the HER reaction the important inhibition factor could be the competition between (bi)sulphate ion and BTA−R for coordinating the Cu surface, while for the anodic dissolution the grains that are more eager to oxidation are also those that can interact better with the inhibitor. In aerated condition, instead, while the general behaviour seems to indicate that O_2 reaching the surface is the most important factor, there are nonetheless some exceptions to this behaviour, particularly on highly stepped grains, where BTA−R seem in general less efficient than the average at inhibiting ORR and more efficient at inhibiting Cu anodic dissolution. These results are an evidence that, as well as for the corrosion process itself (as explored in Chapter 5 and Chapter 6), the corrosion inhibitor action presents a complex grain dependent pattern that cannot be simply rationalised as a combination of the low index planes {001}, {011} and {111}.

This work showed how, with a multi-microscopy approach that is able to evaluate a wide range of different grain orientations of a polycrystalline surface, it is possible to understand what reactions of the corrosion process are more sensitive to interaction with the inhibitor; this may be useful in the future, in close association with surface science and computational studies, for understanding what kind of interactions between the inhibitor and the surface are the most effective, and eventually helping the design of new and more efficient corrosion inhibitors.

7.5. REFERENCES

[1]   Popoola, L. T.; Grema, A. S.; Latinwo, G. K.; Gutti, B.; Balogun, A. S. Corrosion problems during oil and gas production and its mitigation. *Int. J. Ind. Chem.* **2013,** *4* (1), 35.

[2]   Al-Janabi, Y. T. In *Corrosion Inhibitors in the Oil and Gas Industry*; 1 ed.; Saji, V. S.;Umoren, S. A., Eds.; Wiley, 2020.

[3]   Jardine, F. Engine Corrosion - its Causes and Avoidance. *SAE Tech. Pap. 250030* **1925**.

[4]   Lejre, K. H.; Kiil, S.; Glarborg, P.; Christensen, H.; Mayer, S. In *ASME 2017 Internal Combustion Engine Division Fall Technical Conference*, 2017.

[5]   Dugdale, I.; Cotton, J. B. An electrochemical investigation on the prevention of staining of copper by benzotriazole. *Corros. Sci.* **1963,** *3* (2), 69-74.

[6]   Yi, C.; Zhu, B.; Chen, Y.; Du, X.; Yang, Y.; Liu, J.; Zhang, Z. Adsorption and protective behavior of BTAH on the initial atmospheric corrosion process of copper under thin film of chloride solutions. *Sci. Rep.* **2018,** *8* (1), 5606.

[7]   Kokalj, A.; Peljhan, S.; Finšgar, M.; Milošev, I. What Determines the Inhibition Effectiveness of ATA, BTAH, and BTAOH Corrosion Inhibitors on Copper? *J. Am. Chem. Soc.* **2010,** *132* (46), 16657-16668.

[8]   Finšgar, M.; Milošev, I. Inhibition of copper corrosion by 1,2,3-benzotriazole: A review. *Corros. Sci.* **2010,** *52* (9), 2737-2749.

[9]   Kuznetsov, Y. I. Triazoles as a class of multifunctional corrosion inhibitors. A review. Part I. 1,2,3-Benzotriazole and its derivatives. Copper, zinc and their alloys. *Int. J. Corros. Scale Inhib.* **2018,** *7* (3).

[10]   Bajaj, K.; Sakhuja, R. In *The Chemistry of Benzotriazole Derivatives*; Monbaliu, J.-C. M., Ed.; Springer International Publishing: Cham, 2015; Vol. 43.

[11]   Zhao, G.; Zhao, Q.; Wang, X.; Liu, W. A novel benztriazole derivative for enhancing the anti-oxidation properties of synthetic ester-based oils. *Ind. Lubr. Tribol.* **2014,** *66* (3), 353-359.

[12]   El-Ashry, E.-S. H.; El-Rafey, M. E.; El-Nagdi, M. H.; Abou-Elnaga, H. H.; Bakry, W. M. A.; Boghdady, Y. M. Synthesis of benzotriazole derivatives as antioxidants for industrial lubricating oils. *Lubr. Sci.* **2006,** *18* (2), 109-118.

[13]   Vogt, M. R.; Polewska, W.; Magnussen, O. M.; Behm, R. J. In Situ STM Study of (100) Cu Electrodes in Sulfuric Acid Solution in the Presence of Benzotriazole: Adsorption, Cu Corrosion, and Cu Deposition. *J. Electrochem. Soc.* **1997,** *144* (5), L113-L116.

[14]   Polewska, W.; Vogt, M. R.; Magnussen, O. M.; Behm, R. J. In Situ STM Study of Cu(111) Surface Structure and Corrosion in Pure and Benzotriazole-Containing Sulfuric Acid Solution. *J. Phys. Chem. B* **1999,** *103* (47), 10440-10451.

[15]   Grillo, F.; Tee, D. W.; Francis, S. M.; Fruchtl, H.; Richardson, N. V. Initial stages of benzotriazole adsorption on the Cu(111) surface. *Nanoscale* **2013,** *5* (12), 5269-5273.

[16]   Grillo, F.; Tee, D. W.; Francis, S. M.; Früchtl, H. A.; Richardson, N. V.

Passivation of Copper: Benzotriazole Films on Cu(111). *J. Phys. Chem. C* **2014,** *118* (16), 8667-8675.

[17]   Grillo, F.; Batchelor, D.; Larrea, C. R.; Francis, S. M.; Lacovig, P.; Richardson, N. V. On-surface condensation of low-dimensional benzotriazole–copper assemblies. *Nanoscale* **2019,** *11* (27), 13017-13031.

[18]   Kosec, T.; Merl, D. K.; Milošev, I. Impedance and XPS study of benzotriazole films formed on copper, copper–zinc alloys and zinc in chloride solution. *Corros. Sci.* **2008,** *50* (7), 1987-1997.

[19]   Jiang, Y.; Adams, J. B. First principle calculations of benzotriazole adsorption onto clean Cu(111). *Surf. Sci.* **2003,** *529* (3), 428-442.

[20]   Kokalj, A.; Peljhan, S. Density Functional Theory Study of ATA, BTAH, and BTAOH as Copper Corrosion Inhibitors: Adsorption onto Cu(111) from Gas Phase. *Langmuir* **2010,** *26* (18), 14582-14593.

[21]   Saavedra-Torres, M.; Escobar, C. A.; Ocayo, F.; Tielens, F.; Santos, J. C. 1,2,3-Benzotriazole derivatives adsorption on Cu(111) surface: A DFT study. *Chem. Phys. Lett.* **2017,** *689*, 128-134.

[22]   Peljhan, S.; Kokalj, A. DFT study of gas-phase adsorption of benzotriazole on Cu(111), Cu(100), Cu(110), and low coordinated defects thereon. *Phys. Chem. Chem. Phys.* **2011,** *13* (45), 20408-20417.

[23]   Kokalj, A.; Peljhan, S.; Koller, J. The Effect of Surface Geometry of Copper on Dehydrogenation of Benzotriazole. Part II. *J. Phys. Chem. C* **2014,** *118* (2), 944-954.

[24]   Martinez-Lombardia, E.; Lapeire, L.; De Graeve, I.; Verbeken, K.; Kestens, L. A. I.; Terryn, H. Study of the influence of the microstructure on the corrosion properties of pure copper. *Mater. Corros.* **2016,** *67* (8), 847-856.

[25]   Krawiec, H.; Szklarz, Z. Combining the Electrochemical Microcell Technique and the Electron Backscatter Diffraction method to study the electrochemical behaviour of polycrystalline aluminium in sodium chloride solution. *Electrochim. Acta* **2016,** *203*, 426-438.

[26]   Dwivedi, D.; Lepková, K.; Becker, T. Carbon steel corrosion: a review of key surface properties and characterization methods. *RSC Adv.* **2017,** *7* (8), 4580-4610.

[27]   Luo, J.; Hein, C.; Pierson, J.-F.; Mücklich, F. Localised corrosion attacks and oxide growth on copper in phosphate-buffered saline. *Mater. Charact.* **2019,** *158*, 109985.

[28]   Shkirskiy, V.; Yule, L. C.; Daviddi, E.; Bentley, C. L.; Aarons, J.; West, G.; Unwin, P. R. Nanoscale Scanning Electrochemical Cell Microscopy and Correlative Surface Structural Analysis to Map Anodic and Cathodic Reactions on Polycrystalline Zn in Acid Media. *J. Electrochem. Soc.* **2020,** *167* (4).

[29]   Yule, L. C.; Bentley, C. L.; West, G.; Shollock, B. A.; Unwin, P. R. Scanning electrochemical cell microscopy: A versatile method for highly localised corrosion related measurements on metal surfaces. *Electrochim. Acta* **2019,** *298*, 80-88.

[30]   Yule, L. C.; Shkirskiy, V.; Aarons, J.; West, G.; Shollock, B. A.; Bentley, C. L.; Unwin, P. R. Nanoscale electrochemical visualization of grain-dependent

anodic iron dissolution from low carbon steel. *Electrochim. Acta* **2020,** *332*, 135267.

[31] Yule, L. C.; Shkirskiy, V.; Aarons, J.; West, G.; Bentley, C. L.; Shollock, B. A.; Unwin, P. R. Nanoscale Active Sites for the Hydrogen Evolution Reaction on Low Carbon Steel. *J. Phys. Chem. C* **2019,** *123* (39), 24146-24155.

[32] Wiklund, P. Chemical Stability of Benzotriazole Copper Surface Passivators in Insulating Oils. *Industrial & Engineering Chemistry Research* **2007,** *46* (10), 3312-3316.

[33] Facciotti, M.; Amaro, P. S.; Brown, R. C. D.; Lewin, P. L.; Pilgrim, J. A.; Wilson, G.; Jarman, P. N.; Fletcher, I. W. Static secondary ion mass spectrometry investigation of corrosion inhibitor Irgamet®39 on copper surfaces treated in power transformer insulating oil. *Corros. Sci.* **2015,** *98*, 450-456.

[34] Zhao, Y.; Qian, Y.; Su, W.; Li, Y.; Zhong, L.; Yu, Q. Inhibition effectiveness and depletion characteristic of Irgamet 39 in transformer oil. *IEEE Transactions on Dielectrics and Electrical Insulation* **2016,** *23* (6), 3382-3388.

[35] Gattinoni, C.; Michaelides, A. Understanding corrosion inhibition with van der Waals DFT methods: the case of benzotriazole. *Faraday Discuss.* **2015,** *180* (0), 439-458.

[36] Brisard, G.; Bertrand, N.; Ross, P. N.; Marković, N. M. Oxygen reduction and hydrogen evolution–oxidation reactions on Cu(hkl) surfaces. *J. Electroanal. Chem.* **2000,** *480* (1), 219-224.

[37] Climent, V.; Feliu, J. M. In *Advances in Electrochemical Science and Engineering,* 2017.

[38] Hernandez, F.; Baltruschat, H. Hydrogen evolution and Cu UPD at stepped gold single crystals modified with Pd. *J. Solid State Electrochem.* **2007,** *11* (7), 877-885.

[39] Juárez, M. F.; Ávila, M.; Ruderman, A.; Santos, E.; Leiva, E. P. M.; Oviedo, O. A. Hydrogen Evolution Reaction on Nanostructures Electrodes—a Scenario on Stepped Silver Surfaces. *Electrocatalysis* **2017,** *8* (6), 587-593.

[40] Jiang, T.; Brisard, G. M. Determination of the kinetic parameters of oxygen reduction on copper using a rotating ring single crystal disk assembly (RRDCu(hkl)E). *Electrochim. Acta* **2007,** *52* (13), 4487-4496.

Chapter 8

General Conclusion

Several conclusions have already been given in this thesis, one for each piece of fundamental work carried out during the PhD. Each results chapter (Chapter 3 to Chapter 7) represents, in its own way, a finite singular project with its own general outlook. However, all of these contributions are deeply interlinked, and therefore it is useful to give an overall vision on the work as a whole. At the beginning, it was pointed out how the exploration of complex behaviours at the micro/nanoscale represents a fundamental challenge in electrochemistry, and that SECCM can be a powerful technique to carry out such exploration.

All of the work presented in this thesis represents an articulated attempt to expand the fields of application of SECCM. This was achieved both by exploiting "classical" setups of analysis for characterising new kinds of surfaces, such as conductive polymer electrodes, as well as developing novel setups and techniques to extensively widen the use of SECCM, such as exploiting the triple-phase system or introducing the chronopotentiometric waveform. In each case, SECCM was applied to systems that are characterised by the presence of different phases, and as such, the technique can be truly defined as a "multiphase" electrochemical method of analysis. The concept of "correlative electrochemical

241

multi-microscopy" has been applied throughout, whereby the data obtained by SECCM is correlated with complementary information from other microscopy techniques, in order to gain a holistic view of how electrochemical reactivity is driven by the structural complexity of the analysed surfaces.

Firstly, in Chapter 3, double channel voltammetric SECCM was employed to study the complex relation between the structure of a phase-separated polymer blend (P3HT and PMMA) and its electron transfer properties. This work involved some improvement of the technique itself, if compared to previous works with double channel SECCM, *i.e.* the use of the dc current between the two channels as feedback signal, and the use of probe of smaller diameter (down to $\approx 100\,\text{nm}$). Such improvement allowed the collection of large and highly resolved electrochemical movies of both a pure P3HT deposited layer and a blend where active domains of P3HT were surrounded by non-conductive PMMA, and further correlate such results with co-located topography and conductivity measurements.

These analyses revealed that the conductive polymer retains most of its electron transfer capability within the blend, on the contrary of what is seen when macroscopic voltammetry is performed on the same sample. Besides, the P3HT domains are subject to different rates of environmental ageing. The nanoscale measurements, supported by FEM simulations, brought about the conclusion that macroscale electrochemistry is mostly affected by parasitic resistance, and the measured current is not indicative of the effective electron transfer properties of the composite material. To reiterate what was already underlined in the chapter, the implications of this are potentially immense: since most of the researched material are normally characterised by macroscale electrochemistry, the use of SECCM could potentially rehabilitate polymers and polymer blends that were wrongly discarded due to the influence of parasitic resistance, and not the intrinsic electron transfer and charge transfer properties.

Subsequently, in Chapter 4 an expansion of the electroanalytical possibilities of SECCM was developed, consisting in its use in a current controlled mode (chronopotentiometry). The analysis carried out in this chapter demonstrated the reproducibility and stability of chronopotentiometric SECCM experiments with model electrochemical systems of increasing complexity: starting from an outer sphere electron transfer on glassy carbon, to then perform that same process on a HOPG surface, to finally its application on the characterisation of an electrocatalyst for HER. The chronopotentiometric technique was able to achieve similar results to those attained with potential controlled techniques, with high sensitivity and resolution in both the topographical and electrochemical images, but with smaller current passed through the sample, allowing to largely avoid the problems that can arise by surface polarisation. In particular, the characterisation of the electrocatalytic material could be carried out at the "foot" of the voltammetric wave, and some important parameters, such as the onset potential of the process for a given current, could be determined directly.

Even though such analysis is already quite interesting *per se*, in the context of this work it was mainly a foundation for the research carried out in the next chapter. Indeed, in Chapter 5, chronopotentiometric SECCM was employed to characterise the grain dependent corrosion behaviour of polycrystalline copper, and several innovations in the technique were actually introduced throughout the chapter. Firstly, as anticipated, the chronopotentiometric mode of SECCM was used, which enabled the collection of spatially resolved electrochemical movies, characterising both the anodic (Cu electrodissolution) and cathodic reactions (Cu deposition and ORR), as well as the OCP, in two distinct measurements. Secondly, the analysis was carried out in a triple-phase $Cu/H_2SO_4/dodecane$ system, where the dodecane layer surrounding the SECCM nanodroplet acted as a O_2 reservoir. Thirdly, a new way of projecting grain dependent electrochemical data, conjugating SECCM with EBSD co-located

analysis, was introduced, allowing the visualisation of the electrochemical activity of the whole spectrum of grain orientations.

These advances led to the conclusion that Cu corrosion process(es) follow an articulated grain pattern, with each reaction behaving independently, and in a way that cannot be simply described by a simple combination of low index grains behaviour, which has been the focus of past investigations. In particular, the analysis of the cathodic processes consisted in an OCP pulse followed by a cathodic one, where the $E-t$ transient showed two different plateaus, corresponding to the deposition of the Cu^{2+} released during the OCP pulse and the ORR. The transition time between the two cathodic processes could be used as titration parameter of the amount of Cu^{2+} released during the OCP pulse, being dependent on both the susceptibility of Cu oxidation and that of ORR on the same sets of grains. Besides, it was also possible to observe enhanced activity at specific nano-defects (scratches) on the surface within a single grain.

The employment of this triple-phase system, together with the implementation of a full electrochemistry/crystallographic orientation plot, certainly represent the central achievement of this work, useful for studying the corrosion processes in a context that is relevant for automotive and oil industry applications. This approach was the base for the studies in Chapter 6 and Chapter 7, which essentially revolved around the same question: what is the effect of species that are present in the oil but interact with the aqueous phase?

Firstly, Chapter 6 took into consideration the effect of atmospheric O_2 on Cu corrosion processes, especially focusing on the Cu electrodissolution reaction. This work used voltammetric SECCM, comparing a de-aerated (Ar purged) with an aerated case, and found a dramatic increase in the current (at a given potential) in the aerated case. Such shift in the curve can be ascribed to many factors, such as a decreased current in the de-aerated case compared to the bulk, and the presence of a predominant

O$_2$ related pathway in the mechanism of Cu dissolution, enhanced by the extremely high flux of O$_2$ though the nanodroplet/oil interface. Such effect is also grain dependent, *e.g.* with some surfaces of orientations close to the ideal {111} plane being more activated than others in the presence of O$_2$. Also it was possible to identify grains that behave differently despite similar orientation, again underlying the complex relation between electrochemistry and surface structure (crystallography).

Finally, Chapter 7 took into consideration the effect of an oil soluble corrosion inhibitor in the dodecane phase. A derivative of benzotriazole was added to the dodecane and local voltammetric curves were measured both in aerated and de-aerated conditions, allowing direct comparison with the results of the previous chapter. In this case, a cross correlation between the O$_2$ and the inhibitor action was found, *i.e.* whereas in de-aerated condition the anti-corrosion action is more related to the capability of the inhibitor of competing for active sites on the surface, in aerated condition it is mostly dependent on the capability of creating a physical barrier to the O$_2$ itself. The importance of this work arises from the fact that, with a multi-microscopy approach that is able to evaluate a wide range of different grain orientations of a polycrystalline surface, it is possible to understand what reactions of the corrosion process are more sensitive to the action of the inhibitor. Through the strict cooperation with synthetic chemistry and quantomechanical calculations, this knowledge could be employed to design and formulate more effective inhibitors in a targeted manner, largely depending on the surface of interest.

Hopefully, this thesis has demonstrated that this multi-microscopy approach, that involves SECCM in tandem with other co-located surface characterisation techniques, has an expanding set of possibilities. In the future, this approach could be used to systematically examine and "re-discover" electroactive materials that may not be considered valuable nowadays, possibly due to highly complex (and poorly understood) structural

heterogeneity at a microscopic level. It could, as well, help to understand the behaviour of complex triple-phase electrochemical systems, with the effect of each individual component (*e.g.*, corrosion inhibitor or contaminant) being able to be studied in isolation. This would be extremely useful in corrosion research, as demonstrated here, but also in other fields, fuel cells just for citing one, where complex coupling between phase transfer and electron transfer happens on a normal basis. Finally the hope is that this work will help to view each grain dependent electrochemical process as something much more complex than what can be represented on an ideal, completely flat crystallographic plane and that studies employing such single crystal electrodes will take this fact into consideration when drawing conclusions relating to "practically-relevant" electrodes, which often possess significant heterogeneity beyond simple grain structure (*e.g.*, grain boundaries, compositional differences, defects etc.).

Appendix

A.1. ELECTROCHEMICAL MOVIES

All electrochemical movies are attached as multimedia material (*.avi files). Below the captions of such movies are reported, in order of appearance. All voltammetric movies are shown with a potential resolution of 0.01 V per frame. Each frame at a given potential, E_x, is obtained by averaging the current between $E_x - 0.005$ V and $E_x + 0.005$ E. Each Chronopotentiometric movie is shown with a time resolution of 0.01 s per frame, with each frame at a given time t_x obtained by averaging E_{surf} between $t_x - 0.005$ s and $t_x + 0.005$ s.

A.1.1. Chapter 3 Movies

All the movies in Chapter 3 were realised with a double channel nanopipette containing 4.5 mM FcDM + 100 mM KCl, with voltammetric (CV) SECCM ($v = 1$ V s^{-1}).

Movie A1: SECCM Electrochemical movie (101 by 101 pixels, hopping distance 100 nm), visualizing the FcDM$^{0/+}$ process on a freshly prepared P3HT film. Each pixel represents a single CV, obtained by sweeping the potential from −0.14 to 0.65 V vs Ag/AgCl, forward and backward, with a nanopipette probe ≈100 nm in diameter

Movie A2: SECCM Electrochemical movie (97 by 79 pixels, hopping distance 250 nm), visualizing the FcDM$^{0/+}$ process on a freshly prepared 1:5 P3HT:PMMA blend film. Each pixel represents a single CV, obtained by sweeping the potential from −0.15 to 0.72 V vs Ag/AgCl, forward and backward, with a nanopipette probe ≈ 200 nm in diameter.

Movie A3: SECCM Electrochemical movie (98 by 98 pixels, hopping distance 250 nm), visualizing the $FcDM^{0/+}$ process on a 1:5 P3HT:PMMA blend film, aged by exposure to ambient conditions for a period of three weeks. Each pixel represents a single cyclic voltammogram, obtained by sweeping the potential from −0.11 to 0.88 V vs Ag/AgCl, forward and backward, with nanopipette probe ≈ 200 nm in diameter.

A.1.2. Chapter 5 Movies

All the movies in Chapter 5 were realised with a single channel nanopipette containing 0.01 M H_2SO_4, with chronopotentiometric SECCM, on a polycrystalline Cu surface immersed in dodecane. All experiments consist in an open circuit potential (OCP, *i.e.* applied current, i_{app} = 0) step of 1 s (expressed in the movie at negative times, from − 1s to 0) followed by a current pulse at i_{app}.

Movie A4: SECCM E_{surf} movie (127 by 81 pixels, hopping distance 1 μm), obtained by applying an anodic chronopotentiometric pulse. Each pixel represents a single $E−t$ experiment, with i_{app} = + 10.0 pA (applied current density, I_{app} = + 6 mA cm^{-2}), applied for a time t = 1.5 s. The nanopipette probe was ≈ 400 nm in diameter and contacted an area of 1.6×10^{-9} cm^2. The grain boundaries extracted from Figure 5.3b, Chapter 5, are overlapped onto each frame of the video.

Movie A5: SECCM E_{surf} movie (77 by 71 pixels, hopping distance 1 μm), obtained by applying a cathodic chronopotentiometric pulse. Each pixel represents a single $E−t$ experiment, with i_{app} = − 5.65 pA (I_{app} = − 0.88 mA cm^{-2}), applied for a time t = 2 s. The nanopipette probe was ≈ 600 nm in diameter and contacted an area of 6.4×10^{-9} cm^2. The grain boundaries extracted from Figure 5.4b, Chapter 5, are overlapped onto each frame of the video.

Movie A6: SECCM E_{surf} movie (74 by 78 pixels, hopping distance 1 μm), obtained by applying a cathodic chronopotentiometric pulse. Each pixel represents a single $E−t$ experiment, with i_{app} = − 5.65 pA (I_{app} = − 0.88 mA cm^{-2}), applied for a time t = 2 s. The nanopipette probe was ≈ 600 nm in diameter and contacted an area of 6.4×10^{-9} cm^2. The grain boundaries extracted from the Figure A.14b are overlapped onto each frame of the video.

A.1.3. Chapter 6 Movies

All the movies in Chapter 6 were realised with a single channel nano-pipette containing 0.01 M H_2SO_4, with voltammetric (CV) SECCM ($v = 1 \text{ V s}^{-1}$), on a polycrystalline Cu surface immersed in dodecane.

Movie A7: SECCM i_{surf} movie (51 by 49 pixels, hopping distance 2 μm) in de-aerated conditions. Each pixel represents a single CV, obtained by sweeping between $E_i = -0.44$ V vs. Ag/AgCl, $E_f = 0.61$ V, forward and backward. The nanopipette probe was ≈ 400 nm in diameter and contacted an area of 7.59×10^{-9} cm². The grain boundaries extracted from Figure 6.6c are overlapped onto each frame of the movie.

Movie A8: SECCM i_{surf} movie (51 by 51 pixels, hopping distance 2 μm) in de-aerated conditions. Each pixel represents a single CV, obtained by sweeping between $E_i = -0.44$ V vs. Ag/AgCl, $E_f = 0.61$ V, forward and backward. The nanopipette probe was ≈ 400 nm in diameter and contacted an area of 7.59×10^{-9} cm². The grain boundaries extracted from Figure A.17c are overlapped onto each frame of the movie.

Movie A9: SECCM i_{surf} movie (51 by 51 pixels, hopping distance 2 μm) in aerated conditions. Each pixel represents a single CV, obtained by sweeping between $E_i = -0.45$ V vs. Ag/AgCl, $E_f = 0.25$ V, forward and backward. The nanopipette probe was ≈ 400 nm in diameter and contacted an area of 3.79×10^{-9} cm². The grain boundaries extracted from Figure 6.6d are overlapped onto each frame of the movie.

Movie A10: SECCM i_{surf} movie (51 by 51 pixels, hopping distance 2 μm) in aerated conditions. Each pixel represents a single LSV, obtained by sweeping between $E_i = -0.46$ V vs. Ag/AgCl, $E_f = 0.24$ V , forward and backward. The nanopipette probe was ≈ 400 nm in diameter and contacted an area of 3.79×10^{-9} cm². The grain boundaries extracted from in Figure A.17d are overlapped onto each frame of the movie.

A.1.4. Chapter 7 Movies

All the movies in Chapter 7 were realised with a single channel nano-pipette containing 0.01 M H_2SO_4, with voltammetric (CV) SECCM ($v = 1 \text{ V s}^{-1}$), on a polycrystalline Cu surface immersed in a 100 ppm solution of BTA−R in dodecane.

Movie A11: SECCM i_{surf} movie (51 by 45 pixels, hopping distance 2 μm) in de-aerated conditions. Each pixel represents a single CV, obtained by sweeping between $E_i = -0.457$ V vs. Ag/AgCl, $E_f = 0.64$ V, forward and backward. The nanopipette probe was ≈

400 nm in diameter and contacted an area of 6.53×10^{-9} cm². The grain boundaries extracted from Figure 7.2c are overlapped onto each frame of the movie.

Movie A12: SECCM i_{surf}, movie (51 by 50 pixels, hopping distance 2 μm) in de-aerated conditions. Each pixel represents a single CV, obtained by sweeping between $E_i = -0.457$ V vs. Ag/AgCl, $E_f = 0.64$ V. The nanopipette probe was ≈ 400 nm in diameter and contacted an area of 6.53×10^{-9} cm². The grain boundaries extracted from Figure A.22g are overlapped onto each frame of the movie.

Movie A13: SECCM i_{surf}, movie (51 by 51 pixels, hopping distance 2 μm) in de-aerated conditions. Each pixel represents a single CV, obtained by sweeping between $E_i = -0.457$ V vs. Ag/AgCl, $E_f = 0.64$ V, forward and backward. The nanopipette probe was ≈ 400 nm in diameter and contacted an area of 6.53×10^{-9} cm². The grain boundaries extracted from the Figure A.22h are overlapped onto each frame of the movie.

Movie A14: SECCM i_{surf}, movie (51 by 51 pixels, hopping distance 2 μm) in aerated conditions. Each pixel represents a single CV, obtained by sweeping between $E_i = -0.458$ V vs. Ag/AgCl, $E_f = 0.24$ V, forward and backward. The nanopipette probe was ≈ 400 nm in diameter and contacted an area of 3.47×10^{-9} cm². The grain boundaries extracted from Figure A.23e are overlapped onto each frame of the movie.

Movie A15: SECCM i_{surf}, movie (51 by 51 pixels, hopping distance 2 μm) in aerated conditions. Each pixel represents a single CV, obtained by sweeping between $E_i = -0.458$ V vs. Ag/AgCl, $E_f = 0.24$ V, forward and backward. The nanopipette probe was ≈ 400 nm in diameter and contacted an area of 3.47×10^{-9} cm². The grain boundaries extracted from Figure A.23f are overlapped onto each frame of the movie.

A.2. STABILITY OF SECCM DROPLET ON POLYMERS

In order to quantify the area wetted by the droplet cell during scanning on the conductive polymer samples presented in Chapter 3, a constant distance line scan was performed across the boundary between conducting P3HT and non-conducting P3HT domains on a polymer blend electrode, with an experimental setup that has been previously described[1,2] and is shown schematically in Figure A.1a. Briefly, a sinusoidal perturbation was added to the z position of the nanopipette, originating and *ac* component in i_{dc}. The amplitude of such component (A_{ac}) is extremely sensitive to the distance between the probe and the sample. This is valid
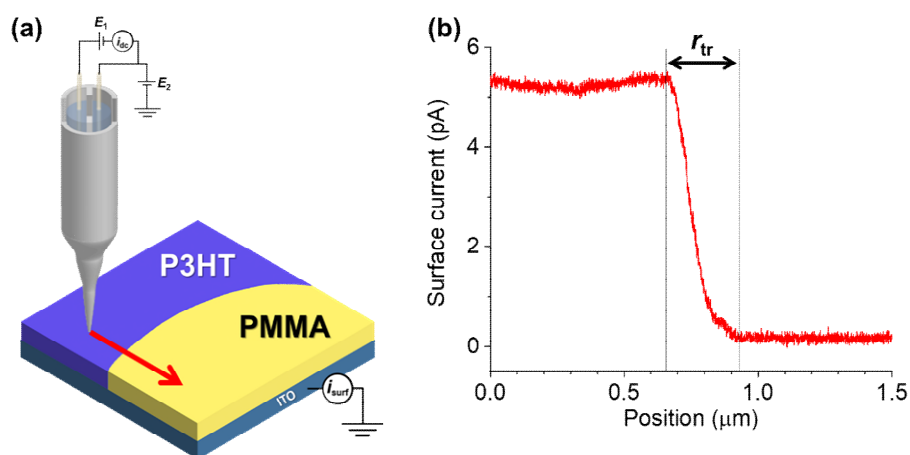
Figure A.1: (**a**) Scheme of the constant distance SECCM setup, with the red arrow representing the direction of the scan, from the conductive area (P3HT) to the non-conductive one (PMMA). (**b**) Line scan profile of i_{surf} vs. x-displacement, collected at 0.88 V vs Ag/AgCl (*i.e.* FcDM$^{0/+}$ is mass-transport controlled on P3HT). The boundary between the two polymeric domains is located at ≈ 0.65 μm.

also when the nanodroplet meniscus is made (on the contrary, i_{dc} has a major change only between before and after the contact), allowing A_{ac} to be used as continuous feedback, with the possibility of the probe to scan the sample at a constant distance.

Since the phase transition (boundary) between P3HT and PMMA is small compared to the probe size (few nanometres, as shown previously by nanoscale characterization), the width of the transition between the current measured on the P3HT (≈ 5.3 pA) and the one measured on the PMMA (≈ 0 pA, insulating) reflects the contact area, as previously described.[1] Such transition, as shown in Figure A.1b, happened in a space r_{tr} ≈ 300 nm. Since the diameter of the probe is ≈ 195 nm (Figure 2.1a), the wetting of the droplet compared to the probe size was estimated to be $\approx$ 1.5 times.

A.3. ADDITIONAL SIMULATIONS

A.3.1. Chapter 3 Simulations

Methods

FEM simulations were carried out to simulate FcDM$^{0/+}$ electrochemistry in the SECCM configuration, employing a previously reported model.[3] In brief, the simulations were carried out with the COMSOL Multiphysics 5.4 software suite, considering the cyclic voltammetric response for a single electron oxidation process [eq. (3.3)] within a 2D axisymmetric geometry, as shown in Figure A.2. Note that a single channel pipette geometry has been considered in the simulations, which is a good approximation of the double-channel geometry when the effects of electrical migration are negligible, as here, where the inter-channel bias was small for the migration of FcDM$^+$.[5,6] The bottom boundary (labelled r_d in Figure A.2) is the working electrode (*i.e.* area wetted by the SECCM meniscus cell), with a potential-dependent flux (J) imposed by Butler-Volmer kinetics:

$$J_{\text{FcDM}} = -k_f[\text{FcDM}] + k_b[\text{FcDM}^+]\qquad\text{(A.1)}$$

$$J_{\text{FcDM}^+} = k_f[\text{FcDM}] - k_b[\text{FcDM}^+]\qquad\text{(A.2)}$$

with

$$k_f = k^0 \exp\left[(1-\alpha)\frac{F}{RT}(E - E^{0'})\right]\qquad\text{(A.3)}$$

and

$$k_b = k^0 \exp\left[-\alpha\frac{F}{RT}(E - E^{0'})\right]\qquad\text{(A.4)}$$

where k^0 is the standard heterogeneous electron-transfer rate constant, α is the transfer coefficient, E is the applied potential, $E^{0'}$ is the formal potential, F is the Faraday constant, R is the Universal gas constant and T is
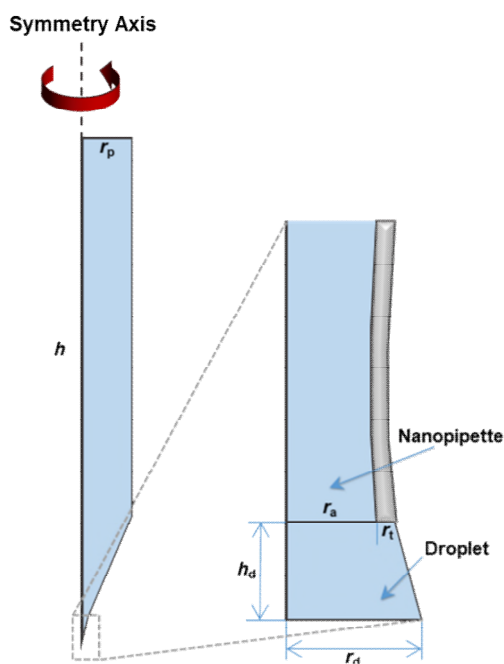
Figure A.2: Scheme of the 2D axisymmetric geometry employed in COMSOL Multiphysics to simulate the FcDM$^{0/+}$ process in the SECCM configuration. Boundary marked with r_d represents the contact area of the droplet meniscus with the working electrode. The following geometric parameters were employed: $h = 50$ mm, $r_p = 350$ μm, $h_d = 100$ nm, $r_d = 140$ nm, $r_a = 90$ nm, $r_t = 28$ nm.

the absolute temperature. Within these simulations, $a = 0.5$, $E^{0'} = 0.271$ V (determined as described in Chapter 5), $T = 298.15$ K and E was swept between -0.2 V and 0.7 V at a voltammetric sweep rate of $v = 1$ V s^{-1}. k^0 values covering the range measured in this study ($k^0 = 10^{-3}$ to 1 cm s^{-1}) were considered. In all the boundaries marking the outer edges of the probe and the droplet, a condition of zero flux was imposed, while in the boundary between the droplet and the tip (marked as r_a in Figure A.2) continuity of flux and concentration was set. The boundary marked with h (h_d within the droplet) was set as the axis of symmetry, as shown in Figure A.2.

Diffusion in the solution domain was modelled using the "Transport of Diluted Species" module within COMSOL, with mass-transport of the redox mediator (FcDM) assumed to be governed solely by diffusion. The diffusion coefficient was set equal for all the species, $D = 8 \cdot 10^{-6}$ cm^2 s^{-1},

while the initial concentration in the solution were C_{FcDM} = 4.5 mM and $C_{\text{FcDM+}}$ = 0. The initial concentrations were imposed as boundary conditions at the top of the tip (labelled r_p in Figure A.2). All simulated data were analysed and plotted using COMSOL Multiphysics 5.4.

Results

Concentration profiles calculated at the voltammetric half-wave potential, $E_{1/2}$, as well as under mass-transport control are shown in Figure A.3. The different k^0 values employed in the simulations were chosen to be representative of a reversible system (Figure A.3a) and two values previously reported for bulk P3HT[8] (Figure A.3b and c). The confined environment of the SECCM meniscus cell suppresses the flux at the edges of the electrode, giving rise to an "inverse edge effect" (*i.e.* flux at the centre of the electrode is slightly higher than that at its edges, contrary to conventional inlaid disk UMEs).

Nonetheless, in all cases the concentration profiles are linear within the nanopipette probe and relatively uniform across the electrode surface (*i.e.* within the droplet cell). For example, in the most extreme case (Figure A.3c2), FcDM flux at the edge of the electrode is only 0.4% lower than that at the centre, justifying the uniformly accessible electrode condition, adopted in the main text.
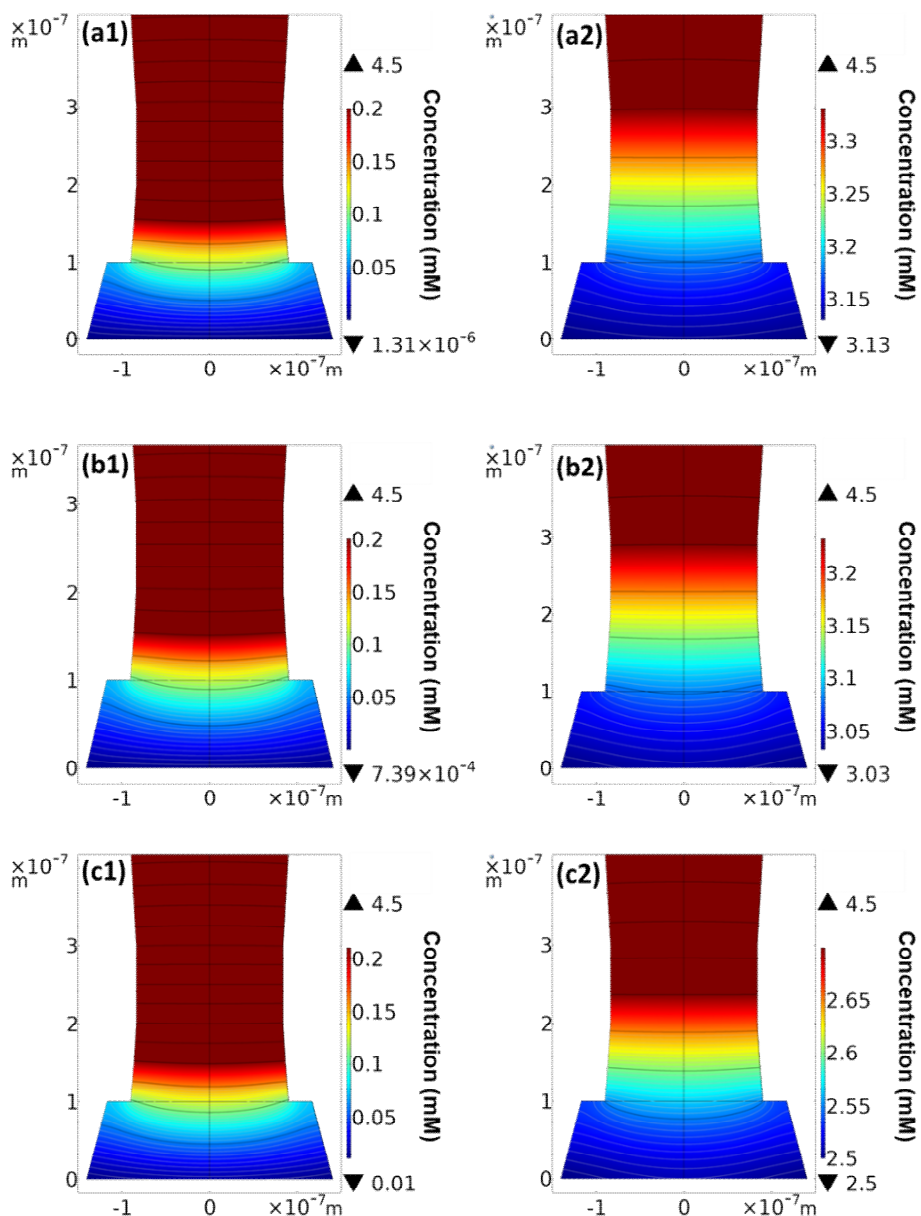
Figure A.3: FcDM concentration distribution figures, taken in the cross section of the nanopipette probe, with k^0 values of **(a)** 1 cm s^{-1}, **(b)** 1×10^{-2} cm s^{-1} and **(c)** 1×10^{-3} cm s^{-1}. For each case, the first figure (a1, b1 and c1) shows the concentration distribution at the end of the forward sweep (*i.e.* mass-transport control, $E = 0.7$ V), while the second (a2, b2 and c2) shows the concentration distribution extracted at $E_{1/2}$ (respectively 0.26 V, 0.30 V and 0.40 V). In each figure, grey and black contours denote increments of 0.005 and 0.05 mM, respectively.

A.3.2. Chapter 5 Simulations

Methods

FEM simulations were carried out with the COMSOL Multiphysics 5.4 software suite, to simulate the reduction of O_2 to H_2O_2 in an SECCM environment under a steady-state diffusion-limited regime.[3] The simulations considered: |1| the meniscus cell is completely isolated from the surrounding environment and |2| the meniscus cell is in contact with a layer of dodecane with which the reactant (O_2) is exchanged. The general geometry is shown in Figure A.4 with the dodecane layer of condition |2| highlighted in orange. In both cases, a single-channel pipette was simulated, with a 2D axisymmetric cylindrical geometry. The bottom boundary (labelled r_{dr} in Figure A.4) represents the working electrode, *i.e.* the contact area between the nanodroplet meniscus and the Cu substrate. A flux (J) was imposed on this boundary:

$$J_{O_2}^{et} = -k_f \left[O_2 \right] \tag{A.5}$$

with $k_f = 1.5 \cdot 10^3$ cm s^{-1} to ensure the reaction was diffusion-controlled.

Mass-transport in all the domains was modelled using the transport of diluted species module in COMSOL, with the mass-transport of O_2 assumed to be governed solely by diffusion. Phase-specific diffusion coefficients (D_{ph}) and bulk concentrations (C_{ph}), where *ph* is aqueous (aq) or dodecane (dodec), were employed in the aqueous phase (*i.e.* within the nanopipette probe and meniscus) and the dodecane phase (where simulated): $D_{aq} = 2 \cdot 10^{-5}$ cm^2 s^{-1} (Ref. [4]), $D_{dodec} = 4.11 \cdot 10^{-5}$ cm^2 s^{-1} (Ref. [5]), $C_{aq} = 0.26$ mM[6] and $C_{dodec} = 2.02$ mM, for aerated solution.[6] The pertinent initial concentrations were imposed as boundary conditions both at the top of the tip (labelled r_p in Figure A.4) and at the top of the dodecane layer (labelled r_{air} in Figure A.4).

In condition |2|, an equilibrium partition flux was imposed at the boundary between the aqueous solution and the dodecane layer (labelled

X_{int} in Figure A.4):

$$J_{O_2,\text{dodec}}^{\text{int}} = -k_{\text{in}}\left[O_2\right]_{\text{dodec}} + k_{\text{out}}\left[O_2\right]_{\text{aq}} \qquad (A.6)$$

$$J_{O_2,\text{aq}}^{\text{int}} = +k_{\text{in}}\left[O_2\right]_{\text{dodec}} - k_{\text{out}}\left[O_2\right]_{\text{aq}} \qquad (A.7)$$

with

$$K_{\text{part}} = \frac{k_{\text{out}}}{k_{\text{in}}} \qquad (A.8)$$

where K_{part} is the partition coefficient between the two phases. In this simulation $K_{\text{part}} = 7.8$ (Ref. [7]) while k_{out} was set to be a high value ($k_{\text{out}} = 10$ cm s^{-1}), such that the system could be considered at equilibrium on the time scale of the calculation. This is reasonable as O_2 transfer across immiscible liquid boundaries is diffusion-limited.[8] In condition |1|, this boundary was set to be a no-flux boundary, to demonstrated that O_2 flux down the nanopipette barrel is negligible compared to the flux across the oil-water boundary. In addition, unless otherwise stated, the no-flux condition was imposed on all boundaries. The system was solved with stationary condition, adopting the PARDISO solver.[9] The current (i) at the electrode (labelled r_{dr} in Figure A.4) was calculated by integration of the O_2 flux through the boundary, assuming a 2 electrons reduction reaction ($n = 2$):[10]

$$i = \int_0^{2\pi} r d\phi \int_0^{r_{\text{dr}}} nFD_{\text{aq}} \frac{\partial\left[O_2\right]}{\partial z} dr \qquad (A.9)$$

with r, z and ϕ being the cylindrical coordinates represented in Figure A.4.
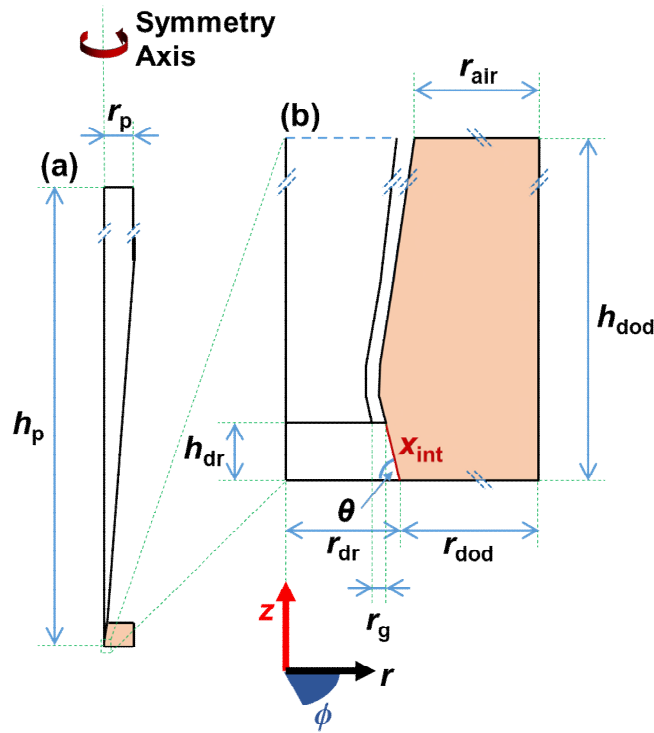
Figure A.4: Geometry of the 2D axisymmetric FEM simulations, with (**a**) defining the entire geometry and (**b**) a magnification of the nanodroplet (meniscus contact) region. When explicitly considered in the simulations, the dodecane layer is represented by the orange-shaded area. $h_p = 5 \cdot 10^{-2}$ m, $r_p = 3.5 \cdot 10^{-4}$ m, $h_{dr} = 200$ nm, $r_{dr} = 400$ nm, $r_g = 50$ nm, $\theta = 87°$, $r_{dod} + r_{dr} = 3 \cdot 10^{-4}$ m, $h_{dod} = 3 \cdot 10^{-4}$ m, $r_{air} = 2.77 \cdot 10^{-4}$ m. x_{int} is either a no-flux boundary (condition |1|) or the boundary representing the interface between aqueous solution and dodecane (condition |2|).

Results

As addressed in previous studies,[3,11,12] the configuration of SECCM mimics a gas diffusion electrode, to some extent, with an enhanced flux of gaseous reactants/products across the meniscus-cell (*i.e.* at the three-phase boundary). Thus FEM simulations were carried out to understand the transport of O_2 across the oil-water interface in SECCM (see Figure 5.1, Chapter 5 for experimental schematic). As outlined above (see Figure A.4), the simulations consider two different conditions: |1| O_2 transport limited to only the aqueous phase (*i.e.* no gas exchange with the surrounding oil phase) and; |2| O_2 transport in both the aqueous and surrounding

oil phase (*i.e.* gas exchange occurs between oil and aqueous phases). Note that condition |1| was explored to determine the relative contributions of mass-transport down the nanopipette barrel vs. across the liquid-liquid (oil-water) phase boundary, to overall O_2 flux. Simulated O_2 concentration profiles, obtained from a diffusion-controlled four-electron process (*e.g.*, the ORR at high overpotentials) are shown in Figure A.5.

Under condition |1| (*i.e.* no gas exchange with the surrounding oil phase), a diffusion-limited current of 7.9 pA (1.6 mA cm^{-2}) was calculated, which is 5 % of that expected at the same sized inlaid disc microelectrode, in agreement with previous reports of mass transport in SECCM,[13] as well as with the data presented in Chapter 3 and Chapter 4 In this case (Figure A.5a), as the O_2 is depleted exclusively from the reserve in aqueous solution, the diffusion layer extends tens of μm into the probe, with the concentration reaching 90% of the bulk value ($C_{O_2} = 0.26$ mM) at *ca.* 80 μm from the working electrode surface.

Under condition |2| (*i.e.* gas exchange occurs between oil and aqueous phases), because the solubility and the diffusion coefficient for O_2 are greater in the oil phase (2.02 mM and 4.11·10^{-5} cm^2 s^{-1}, respectively) than the aqueous phase, O_2 transport across the oil-water boundary leads to a greatly enhanced flux (Figure A.5b), and diffusion-limited current of 423 pA (84 mA cm^{-2}). As such, the diffusion layer is compressed compared to condition |1|, with the concentration reaching 90% of the bulk value at only *ca.* 20 μm into the pipette probe from the working electrode surface. As highlighted by the constant concentration contours within the oil phase (Figure A.5b), the O_2 assumes a radial-spherical diffusion profile, with the oil supplying > 98% of the reactant flux to the electrode surface, at diffusion-control.

As alluded to above, as I_{app} (0.88 mA cm^{-2}) is small compared the steady-state limiting current [*ca.* 1.6 and 84 mA cm^{-2} under condition |1| and |2|, respectively], so no transition from the ORR to the HER plateau
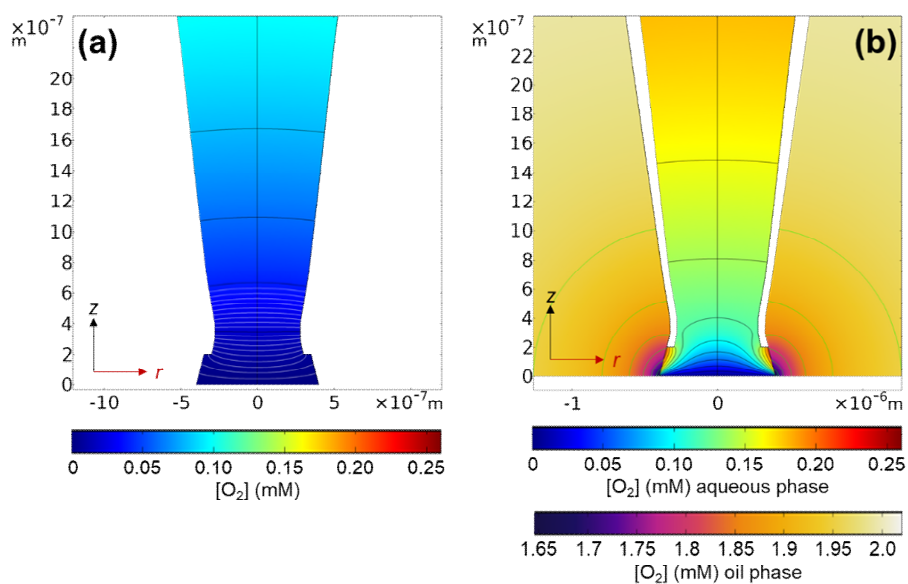
Figure A.5: O$_2$ concentration profiles, taken in the cross section of the nanopipette probe, under steady-state conditions. (**a**) Condition |1|, where O$_2$ transport is limited to only the aqueous phase. (**b**) Condition |2|, where O$_2$ transport occurs in both the aqueous and surrounding oil phase. In both cases, the green, black and white contours represent increments of 0.05, 0.02 and 0.002 mM, respectively.

is observed experimentally. Indeed, given the ease with which O$_2$ can be supplied through a nanodroplet environment, the simulations carried out above demonstrate the importance of O$_2$ availability and ORR kinetics for modulating the corrosion-action of acidic nanodroplets.

A.4.   SEM CONTACT AREAS CHARACTERISATION

A.4.1. Chapter 5 contact areas
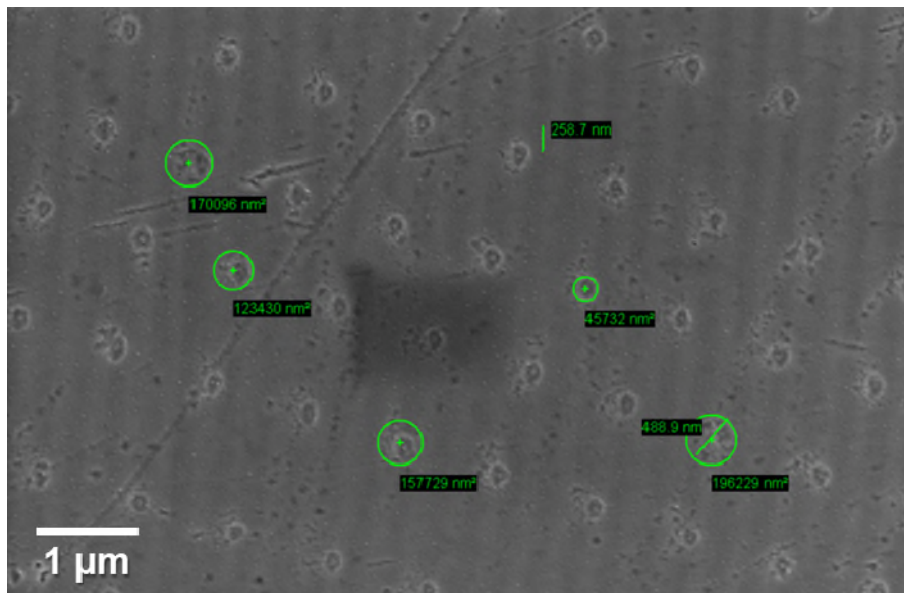
Figure A.6: SEM images of the droplet "footprint" residue remaining on the polycrystalline Cu surface after the chronopotentiometric anodic pulse (Movie A4).
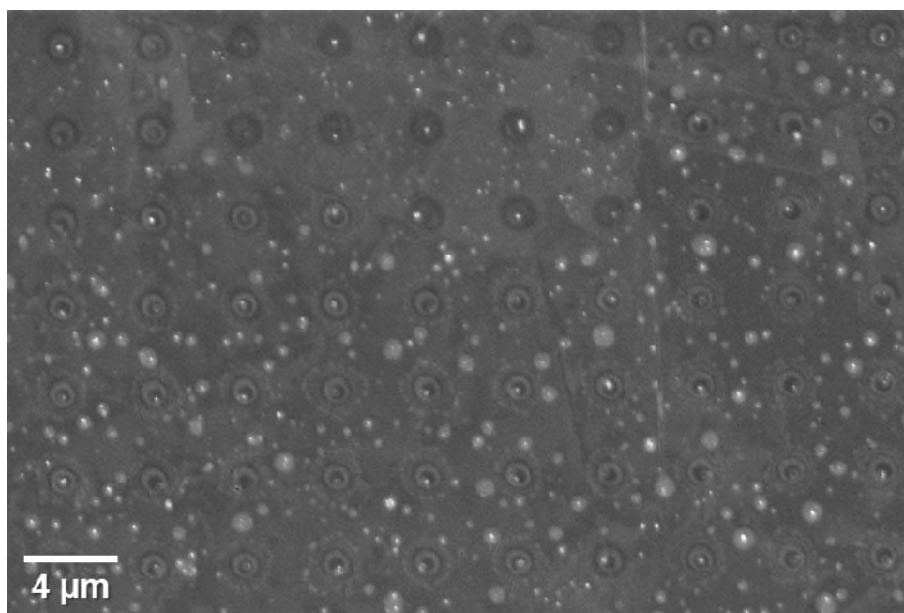
Figure A.7: SEM images of the droplet "footprint" residue remaining on the polycrystalline Cu surface after the chronopotentiometric anodic pulse in de-aerated atmosphere. The area used for the calculation of the average wetted area is the wider area of each meniscus trace (the third crown around each point). The average wetted area measured from the present image is $3.16 \cdot 10^{-8}$ cm^2.
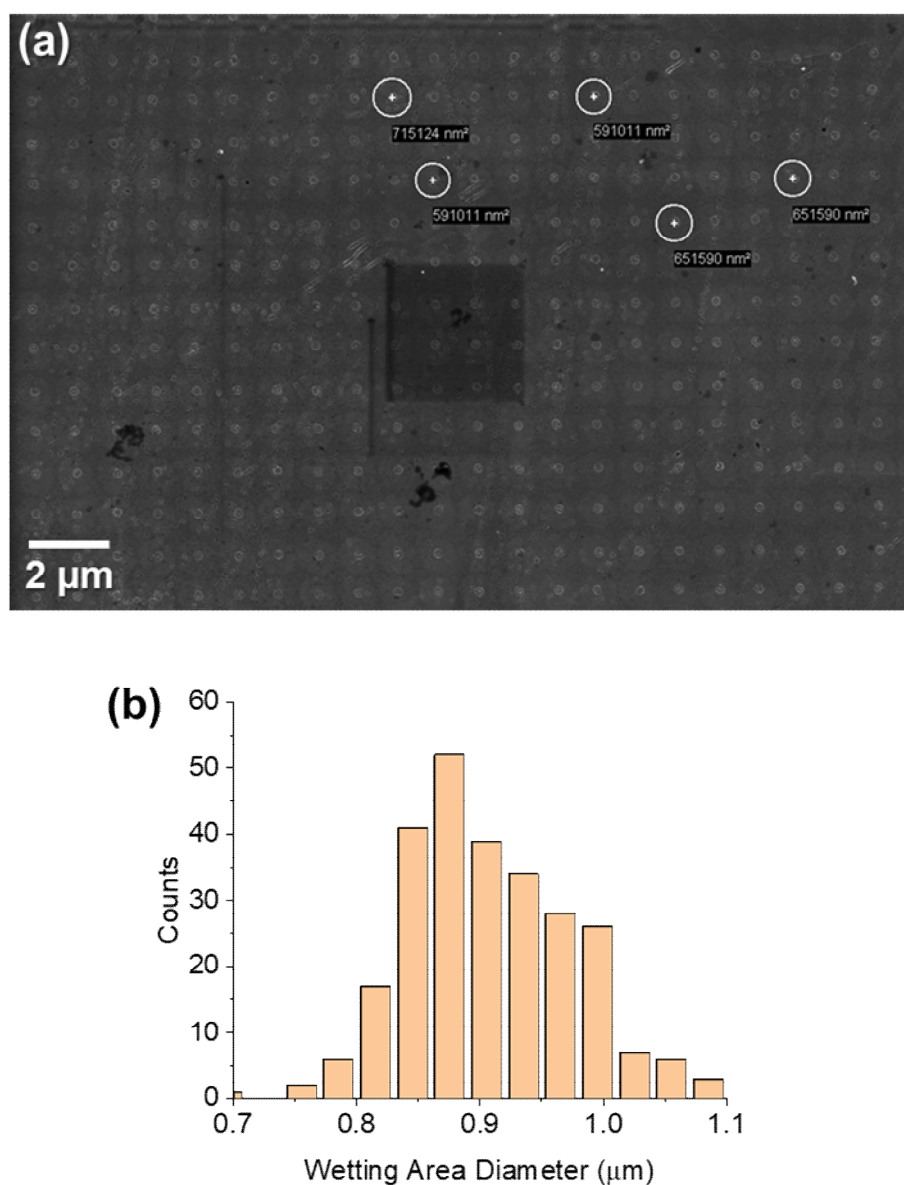
Figure A.8: (**a**) SEM images of the droplet "footprint" residue remaining on the poly-crystalline Cu surface after the chronopotentiometric cathodic pulse (Movie A5). (**b**) Statistical analysis of the wetted area of the droplet meniscus extracted from (a). The average value of the diameter is 0.9 µm, with a standard deviation of 0.16 µm. No significant variation of the wetted area was observed within the scanned area.
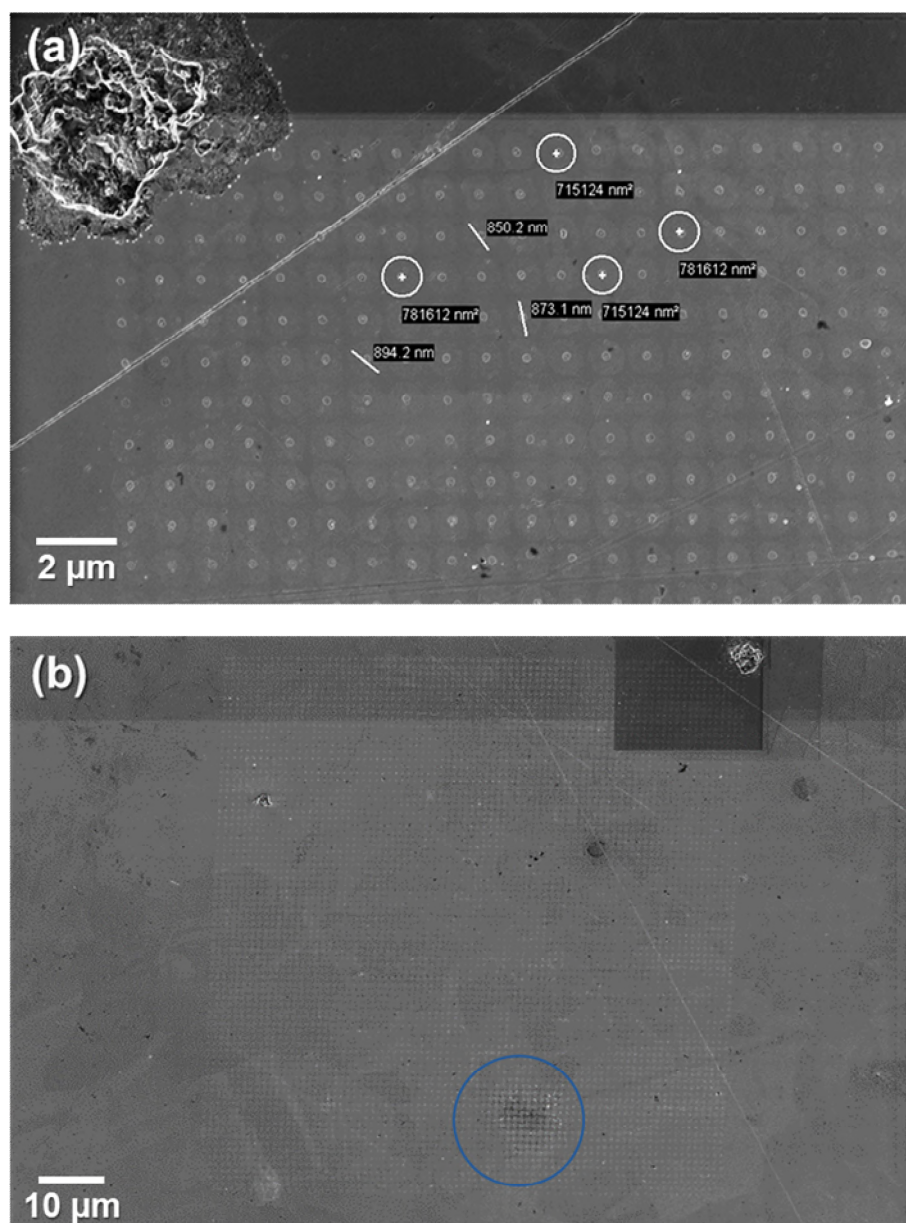
Figure A.9: SEM images of the droplet "footprint" residue remaining on the polycrystalline Cu surface after the chronopotentiometric cathodic pulse (Movie A6) at magnifications of (**a**) 5150× and (**b**) 835×. In (b), it is possible to note a contaminated area of the surface that was discarded during grain analysis (highlighted with a circle).

A.4.2. Chapter 6 contact areas
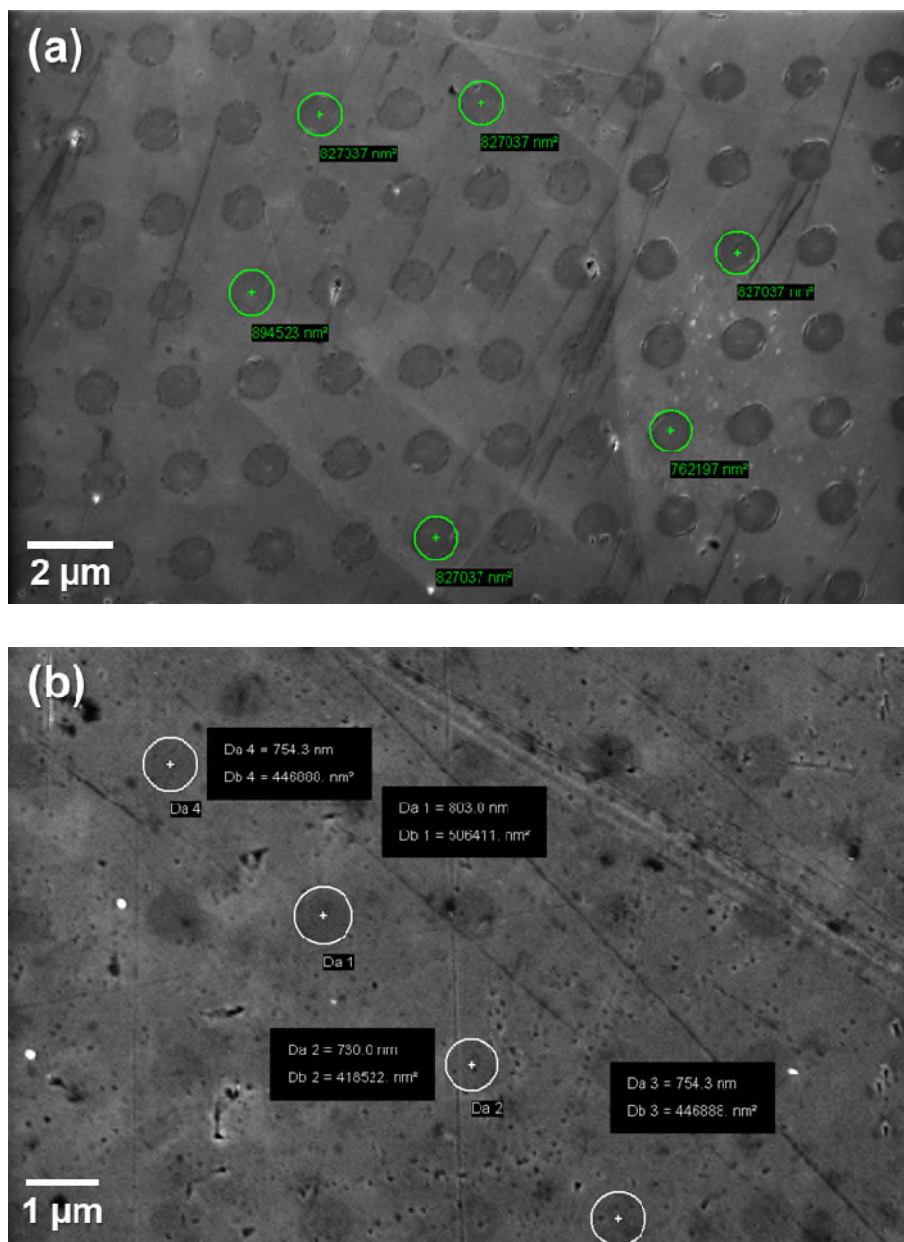
Figure A.10: Representative SEM images of the droplet "footprint" residue remaining on the polycrystalline Cu surface after the voltammetric SECCM was performed under (**a**) de-aerated (Movie A7) and (**b**) aerated (Movie A9) conditions, in both cases with dodecane as oil phase. The extracted average values of the footprint areas were respectively $7.59 \cdot 10^{-9}$ cm^2 and $3.79 \cdot 10^{-9}$ cm^2.

A.4.3. Chapter 7 contact areas
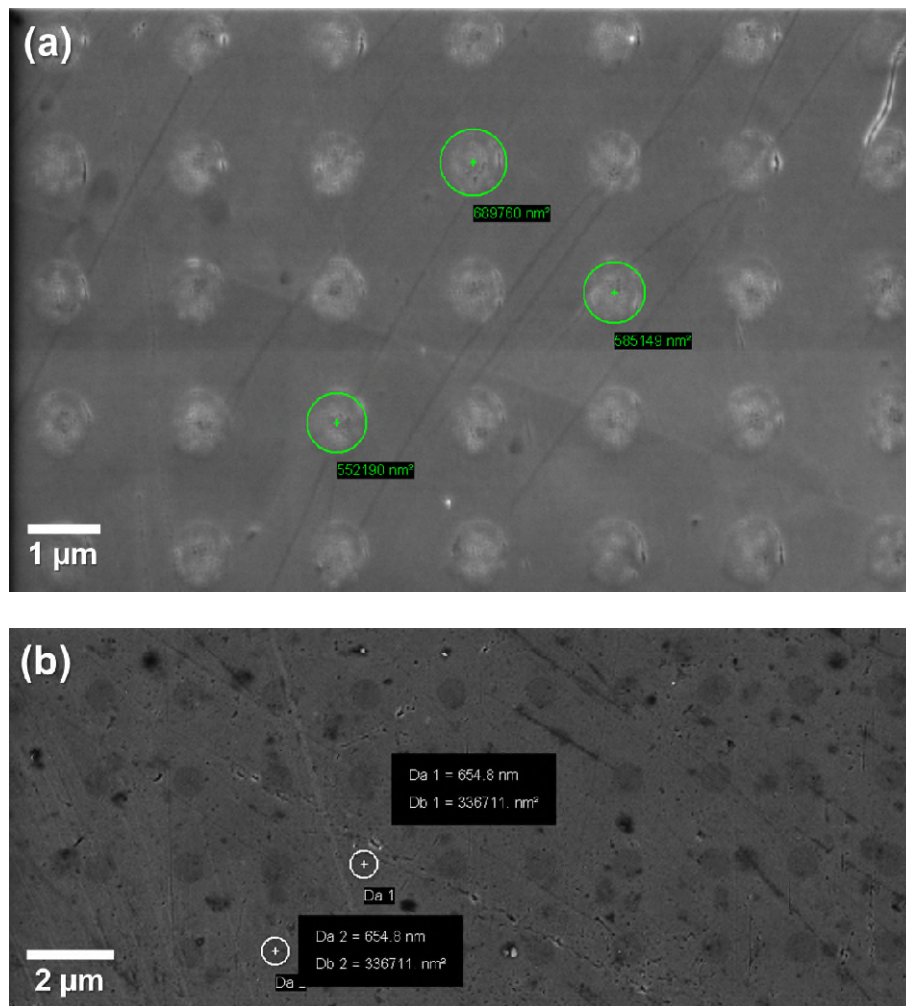
Figure A.11: Representative SEM images of the droplet "footprint" residue remaining on the polycrystalline Cu surface after the voltammetric SECCM was performed under (**a**) de-aerated (Movie A11) and (**b**) aerated (Movie A14) conditions, in both cases with a 100 ppm BTA−R solution in dodecane as oil phase. The extracted average values of the footprint areas were respectively $6.53 \cdot 10^{-9}$ cm^2 and $3.47 \cdot 10^{-9}$ cm^2.

A.5. DETAILS OF SCANNED GRAINS AND ADDITIONAL MAPS

A.5.1. Chapter 5 scans

Anodic chronopotentiometric pulse
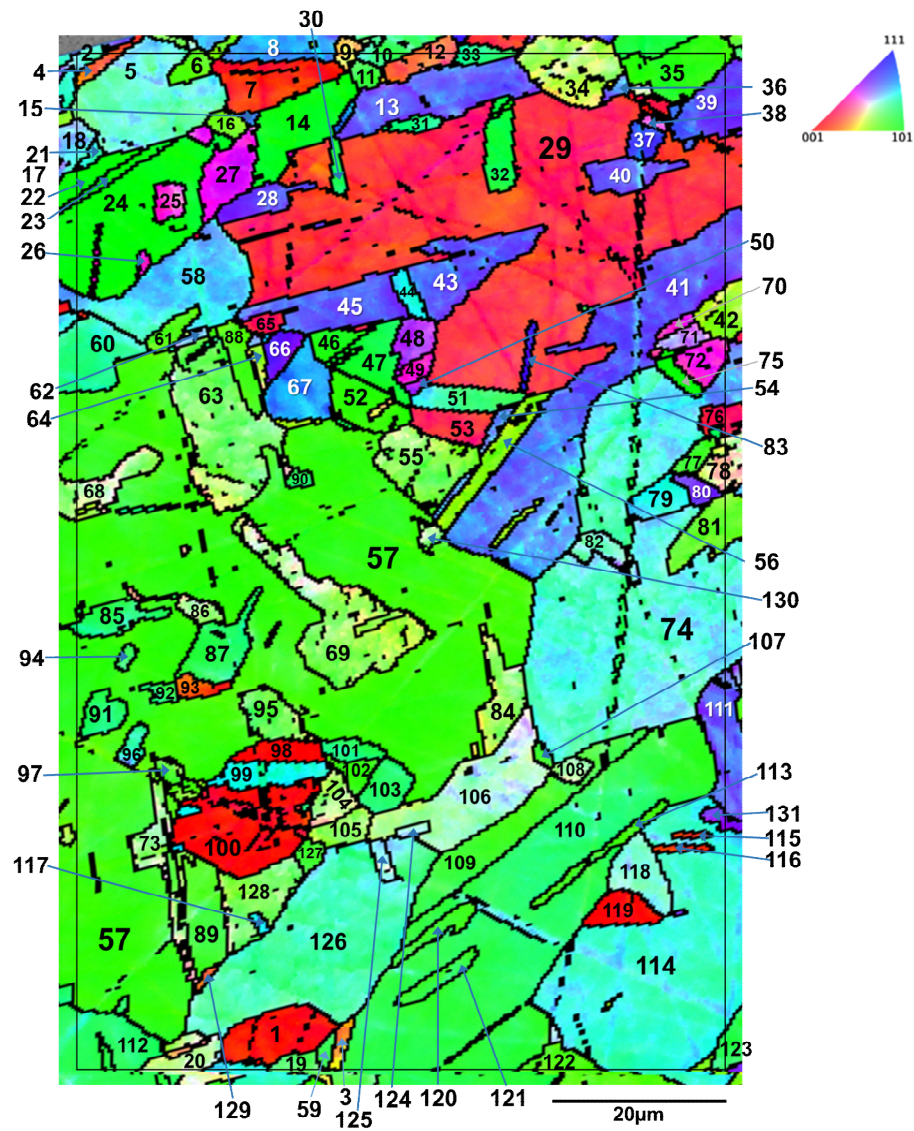
Figure A.12: Definition of the grain ID for each grain analysed from Movie S1 (reproduction of Figure 5.3b).

Table A.1: List of all grains analysed by SECCM (Movie A4 and Figure 5.3), with the average Euler angles, Miller indices and Projection Coordinates and E_{surf} listed for each one. The grain IDs correspond to those defined in Figure A.12.

ID	Average Euler angles (°)			Average Miller indices			Projection Coordinates (°)		Average E_{surf} t = 2s (V vs Ag/AgCl)	Average E_{OCP} t = − 0.01s (V vs Ag/AgCl)	Size (pixels)
	φ_1	Φ	φ_2	h	k	l	C_1	C_2			
1	182.61	4.67	21.64	0.030	0.076	0.997	7.32	1.88	0.0742	0.00611	63
2	257.65	37.98	25.05	0.261	0.558	0.788	53.59	18.71	0.0710	0.00072	7
3	295.68	20.18	9.69	0.058	0.340	0.939	31.43	5.11	0.0664	0.00062	7
4	132.72	15.93	15.22	0.072	0.265	0.962	24.90	5.23	0.0696	0.00057	6
5	297.51	38.16	67.99	0.573	0.232	0.786	54.57	16.64	0.0663	0.00204	146
6	215.84	34.34	87.36	0.564	0.026	0.826	52.06	3.54	0.0695	0.00143	11
7	212.25	8.56	78.45	0.146	0.030	0.989	13.48	2.55	0.0803	0.00107	49
8	88.07	43.61	60.42	0.600	0.340	0.724	57.31	26.33	0.0761	0.00331	20
9	21.15	25.3	74.37	0.412	0.115	0.904	38.96	8.13	0.0700	0.00876	3
10	286.4	39.9	73.26	0.614	0.185	0.767	57.67	13.44	0.0698	− 0.00165	8
11	159.29	38.14	10.85	0.116	0.607	0.787	56.92	8.42	0.0704	0.00158	7
12	124.44	19.62	19.87	0.114	0.316	0.942	30.30	7.50	0.0754	− 0.00442	18
13	97.38	39.37	56.05	0.526	0.354	0.773	52.27	25.81	0.0722	− 0.00778	90
14	166.95	44.24	85.25	0.695	0.058	0.716	64.69	4.31	0.0691	− 0.00183	74
15	90.09	42.47	56.55	0.563	0.372	0.738	55.17	28.32	0.0700	− 0.00004	2
16	219.56	32.18	83.99	0.530	0.056	0.846	49.16	5.18	0.0728	− 0.00376	10
17	260.23	28.44	41.15	0.313	0.359	0.879	38.39	19.37	0.0675	− 0.00045	4
18	256.5	39.7	27.2	0.292	0.568	0.769	54.67	21.44	0.0670	0.00372	23
19	283.6	36.42	13.55	0.139	0.577	0.805	54.40	9.95	0.0636	0.00766	3
20	293.2	30.6	70.45	0.480	0.170	0.861	46.00	11.60	0.0635	− 0.00259	14
21	165.02	42.65	68.64	0.631	0.247	0.736	58.94	18.71	0.0705	− 0.00765	4
22	164.3	44.51	0.14	0.002	0.701	0.713	65.91	0.23	0.0671	− 0.00345	22
23	55.01	44.66	1.83	0.022	0.703	0.711	65.80	1.66	0.0673	− 0.00002	14
24	165.4	44.36	88.58	0.699	0.017	0.715	65.61	1.27	0.0686	− 0.00389	192
25	263.53	26.44	36.95	0.268	0.356	0.895	37.13	16.39	0.0726	− 0.00368	12
26	71.11	25.22	49.64	0.325	0.276	0.905	34.79	16.48	0.0683	− 0.00050	3
27	257.24	28.58	44.33	0.334	0.342	0.878	37.59	20.47	0.0713	− 0.00516	40
28	101.9	39.02	52.37	0.499	0.384	0.777	50.67	27.66	0.0717	− 0.00658	20
29	235.69	15.15	62.07	0.231	0.122	0.965	23.06	7.20	0.0788	− 0.00447	987
30	351.22	42.2	77.86	0.657	0.141	0.741	61.02	10.43	0.0697	0.00199	12
31	61.74	44.39	16.72	0.201	0.670	0.715	61.57	15.52	0.0678	− 0.00325	8
32	349.23	43.73	80.27	0.681	0.117	0.723	62.97	8.78	0.0666	− 0.00101	31
33	61.51	42.36	16.48	0.191	0.646	0.739	60.03	14.30	0.0668	0.00047	6
34	348.35	29.65	13.93	0.119	0.480	0.869	45.33	8.58	0.0689	0.00041	57
35	56.38	39.11	86.76	0.630	0.036	0.776	58.79	3.30	0.0702	− 0.00394	56
36	96.16	39.2	58.97	0.542	0.326	0.775	53.04	23.75	0.0665	0.00169	3
37	316.16	43.64	36.74	0.413	0.553	0.724	55.00	31.79	0.0737	0.00224	13
38	120.96	29.09	58.52	0.415	0.254	0.874	41.73	16.30	0.0755	0.00209	2
39	100.15	39.44	52.41	0.503	0.388	0.772	51.08	28.05	0.0725	− 0.00587	52
40	97.89	38.66	55.52	0.515	0.354	0.781	51.42	25.49	0.0727	− 0.00833	31
41	98	39.93	56.86	0.537	0.351	0.767	53.05	25.79	0.0715	− 0.00427	325
42	204.42	29.34	81.8	0.485	0.070	0.872	45.09	6.00	0.0690	− 0.00022	28
43	98.7	40.23	55	0.529	0.370	0.763	52.70	27.27	0.0722	− 0.00656	71
44	177.42	45.23	23.97	0.288	0.649	0.704	60.13	22.68	0.0697	− 0.00483	12
45	98.95	39.96	55.41	0.529	0.365	0.766	52.60	26.76	0.0717	− 0.00661	67
46	231.04	41.11	4.51	0.052	0.655	0.753	61.37	3.94	0.0695	− 0.00630	15
47	349.61	42.9	81.04	0.672	0.106	0.733	62.45	7.83	0.0648	− 0.00417	36
48	81.87	32.85	38.15	0.335	0.427	0.840	44.26	22.11	0.0692	− 0.00676	21
49	286.85	24.92	46.28	0.305	0.291	0.907	33.56	17.14	0.0713	− 0.00877	10
50	79.65	32.75	40.66	0.352	0.410	0.841	43.33	23.04	0.0749	− 0.01307	2
51	62.12	39.97	18.18	0.200	0.610	0.766	57.38	14.63	0.0646	− 0.00137	29
52	272.1	38.43	0.65	0.007	0.622	0.783	57.62	2.02	0.0672	− 0.00424	36
53	239.02	15.76	59.4	0.234	0.138	0.962	23.71	7.98	0.0772	− 0.00434	28
54	96.52	39.61	60.4	0.554	0.315	0.770	53.87	23.10	0.0667	− 0.00170	6

Follows Table A.1.

ID	Average Euler angles (°)			Average Miller indices			Projection Coordinates (°)		Average E_{surf} t = 2s (V vs Ag/AgCl)	Average E_{OCP} t = − 0.01s (V vs Ag/AgCl)	Size (pixels)
	φ_1	Φ	φ_2	h	k	l	C_1	C_2			
55	79.58	33.05	77.89	0.533	0.114	0.838	50.19	8.37	0.0646	0.00087	67
56	4.82	30.23	89.91	0.503	0.001	0.864	45.83	2.84	0.0646	0.00214	38
57	200.12	37.45	89.09	0.608	0.010	0.794	56.28	2.32	0.0672	− 0.00305	1654
58	77.88	40.98	63.89	0.589	0.289	0.755	56.16	21.53	0.0639	0.00291	147
59	162.44	38.81	12.17	0.132	0.613	0.779	57.49	9.52	0.0597	0.00306	3
60	117.65	42.21	17.61	0.203	0.640	0.741	59.60	15.22	0.0640	− 0.00267	64
61	343.47	34.84	3.99	0.040	0.570	0.821	52.87	4.14	0.0664	0.00143	13
62	63.11	36.86	62.68	0.533	0.275	0.800	51.80	19.50	0.0655	0.00364	4
63	317.5	33.76	14.67	0.141	0.538	0.831	50.86	9.98	0.0654	0.00214	137
64	321.28	28.76	11.2	0.093	0.472	0.877	44.20	7.19	0.0617	− 0.00025	3
65	247.08	14.28	52	0.194	0.152	0.969	20.80	8.29	0.0799	− 0.00320	11
66	30.47	39.65	47.62	0.471	0.430	0.770	49.45	30.72	0.0702	− 0.00661	16
67	103.19	45.22	29.37	0.348	0.619	0.704	58.57	27.46	0.0687	− 0.00124	52
68	81.77	31.43	73.83	0.501	0.145	0.853	47.57	10.16	0.0642	0.00156	44
69	80.47	31.54	75.44	0.506	0.132	0.852	47.90	9.35	0.0662	− 0.00020	131
70	286.19	26.29	49.87	0.339	0.285	0.897	36.15	17.27	0.0725	− 0.00473	6
71	93.38	32.79	31.01	0.279	0.464	0.841	46.29	18.71	0.0729	− 0.00663	10
72	287.86	26.3	48.55	0.332	0.293	0.896	35.81	17.67	0.0729	− 0.01017	22
73	314.52	32.55	17.64	0.163	0.513	0.843	48.86	11.31	0.0658	− 0.00234	27
74	84.71	39.77	66.57	0.587	0.254	0.769	55.81	18.65	0.0665	0.00113	707
75	23.48	44.14	89.49	0.696	0.006	0.718	65.44	0.58	0.0680	− 0.00417	9
76	254.61	14.37	37.33	0.150	0.197	0.969	21.00	8.25	0.0768	− 0.00518	16
77	133.18	37.21	82.04	0.599	0.084	0.796	56.09	6.35	0.0689	− 0.00076	11
78	327.81	28.68	23.26	0.190	0.441	0.877	42.85	12.50	0.0728	− 0.00684	30
79	357.27	44.18	23.9	0.282	0.637	0.717	59.41	21.90	0.0671	− 0.00121	25
80	277.72	38.24	51.69	0.486	0.384	0.785	49.69	27.25	0.0718	− 0.00376	12
81	349.83	33.49	7.54	0.072	0.547	0.834	51.03	5.97	0.0659	0.00214	45
82	175.77	36.69	22.62	0.230	0.552	0.802	52.85	16.26	0.0643	0.00115	14
83	313.7	43.97	42	0.465	0.516	0.720	53.27	35.36	0.0736	− 0.00305	6
84	317.08	31.12	14.56	0.130	0.500	0.856	47.32	9.25	0.0669	0.00128	47
85	120.23	41.86	14.33	0.165	0.647	0.745	60.15	12.22	0.0649	0.00018	26
86	82.93	31.82	72.25	0.502	0.161	0.850	47.88	11.12	0.0675	0.00258	10
87	277.53	41.28	76.89	0.643	0.150	0.751	59.91	10.96	0.0628	− 0.00091	37
88	203.22	35.7	85.53	0.582	0.045	0.812	54.11	4.33	0.0672	− 0.00203	28
89	207.24	36.42	80.58	0.586	0.097	0.805	54.93	7.24	0.0639	− 0.00355	55
90	120.58	41.61	13.4	0.154	0.646	0.748	60.16	11.32	0.0668	− 0.00561	6
91	278.38	42.11	75.59	0.649	0.167	0.742	60.36	12.39	0.0692	− 0.00401	19
92	121.6	40.84	13.85	0.157	0.635	0.757	59.30	11.44	0.0685	0.00031	5
93	140.87	11.64	83.43	0.200	0.023	0.979	18.23	2.79	0.0761	0.00509	13
94	277.53	39.17	75.53	0.612	0.158	0.775	57.43	11.38	0.0670	− 0.00104	4
95	79.87	34.31	77.09	0.549	0.126	0.826	51.80	9.07	0.0654	0.00148	37
96	283.17	41.88	68.87	0.623	0.241	0.745	58.36	18.06	0.0667	− 0.00075	12
97	76.39	34.47	80.13	0.558	0.097	0.824	52.29	7.31	0.0668	0.00128	19
98	34.21	0.7	79.01	0.012	0.002	1.000	1.11	0.21	0.0791	0.00931	28
99	84.18	46.17	67.2	0.665	0.280	0.693	61.08	22.23	0.0662	0.00204	31
100	84.83	3.49	28.46	0.029	0.054	0.998	5.39	1.63	0.0795	0.00509	130
101	119.36	42.39	15.06	0.175	0.651	0.739	60.44	13.07	0.0662	− 0.00142	16
102	196	37.73	3.35	0.036	0.611	0.791	56.90	3.54	0.0686	− 0.00630	11
103	278.11	41.52	75.24	0.641	0.169	0.749	59.73	12.45	0.0629	0.00097	24
104	82.05	30.75	72.77	0.488	0.151	0.859	46.52	10.49	0.0680	− 0.00009	23
105	280.78	31.94	13.1	0.120	0.515	0.849	48.58	8.69	0.0652	0.00474	22
106	122	33.7	21.59	0.204	0.516	0.832	49.60	14.06	0.0660	0.00103	135
107	10.62	37.86	81.38	0.607	0.092	0.790	56.87	6.83	0.0676	0.00097	4
108	353.44	32.94	19.57	0.182	0.512	0.839	49.04	12.55	0.0703	− 0.00287	8
109	251.53	37.49	80.57	0.600	0.100	0.793	56.31	7.35	0.0682	− 0.00305	84
110	163.45	40.47	12.41	0.139	0.634	0.761	59.26	10.13	0.0633	− 0.00009	497
111	277.79	39.02	57.72	0.532	0.336	0.777	52.48	24.43	0.0683	0.00051	73
112	255.03	40.68	75.25	0.630	0.166	0.758	58.93	12.13	0.0577	− 0.00320	61

Follows Table A.1.

ID	Average Euler angles (°)			Average Miller indices			Projection Coordinates (°)		Average E_{surf} t = 2s (V vs Ag/AgCl)	Average E_{OCP} t = − 0.01s (V vs Ag/AgCl)	Size (pixels)
	φ_1	Φ	φ_2	h	k	l	C_1	C_2			
113	248.78	36.92	84.54	0.598	0.057	0.799	55.81	4.81	0.0659	− 0.00239	19
114	265.43	42.28	67.44	0.621	0.258	0.740	58.30	19.51	0.0636	0.00240	465
115	102.91	9.56	11.07	0.032	0.163	0.986	15.04	2.79	0.0711	0.00484	5
116	106.64	8.55	8.21	0.021	0.147	0.989	13.44	2.26	0.0767	0.00291	5
117	242.78	45.57	25.15	0.303	0.646	0.700	60.03	23.98	0.0647	0.00128	4
118	123.05	36.96	22.7	0.232	0.555	0.799	53.12	16.46	0.0634	0.00298	34
119	67.88	2.64	46.56	0.033	0.032	0.999	3.83	1.57	0.0778	0.00703	27
120	250.35	37.44	82.21	0.602	0.082	0.794	56.41	6.25	0.0630	− 0.00050	20
121	251.81	38.82	79.99	0.617	0.109	0.779	57.87	7.92	0.0635	− 0.00030	15
122	8.13	35.13	3.32	0.033	0.574	0.818	53.24	3.79	0.0641	0.00054	6
123	315.33	40.73	11.88	0.134	0.639	0.758	59.65	9.77	0.0641	0.00351	20
124	230.3	35.11	66.12	0.526	0.233	0.818	50.77	16.19	0.0658	0.00199	4
125	229.38	35.81	65.62	0.533	0.242	0.811	51.44	16.92	0.0681	0.00016	7
126	319.84	40.02	19.87	0.219	0.605	0.766	57.00	16.00	0.0631	0.00357	295
127	206.16	37.33	81.7	0.600	0.088	0.795	56.22	6.58	0.0703	− 0.00630	7
128	317.33	33.59	14.39	0.137	0.536	0.833	50.67	9.78	0.0624	0.00507	46
129	124.88	16.58	75.4	0.276	0.072	0.958	25.91	5.31	0.0675	0.00382	3
130	84.72	32.75	72.96	0.517	0.159	0.841	49.21	11.05	0.0653	0.00341	5
131	341.09	37.15	40.94	0.396	0.456	0.797	47.68	27.44	0.0657	0.00519	11
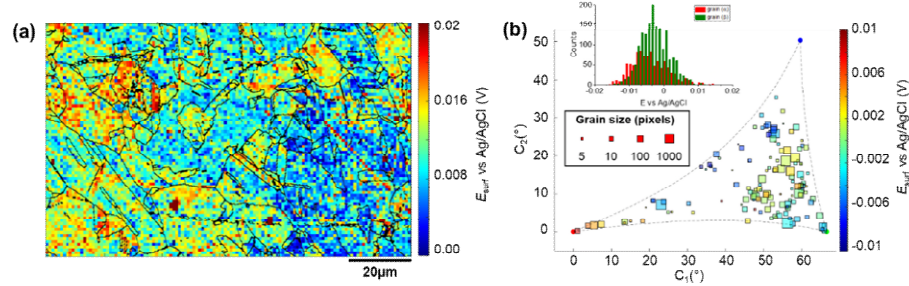
Figure A.13: (**a**) SECCM E_{surf} map at OCP (named E_{OCP}) on a polycrystalline Cu foil electrode immersed in dodecane. The nanopipette probe contained aerated 10 mM H_2SO_4 and contacted an area of 1.6×10^{-9} cm² at each location in the map. The map was extracted at time − 0.01 s of Movie A4, with overlapped grain boundaries from Figure 5.3b. (**b**) E_{OCP}/crystallographic orientation correlation plot, extracted from (a) and Figure 5.3b. The inset in (b) shows the statistical distribution of E_{OCP} extracted from grains α and β, marked in Figure 5.3b.

Cathodic chronopotentiometric pulse
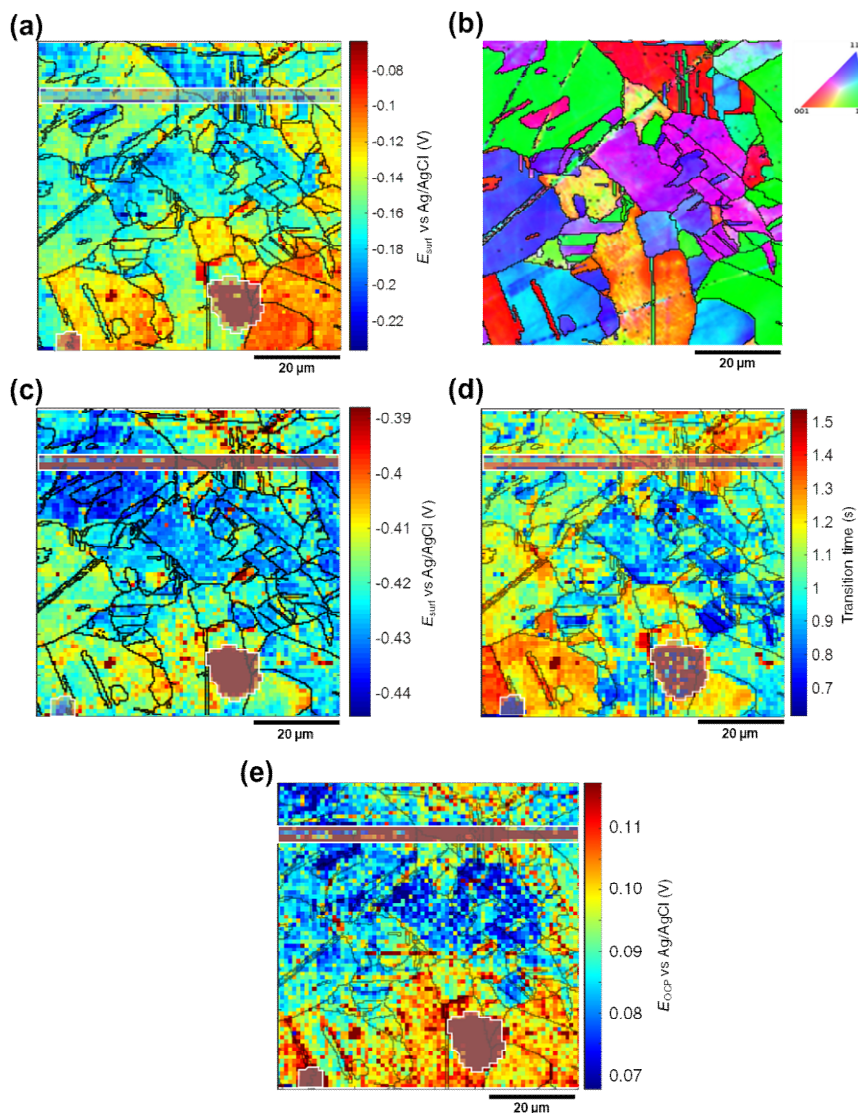
Figure A.14: Maps and graphs of grain dependent analysis of the cathodic chronopotentiometric pulse measured in Movie A6. (**a**) E_{surf} map of the Cu reduction (Cu^{2+}/Cu) process, extracted at t = 0.1 s. (**b**) Co-located crystallographic orientation map (IPFz from EBSD). (**c**) E_{surf} map of the ORR process, extracted at t = 2 s. (**d**) Map of $\tau_{Cu^{2+}/Cu_{(s)}}$, extracted from Movie A6. (**e**) E_{OCP} map, extracted at t = − 0.01 s of Movie A6. During these measurements, the nanopipette probe contained aerated 10 mM H_2SO_4 and contacted an area of 6.4×10^{-9} cm², with I_{app} = − 0.88 mA cm⁻². All the grain boundaries from Figure A.14b were overlapped to Figure A.14a-e. Shaded areas in (a,c-e) were not taken into consideration during the grain analysis, due to image artefacts caused by surface contamination (*e.g.*, dust or dirt), shown in Figure A.9b.
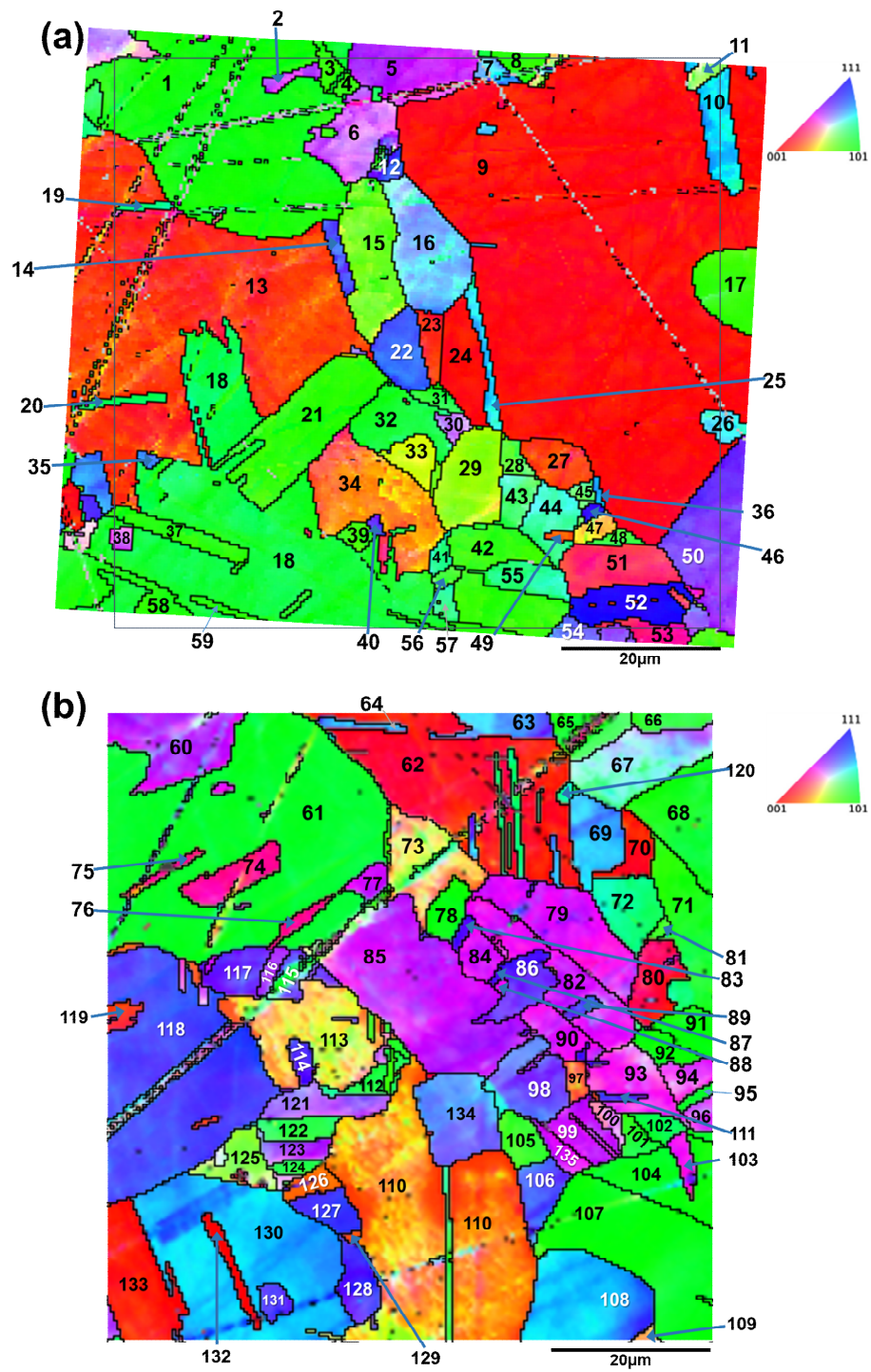
Figure A.15: Definition of the grain ID for each grain analysed from (**a**) Movie A5 (reproduction of Figure 5.4b) and (**b**) Movie A6 (reproduction of Figure A.14b).

Table A.2: List of all grains analysed by SECCM (Movie A5, Movie A6 and Figure A.14, Figure 5.4 and Figure 5.5), with the average Euler angles, Miller indices and Projection Coordinates, τ and E_{surf} listed for each one. The grain IDs correspond to those defined in Figure A.15.

ID	Average Euler angles (°)			Average Miller indices			Projection Coordinates. (°)		Average E_{surf} (V vs Ag/AgCl)		Average τ (s)	Average E_{OCP} − 0.01s (V vs Ag/AgCl)	Size (pix.)
	φ_1	Φ	φ_2	h	k	l	C_1	C_2	Cu depos.	ORR			
1	46.18	42.47	2.72	0.032	0.674	0.738	63.22	2.49	-0.132	-0.437	1.102	0.0097	519
2	305.1	31.93	52.89	0.422	0.319	0.849	43.57	20.87	-0.156	-0.433	0.933	0.0047	15
3	84.07	38.52	88.19	0.622	0.020	0.782	57.89	2.59	-0.128	-0.440	1.087	0.0084	9
4	87.60	37.71	85.96	0.610	0.043	0.791	56.89	3.93	-0.138	-0.440	1.143	0.0085	7
5	279.36	31.39	49.97	0.399	0.335	0.854	42.06	21.56	-0.166	-0.431	1.005	0.0058	61
6	302.65	31.28	56.73	0.434	0.285	0.855	43.92	18.66	-0.163	-0.433	0.933	0.0052	74
7	98.77	40.19	62.97	0.575	0.293	0.764	55.18	21.67	-0.116	-0.402	1.200	0.0153	9
8	202.51	38.94	88.45	0.628	0.017	0.778	58.45	2.37	-0.133	-0.434	1.038	0.0090	6
9	248.33	4.52	57.84	0.067	0.042	0.997	6.89	2.27	-0.164	-0.422	1.203	0.0161	1601
10	332.84	46.80	25.56	0.315	0.658	0.685	60.70	25.23	-0.126	-0.418	1.265	0.0131	40
11	111.00	31.91	75.08	0.511	0.136	0.849	48.36	9.64	-0.143	-0.422	1.260	0.0119	8
12	139.90	42.78	37.70	0.415	0.537	0.734	53.96	31.53	-0.114	-0.419	1.187	0.0124	12
13	41.25	10.79	80.62	0.185	0.031	0.982	16.95	2.93	-0.175	-0.428	1.138	0.0125	668
14	140.50	41.49	35.36	0.383	0.540	0.749	53.69	28.71	-0.129	-0.422	1.190	0.0121	18
15	28.97	32.16	6.26	0.058	0.529	0.847	49.14	5.30	-0.136	-0.437	1.287	0.0111	99
16	122.96	38.51	63.26	0.556	0.280	0.782	53.65	20.26	-0.152	-0.427	1.213	0.0070	118
17	221.31	37.18	1.27	0.013	0.604	0.797	55.95	2.54	-0.124	-0.435	1.098	0.0119	30
18	336.08	43.83	9.51	0.114	0.683	0.721	63.11	8.61	-0.119	-0.430	1.125	0.0154	547
19	245.76	46.01	16.04	0.199	0.691	0.695	62.84	15.75	-0.116	-0.427	1.028	0.0158	6
20	248.06	44.73	12.54	0.153	0.687	0.710	62.96	11.79	-0.133	-0.432	1.056	0.0109	8
21	92.58	38.91	1.31	0.014	0.628	0.778	58.38	2.26	-0.127	-0.438	1.095	0.0120	158
22	143.52	43.20	33.64	0.379	0.570	0.729	55.70	29.14	-0.112	-0.418	1.245	0.0148	58
23	50.62	10.31	71.44	0.170	0.057	0.984	16.15	3.82	-0.165	-0.427	1.125	0.0145	20
24	229.20	3.92	77.25	0.067	0.015	0.998	6.19	1.24	-0.165	-0.424	1.228	0.0158	59
25	332.89	44.17	25.61	0.301	0.628	0.717	58.91	23.40	-0.129	-0.419	1.321	0.0152	27
26	99.51	41.33	65.32	0.600	0.276	0.751	56.88	20.64	-0.123	-0.418	1.239	0.0142	9
27	127.86	11.59	11.30	0.039	0.197	0.980	18.21	3.37	-0.165	-0.427	1.195	0.0153	37
28	44.43	35.70	78.85	0.573	0.113	0.812	53.81	8.24	-0.128	-0.428	1.268	0.0136	18
29	213.55	28.65	2.74	0.023	0.479	0.878	43.82	3.85	-0.125	-0.430	1.352	0.0153	87
30	268.63	32.75	31.08	0.279	0.463	0.841	46.22	18.72	-0.136	-0.425	1.137	0.0121	8
31	49.01	40.33	9.69	0.109	0.638	0.762	59.67	7.91	-0.111	-0.430	1.084	0.0135	13
32	170.60	42.16	81.19	0.663	0.103	0.741	61.79	7.52	-0.117	-0.429	1.143	0.0139	69
33	212.08	25.27	2.79	0.021	0.426	0.904	38.82	3.81	-0.123	-0.417	1.267	0.0159	29
34	36.37	17.95	83.20	0.306	0.036	0.951	27.97	4.04	-0.159	-0.429	1.015	0.0151	150
35	279.63	42.63	58.68	0.579	0.352	0.736	55.99	26.88	-0.099	-0.413	1.224	0.0156	4
36	332.14	46.41	28.79	0.349	0.635	0.689	59.54	27.90	-0.100	-0.407	1.314	0.0198	4
37	55.20	39.44	86.37	0.634	0.040	0.772	59.24	3.50	-0.117	-0.432	1.136	0.0143	33
38	243.44	30.69	56.92	0.428	0.279	0.860	43.28	18.13	-0.122	-0.434	1.059	0.0131	5
39	91.53	36.97	4.27	0.045	0.600	0.799	55.88	4.13	-0.140	-0.437	1.128	0.0117	9
40	138.98	39.82	38.76	0.401	0.499	0.768	51.00	29.09	-0.149	-0.422	1.053	0.0129	3
41	122.32	42.90	72.53	0.649	0.204	0.733	60.22	15.44	-0.103	-0.424	1.060	0.0162	6
42	41.91	37.89	88.80	0.614	0.013	0.789	56.94	2.38	-0.117	-0.432	1.151	0.0170	107
43	314.90	38.27	16.26	0.173	0.595	0.785	56.05	12.44	-0.129	-0.425	1.280	0.0143	25
44	91.12	41.01	69.83	0.616	0.226	0.755	57.85	16.77	-0.122	-0.426	1.212	0.0121	44
45	50.65	36.38	73.64	0.569	0.167	0.805	53.86	11.84	-0.125	-0.425	1.221	0.0142	6
46	201.72	46.12	47.91	0.535	0.483	0.693	54.92	37.91	-0.106	-0.413	1.240	0.0190	6
47	112.91	24.33	77.71	0.403	0.088	0.911	37.67	6.73	-0.153	-0.427	1.136	0.0141	15
48	243.17	37.82	79.46	0.603	0.112	0.790	56.58	8.15	-0.124	-0.428	1.177	0.0158	11
49	295.90	12.65	5.82	0.022	0.218	0.976	19.78	2.90	-0.163	-0.426	1.249	0.0144	4
50	300.56	36.78	52.23	0.473	0.367	0.801	48.47	25.56	-0.136	-0.422	0.856	0.0132	97
51	179.03	17.72	31.26	0.158	0.260	0.953	26.46	9.19	-0.158	-0.427	0.907	0.0143	55

Follows Table A.2.

ID	Average Euler angles (°)			Average Miller indices			Projection Coordinates. (°)		Average E_{surf} (V vs Ag/AgCl)		Average τ (s)	Average E_{OCP} − 0.01s (V vs Ag/AgCl)	Size (pix.)
	φ_1	Φ	φ_2	h	k	l	C_1	C_2	Cu depos.	ORR			
52	106.23	48.94	45.28	0.536	0.531	0.657	55.86	42.70	-0.084	-0.403	1.167	0.0254	67
53	169.63	19.98	41.00	0.224	0.258	0.940	28.04	12.66	-0.141	-0.428	0.821	0.0173	4
54	319.97	39.16	33.03	0.344	0.529	0.775	52.37	25.03	-0.128	-0.412	1.047	0.0228	2
55	319.44	42.33	17.20	0.199	0.643	0.739	59.82	14.92	-0.114	-0.422	1.206	0.0180	36
56	354.16	36.82	9.74	0.101	0.591	0.801	55.42	7.48	-0.112	-0.425	1.187	0.0182	8
57	121.93	41.02	71.90	0.624	0.204	0.754	58.41	15.06	-0.098	-0.426	1.107	0.0198	16
58	54.94	40.47	86.17	0.648	0.043	0.761	60.60	3.51	-0.107	-0.433	1.140	0.0195	26
59	54.70	39.98	87.58	0.642	0.027	0.766	59.95	2.68	-0.103	-0.433	1.133	0.0210	14
60	328.76	32.32	41.25	0.353	0.402	0.845	42.67	22.87	-0.176	-0.425	1.066	0.0023	101
61	244.98	45.12	82.89	0.703	0.088	0.706	64.70	6.82	-0.151	-0.431	1.105	0.0059	474
62	64.84	7.41	66.92	0.119	0.051	0.992	11.56	3.09	-0.185	-0.414	1.146	0.0092	229
63	287.01	41.94	60.82	0.584	0.326	0.744	56.08	24.65	-0.137	-0.403	1.278	0.0117	24
64	287.01	42.88	61.07	0.596	0.329	0.733	56.93	25.21	-0.125	-0.407	1.269	0.0109	9
65	5.45	41.35	6.59	0.076	0.656	0.751	61.38	5.55	-0.124	-0.404	1.208	0.0115	33
66	232.67	38.51	10.45	0.113	0.612	0.782	57.43	8.19	-0.143	-0.421	1.156	0.0074	18
67	129.55	36.52	65.63	0.542	0.246	0.804	52.22	17.34	-0.156	-0.417	1.259	0.0062	89
68	4.79	42.28	6.96	0.082	0.668	0.740	62.32	5.95	-0.141	-0.426	1.086	0.0065	68
69	156.96	43.53	28.02	0.324	0.608	0.725	57.72	24.98	-0.124	-0.413	1.262	0.0112	33
70	14.33	5.19	27.09	0.041	0.081	0.996	8.04	2.36	-0.176	-0.417	1.113	0.0114	15
71	86.40	41.39	83.23	0.657	0.078	0.750	61.39	5.69	-0.131	-0.429	1.061	0.0089	97
72	99.23	44.99	72.89	0.676	0.208	0.707	61.88	16.20	-0.138	-0.417	1.074	0.0086	59
73	56.95	26.01	73.24	0.420	0.126	0.899	39.91	8.76	-0.160	-0.418	1.110	0.0085	69
74	148.18	20.35	46.50	0.252	0.239	0.938	28.02	13.45	-0.200	-0.432	0.929	-0.0007	42
75	155.00	19.00	39.67	0.208	0.251	0.946	27.00	11.69	-0.184	-0.425	0.961	0.0020	9
76	149.67	18.91	44.55	0.227	0.231	0.946	25.98	12.55	-0.190	-0.428	1.091	0.0042	12
77	330.04	30.71	42.91	0.348	0.374	0.860	40.38	21.97	-0.168	-0.429	0.881	0.0028	15
78	24.83	44.90	2.54	0.031	0.705	0.708	65.79	2.39	-0.138	-0.426	1.143	0.0089	31
79	113.74	29.21	46.73	0.355	0.335	0.873	38.62	20.72	-0.173	-0.426	0.922	0.0027	129
80	84.90	12.31	48.12	0.159	0.142	0.977	17.62	7.52	-0.177	-0.422	1.046	0.0085	46
81	333.40	37.13	6.77	0.071	0.599	0.797	56.06	5.60	-0.136	-0.424	1.221	0.0129	7
82	329.65	29.25	43.37	0.336	0.355	0.872	38.63	20.79	-0.185	-0.427	0.926	0.0029	94
83	296.10	42.80	45.03	0.481	0.480	0.734	51.05	35.38	-0.166	-0.419	0.915	0.0053	6
84	117.96	29.63	42.72	0.335	0.363	0.869	39.26	20.92	-0.178	-0.429	0.901	0.0027	26
85	329.90	31.31	41.57	0.345	0.389	0.854	41.47	22.06	-0.173	-0.427	0.966	0.0037	272
86	151.42	39.73	40.73	0.417	0.484	0.769	50.17	30.02	-0.152	-0.419	1.087	0.0063	38
87	295.60	44.61	44.05	0.488	0.505	0.712	52.91	37.11	-0.150	-0.409	1.105	0.0097	2
88	117.81	28.22	45.24	0.336	0.333	0.881	37.05	20.27	-0.165	-0.425	0.919	0.0052	4
89	144.28	40.99	50.38	0.505	0.418	0.755	51.72	30.78	-0.148	-0.416	1.159	0.0081	8
90	113.27	29.22	48.09	0.363	0.326	0.873	39.05	20.30	-0.173	-0.429	0.865	0.0015	32
91	164.62	43.56	0.22	0.003	0.689	0.725	64.64	0.56	-0.126	-0.429	1.074	0.0098	31
92	235.74	44.93	89.01	0.706	0.012	0.708	66.23	0.92	-0.120	-0.426	1.098	0.0121	22
93	173.02	28.03	46.76	0.342	0.322	0.883	37.31	19.66	-0.155	-0.426	0.974	0.0066	61
94	325.13	29.06	37.35	0.295	0.386	0.874	40.20	18.58	-0.145	-0.422	0.940	0.0085	21
95	237.52	45.02	83.96	0.703	0.074	0.707	64.93	5.76	-0.139	-0.418	0.983	0.0104	6
96	325.88	30.54	37.01	0.306	0.406	0.861	42.02	19.66	-0.138	-0.425	0.971	0.0093	13
97	24.86	17.78	18.72	0.098	0.289	0.952	27.60	6.55	-0.157	-0.421	1.098	0.0113	14
98	154.45	38.95	33.92	0.351	0.522	0.778	51.88	25.41	-0.135	-0.412	1.093	0.0088	66
99	325.98	30.90	45.27	0.365	0.361	0.858	39.98	22.73	-0.153	-0.426	0.809	0.0053	36
100	124.80	29.40	28.96	0.238	0.430	0.871	42.69	15.43	-0.126	-0.415	0.930	0.0105	10
101	24.56	40.57	81.91	0.644	0.092	0.760	60.23	6.67	-0.109	-0.421	1.128	0.0125	13
102	257.72	45.24	10.72	0.132	0.698	0.704	63.80	10.30	-0.120	-0.423	0.988	0.0111	16
103	73.73	27.33	47.90	0.341	0.308	0.888	36.84	18.72	-0.137	-0.424	0.764	0.0078	14
104	161.80	44.00	3.17	0.038	0.694	0.719	64.87	2.81	-0.108	-0.421	1.035	0.0127	76
105	69.20	37.74	82.58	0.607	0.079	0.791	56.83	6.02	-0.124	-0.428	1.151	0.0110	29
106	149.70	41.64	35.10	0.382	0.544	0.747	53.91	28.68	-0.116	-0.405	1.205	0.0113	33
107	232.44	42.71	3.34	0.040	0.677	0.735	63.44	2.95	-0.113	-0.421	1.047	0.0125	224
108	9.91	46.92	62.06	0.645	0.342	0.683	60.11	27.52	-0.103	-0.417	1.197	0.0125	136

Follows Table A.2.

ID	Average Euler angles (°)			Average Miller indices			Projection Coordinates. (°)		Average E_{surf} (V vs Ag/AgCl)		Average τ (s)	Average E_{OCP} − 0.01s (V vs Ag/AgCl)	Size (pix.)
	φ_1	Φ	φ_2	h	k	l	C_1	C_2	Cu depos.	ORR			
109	297.51	23.06	73.30	0.375	0.113	0.920	35.61	7.81	-0.118	-0.417	1.010	0.0151	7
110	48.34	19.33	83.03	0.329	0.040	0.944	30.08	4.31	-0.151	-0.415	1.087	0.0133	395
111	355.10	43.32	50.83	0.532	0.433	0.728	53.86	33.02	-0.126	-0.415	0.868	0.0103	7
112	56.81	41.82	12.47	0.144	0.651	0.745	60.58	10.59	-0.132	-0.425	1.084	0.0103	30
113	52.53	25.26	76.23	0.414	0.102	0.904	39.00	7.46	-0.182	-0.430	1.107	0.0075	145
114	138.09	41.93	49.55	0.508	0.434	0.744	52.21	32.24	-0.173	-0.415	1.098	0.0050	14
115	309.15	38.26	29.39	0.304	0.540	0.785	52.64	21.90	-0.174	-0.425	1.167	0.0048	29
116	110.26	33.40	52.23	0.435	0.337	0.835	44.97	22.43	-0.173	-0.425	0.994	0.0034	13
117	299.96	39.30	40.04	0.407	0.485	0.774	50.04	29.22	-0.186	-0.422	1.143	0.0039	36
118	90.36	41.96	53.53	0.538	0.397	0.744	53.71	29.90	-0.158	-0.416	1.156	0.0063	339
119	217.01	11.38	73.11	0.189	0.057	0.980	17.84	4.00	-0.183	-0.417	1.172	0.0075	13
120	102.59	45.73	69.79	0.672	0.247	0.698	61.52	19.53	-0.136	-0.410	1.217	0.0061	4
121	321.42	33.94	56.65	0.466	0.307	0.830	46.93	20.79	-0.162	-0.422	0.976	0.0062	36
122	55.89	40.23	12.13	0.136	0.631	0.763	59.07	9.84	-0.140	-0.425	1.105	0.0100	29
123	321.49	33.60	53.64	0.446	0.328	0.833	45.64	21.97	-0.161	-0.424	0.863	0.0045	19
124	56.20	40.87	11.31	0.128	0.642	0.756	59.92	9.34	-0.141	-0.426	1.021	0.0072	8
125	215.50	31.46	12.20	0.110	0.510	0.853	47.99	8.13	-0.154	-0.422	1.260	0.0087	42
126	202.14	13.38	87.49	0.231	0.010	0.973	20.79	2.57	-0.175	-0.422	1.227	0.0093	18
127	91.28	44.18	51.29	0.544	0.436	0.717	54.72	33.66	-0.129	-0.410	1.123	0.0106	31
128	64.07	42.20	46.93	0.491	0.459	0.741	51.37	33.86	-0.119	-0.407	0.938	0.0121	37
129	207.74	11.43	81.63	0.196	0.029	0.980	17.93	2.97	-0.155	-0.417	1.138	0.0122	4
130	137.67	47.06	27.97	0.343	0.647	0.681	60.19	27.65	-0.123	-0.415	1.233	0.0106	366
131	72.52	41.03	37.90	0.403	0.518	0.754	52.39	29.84	-0.137	-0.413	1.154	0.0108	10
132	51.50	0.58	60.17	0.009	0.005	1.000	0.90	0.28	-0.156	-0.418	1.344	0.0167	17
133	93.38	6.18	19.54	0.036	0.101	0.994	9.71	2.36	-0.166	-0.418	1.334	0.0137	93
134	112.54	29.71	47.46	0.365	0.335	0.869	39.41	20.94	-0.127	-0.419	1.159	0.0102	92
135	325.98	30.90	45.27	0.365	0.361	0.858	39.98	22.73	-0.153	-0.427	0.749	0.0045	18
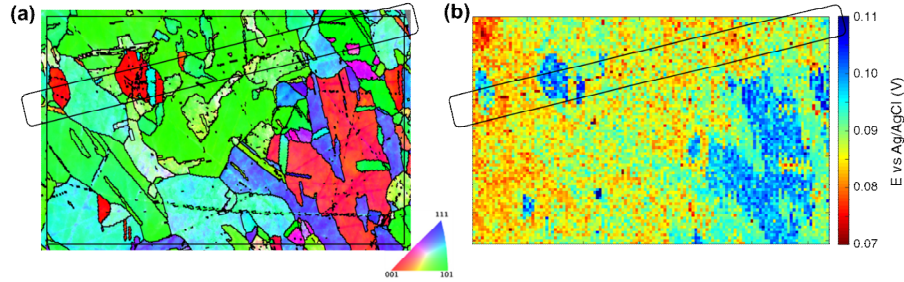
Figure A.16: Reproduction of (**a**) the EBSD (IPFz) map and (**b**) the E_{surf} map reported in Figure 5.3 (i.e., Cu oxidation activity on polycrystalline Cu). In both images, the marked area contains a visible microscratch, identified in (a), which gives rise to enhanced oxidation activity, visible in (b). Other scratches can also be identified in (a), but they do not appear to give rise to an electrochemical behaviour that is significantly different from underlying grains, in (b).

A.5.2. Chapter 6 scans
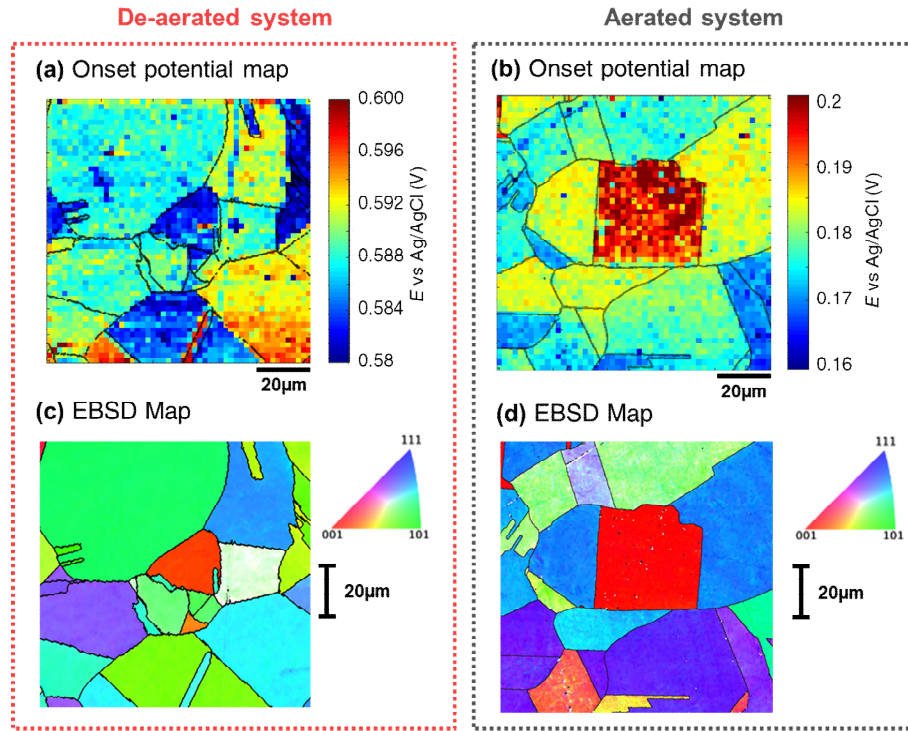
Figure A.17: **(a,b)** Maps of E_{SmA} obtained under **(a)** de-aerated (extracted from Movie A8) and **(b)** aerated (extracted from Movie A10) conditions, obtained in the SECCM configuration with a nanopipette probe containing 0.01 M H_2SO_4. **(c,d)** Co-located crystallographic orientation maps, (IPFz from EBSD) for the scanned area of **(c)** Movie A8 and **(d)** Movie A10. The grain boundaries extracted from (c) and (d) are overlapped to (a) and (b) respectively

De-aerated system

Figure A.18: Definition of the grain ID for each grain analysed from **(a)** Movie A8 (reproduction of Figure A.17c) and **(b)** Movie A7 (reproduction of Figure 6.6c).

Table A.3: List of all grains analysed by SECCM in de-aerated conditions (Movie A7 and Movie A8), with the average Euler angles, Miller indices and Projection Coordinates, anodic E_{5mA} and E_{2mA} and cathodic E_{2mA} listed for each one. The grain IDs correspond to those defined in Figure A.18.

ID	Average Euler angles (°)			Average Miller indices			Projection Coordinates (°)		Average anodic E_{5mA} (V)	Average anodic E_{2mA} (V)	Average cathodic E_{2mA} (V)	Size (pixels)
	φ_1	Φ	φ_2	h	k	l	C_1	C_2				
1	350.96	43.10	76.20	0.664	0.163	0.730	61.372	12.529	0.5881	0.5612	−0.3504	678
2	158.86	45.14	29.60	0.350	0.616	0.705	58.440	27.479	0.5914	0.5614	−0.3711	222
3	248.82	27.34	3.09	0.025	0.459	0.888	41.916	4.617	0.5836	0.5566	−0.3770	15
4	248.64	29.65	2.56	0.022	0.494	0.869	45.268	4.393	0.5818	0.5542	−0.3773	38
5	120.48	32.57	88.29	0.538	0.016	0.843	49.425	3.837	0.5816	0.5548	−0.3698	35
6	248.37	25.64	3.80	0.029	0.432	0.902	39.446	4.815	0.5809	0.5542	−0.3719	8
7	119.15	32.01	0.13	0.001	0.530	0.848	48.412	3.178	0.5807	0.5545	−0.3707	19
8	247.88	26.85	4.08	0.032	0.451	0.892	41.264	4.979	0.5809	0.5548	−0.3821	38
9	270.96	36.68	89.25	0.597	0.008	0.802	55.172	2.778	0.5826	0.5566	−0.3545	10
10	357.23	8.91	1.15	0.003	0.155	0.988	13.849	1.997	0.5828	0.5568	−0.3365	104
11	308.49	31.95	67.58	0.489	0.202	0.849	47.263	14.662	0.5888	0.5620	−0.3660	107
12	343.56	40.43	60.64	0.565	0.318	0.761	54.700	23.986	0.5922	0.5635	−0.3720	39
13	150.27	28.55	81.83	0.473	0.068	0.878	43.933	6.761	0.5832	0.5570	−0.3833	24
14	124.76	35.30	55.24	0.475	0.329	0.816	47.957	23.210	0.5855	0.5593	−0.3703	8
15	320.94	37.33	35.55	0.353	0.493	0.795	49.770	25.306	0.5918	0.5637	−0.3719	13
16	124.68	36.47	55.28	0.489	0.339	0.804	49.180	24.156	0.5887	0.5627	−0.3663	200
17	208.20	42.87	21.90	0.254	0.631	0.733	58.969	19.573	0.5889	0.5623	−0.3580	13
18	346.50	35.79	73.73	0.561	0.164	0.811	53.171	12.471	0.5890	0.5627	−0.3548	74
19	209.49	41.88	20.18	0.230	0.627	0.745	58.621	17.653	0.5864	0.5606	−0.3558	6
20	138.64	36.91	77.68	0.587	0.128	0.800	55.197	10.038	0.5834	0.5581	−0.3617	16
21	147.56	41.91	69.24	0.625	0.237	0.744	58.488	18.153	0.5867	0.5605	−0.3510	4
22	47.35	36.66	14.63	0.151	0.578	0.802	54.515	11.589	0.5903	0.5645	−0.3540	14
23	194.59	16.44	5.87	0.029	0.282	0.959	25.621	4.191	0.5854	0.5599	−0.3303	9
24	208.46	42.99	21.43	0.249	0.635	0.731	59.197	19.227	0.5905	0.5645	−0.3520	98
25	329.39	34.66	55.25	0.467	0.324	0.823	47.281	22.684	0.5896	0.5653	−0.3591	11
26	132.14	44.04	24.52	0.288	0.632	0.719	59.128	22.443	0.5955	0.5687	−0.3608	32
27	218.59	30.88	2.50	0.022	0.513	0.858	47.058	4.319	0.5841	0.5585	−0.3718	247
28	308.58	41.27	66.79	0.606	0.260	0.752	57.248	19.848	0.5968	0.5687	−0.3639	17
29	132.22	44.07	24.38	0.287	0.634	0.718	59.190	22.338	0.5932	0.5657	−0.3639	298
30	179.34	49.12	54.68	0.617	0.437	0.654	59.327	35.308	0.5951	0.5665	−0.3671	121
31	23.12	25.29	26.22	0.189	0.383	0.904	37.782	12.906	0.5883	0.5630	−0.3528	32
32	173.08	42.04	88.75	0.669	0.015	0.743	62.678	1.800	0.5897	0.5655	−0.3364	11
33	292.58	39.41	34.84	0.363	0.521	0.773	52.006	26.711	0.5954	0.5686	−0.3598	38
34	49.84	35.24	80.87	0.570	0.092	0.817	53.384	7.771	0.5899	0.5650	−0.3388	43
35	318.66	37.63	18.12	0.190	0.580	0.792	54.937	14.343	0.5901	0.5652	−0.3383	44
36	163.30	36.04	86.91	0.587	0.032	0.809	54.516	4.152	0.5904	0.5655	−0.3474	7
37	338.72	30.58	54.16	0.412	0.298	0.861	42.398	19.883	0.5956	0.5701	−0.3521	99
38	171.08	42.79	38.82	0.426	0.529	0.734	53.556	32.097	0.5952	0.5685	−0.3620	498
39	99.94	22.84	71.61	0.368	0.122	0.922	35.174	9.209	0.5877	0.5624	−0.3641	4
40	224.94	39.87	28.4	0.305	0.564	0.768	54.476	22.920	0.5938	0.5674	−0.3546	59
41	309.28	10.9	88.95	0.189	0.003	0.982	16.913	2.356	0.5899	0.5660	−0.3306	52
42	123.73	27.75	89.21	0.466	0.006	0.885	42.296	3.739	0.5872	0.5628	−0.3697	111
43	251.61	38.04	73.7	0.591	0.173	0.788	55.791	13.151	0.5916	0.5669	−0.3579	9
44	256.45	30.83	88.38	0.512	0.014	0.859	46.894	3.935	0.5863	0.5608	−0.3601	110
45	272.61	21.08	87.56	0.359	0.015	0.933	32.512	4.043	0.5901	0.5663	−0.3624	23
46	271.94	20.56	88.25	0.351	0.011	0.936	31.678	3.808	0.5888	0.5647	−0.3564	9
47	65.83	32.58	23.26	0.213	0.495	0.843	47.885	15.413	0.5935	0.5688	−0.3553	15
48	31.01	41.48	29.32	0.324	0.578	0.749	55.641	24.701	0.5956	0.5682	−0.3628	15
49	214.6	42.9	61.3	0.597	0.327	0.733	57.014	25.214	0.5960	0.5694	−0.3611	145
50	292.94	39.33	34.51	0.359	0.522	0.774	52.042	26.451	0.5966	0.5704	−0.3589	27
51	93.68	34.28	57.84	0.477	0.300	0.826	47.648	21.139	0.5913	0.5666	−0.3544	110
52	49.77	35.26	80.9	0.570	0.091	0.817	53.413	7.754	0.5909	0.5661	−0.3362	347

Follows Table A.3.

ID	Average Euler angles (°)			Average Miller indices			Projection Coordinates (°)		Average anodic E_{5mA} (V)	Average anodic E_{2mA} (V)	Average cathodic E_{2mA} (V)	Size (pixels)
	φ_1	Φ	φ_2	h	k	l	C_1	C_2				
53	319.79	37.96	16.17	0.171	0.591	0.788	55.729	13.031	0.5930	0.5679	− 0.3362	9
54	320.36	38.32	15.9	0.170	0.596	0.785	56.187	12.936	0.5925	0.5674	− 0.3357	23
55	348.27	30.39	3.52	0.031	0.505	0.863	46.432	4.790	0.5875	0.5630	− 0.3509	99
56	292.98	39.51	34.35	0.359	0.525	0.772	52.263	26.511	0.5962	0.5698	− 0.3574	78
57	320.42	37.95	15.99	0.169	0.591	0.789	55.756	12.896	0.5939	0.5687	− 0.3414	5
58	280.1	45.3	18.71	0.228	0.673	0.703	61.651	17.804	0.5963	0.5716	− 0.3402	53
59	93.87	34.54	57.67	0.479	0.303	0.824	47.883	21.419	0.5920	0.5672	− 0.3559	46
60	338.94	27.48	22.85	0.179	0.425	0.887	41.294	12.758	0.5861	0.5618	− 0.3569	79
61	284.61	30.31	49.21	0.382	0.330	0.863	40.622	21.318	0.5929	0.5676	− 0.3576	39

Aerated system
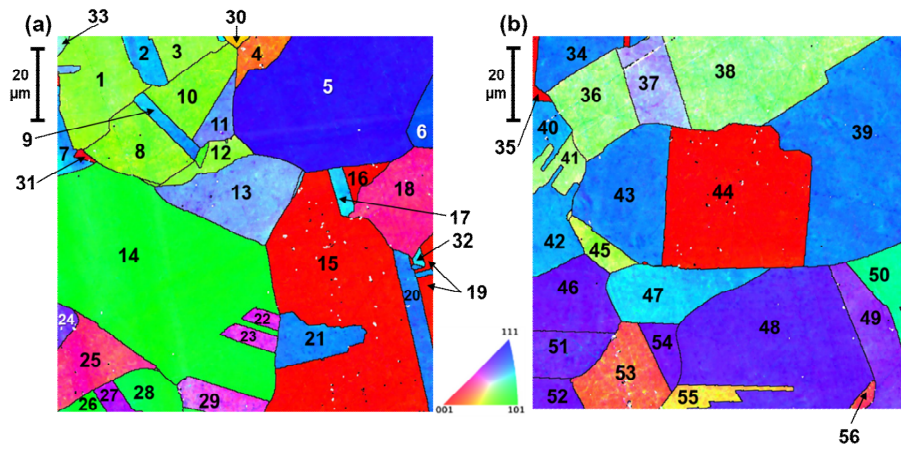
Figure A.19: Definition of the grain ID for each grain analysed from (**a**) Movie A9 (reproduction of Figure 6.6d) and (**b**) Movie A10 (reproduction of Figure A.17d).

Table A.4: List of all grains analysed by SECCM in aerated condition (Movie A9 and Movie A10), with the average Euler angles, Miller indices and Projection Coordinates, anodic E_{5mA} and E_{2mA} ,cathodic E_{2mA} and GOS listed for each one. The grain IDs correspond to those defined in Figure A.19.
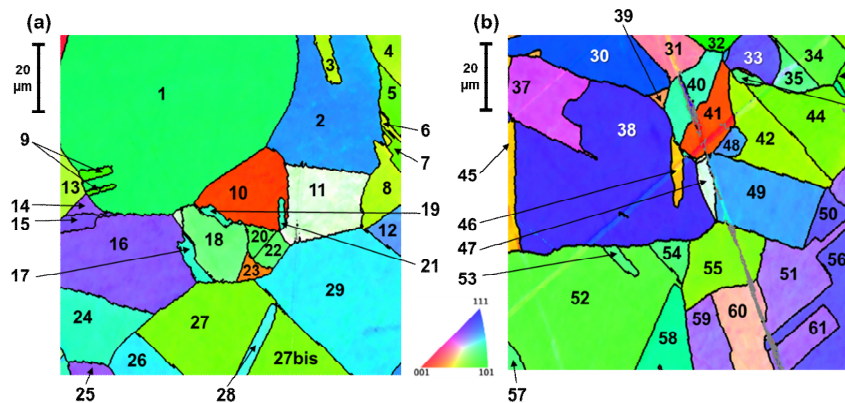
ID	Average Euler angles (°)			Average Miller indices			Projection Coordinates (°)		Average anodic E_{5mA} (V)	Average anodic E_{2mA} (V)	Average cathodic E_{2mA} (V)	GOS (°)	Size (pixels)
	φ_1	Φ	φ_2	h	k	l	C_1	C_2					
1	320.73	30.87	9.06	0.081	0.507	0.858	47.29	6.53	0.1727	0.1446	− 0.3800	1.78	108
2	237.96	47.28	27.69	0.341	0.651	0.678	60.40	27.56	0.1767	0.1469	− 0.3250	1.41	26
3	319.04	31.13	11.34	0.102	0.507	0.856	47.58	7.65	0.1732	0.1445	− 0.3712	1.27	31
4	211.30	17.45	77.40	0.293	0.065	0.954	27.27	5.14	0.1818	0.1527	− 0.3556	1.76	28
5	301.28	46.05	46.92	0.526	0.492	0.694	54.45	38.36	0.1877	0.1559	− 0.3293	1.10	368
6	8.15	49.83	36.11	0.450	0.617	0.645	59.51	37.44	0.1884	0.1562	− 0.3322	1.17	24
7	238.06	47.26	27.29	0.337	0.653	0.679	60.50	27.17	0.1771	0.1458	− 0.3277	1.95	26
8	105.62	31.07	83.41	0.513	0.059	0.857	47.57	5.42	0.1722	0.1437	− 0.3771	2.21	86
9	192.84	47.01	61.68	0.644	0.347	0.682	60.06	27.94	0.1772	0.1472	− 0.3307	1.69	15
10	105.32	31.23	83.88	0.516	0.055	0.855	47.79	5.21	0.1737	0.1448	− 0.3756	1.66	73

Follows Table A.4.

ID	Average Euler angles (°)			Average Miller indices			Projection Coordinates (°)		Average anodic E_{5mA} (V)	Average anodic E_{2mA} (V)	Average cathodic E_{2mA} (V)	GOS (°)	Size (pixels)
	φ_1	Φ	φ_2	h	k	l	C_1	C_2					
11	7.49	39.34	30.21	0.319	0.548	0.773	53.43	23.31	0.1832	0.1529	− 0.3298	1.48	24
12	319.76	30.81	9.68	0.086	0.505	0.859	47.19	6.81	0.1712	0.1425	− 0.3766	1.64	27
13	60.65	38.18	61.44	0.543	0.296	0.786	52.80	21.28	0.1719	0.1422	− 0.3270	1.28	130
14	243.74	43.89	6.53	0.079	0.689	0.721	63.94	5.87	0.1706	0.1421	− 0.3739	1.73	571
15	165.27	2.53	77.12	0.043	0.010	0.999	4.00	0.81	0.1929	0.1621	− 0.3546	1.58	434
16	169.00	2.78	73.30	0.046	0.014	0.999	4.39	0.99	0.1876	0.1568	− 0.3485	1.93	15
17	359.38	45.53	26.16	0.315	0.641	0.701	59.72	24.87	0.1815	0.1513	− 0.3317	1.48	13
18	345.04	20.94	37.88	0.219	0.282	0.934	29.89	12.66	0.1730	0.1453	− 0.3441	1.64	101
19	156.08	3.93	86.26	0.068	0.004	0.998	6.16	0.90	0.1898	0.1619	− 0.3511	1.26	17
20	39.24	45.89	57.79	0.608	0.383	0.696	58.18	30.46	0.1845	0.1543	− 0.3438	1.29	37
21	265.66	47.17	31.01	0.378	0.629	0.680	59.39	30.51	0.1817	0.1517	− 0.3352	1.14	56
22	152.94	28.66	49.99	0.367	0.308	0.877	38.98	19.19	0.1736	0.1451	− 0.3591	1.79	8
23	150.96	29.12	51.79	0.382	0.301	0.874	40.03	18.94	0.1726	0.1448	− 0.3626	1.64	16
24	130.13	38.52	39.08	0.393	0.483	0.782	49.68	27.93	0.1771	0.1490	− 0.3495	1.52	16
25	349.18	20.91	34.23	0.201	0.295	0.934	30.49	11.77	0.1739	0.1461	− 0.3566	2.46	88
26	36.02	43.93	81.27	0.686	0.105	0.720	63.39	7.92	0.1724	0.1444	− 0.3860	1.97	11
27	118.86	31.68	45.59	0.375	0.368	0.851	40.91	23.37	0.1732	0.1455	− 0.3551	1.91	16
28	35.60	43.60	81.49	0.682	0.102	0.724	63.18	7.61	0.1733	0.1457	− 0.3541	2.17	15
29	149.77	29.39	54.31	0.399	0.286	0.871	41.04	18.21	0.1733	0.1453	− 0.3647	2.04	36
30	305.88	21.53	1.97	0.013	0.367	0.930	33.16	3.38	0.1763	0.1649	− 0.3228	1.26	4
31	78.20	6.48	44.75	0.079	0.080	0.994	9.25	3.99	0.1832	0.1609	− 0.3613	1.55	4
32	359.56	44.75	24.96	0.297	0.638	0.710	59.52	23.24	0.1853	0.1470	− 0.3791	1.62	4
33	279.01	36.94	23.85	0.243	0.550	0.799	52.81	17.24	0.1725	0.1484	− 0.3445	1.33	5
34	23.78	47.27	58.42	0.626	0.385	0.679	59.29	31.10	0.1955	0.1470	− 0.3803	1.57	45
35	82.32	3.53	54.69	0.050	0.036	0.998	5.33	1.86	0.1921	0.1518	− 0.3420	1.11	8
36	239.02	32.90	17.19	0.161	0.519	0.840	49.38	11.18	0.1760	0.1446	− 0.3441	1.00	112
37	344.96	35.01	61.96	0.506	0.270	0.819	49.60	18.67	0.1783	0.1418	− 0.3681	1.26	77
38	238.52	33.29	17.73	0.167	0.523	0.836	49.80	11.63	0.1763	0.1549	− 0.3532	1.61	234
39	23.85	47.30	58.59	0.627	0.383	0.678	59.35	30.98	0.1806	0.1517	− 0.3439	1.16	365
40	252.47	46.88	28.58	0.349	0.641	0.684	59.90	28.08	0.1751	0.1629	− 0.3681	1.77	98
41	35.72	31.91	73.17	0.506	0.153	0.849	48.13	10.66	0.1718	0.1428	− 0.3675	1.93	36
42	104.18	3.82	33.45	0.037	0.056	0.998	5.80	1.96	0.1876	0.1516	− 0.3415	1.18	1
43	23.83	47.01	58.82	0.626	0.379	0.682	59.24	30.53	0.1825	0.1511	− 0.3434	1.10	178
44	83.74	2.51	53.53	0.035	0.026	0.999	3.77	1.34	0.1933	0.1475	− 0.3455	1.12	356
45	302.09	29.63	78.25	0.484	0.101	0.869	45.43	7.58	0.1716	0.1404	− 0.3595	1.36	28
46	4.87	38.72	41.60	0.415	0.468	0.780	48.91	29.37	0.1827	0.1398	− 0.3503	1.07	90
47	290.62	46.08	63.60	0.645	0.320	0.694	60.01	25.49	0.1822	0.1420	− 0.3593	1.36	114
48	299.25	39.95	40.24	0.415	0.490	0.767	50.56	30.00	0.1776	0.1465	− 0.3348	1.07	362
49	109.53	36.35	51.36	0.463	0.370	0.805	47.74	25.57	0.1688	0.1453	− 0.3775	2.14	90
50	192.16	46.21	18.58	0.230	0.684	0.692	62.27	18.28	0.1696	0.1496	− 0.3414	1.02	45
51	177.59	38.13	50.50	0.476	0.393	0.787	49.16	27.75	0.1711	0.1398	− 0.3860	1.54	65
52	5.70	37.87	41.05	0.403	0.463	0.789	48.33	28.23	0.1770	0.1575	− 0.3562	2.12	24
53	237.76	19.29	22.03	0.124	0.306	0.944	29.66	7.90	0.1747	0.1481	− 0.3676	0.93	101
54	4.69	38.18	41.88	0.413	0.460	0.786	48.30	28.92	0.1806	0.1520	− 0.3524	1.52	33
55	49.55	24.19	79.12	0.402	0.077	0.912	37.48	6.24	0.1694	0.1544	− 0.3397	2.46	30
56	164.91	17.53	27.44	0.139	0.267	0.954	26.60	8.30	0.1868	0.1433	− 0.3434	1.79	6

A.5.3. Chapter 7 scans

Un-inhibited case
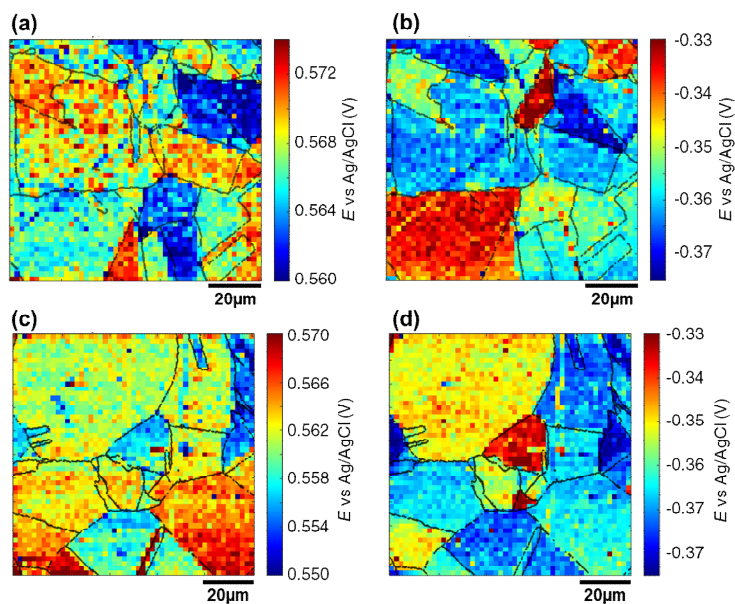
Figure A.20: E_{2mA} maps obtained in de-aerated conditions with dodecane as oil phase (Movies A7-A8). **(a-b)** Anodic **(a)** and cathodic **(b)** E_{2mA} from Movie A7, with overlapped grain boundaries from Figure 6.6c. **(c-d)** Anodic **(c)** and cathodic **(d)** E_{2mA} from Movie A8, with overlapped grain boundaries from Figure A.17c.
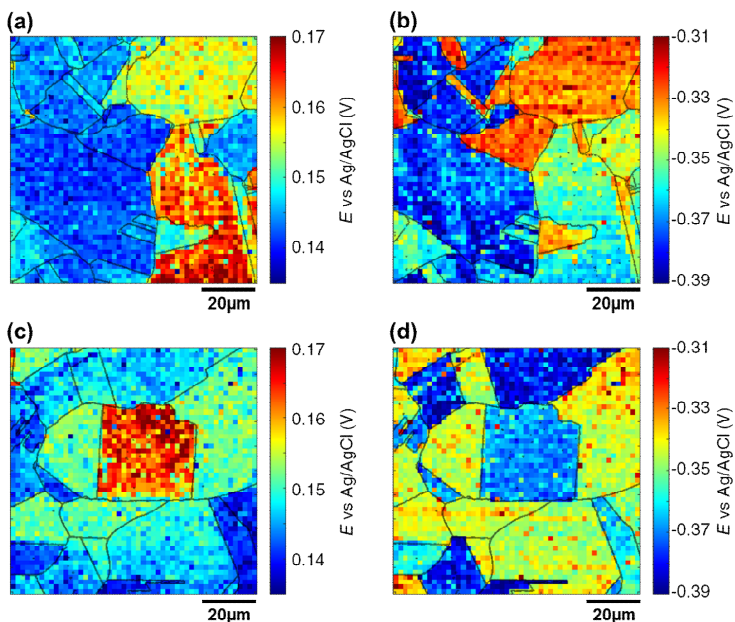
Figure A.21: E_{2mA} maps obtained in aerated conditions with dodecane as oil phase (Movies A9-A10). **(a-b)** Anodic **(a)** and cathodic **(b)** E_{2mA} from Movie A9, with overlapped grain boundaries from Figure 6.6d. **(c-d)** Anodic **(c)** and cathodic **(d)** E_{2mA} from Movie A10, with overlapped grain boundaries from Figure A.17d.

Inhibited case
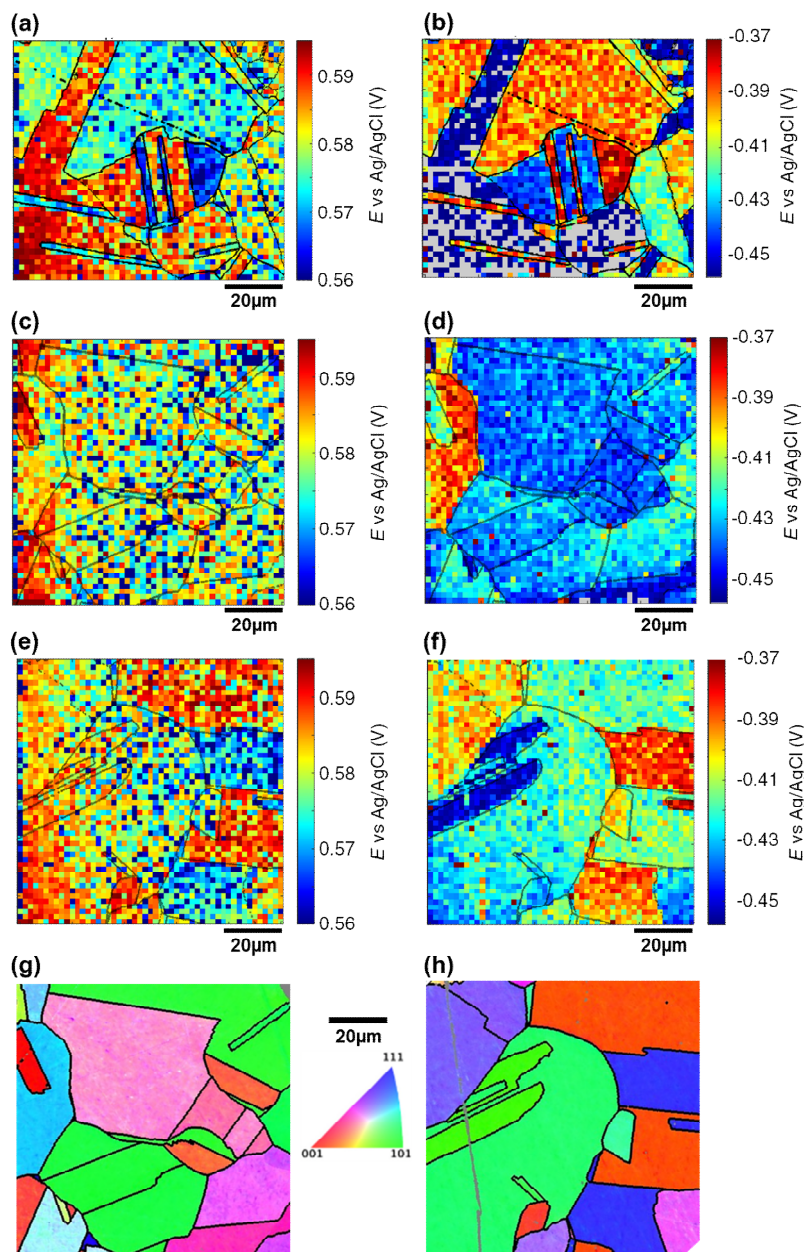
Figure A.22: E_{2mA} maps obtained in de-aerated conditions with 100 ppm BTA–R in dodecane as oil phase (Movies A11-A13) and related EBSD maps. **(a-b)** Anodic **(a)** and cathodic **(b)** E_{2mA} from Movie A11, with overlapped grain boundaries from Figure 7.2c. The grey points in (b) represents single measures where the cathodic current never reached the value of – 2 mA cm^{-2} in the considered potential range. **(c-d)** Anodic **(c)** and cathodic **(d)** E_{2mA} from Movie A12, with overlapped grain boundaries from **(g)**. **(e-f)** Anodic **(e)** and cathodic **(f)** E_{2mA} from Movie A13, with overlapped grain boundaries from **(h)**. **(g-h)** Co-located crystallographic orientation maps (IPFz) measured for **(g)** Movie A12 and **(h)** Movie A13.
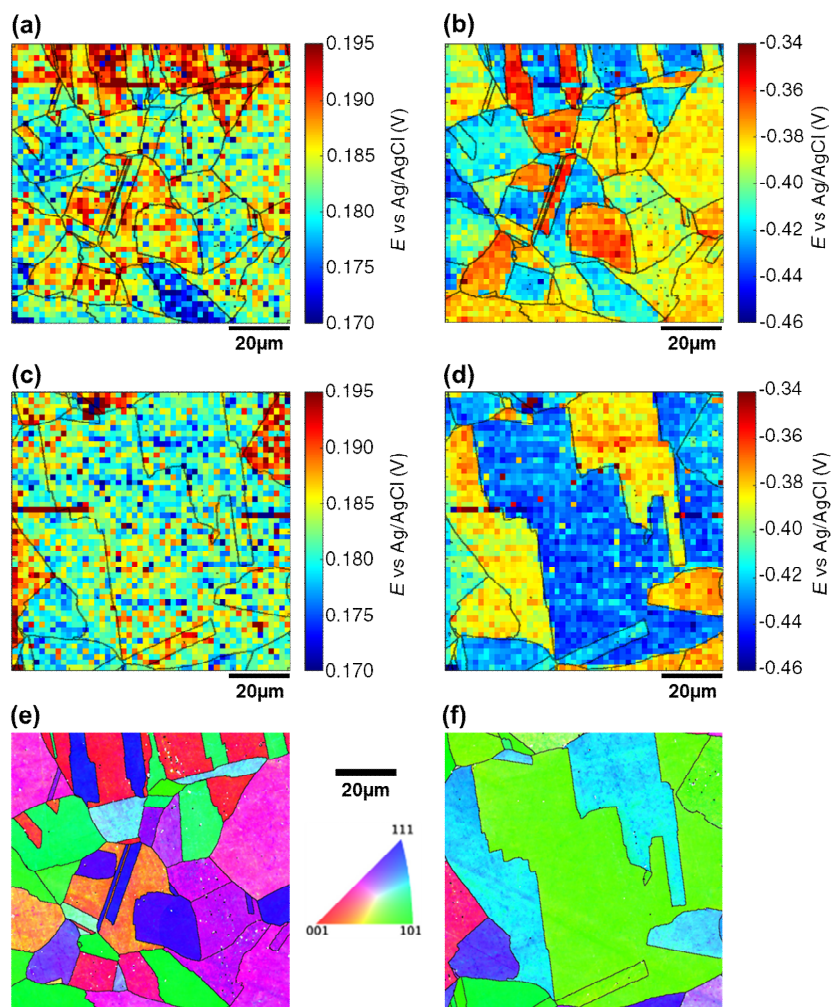
Figure A.23: E_{2mA} maps obtained in aerated conditions with 100 ppm BTA–R in do-decane as oil phase (Movies A14-A15) and related EBSD maps. **(a-b)** Anodic **(a)** and cathodic **(b)** E_{2mA} from Movie A14, with overlapped grain boundaries from (e). **(c-d)** Anodic **(c)** and cathodic **(d)** E_{2mA} from Movie A15, with overlapped grain boundaries from (f). **(e-f)** Co-located crystallographic orientation maps (IPFz) measured for **(e)** Movie A14 and **(f)** Movie A15.

Figure A.24: Definition of the grain ID for each grain analysed from (**a**) Movie A12 (reproduction of Figure A.22g), (**b**) Movie A13 (reproduction of Figure A.22h) and (**c**) Movie A11 (reproduction of Figure 7.2c).

Table A.5: List of all grains analysed by SECCM in aerated condition (Movie A11-A13), with the average Euler angles, Miller indices and Projection Coordinates and anodic and cathodic E_{2mA} listed for each one. The grain IDs correspond to those defined in Figure A.24.

ID	Average Euler angles (°)			Average Miller indices			Projection Coordinates (°)		Average anodic E_{2mA} (V)	Average cathodic E_{2mA} (V)	Size (pixels)
	φ_1	Φ	φ_2	h	k	l	C_1	C_2			
1	263.40	29.21	8.53	0.072	0.483	0.873	44.898	6.123	0.5857	−0.4533	13
2	1.26	39.09	63.41	0.564	0.282	0.776	54.266	20.558	0.5879	−0.4038	21
3	155.75	40.48	81.09	0.641	0.101	0.761	59.986	7.309	0.5762	−0.4336	317
4	31.86	43.43	12.00	0.143	0.672	0.726	62.121	10.748	0.5746	−0.4220	14
5	256.55	28.10	28.72	0.226	0.413	0.882	41.083	14.512	0.5783	−0.4377	588
6	180.96	45.74	26.64	0.321	0.640	0.698	59.719	25.454	0.5811	−0.3895	193
7	2.56	2.61	61.88	0.040	0.021	0.999	4.041	1.207	0.5905	−0.4142	39
8	37.32	17.93	70.16	0.290	0.104	0.951	27.771	6.851	0.5793	−0.4381	65
9	80.78	25.12	61.13	0.372	0.205	0.905	37.114	12.785	0.5759	−0.4427	78
10	256.28	27.61	29.10	0.225	0.405	0.886	40.371	14.364	0.5769	−0.4391	40
11	32.63	43.18	11.18	0.133	0.671	0.729	62.130	9.911	0.5747	−0.4219	64
12	81.70	25.22	60.30	0.370	0.211	0.905	37.101	13.129	0.5794	−0.4410	19
13	157.84	39.58	81.67	0.630	0.092	0.771	59.036	6.759	0.5753	−0.4391	43
14	229.36	41.89	10.35	0.120	0.657	0.744	61.163	8.785	0.5811	−0.4288	96

Follows Table A.5.

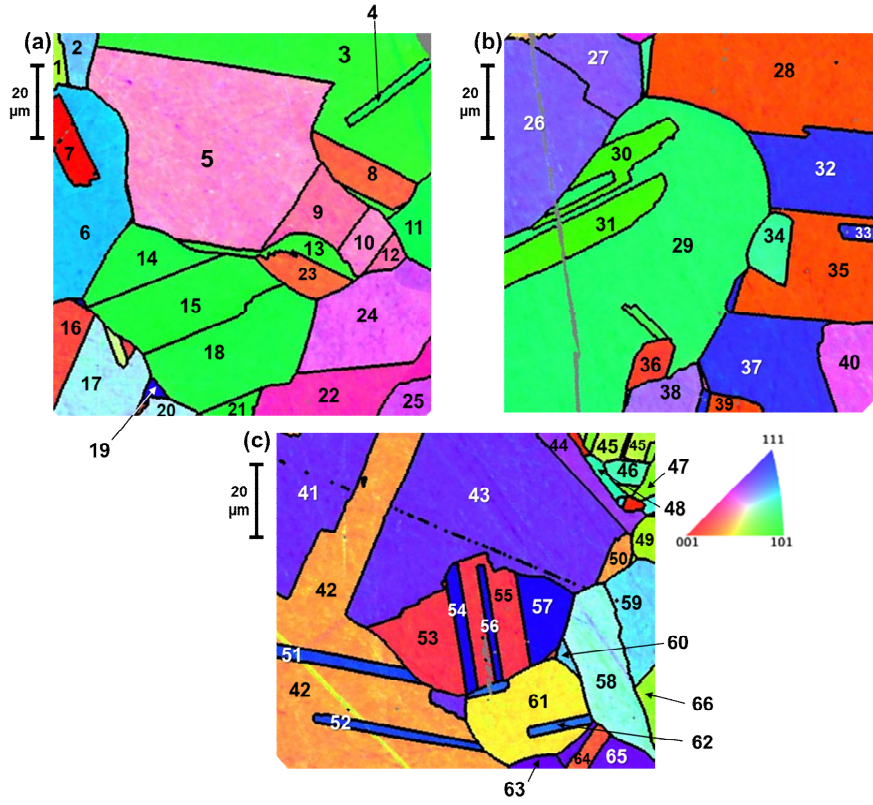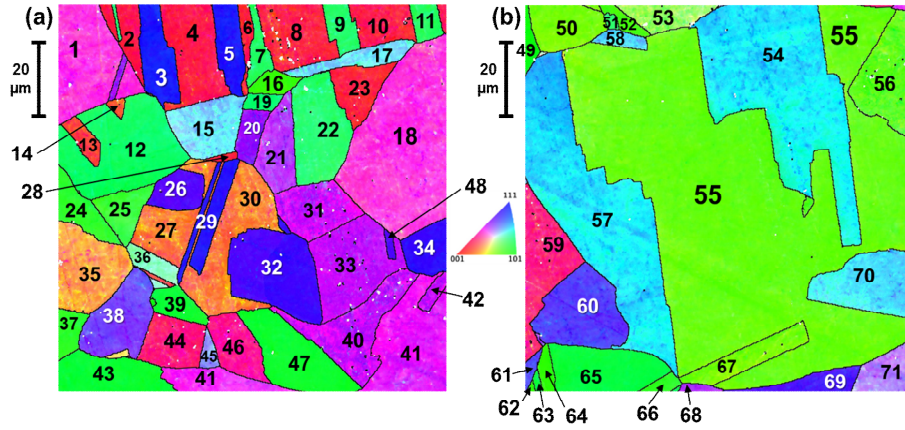| ID	Average Euler angles (°)			Average Miller indices			Projection Coordinates (°)		Average anodic E_{2mA} (V)	Average cathodic E_{2mA} (V)	Size (pixels)
	φ_1	Φ	φ_2	h	k	l	C_1	C_2			
15	353.13	41.57	80.97	0.655	0.104	0.748	61.139	7.587	0.5772	− 0.4343	167
16	235.41	15.96	66.89	0.253	0.108	0.961	24.615	6.716	0.5906	− 0.4342	35
17	60.36	35.98	24.60	0.245	0.534	0.809	51.573	17.162	0.5845	− 0.4247	73
18	229.25	42.00	10.41	0.121	0.658	0.743	61.255	8.865	0.5755	− 0.4320	214
19	316.60	49.60	45.43	0.543	0.534	0.648	56.391	43.467	0.5720	− 0.4236	7
20	60.36	35.98	24.60	0.245	0.534	0.809	51.573	17.162	0.5696	− 0.4183	2
21	352.67	41.63	81.48	0.657	0.098	0.747	61.311	7.169	0.5704	− 0.4170	2
22	299.68	24.20	37.73	0.251	0.324	0.912	34.142	14.957	0.5798	− 0.4504	80
23	35.9	17.61	72.09	0.288	0.093	0.953	27.380	6.317	0.5817	− 0.4376	45
24	136.87	29.59	55.58	0.407	0.279	0.870	41.614	17.865	0.5774	− 0.4267	189
25	137.78	29.71	54.07	0.401	0.291	0.869	41.354	18.560	0.5776	− 0.4408	17
26	83.77	38.12	34.52	0.350	0.509	0.787	50.887	25.022	0.5825	− 0.4007	225
27	246.10	36.75	55.34	0.492	0.340	0.801	49.484	23.874	0.5800	− 0.4038	100
28	3.75	11.06	4.94	0.017	0.191	0.981	17.289	2.480	0.5851	− 0.4175	335
29	244.49	42.65	75.53	0.656	0.169	0.735	60.818	12.659	0.5792	− 0.4222	716
30	159.76	36.79	2.27	0.024	0.598	0.801	55.507	3.087	0.5815	− 0.4461	67
31	161.72	36.46	2.00	0.021	0.594	0.804	55.022	2.999	0.5817	− 0.4514	98
32	116.72	44.40	38.66	0.437	0.546	0.714	54.917	33.869	0.5685	− 0.3852	174
33	116.50	44.36	39.22	0.442	0.542	0.715	54.678	34.184	0.5675	− 0.3779	11
34	220.88	40.90	18.63	0.209	0.620	0.756	58.158	15.438	0.5726	− 0.4048	42
35	3.86	10.89	4.80	0.016	0.188	0.982	17.021	2.431	0.5866	− 0.4144	190
36	117.87	13.31	70.25	0.217	0.078	0.973	20.749	5.085	0.5899	− 0.4297	23
37	116.76	44.46	38.61	0.437	0.547	0.714	54.983	33.901	0.5708	− 0.3938	169
38	135.78	33.76	55.66	0.459	0.313	0.831	46.432	21.140	0.5847	− 0.4163	38
39	2.07	10.98	6.95	0.023	0.189	0.982	17.210	2.696	0.5774	− 0.4131	9
40	283.18	29.70	55.25	0.407	0.282	0.869	41.659	18.082	0.5798	− 0.4330	76
41	93.64	38.79	39.37	0.397	0.484	0.779	49.823	28.355	0.5773	− 0.3964	163
42	207.13	21.55	75.19	0.355	0.094	0.930	33.445	6.799	0.5882	< − 0.457	495
43	93.68	38.74	39.25	0.396	0.485	0.780	49.821	28.243	0.5738	− 0.3932	491
44	263.79	34.76	51.54	0.446	0.355	0.822	46.181	23.983	0.5760	− 0.4025	61
45	27.21	29.20	10.02	0.085	0.480	0.873	44.870	6.754	0.5784	− 0.4544	27
46	178.82	40.26	20.37	0.225	0.606	0.763	57.097	16.526	0.5736	− 0.4069	18
47	341.00	31.35	4.19	0.038	0.519	0.854	47.877	4.379	0.5809	− 0.4464	10
48	344.96	43.52	20.41	0.240	0.645	0.725	59.899	18.389	0.5717	− 0.3995	11
49	77.16	27.48	4.07	0.033	0.460	0.887	42.196	4.300	0.5793	− 0.4506	17
50	206.98	21.33	75.20	0.352	0.093	0.932	33.115	6.734	0.5813	− 0.4545	19
51	291.07	47.73	53.28	0.593	0.442	0.673	58.021	35.945	0.5700	− 0.3890	24
52	290.93	47.69	53.46	0.594	0.440	0.673	58.052	35.758	0.5728	− 0.3891	22
53	318.56	15.76	28.18	0.128	0.239	0.962	23.937	7.550	0.5875	− 0.4418	96
54	242.27	50.28	44.62	0.540	0.547	0.639	56.842	44.354	0.5661	− 0.3801	27
55	318.50	15.66	28.24	0.128	0.238	0.963	23.784	7.510	0.5842	− 0.4388	96
56	242.51	50.34	44.20	0.537	0.552	0.638	57.073	44.225	0.5640	− 0.3840	14
57	241.95	50.01	45.28	0.544	0.539	0.643	56.609	44.056	0.5652	− 0.3776	64
58	270.22	36.60	66.65	0.547	0.236	0.803	52.569	16.702	0.5773	− 0.4161	140
59	123.60	40.05	25.24	0.274	0.582	0.765	55.565	20.217	0.5763	− 0.4006	78
60	123.00	40.44	26.31	0.288	0.581	0.761	55.617	21.304	0.5683	− 0.4023	4
61	180.31	24.29	81.29	0.407	0.062	0.911	37.628	5.562	0.5830	< − 0.457	145
62	266.85	45.65	57.56	0.603	0.384	0.699	57.940	30.437	0.5761	− 0.3908	10
63	238.89	38.85	45.02	0.444	0.443	0.779	47.655	30.924	0.5719	− 0.4080	15
64	43.18	16.75	69.56	0.270	0.101	0.958	25.959	6.524	0.5864	− 0.4553	15
65	278.50	38.92	46.59	0.456	0.432	0.778	48.370	30.374	0.5708	− 0.4031	21
66	217.85	30.00	83.97	0.497	0.053	0.866	46.004	5.135	0.5781	− 0.4523	18

Figure A.25:Definition of the grain ID for each grain analysed from (**a**) Movie A14 (reproduction of Figure A.23e) and (**b**) Movie A15 (reproduction of Figure A.23f).

Table A.6: List of all grains analysed by SECCM in aerated condition (Movie A14 and A15), with the average Euler angles, Miller indices and Projection Coordinates and anodic and cathodic E_{2mA} listed for each one. The grain IDs correspond to those defined in Figure A.25.

ID	Average Euler angles (°)			Average Miller indices			Projection Coordinates (°)		Average anodic E_{2mA} (V)	Average cathodic E_{2mA} (V)	Size (pixels)
	φ_1	Φ	φ_2	h	k	l	C_1	C_2			
1	319.95	26.97	53.28	0.364	0.271	0.891	37.843	16.720	0.1847	−0.3891	110
2	109.61	12.98	36.20	0.133	0.181	0.974	19.150	7.246	0.1914	−0.4244	23
3	39.11	49.28	48.56	0.568	0.502	0.652	57.454	41.237	0.1859	−0.3610	50
4	111.47	13.86	34.33	0.135	0.198	0.971	20.596	7.508	0.1912	−0.4255	76
5	39.61	48.99	47.94	0.560	0.506	0.656	57.020	41.308	0.1838	−0.3610	31
6	115.27	12.08	30.79	0.107	0.180	0.978	18.296	6.050	0.1867	−0.4165	11
7	1.33	41.82	13.90	0.160	0.647	0.745	60.227	11.831	0.1825	−0.3957	19
8	114.44	14.15	31.33	0.127	0.209	0.970	21.298	7.227	0.1910	−0.4260	69
9	1.37	41.79	14.15	0.163	0.646	0.746	60.136	12.035	0.1854	−0.3865	24
10	112.49	14.49	33.12	0.137	0.210	0.968	21.623	7.689	0.1918	−0.4272	36
11	1.72	41.40	13.40	0.153	0.643	0.750	59.957	11.250	0.1838	−0.3900	15
12	224.07	44.12	13.89	0.167	0.676	0.718	62.149	12.775	0.1792	−0.4140	143
13	345.07	15.06	23.58	0.104	0.238	0.966	23.232	6.412	0.1852	−0.4131	16
14	350.47	15.67	17.77	0.082	0.257	0.963	24.431	5.615	0.1868	−0.4190	6
15	299.36	38.64	64.58	0.564	0.268	0.781	54.154	19.407	0.1841	−0.3681	62
16	82.86	37.70	88.81	0.611	0.013	0.791	56.670	2.413	0.1815	−0.4203	13
17	298.91	38.78	64.53	0.565	0.269	0.780	54.279	19.536	0.1896	−0.3764	26
18	320.15	27.09	53.19	0.365	0.273	0.890	37.968	16.842	0.1840	−0.3845	238
19	101.02	45.43	75.22	0.689	0.182	0.702	62.815	14.245	0.1814	−0.4150	9
20	180.98	35.48	44.34	0.406	0.415	0.814	44.770	27.115	0.1837	−0.3856	24
21	274.85	32.52	52.26	0.425	0.329	0.843	44.025	21.643	0.1822	−0.3811	48
22	0.35	41.36	15.32	0.175	0.637	0.751	59.440	12.868	0.1831	−0.3795	87
23	116.09	12.93	29.75	0.111	0.194	0.975	19.631	6.354	0.1890	−0.4177	43
24	267.40	39.32	7.60	0.084	0.628	0.774	58.818	6.203	0.1803	−0.4335	33
25	350.60	38.20	80.50	0.610	0.102	0.786	57.191	7.469	0.1807	−0.3949	28
26	106.63	41.44	44.91	0.467	0.469	0.750	49.941	33.787	0.1829	−0.3710	28
27	225.97	18.88	74.34	0.312	0.087	0.946	29.388	6.228	0.1883	−0.4243	53
28	114.07	11.85	32.33	0.110	0.174	0.979	17.844	6.117	0.1958	−0.4185	2
29	312.45	47.30	47.80	0.544	0.494	0.678	55.755	39.373	0.1834	−0.3639	35
30	226.16	19.19	74.00	0.316	0.091	0.944	29.847	6.405	0.1872	−0.4200	96

A.6 – References

Follows Table A.6.

ID	Average Euler angles (°)			Average Miller indices			Projection Coordinates (°)		Average anodic E_{2mA} (V)	Average cathodic E_{2mA} (V)	Size (pixels)
	φ_1	Φ	φ_2	h	k	l	C_1	C_2			
31	134.78	30.49	43.72	0.351	0.367	0.862	39.877	22.031	0.1842	−0.3959	58
32	103.04	43.83	44.92	0.489	0.490	0.721	51.902	36.561	0.1858	−0.3698	110
33	281.27	31.37	44.47	0.365	0.371	0.854	40.562	23.098	0.1811	−0.3890	105
34	168.69	46.02	43.21	0.493	0.524	0.694	54.373	38.389	0.1862	−0.3762	33
35	30.30	22.21	16.25	0.106	0.363	0.926	34.371	7.410	0.1845	−0.4066	81
36	60.64	35.82	20.95	0.209	0.547	0.811	52.259	14.689	0.1828	−0.3824	21
37	267.57	39.37	7.25	0.080	0.629	0.773	58.922	5.953	0.1747	−0.4278	11
38	321.24	37.79	37.01	0.369	0.489	0.790	49.722	26.123	0.1849	−0.3698	70
39	71.17	43.36	8.32	0.099	0.679	0.727	63.023	7.372	0.1829	−0.3793	19
40	134.54	30.97	43.92	0.357	0.371	0.857	40.326	22.543	0.1833	−0.3888	79
41	343.55	28.85	49.64	0.368	0.312	0.876	39.097	19.464	0.1824	−0.3818	147
42	134.02	30.86	45.15	0.364	0.362	0.858	39.892	22.734	0.1843	−0.3902	10
43	71.49	44.05	8.15	0.099	0.688	0.719	63.642	7.419	0.1818	−0.3793	62
44	173.42	18.39	38.92	0.198	0.245	0.949	26.310	11.128	0.1881	−0.4182	47
45	8.56	36.59	60.14	0.517	0.297	0.803	50.798	20.915	0.1865	−0.3800	8
46	310.65	20.82	48.75	0.267	0.234	0.935	29.076	13.332	0.1839	−0.3888	43
47	49.68	43.49	82.55	0.682	0.089	0.725	63.357	6.614	0.1750	−0.4135	86
48	99.52	42.21	45.84	0.482	0.468	0.741	50.915	34.357	0.1867	−0.3744	3
49	206.48	43.63	2.28	0.027	0.689	0.724	64.658	2.030	0.1799	−0.4271	9
50	51.44	31.16	1.50	0.014	0.517	0.856	47.360	3.302	0.1853	−0.4257	46
51	345.40	40.65	15.09	0.170	0.629	0.759	58.815	12.397	0.1807	−0.3874	3
52	68.22	36.03	87.42	0.588	0.026	0.809	54.462	3.336	0.1864	−0.4315	8
53	185.12	32.16	14.06	0.129	0.516	0.847	48.793	9.242	0.1900	−0.4206	23
54	228.43	45.40	24.63	0.297	0.647	0.702	60.063	23.392	0.1809	−0.3828	307
55	314.88	32.84	3.22	0.030	0.541	0.840	49.961	3.908	0.1825	−0.4320	1073
56	189.68	34.49	85.30	0.564	0.046	0.824	52.412	4.517	0.1895	−0.4208	82
57	227.71	45.23	25.63	0.307	0.640	0.704	59.662	24.175	0.1823	−0.3849	302
58	47.74	40.94	64.07	0.589	0.287	0.755	56.179	21.364	0.1801	−0.3833	14
59	294.06	19.44	54.49	0.271	0.193	0.943	28.281	11.122	0.1883	−0.4059	87
60	149.13	41.00	52.48	0.520	0.400	0.755	52.505	29.585	0.1795	−0.3849	94
61	148.34	41.20	53.39	0.529	0.393	0.752	53.006	29.230	0.1816	−0.3968	5
62	322.33	38.73	0.18	0.002	0.626	0.780	57.963	1.736	0.2002	−0.4577	1
63	243.54	44.33	9.97	0.121	0.688	0.715	63.369	9.216	0.1804	−0.4246	2
64	322.31	38.72	0.09	0.001	0.626	0.780	57.934	1.697	0.1822	−0.4183	11
65	244.34	44.46	9.74	0.118	0.690	0.714	63.527	9.051	0.1802	−0.4257	82
66	5.06	39.13	83.52	0.627	0.071	0.776	58.699	5.404	0.1806	−0.4149	9
67	86.81	31.08	1.29	0.012	0.516	0.856	47.219	3.227	0.1857	−0.4217	43
68	16.60	32.51	39.28	0.340	0.416	0.843	43.523	22.275	0.1827	−0.3753	6
69	189.31	42.80	48.01	0.505	0.455	0.734	52.323	34.017	0.1799	−0.3791	28
70	45.30	41.66	64.72	0.601	0.284	0.747	56.998	21.349	0.1829	−0.3764	87
71	321.01	33.57	60.34	0.481	0.274	0.833	47.546	18.572	0.1818	−0.3760	36

A.6.   REFERENCES

[1]   Guell, A. G.; Meadows, K. E.; Dudin, P. V.; Ebejer, N.; Macpherson, J. V.; Unwin, P. R. Mapping nanoscale electrochemistry of individual single-walled carbon nanotubes. *Nano Lett.* **2014,** *14* (1), 220-224.

[2]   Byers, J. C.; Güell, A. G.; Unwin, P. R. Nanoscale Electrocatalysis: Visualizing Oxygen Reduction at Pristine, Kinked, and Oxidized Sites on Individual Carbon Nanotubes. *J. Am. Chem. Soc.* **2014,** *136* (32), 11252-11255.

[3]   Ustarroz, J.; Ornelas, I. M.; Zhang, G.; Perry, D.; Kang, M.; Bentley, C. L.; Walker, M.; Unwin, P. R. Mobility and Poisoning of Mass-Selected Platinum

Nanoclusters during the Oxygen Reduction Reaction. *ACS Catal.* **2018,** *8* (8), 6775-6790.

[4]   Xing, W.; Yin, M.; Lv, Q.; Hu, Y.; Liu, C.; Zhang, J. In *Rotating Electrode Methods and Oxygen Reduction Electrocatalysts*; Xing, W.;Yin, G.;Zhang, J., Eds.; Elsevier: Amsterdam, 2014.

[5]   Kowert, B. A.; Dang, N. C. Diffusion of Dioxygen in n-Alkanes. *J. Phys. Chem. A* **1999,** *103* (7), 779-781.

[6]   Battino, R.; Seybold, P. G. The O2/N2 Ratio Gas Solubility Mystery. *J. Chem. Eng. Data* **2011,** *56* (12), 5036-5044.

[7]   Abraham, M. H.; Acree Jr, W. E. Correlation and prediction of partition coefficients between the gas phase and water, and the solvents dodecane and undecane. *New J. Chem.* **2004,** *28* (12), 1538-1543.

[8]   Barker, A. L.; Macpherson, J. V.; Slevin, C. J.; Unwin, P. R. Scanning Electrochemical Microscopy (SECM) as a Probe of Transfer Processes in Two-Phase Systems: Theory and Experimental Applications of SECM-Induced Transfer with Arbitrary Partition Coefficients, Diffusion Coefficients, and Interfacial Kinetics. *J. Phys. Chem. B* **1998,** *102* (9), 1586-1598.

[9]   Kourounis, D.; Fuchs, A.; Schenk, O. Toward the Next Generation of Multiperiod Optimal Power Flow Solvers. *IEEE Trans. Power Syst.* **2018,** *33* (4), 4005-4014.

[10]   Andersen, T. N.; Ghandehari, M. H.; Eyring, H. A Limitation to the Mixed Potential Concept of Metal Corrosion: Copper in Oxygenated Sulfuric Acid Solutions. *J. Electrochem. Soc.* **1975,** *122* (12), 1580-1585.

[11]   Chen, C.-H.; Meadows, K. E.; Cuharuc, A.; Lai, S. C. S.; Unwin, P. R. High resolution mapping of oxygen reduction reaction kinetics at polycrystalline platinum electrodes. *Phys. Chem. Chem. Phys.* **2014,** *16* (34), 18545-18552.

[12]   Mariano, R. G.; McKelvey, K.; White, H. S.; Kanan, M. W. Selective increase in CO_2 electroreduction activity at grain-boundary surface terminations. *Science* **2017,** *358* (6367), 1187.

[13]   Snowden, M. E.; Güell, A. G.; Lai, S. C. S.; McKelvey, K.; Ebejer, N.; O'Connell, M. A.; Colburn, A. W.; Unwin, P. R. Scanning Electrochemical Cell Microscopy: Theory and Experiment for Quantitative High Resolution Spatially-Resolved Voltammetry and Simultaneous Ion-Conductance Measurements. *Anal. Chem.* **2012,** *84* (5), 2483-2491.